

**Formulation Enhancement of Poorly Water-Soluble Pharmaceuticals by CO<sub>2</sub>-Based Crystallization Technologies**

by

Courtney Ann Ober

A dissertation submitted to the Graduate Faculty of  
Auburn University  
in partial fulfillment of the  
requirements for the Degree of  
Doctor of Philosophy

Auburn, Alabama  
May 5, 2013

Keywords: Carbon Dioxide, Cocrystallization, Dissolution Enhancement, Micronization,  
Pharmaceuticals, Supercritical Fluids

Copyright 2013 by Courtney Ann Ober

Approved by

Ram B. Gupta, Chair, Professor of Chemical Engineering  
Christopher B. Roberts, Dean of Samuel Ginn College of Engineering  
Elizabeth A. Lipke, Assistant Professor of Chemical Engineering  
Jayachandra B. Ramapuram, Assistant Professor of Pharmacal Sciences

## Abstract

This dissertation demonstrates the applicability of tunable solvent systems to the development of novel particulate formulations which enhance the deliverability and dissolution of poorly water-soluble active pharmaceutical ingredients (APIs). With approximately 40% of APIs discovered through combinatorial chemistry and high throughput screening having an aqueous solubility of less than 10  $\mu\text{M}$ , there is a significant need for formulations which enhance drug dissolution. Furthermore, the processing techniques used must be scalable and environmentally benign while producing formulations which conform to the existing standards of purity and reproducibility. To this end, particulate formulations of two poorly water-soluble APIs were developed using two novel  $\text{CO}_2$ -based crystallization technologies: supercritical antisolvent-drug excipient mixing (SAS-DEM) and gas antisolvent (GAS) cocrystallization.

Using a supercritical antisolvent (SAS) crystallization process, rifampicin microparticles were crystallized in the presence of inhalation size appropriate lactose monohydrate particles to create rifampicin/lactose microparticle composites intended to increase the respirable fraction of rifampicin when delivered via a dry powder inhaler. In addition to a decrease in particle size observed by scanning electron microscopy, powder X-ray diffraction (PXRD) revealed conversion of the less soluble ( $0.59 \pm 0.05$  mg/mL) crystalline form I of rifampicin to the more soluble rifampicin dihydrate ( $1.28 \pm 0.01$  mg/mL) during SAS crystallization from methanol. Through the preparation of

rifampicin/lactose microparticle composites, the SAS-DEM process was found effective at preparing inhalation size appropriate rifampicin microparticles ( $d < 8 \mu\text{m}$ ), preventing particle agglomeration, and providing excellent mixture homogeneity (RSDs  $< 5.7\%$ ), all in a single-step.

Guided by the Noyes-Whitney equation, itraconazole microflakes with increased surface area were crystallized from dichloromethane by a SAS process and simultaneously deposited on the surface of excipient lactose particles ( $d \sim 100 \mu\text{m}$ ) to prevent microflake agglomeration. At low drug loadings (6 wt. %) the presence of lactose prevented microflake agglomeration and facilitated rapid itraconazole dissolution ( $D_{60} = 91\%$ ), but at high drug loadings (40 wt. %) the surface of the lactose became saturated and the excess microflakes agglomerated, reducing the dissolution rate ( $D_{60} = 64\%$ ). By adding a tri-block copolymer (Pluronic F-127) in solution with itraconazole during crystallization, particle morphology was altered such that the dissolution of itraconazole was enhanced ( $D_{60} = 85\%$ ) even at high drug to lactose loadings (50 wt. %). Pluronic F-127 did not affect the crystallinity of itraconazole, as verified by PXRD, but is thought to associate on the surface, thus improving the drug's wettability.

GAS cocrystallization was investigated as a novel means of preparing itraconazole–dicarboxylic acid cocrystals with enhanced dissolution. The crystal lattice of itraconazole, as characterized by PXRD, was unaffected following dissolution in tetrahydrofuran (THF) and subsequent recrystallization by pressurization with  $\text{CO}_2$ . Simultaneous dissolution and recrystallization of itraconazole and L-malic acid from THF gave a primarily amorphous product, attributed to the high solubility of L-malic acid in THF, which demonstrated only marginal improvements in dissolution. Alternatively,

GAS cocrystallization of itraconazole with succinic acid from THF gave a stable, crystalline product which featured rapid dissolution ( $D_{60} = 76\%$ ). Thermal analysis, which revealed the presence of an itraconazole/succinic acid eutectic, confirmed that a greater extent of cocrystallization was achievable using  $\text{CO}_2$  as the antisolvent compared to a traditional liquid antisolvent, *n*-heptane. GAS cocrystallization is governed by the pressure-dependent solubilities of drug and former in the  $\text{CO}_2$ -expanded liquid, solubilities which are predictable by thermodynamic modeling. This work lays the foundation for the development of a thermodynamically predictable, highly tunable, and widely applicable technique for producing pharmaceutical cocrystals.

## Acknowledgements

I would like to thank my advisor, Dr. Ram Gupta, for his ideas and direction on this work, as well as my committee members, Dr. Chris Roberts, Dr. Elizabeth Lipke, and Dr. Jay Ramapuram, for their willingness to serve on my committee and their input. I would like to thank Dr. Bernhard Kaltenboeck for his willingness to serve as my outside reader. I would also like to acknowledge Lonji Kalombo, Sateesh Sathigari, and Stephen Montgomery for their contributions to the work presented in this dissertation. I would like to thank my fellow lab mates, Hema Ramsurn and Shaima Nahreen, for their helpful discussions and support over the last four years and my previous lab mates, Ganesh Sanganwar and Adam Byrd, for their assistance when I first started in the lab. Funding for a portion of this work was provided by the National Science Foundation through NIRT grant DMI-0506722 and REU grant 1063107. Last but not least, I would like to acknowledge my parents and family, my best friend Matthew Kayatin, and Jennifer Duggan, Pranav Vengsarkar, and all of my other friends that have made my time here in Auburn so enjoyable.

*“To give anything less than your best is to sacrifice the gift.”*

*Steve Prefontaine*

## Table of Contents

Abstract .....	ii
Acknowledgements .....	v
List of Tables .....	xii
List of Figures .....	xiv
List of Abbreviations .....	xxi
Chapter 1. Introduction .....	1
1.1 Pharmaceutical Formulation .....	1
1.1.1 Drug Delivery .....	1
1.1.2 Dosage Formulation .....	2
1.1.3 Polymorphism .....	3
1.2 Poorly Water-Soluble Pharmaceuticals .....	4
1.2.1 BCS Class II Biopharmaceuticals .....	4
1.2.2 Strategies for Dissolution Enhancement .....	5
1.3 Particle Size Reduction for Dissolution Enhancement .....	6
1.3.1 The Noyes-Whitney Equation .....	6
1.3.2 Microparticle Agglomeration .....	7
1.3.3 Microparticle Deagglomeration .....	8
1.3.4 Approaches to Micronization .....	9
1.4 Particle Formation Using Supercritical CO <sub>2</sub> .....	10

1.4.1 Supercritical CO <sub>2</sub> .....	10
1.4.2 Solubility in Supercritical CO <sub>2</sub> .....	11
1.4.3 Micronization Using Supercritical CO <sub>2</sub> .....	13
1.5 Pharmaceutical Cocrystal Engineering .....	15
1.5.1 Physical Property Enhancement Through Cocrystallization .....	16
1.5.2 Methods for Cocrystallization.....	18
1.6 Crystallization in CO <sub>2</sub> -Expanded Liquids .....	19
1.6.1 Gas-Expanded Liquids.....	19
1.6.2 Modeling VLE Behavior Using the Peng-Robinson Equation of State .....	20
1.6.3 Tunable Properties of CO <sub>2</sub> -Expanded Liquids .....	21
1.6.4 Gas Antisolvent Crystallization .....	23
1.7 Summary of Chapters .....	25
1.7.1 Chapter 2 .....	25
1.7.2 Chapter 3 .....	25
1.7.3 Chapter 4 .....	26
1.7.4 Chapter 5 .....	27
1.7.5 Chapter 6 .....	27
Chapter 2. Materials and Methods .....	29
2.1 Materials .....	29
2.1.1 Active Pharmaceutical Ingredients .....	29
2.1.2 Excipients, Stabilizers, and Formers .....	31
2.1.3 Solvents and Antisolvents .....	34
2.2 Crystallization Technologies .....	35

2.2.1 Supercritical Antisolvent Crystallization .....	35
2.2.2 Supercritical Antisolvent-Drug Excipient Mixing .....	36
2.2.3 Liquid Antisolvent Cocrystallization .....	37
2.2.4 Gas Antisolvent Cocrystallization .....	38
2.3 Characterization Techniques .....	42
2.3.1 Scanning Electron Microscopy .....	42
2.3.2 Powder X-ray Diffraction .....	42
2.3.3 Differential Scanning Calorimetry .....	43
2.3.4 Fourier Transform Infrared Spectroscopy .....	43
2.3.5 Drug Loading and Content Uniformity .....	43
2.3.6 Dynamic Light Scattering .....	44
2.3.7 Brunauer-Emmett-Teller Surface Area .....	45
2.3.8 Saturation Solubility .....	45
2.3.9 High Pressure Liquid Chromatography .....	45
2.3.10 Gas-Expanded Liquid Solubility .....	46
2.3.11 Dissolution Studies .....	47
2.3.12 Physical Stability .....	48
Chapter 3. Preparation of Rifampicin/Lactose Microparticle Composites by a Supercritical Antisolvent-Drug Excipient Mixing Technique for Inhalation Delivery ....	49
3.1 Rifampicin for the Treatment of Tuberculosis.....	49
3.2 SAS Crystallization of Rifampicin Micro- and Nanoparticles .....	52
3.2.1 Scanning Electron Microscopy .....	52
3.2.2 Powder X-ray Diffraction .....	58
3.3 Rifampicin/Lactose Microparticle Composites by SAS-DEM .....	60



3.4 Characterization of Rifampicin/Lactose Microparticle Composites .....	63
3.4.1 Scanning Electron Microscopy .....	63
3.4.2 Powder X-ray Diffraction .....	64
3.4.3 Differential Scanning Calorimetry .....	66
3.4.4 Fourier Transform Infrared Spectroscopy .....	68
3.5 Conclusions .....	70
Chapter 4. Simultaneous Production and Deagglomeration of Itraconazole Microflakes by Supercritical Antisolvent-Drug Excipient Mixing .....	72
4.1 Dissolution Enhancement of Itraconazole .....	72
4.2 SAS Crystallization of Itraconazole Microflakes .....	75
4.3 SAS-DEM Mixtures of Itraconazole and Lactose .....	80
4.4 SAS-DEM Mixtures of Itraconazole and Lactose with Stabilizers .....	88
4.4.1 Electrostatic Stabilization with Sodium Dodecyl Sulfate .....	90
4.4.2 Steric Stabilization with Pluronic F-127 .....	92
4.5 Characterization of Itraconazole Products .....	98
4.5.1 Powder X-ray Diffraction .....	98
4.5.2 Differential Scanning Calorimetry .....	101
4.5.3 Fourier Transform Infrared Spectroscopy .....	104
4.6 Conclusions .....	105
Chapter 5. Formation of Itraconazole/L-Malic Acid Cocrystals in a CO <sub>2</sub> -Expanded Liquid .....	107
5.1 Crystallization in CO <sub>2</sub> -Solvent Systems .....	107
5.2 Recrystallization from CO <sub>2</sub> -Expanded Tetrahydrofuran .....	109
5.2.1 Scanning Electron Microscopy .....	112

5.2.2 Powder X-ray Diffraction .....	113
5.3 GAS Cocrystallization of Itraconazole and L-malic Acid .....	115
5.4 Characterization of Cocrystal Products .....	120
5.4.1 Powder X-ray Diffraction .....	120
5.4.2 Differential Scanning Calorimetry .....	122
5.4.3 Scanning Electron Microscopy .....	127
5.4.4 Compositional Analysis .....	128
5.4.5 Dissolution Studies .....	130
5.5 Conclusions .....	135
Chapter 6. Formation of Itraconazole–Succinic Acid Cocrystals by Gas Antisolvent Cocrystallization .....	137
6.1 Gas Antisolvent Cocrystallization .....	137
6.2 Cocrystal Formation by GAS Cocrystallization .....	139
6.3 Characterization of Cocrystallization .....	141
6.3.1 Powder X-ray Diffraction .....	141
6.3.2 Fourier Transform Infrared Spectroscopy .....	143
6.3.3 Compositional Analysis .....	146
6.3.4 Differential Scanning Calorimetry .....	147
6.4 Dissolution Enhancement by GAS Cocrystallization .....	151
6.4.1 Scanning Electron Microscopy .....	151
6.4.2 Dissolution Studies .....	153
6.4.3 Stability Studies .....	156
6.5 Conclusions .....	159
Chapter 7. Conclusions .....	161

Chapter 8. Future Directions .....	164
References .....	167
Appendices .....	185
A. Particle Stabilization in Antisolvent Crystallization .....	185
A.1 Electrostatic Stabilization .....	185
A.2 Steric Stabilization .....	188
A.3 Stabilization of Itraconazole .....	190
A.4 References .....	193
B. Thermodynamic Modeling of GAS Cocrystallization .....	194
B.1 Phase Equilibria.....	196
B.2 Binary Interaction Parameters .....	201
B.3 References .....	206
C. Peer-Reviewed Publications .....	209
D. Conference Presentations and Posters .....	210

## List of Tables

Table 1.1 Cocrystals of poorly water-soluble APIs .....	17
Table 2.1 Solvents and antisolvents .....	35
Table 3.1 Rifampicin loading, relative standard deviation (RSD), and maximum and minimum concentrations observed in RSD analysis for rifampicin/lactose microparticle composites produced by SAS-DEM .....	61
Table 4.1 Particle size distribution (PSD) and specific surface area of supplier (micronized) itraconazole and SAS itraconazole microflakes.....	78
Table 4.2 PSDs of SAS-DEM itraconazole and lactose mixtures .....	87
Table 4.3 PSDs of SAS-DEM itraconazole and lactose mixtures with Pluronic F-127 ..	97
Table 4.4 Relative standard deviation (RSD) of itraconazole content for SAS-DEM mixtures at various drug loadings .....	98
Table 5.1 Summary of melting temperatures ( $T_m$ ) and enthalpies of fusion ( $\Delta H_f$ ) .....	126
Table 5.2 RSD of itraconazole content in cocrystal products .....	129
Table 5.3 Mean cumulative dissolved itraconazole after 60 ( $D_{60}$ ) and 120 ( $D_{120}$ ) minutes for various formulations (mean $\pm$ standard error) .....	131
Table 5.4 Physical properties of itraconazole .....	133
Table 5.5 Physical properties of an itraconazole/L-malic acid cocrystal .....	134
Table 6.1 Relevant hydrogen bonding functional groups in an itraconazole–succinic acid cocrystal .....	145
Table 6.2 Physical mixtures of itraconazole and succinic acid for DSC analysis .....	150
Table B.1 Phase equilibria equations for ternary three phase systems .....	197

Table B.2 Critical properties and acentric factors for CO<sub>2</sub>, ethanol, acetaminophen, and oxalic acid ..... 199

Table B.3 Physical properties of acetaminophen and oxalic acid ..... 201

## List of Figures

Figure 1.1 Drug development process .....	1
Figure 1.2 Solid forms of an API .....	3
Figure 1.3 Biopharmaceutics classification system (BCS) .....	5
Figure 1.4 Specific surface area as a function of particle size for spherical particles ( $m = 10 \text{ g}$ , $\rho = 1 \text{ g/cm}^3$ ) .....	8
Figure 1.5 Top-down versus bottom-up approaches to micronization .....	9
Figure 1.6 Pressure versus temperature phase diagram for $\text{CO}_2$ .....	11
Figure 1.7 Pressure and temperature dependence of $\text{CO}_2$ density ( — 32 °C, — 36 °C, — 40 °C, — 50 °C, — 75 °C, — 100 °C) .....	12
Figure 1.8 Solubility of itraconazole in supercritical $\text{CO}_2$ at 50 °C (◆), 100 °C (■), and 130 °C (●) .....	13
Figure 1.9 Schematic of the SAS process .....	15
Figure 1.10 Vapor-liquid equilibria for $\text{CO}_2$ -organic solvent mixtures: methanol at 40 °C (■), ethanol at 40 °C (●), methanol at 25 °C (■), ethanol at 25 °C (●), acetone at 40 °C (▲), acetone at 25 °C (▲) .....	20
Figure 1.11 Volumetric expansion ( $V/V_0$ ) of methanol as a function of $\text{CO}_2$ pressure at 25 °C (■) and solubility parameter ( $\delta$ ) of $\text{CO}_2$ -expanded methanol (●) .....	22
Figure 1.12 Solubility of acetaminophen in $\text{CO}_2$ -expanded ethanol at 22 °C (◆), 42 °C (■), and 44 °C (▲) .....	23
Figure 2.1 (a) Chemical structure and (b) 3-D depiction of rifampicin .....	30
Figure 2.2 (a) Chemical structure and (b) 3-D depiction of itraconazole .....	31

Figure 2.3 Particle size distribution of Lactochem® Microfine (as reported by the manufacturer) .....	32
Figure 2.4 Chemical structure of sodium dodecyl sulfate (SDS) .....	32
Figure 2.5 Chemical structure of Pluronic® F-127 (x ~ 98 and y ~ 57) .....	33
Figure 2.6 (a) Chemical structure and (b) 3-D representation of L-malic acid .....	34
Figure 2.7 (a) Chemical structure and (b) 3-D representation of succinic acid .....	34
Figure 2.8 Schematic of apparatus for SAS crystallization .....	36
Figure 2.9 Schematic of GAS cocrystallization apparatus (Version 1.0) .....	38
Figure 2.10 Pressure profile for GAS cocrystallization (Version 1.0) Ia. Pressurization at 6.89 bar/min, Ib. Pressurization by CO <sub>2</sub> pumping at 1 g/min, II. Cocrystal drying at 103 bar, and III. Depressurization .....	39
Figure 2.11 Schematic of apparatus for GAS cocrystallization (Version 2.0) .....	40
Figure 2.12 Pressure profile for GAS cocrystallization (Version 2.0) .....	41
Figure 3.1 Chemical structures of (a) isoniazid, (b) pyrazinamide, and (c) rifampicin ...	50
Figure 3.2 SEM images of (a) supplier rifampicin and (b) rifampicin nanoparticles precipitated from DMSO at 10 mg/mL, 124 bar, and 40 °C .....	53
Figure 3.3 SEM image of supplier lactose monohydrate .....	55
Figure 3.4 SEM images of (a) rifampicin microflakes crystallized from methanol at 10 mg/mL, 124 bar, and 40 °C and (b) rifampicin microparticles crystallized from methanol at 5 mg/mL, 124 bar, and 40 °C .....	56
Figure 3.5 SEM image of lactose monohydrate following SAS processing with pure methanol (no rifampicin) at 124 bar and 40 °C .....	57
Figure 3.6 PXRD patterns (from bottom to top) for (a) rifampicin, (b) SAS rifampicin precipitated from DMSO, and (c) SAS rifampicin crystallized from methanol .....	59
Figure 3.7 Visual observation of increasing rifampicin content in rifampicin/lactose composites .....	62
Figure 3.8 SEM images of composites obtained from SAS-DEM with (a) 1.2 wt. % rifampicin loading (run 1), (b) 7.2 wt. % rifampicin loading (run 2), (c) 14.0 wt. % rifampicin loading (run 3), and (d) 25.7 wt. % rifampicin loading (run 4) .....	64

Figure 3.9 PXRD patterns (from bottom to top) for (a) SAS processed lactose monohydrate, (b) SAS-DEM composite with 1.2 wt. % rifampicin loading, (c) SAS-DEM composite with 7.2 wt. % rifampicin loading, (d) SAS-DEM composite with 14.0 wt. % rifampicin loading, (e) SAS-DEM composite with 25.7 wt. % rifampicin loading, and (f) SAS rifampicin ..... 66

Figure 3.10 DSC thermographs (from top to bottom) for (a) rifampicin, (b) SAS rifampicin, (c) SAS-DEM composite with 25.7 wt. % rifampicin loading, (d) SAS-DEM composite with 14.0 wt. % rifampicin loading, (e) SAS-DEM composite with 7.2 wt. % rifampicin loading, (f) SAS-DEM composite with 1.2 wt. % rifampicin loading, and (g) lactose monohydrate ..... 68

Figure 3.11 FTIR spectra (from top to bottom) for (a) rifampicin, (b) SAS rifampicin, (c) SAS-DEM composite with 25.7 wt. % rifampicin loading, (d) SAS-DEM composite with 14.0 wt. % rifampicin loading, (e) SAS-DEM composite with 7.2 wt. % rifampicin loading, (f) SAS-DEM composite with 1.2 wt. % rifampicin loading, and (g) lactose monohydrate ..... 70

Figure 4.1 Chemical structures of azole antifungal agents (a) ketoconazole, (b) miconazole, (c) fluconazole, and (d) itraconazole ..... 73

Figure 4.2 SEM images of (a) supplier (micronized) itraconazole and (b) SAS-produced itraconazole microflakes ..... 76

Figure 4.3 SEM image of SAS itraconazole microflakes with dimensions ..... 77

Figure 4.4 Dissolution profiles for supplier (micronized) itraconazole (●) and SAS itraconazole microflakes (■) ..... 79

Figure 4.5 SEM image of spray dried lactose excipient particles ..... 82

Figure 4.6 SEM image of SAS-DEM mixture with 6 wt. % itraconazole loading ..... 83

Figure 4.7 Dissolution profiles for supplier itraconazole (●), SAS itraconazole microflakes (■), and SAS-DEM mixture with 6 wt. % itraconazole loading (◆) ..... 84

Figure 4.8 Dissolution profiles for supplier itraconazole (●), SAS itraconazole microflakes (■), SAS-DEM mixture with 6 wt. % itraconazole loading (◆), SAS-DEM mixture with 23 wt. % itraconazole loading (●), physical mixture with 25 wt. % itraconazole loading (▲), and SAS-DEM mixture with 40 wt. % itraconazole loading (▲) ..... 85

Figure 4.9 SEM image of SAS-DEM mixture with 23 wt. % itraconazole loading ..... 86

Figure 4.10 SEM image of itraconazole microflakes stabilized with 10 wt. % SDS ..... 90



Figure 4.11 Dissolution profiles for supplier itraconazole (●), SAS itraconazole microflakes (■), SAS itraconazole microflakes stabilized with 1 wt. % SDS (◆), and SAS itraconazole microflakes stabilized with 10 wt. % SDS (●) .....	91
Figure 4.12 SEM image of itraconazole microflakes stabilized with 10 wt. % Pluronic F-127 .....	93
Figure 4.13 Dissolution profiles for supplier itraconazole (●), SAS itraconazole microflakes (■), SAS itraconazole microflakes stabilized with 1 wt. % Pluronic F-127 (◆), physical mixture of SAS itraconazole microflakes with 10 wt. % Pluronic F-127 (▲), and SAS itraconazole microflakes with 10 wt. % Pluronic F-127 (●) .....	94
Figure 4.14 Adsorption of Pluronic F-127 on the surface of a hydrophobic drug particle .....	95
Figure 4.15 SEM image of SAS-DEM mixture with 50 wt. % itraconazole loading stabilized with 10 wt. % Pluronic F-127 .....	96
Figure 4.16 Dissolution profiles for supplier itraconazole (●), SAS itraconazole microflakes (■), SAS-DEM mixture with 40 wt. % itraconazole (◆), and SAS-DEM mixture with 50 wt. % itraconazole stabilized with 10 wt. % Pluronic F-127 (▲) .....	97
Figure 4.17 PXRD patterns for (a) supplier itraconazole, (b) SAS itraconazole microflakes, (c) itraconazole microflakes stabilized with 10 wt. % SDS, and (d) itraconazole microflakes stabilized with 10 wt. % Pluronic F-127 .....	100
Figure 4.18 DSC thermographs (from bottom to top) for (a) itraconazole, (b) SAS itraconazole microflakes, (c) SDS, (d) itraconazole microflakes stabilized with 10 wt. % SDS, (e) Pluronic F-127, (f) itraconazole microflakes stabilized with 10 wt. % Pluronic F-127, (g) lactose, (h) SAS-DEM mixture of itraconazole (40 wt. %) and lactose, and (i) SAS-DEM mixture of itraconazole (15 wt. %) and lactose stabilized with 10 wt. % Pluronic F-127 .....	103
Figure 4.19 FTIR spectra (from bottom to top) for (a) itraconazole, (b) SAS itraconazole microflakes, (c) itraconazole microflakes stabilized with 10 wt. % SDS, (d) itraconazole microflakes stabilized with 10 wt. % Pluronic F-127, (e) SAS-DEM mixture of itraconazole (40 wt. %) and lactose, and (f) SAS-DEM mixture of itraconazole (15 wt. %) and lactose stabilized with 10 wt. % Pluronic F-127 .....	105
Figure 5.1 Mole fraction of CO <sub>2</sub> ( $x_{CO_2}$ ) in THF at 40 °C (●) and volume expansion ( $V/V_0$ ) of a CO <sub>2</sub> /THF mixture at 40 °C (■) .....	110
Figure 5.2 SEM images of (a) supplier itraconazole, (b) CO <sub>2</sub> -recrystallized itraconazole, (c) supplier L-malic acid, and (d) CO <sub>2</sub> -recrystallized L-malic acid .....	113

Figure 5.3 PXRD patterns of supplier itraconazole (—) and CO <sub>2</sub> -recrystallized itraconazole (.....)	114
Figure 5.4 PXRD patterns of supplier L-malic acid (—) and CO <sub>2</sub> -recrystallized L-malic acid (.....)	115
Figure 5.5 Chemical structure of a 2:1 itraconazole–succinic acid cocrystal	117
Figure 5.6 Visualization of the GAS cocrystallization process: (a) Clear solution of dissolved itraconazole and L-malic acid in THF, (b) onset of particle crystallization around 41 bar, (c) near complete crystallization around 70 bar, and (d) dry powder following supercritical CO <sub>2</sub> flushing at 103 bar	118
Figure 5.7 Itraconazole concentration in THF (CO <sub>2</sub> -free basis) at 40 °C and in the presence of L-malic acid as a function of pressure	120
Figure 5.8 PXRD patterns of itraconazole/L-malic acid cocrystals produced using a liquid antisolvent, <i>n</i> -heptane, (—) and itraconazole/L-malic acid cocrystals produced by GAS cocrystallization (—)	121
Figure 5.9 DSC thermographs for (a) itraconazole, (b) L-malic acid, (c) itraconazole/L-malic acid cocrystals from <i>n</i> -heptane, and (d) itraconazole/L-malic acid cocrystals produced by GAS cocrystallization	124
Figure 5.10 DSC thermograph for a 1:1 by mass physical mixture of itraconazole and L-malic acid	125
Figure 5.11 SEM images of (a and b) itraconazole/L-malic acid cocrystals obtained from <i>n</i> -heptane, and (c and d) itraconazole/L-malic acid cocrystals produced by GAS cocrystallization	128
Figure 5.12 Dissolution profiles for itraconazole (◆), a 1:1 by mass physical mixture of itraconazole and L-malic acid (●), itraconazole/L-malic acid cocrystals produced from <i>n</i> -heptane (■), and itraconazole/L-malic acid cocrystals produced by GAS cocrystallization (▲)	131
Figure 6.1 PXRD patterns for (a) itraconazole, (b) succinic acid, (c) a 1:1 by mass physical mixture of itraconazole and succinic acid, (d) itraconazole–succinic acid cocrystals from <i>n</i> -heptane, and (e) itraconazole–succinic acid cocrystals produced by GAS cocrystallization (★ = characteristic peak)	142
Figure 6.2 FTIR spectra for (a) itraconazole, (b) succinic acid, (c) a 1:1 by mass physical mixture of itraconazole and succinic acid, (d) itraconazole–succinic acid cocrystals from <i>n</i> -heptane, and (e) itraconazole–succinic acid cocrystals produced by GAS cocrystallization	145

Figure 6.3 DSC thermographs (from top to bottom) for (a) itraconazole, (b) itraconazole–succinic acid cocrystals from <i>n</i> -heptane, (c) itraconazole–succinic acid cocrystals formed by GAS cocrystallization, and (d) succinic acid .....	148
Figure 6.4 DSC thermographs (from top to bottom) for (a) itraconazole, physical mixtures of itraconazole and succinic acid with itraconazole mole fractions ( $x_{itz}$ ) of (b) 0.67, (c) 0.46, (d) 0.30, (e) 0.14, and (f) 0.06, and (g) succinic acid .....	150
Figure 6.5 SEM images of (a) itraconazole, (b) succinic acid, (c) itraconazole–succinic acid cocrystals formed by liquid antisolvent ( <i>n</i> -heptane), and (d) itraconazole–succinic acid cocrystals formed by GAS cocrystallization .....	152
Figure 6.6 Dissolution profiles for itraconazole (▲), a 1:1 by mass physical mixture of itraconazole and succinic acid (●), itraconazole–succinic acid cocrystals produced from <i>n</i> -heptane (■), and itraconazole–succinic acid cocrystals formed by GAS cocrystallization (◆) .....	154
Figure 6.7 PXRD patterns for itraconazole–succinic acid cocrystals formed by liquid antisolvent using <i>n</i> -heptane after (a) 0 days at 90 °C, (b) 7 days at 90 °C, (c) 14 days at 90 °C, and (d) 28 days at 90 °C .....	157
Figure 6.8 PXRD patterns for itraconazole–succinic acid cocrystals formed by GAS cocrystallization after (a) 0 days at 90 °C, (b) 7 days at 90 °C, (c) 14 days at 90 °C, and (d) 28 days at 90 °C .....	158
Figure A.1 Schematic of electrostatic stabilization for a poorly water-soluble drug particle in aqueous media .....	186
Figure A.2 Ionic concentration and electrokinetic potential as a function of distance from a negatively charged particle suspended in a dispersion medium .....	187
Figure A.3 Potential energy as a function of interparticle distance according to classical DLVO theory ( $V_T$ = total potential energy, $V_R$ = repulsive potential, and $V_A$ = attractive potential) .....	188
Figure A.4 Schematic of steric stabilization for a poorly water-soluble drug particle in aqueous media .....	189
Figure B.1 Chemical structures of (a) acetaminophen and (b) oxalic acid .....	195
Figure B.2 Hydrogen bonding motif in a 1:1 acetaminophen–oxalic acid cocrystal ....	195

Figure B.3 Vapor liquid equilibrium of CO<sub>2</sub>-ethanol at 40 °C (Experimental data: Secuianu et al. 2008 (■), Knez et al. 2008 (▲), Joung et al. 2001 (●), Galicia-Luna et al. 2000 (○), Suzuki et al. 1990 (◆), Chang et al. 1997 (+); ..... Peng-Robinson correlation with  $\delta_{ij} = 0$ , — Peng-Robinson correlation with  $\delta_{ij} = 0.0938$ ) ..... 203

Figure B.4 Solubility of acetaminophen in ethanol as a function of temperature (Experimental data: Granberg and Rasmuson 1999 and Mota et al. 2009 (◆); ..... Peng-Robinson correlation with  $\delta_{ij} = 0$ , — Peng-Robinson correlation with  $\delta_{ij} = 0.0051$ ) ..... 204

Figure B.5 Solubility of acetaminophen in supercritical CO<sub>2</sub> (Experimental data: Bristow et al. 2001 (◆); ..... Peng-Robinson correlation with  $\delta_{ij} = 0$ , — Peng-Robinson correlation with  $\delta_{ij} = 0.0150$ ) ..... 205

## List of Abbreviations

<i>a</i>	Van der Waals energy parameter
<i>A</i>	Hamaker constant
AARD	Absolute average relative deviation
AAS	Atomization and antisolvent
ACS	American Chemical Society
AIDS	Acquired immunodeficiency syndrome
API	Active pharmaceutical ingredient
ASES	Aerosol solvent extraction system
<i>b</i>	Van der Waals volume parameter
BCS	Biopharmaceutics classification system
BET	Brunauer-Emmett-Teller
BP	British pharmacopoeia
<i>C</i>	Concentration
$\bar{C}$	Average concentration
$C_s$	Solubility
$C_b$	Bulk concentration
$\Delta C_p$	Isobaric heat capacity
CFC	Critical flocculation concentration
CMC	Critical micelle concentration
CO <sub>2</sub>	Carbon dioxide

CSS	Cocrystallization with supercritical solvent
CXL	CO <sub>2</sub> -expanded liquid
$\delta$	Solubility parameter
$\delta_{ij}$	Binary interaction parameter
$d$	Diameter (or $d$ -spacing)
$D$	Diffusivity
$d_{50}$	Diameter of the 50 <sup>th</sup> percentile of the particle size distribution
$d_{90}$	Diameter of the 90 <sup>th</sup> percentile of the particle size distribution
$D_{60}$	Mean cumulative amount dissolved in 60 minutes
$D_{120}$	Mean cumulative amount dissolved in 120 minutes
$\frac{dc}{dt}$	Dissolution rate
DCM	Dichloromethane
DELOS	Depressurization of an expanded liquid organic solution
DMF	Dimethylformamide
DMSO	Dimethyl sulfoxide
DNA	Deoxyribonucleic acid
DPI	Dry powder inhaler
DSC	Differential scanning calorimetry
$\Delta E$	Change in internal energy
EAFUS	Everything added to food in the United States
$f$	Fugacity
$F_{vdW}$	Van der Waals force
FDA	Food and Drug Administration
FTIR	Fourier transform infrared spectroscopy

$\gamma$	Interfacial tension
$\gamma_i$	Activity coefficient
GAS	Gas antisolvent
GRAS	Generally regarded as safe
GXL	Gas-expanded liquid
$h$	Boundary layer thickness
$\Delta H_f$	Enthalpy of fusion
HCl	Hydrogen chloride
HIV	Human immunodeficiency virus
HP $\beta$ CD	Hydroxyl-propyl- $\beta$ -cyclodextrin
HPLC	High pressure liquid chromatography
HPMC	Hydroxypropyl methylcellulose
ICH	International conference on harmonisation of technical requirements for registration of pharmaceuticals for human use
IND	Investigational new drug
$K$	Proportionality constant
$K_I$	Intrinsic dissolution rate constant
KBr	Potassium bromide
$\lambda$	Wavelength
$l$	Interparticle distance
$m$	Mass
MCP	Mixture critical point
MeOH	Methanol
$MW$	Molecular weight
$n$ or $N$	Number of samples

NDA	New drug application
NF	National formulary
$\phi$	Fugacity coefficient
$P$	Pressure
$P_c$	Critical pressure
$P_{tp}$	Triple point pressure
PCA	Precipitation with compressed antisolvent
PEG	Polyethylene glycol
PEO	Polyethylene oxide
PLA	Poly L-lactide
PLGA	Poly Lactic- <i>co</i> -glycolic acid
PPO	Polypropylene oxide
PSD	Particle size distribution
PVP	Polyvinylpyrrolidone
PXRD	Powder X-ray diffraction
$\rho$	Density
$r$	Radius
$R$	Gas constant
RAMEB	Randomly methylated $\beta$ -cyclodextrin
RESS	Rapid expansion of supercritical solutions
RNA	Ribonucleic acid
RSD	Relative standard deviation
$\sigma$	Standard deviation
$\sigma^2$	Variance
$S$	Surface area



$S_{\infty}$	Saturation solubility
SAA	Supercritical assisted atomization
SAS	Supercritical antisolvent
SAS-DEM	Supercritical antisolvent-drug excipient mixing
SDS	Sodium dodecyl sulfate
SEA	Supercritical fluid enhanced atomization
SEDS	Solution enhanced dispersion by supercritical fluids
SEM	Scanning electron microscopy
SLE	Solid-liquid equilibrium
SLS	Sodium lauryl sulfate
SVE	Solid-vapor equilibrium
$\theta$	Diffraction angle
$t$	Time
$T$	Temperature
$T_c$	Critical temperature
$T_g$	Glass transition temperature
$T_m$	Melting temperature
$T_r$	Reduced temperature
$T_{tp}$	Triple point temperature
TB	Tuberculosis
THF	Tetrahydrofuran
USP	United States Pharmacopeia
UV-Vis	Ultraviolet-visible spectrophotometry
$v$	Molar volume
$V$	Volume

$V_0$	Initial volume
$V_A$	Attractive potential
$V_R$	Repulsive potential
$V_T$	Total potential energy
VLE	Vapor-liquid equilibrium
$\omega$	Acentric factor
WHO	World Health Organization
$x$	Liquid phase mole fraction
$y$	Vapor phase mole fraction
$Y_S$	Solubility
$\zeta$	Zeta potential

## Chapter 1

### Introduction

#### 1.1 Pharmaceutical Formulation

The discovery of a therapeutic molecule is only the beginning of the drug development process (Figure 1.1). Development of the molecule into a suitable dosage formulation is necessary for successful patient delivery. Formulation considerations include the route of delivery to the patient, the form in which the drug will be delivered, and the inactive ingredients that will be combined with the drug. The elements of a dosage formulation must synergistically work to enhance the drug's administration, efficacy, and stability. The following subsections will elaborate upon drug delivery, dosage formulation, and polymorphism.

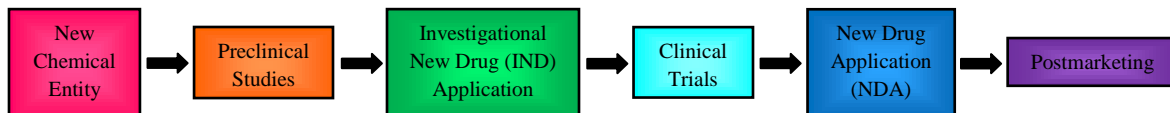


Figure 1.1 Drug development process (Ansel et al. 1999)

##### 1.1.1 Drug Delivery

There are a number of routes by which pharmaceuticals can be delivered to the patient. The most common routes include peroral, topical, transmucosal (e.g. nasal, ocular), inhalation, and intravenous. The relatively lower cost, applicability to a wide

range of drug types, noninvasive nature, and high rate of patient compliance make peroral delivery the route of choice (Sastry et al. 2000). However, the route of delivery is often dictated by the disease type and location and therapeutic to be delivered. For example, systemic toxicity caused by high oral dosing of the anti-tuberculosis drug rifampicin has prompted development of inhalable formulations of the drug for delivery directly to the primary site of the infection, the lungs (O'Hara and Hickey 2000). Depending on the intended method of delivery, additional formulation considerations are necessary. For example, inhalable formulations require microspheres with aerodynamic diameters of 1-5  $\mu\text{m}$  since larger diameters cannot effectively penetrate the alveoli while smaller diameters are exhaled due to low inertia (Patomchaivivat et al. 2008; Sung et al. 2009). These few examples serve to illustrate the complex interplay between disease, drug, and formulation.

### 1.1.2 Dosage Formulation

Drug formulations are most frequently solids, but can occasionally be liquids and rarely gases. The volatility of most liquid formulations prevents their long term stability while administration of gas phase pharmaceuticals remains challenging. Due to ease of production, handling, and storage, active pharmaceutical ingredients (APIs) are most commonly developed and delivered as solid dosage formulations (Banerjee et al. 2005; Shan and Zaworotko 2008). It is estimated that 70% of the pharmaceuticals dispensed are solid tablet or capsule formulations (Ansel et al. 1999). The solid forms of an API can include amorphs, crystals, polymorphs, salts, hydrates, solvates, and cocrystals, as shown

in Figure 1.2. Of these alternatives, crystalline forms are strongly preferred based on stability, reproducibility, and ease of purification (Shan and Zaworotko 2008).

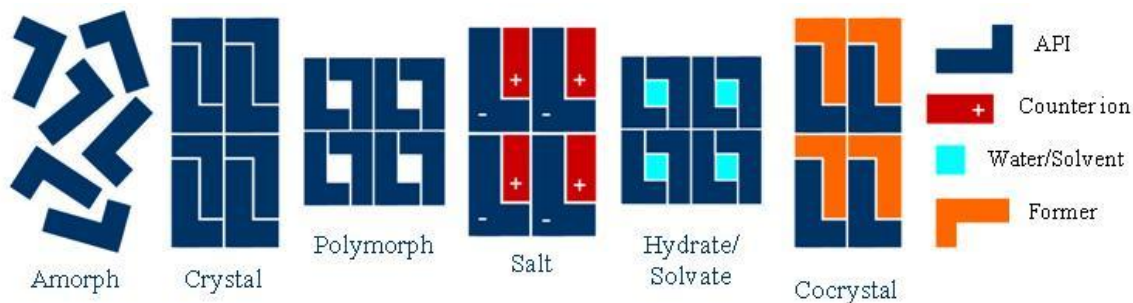


Figure 1.2 Solid forms of an API

### 1.1.3 Polymorphism

Crystalline pharmaceutical solids, however, often exhibit polymorphism, crystallizing in multiple forms with greatly varying physical properties (Bauer et al. 2001; Bernstein 2002). Discovery of a compound's polymorphs is an integral part of early drug development. With very few exceptions, the thermodynamically most stable polymorph is the most desirable crystalline form for pharmaceutical development (Miller et al. 2005). Unanticipated conversion between polymorphs can lead to significant problems if it occurs late in the development process. For example, ritonavir, a human immunodeficiency virus (HIV) treatment drug, had to be recalled due to spontaneous conversion from its metastable (fast dissolving) to stable (slow dissolving) crystal form during shelf storage, resulting in significant under-treatment of HIV patients (Bauer et al. 2001). Numerous crystallization screening methods have been implemented to enumerate the possible polymorphs of a compound and determine the most stable one. While

significant attention is paid to selecting the most stable crystalline form of an API, the solubility is often compromised by such a selection.

## **1.2 Poorly Water-Soluble Pharmaceuticals**

Poor aqueous solubility is one of the biggest formulation challenges facing the pharmaceutical industry today. Approximately 40% of the drugs discovered through combinatorial chemistry and high throughput screening have an aqueous solubility of less than 10  $\mu\text{M}$  (Lipinski 2001, 2002). Poor aqueous solubility can lead to poor bioavailability with high variability depending on the fed versus fasted state, uncontrollable precipitation following dosing, necessitate the use of harsh excipients or cosolvents which limit dose escalation leading to suboptimal dosing, or require an extreme acidic or basic environment to enhance solubilization resulting in poor patient compliance due to an inconvenient dosage platform (Merisko-Liversidge and Liversidge 2008).

### **1.2.1 BCS Class II Biopharmaceuticals**

Poorly water-soluble compounds whose absorption is rate-limited by dissolution are commonly known as Class II biopharmaceuticals according to the biopharmaceutics classification system (BCS), as shown in Figure 1.3 (Löbenberg and Amidon 2000). These compounds have high membrane permeability but an aqueous solubility on the order of  $\mu\text{g/mL}$ . The bioavailability of these compounds is best improved through formulation strategies aimed at increasing the dissolution rate and achieving sustained solubilization of the compound.

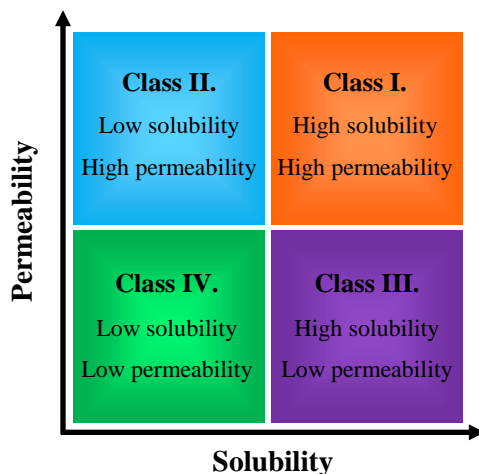


Figure 1.3 Biopharmaceutics classification system (BCS)

### 1.2.2 Strategies for Dissolution Enhancement

A number of strategies have been employed for increasing the dissolution rate of poorly water-soluble pharmaceuticals, specifically in solid dosage formulations. While a number of API-specific techniques have also been developed, the most broadly applied techniques for dissolution enhancement include salt formation (Serajuddin 2007), solid dispersion (Serajuddin 1999; Leuner and Dressman 2000; Vasconcelos et al. 2007), cyclodextrin complexation (Loftsson and Brewster 1996; Challa et al. 2005; Brewster and Loftsson 2007), micronization (Radtke 2001; Merisko-Liversidge et al. 2003; Hu et al. 2004; Merisko-Liversidge and Liversidge 2008), and cocrystallization (Blagden et al. 2007; Shiraki et al. 2008; Good and Rodríguez-Hornedo 2009; Babu and Nangia 2011). The two strategies explored in this dissertation are micronization and cocrystallization.

### 1.3 Particle Size Reduction for Dissolution Enhancement

#### 1.3.1 The Noyes-Whitney Equation

Noyes and Whitney stated that the rate of dissolution of a solid substance in its own solution is proportional to the difference between the concentration of the solution and the concentration of the saturated solution,

$$\frac{dc}{dt} = K(C_s - C_b) \quad (1)$$

where  $\frac{dc}{dt}$  is the dissolution rate,  $K$  is a proportionality constant,  $C_s$  is the solubility of the solute, and  $C_b$  is the concentration of the bulk solution at time  $t$ . The proportionality constant can be found from integration of (1),

$$K = \frac{1}{t} \ln \left( \frac{C_s}{C_s - C_b} \right) \quad (2)$$

if the solubility is known (Noyes and Whitney 1897). The Noyes-Whitney equation describes a thin layer of saturated solution at the surface of the solid and postulates that the rate of dissolution of the solid is governed by the rate of diffusion from the boundary layer to the bulk solution. The Noyes-Whitney equation also assumes that the change in surface area during dissolution is negligible, a valid assumption for describing the dissolution of poorly water-soluble compounds in aqueous solutions. For defined conditions of temperature and agitation, the Noyes-Whitney equation was modified to,

$$\frac{dc}{dt} = K_I S (C_s - C_b) \quad (3)$$

where  $K_I$  is the intrinsic dissolution rate constant and  $S$  is the surface area (Bruner and Tolloczko 1900). Invoking Fick's law of diffusion the equation becomes,



$$\frac{dc}{dt} = \frac{DS}{hV}(C_s - C_b) \quad (4)$$

where  $D$  is the diffusivity,  $S$  is the surface area,  $h$  is the boundary layer thickness, and  $V$  is the volume of the dissolution medium (Nernst 1904; Brunner 1904). From this equation it is clear that the dissolution rate of a substance is directly proportional to surface area, and thus, particle size.

### 1.3.2 Microparticle Agglomeration

Micronization is a widely applicable and straightforward way to increase the surface area, and thus dissolution rate, of a poorly water-soluble API. Figure 1.4 shows the dramatic increase in surface area as particle diameter is decreased to the submicron region for an equivalent mass of material. The primary challenge faced in micronization is that the theoretically predicted dissolution benefits are often precluded in practice due to microparticle agglomeration. As particle size is decreased, attractive forces such as capillary, electrostatic, and van der Waals become dominant as compared to gravitational forces. Assuming the absence of capillary forces and particle charge, valid assumptions for poorly water-soluble drug particles, van der Waals forces are the prevailing cause of particle cohesiveness for hydrophobic organic particles with diameters less than 30  $\mu\text{m}$  (Sanganwar 2010; Meyer and Zimmermann 2004). The van der Waals force ( $F_{vdW}$ ) between two particles separated by a distance  $l$  is,

$$F_{vdW} = \frac{A}{12} \times \frac{d}{2l^2} \quad (5)$$

where  $A$  is the Hamaker constant and  $d$  is the particle diameter (Linsenbühler and Wirth 2005). By increasing the distance between particles, van der Waals forces can be overcome and agglomeration prevented.

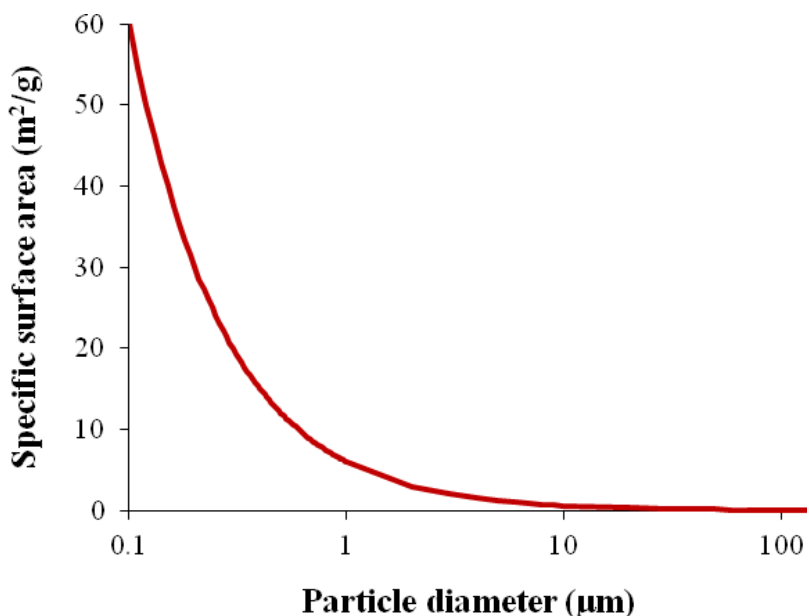


Figure 1.4 Specific surface area as a function of particle size for spherical particles ( $m = 10 \text{ g}$ ,  $\rho = 1 \text{ g/cm}^3$ )

### 1.3.3 Microparticle Deagglomeration

Microparticle deagglomeration is most commonly accomplished by mixing the microparticles with excipients, or materials other than the active pharmaceutical ingredient(s). Mixing, however, can take on a variety of forms. The tumbler mixer, the most common mixer in the pharmaceutical industry, has been used to mix APIs with pharmaceutically acceptable excipients, and has shown marginal improvements in dissolution when run for sufficient times and at sufficient speeds (Kale et al. 2009), despite its inability to deagglomerate cohesive drug microparticles (Harnby 2000).

Dissolution improvements have been seen from co-grinding excipients with poorly water-soluble APIs using a jet-milling technique (Vogt et al. 2008). Similarly, the dissolution of poorly water-soluble APIs has been improved by co-grinding with water-soluble polymers in a vibratory ball mill (Sugimoto et al. 1998). The high energy used in rotary and vibratory ball mills, however, may affect the crystal lattice of the drug and influence its physicochemical stability (Krycer and Hersey 1980). Other work has focused on the use of stabilizers to prevent particle agglomeration by providing ionic and steric barriers surrounding the drug microparticles, as discussed in detail in Appendix A.

#### 1.3.4 Approaches to Micronization

Micronization technologies are commonly classified into two categories: top-down and bottom-up (Reverchon and Adami 2006). These two categories are illustrated in Figure 1.5. In top-down micronization, macroscale materials are disassembled into their microscale constituents. Examples of top-down micronization technologies are pearl/ball milling and high pressure homogenization. In bottom-up micronization, microscale materials are synthesized from their molecular constituents. Examples of bottom-up micronization technologies are emulsification-diffusion and supercritical fluid precipitation.

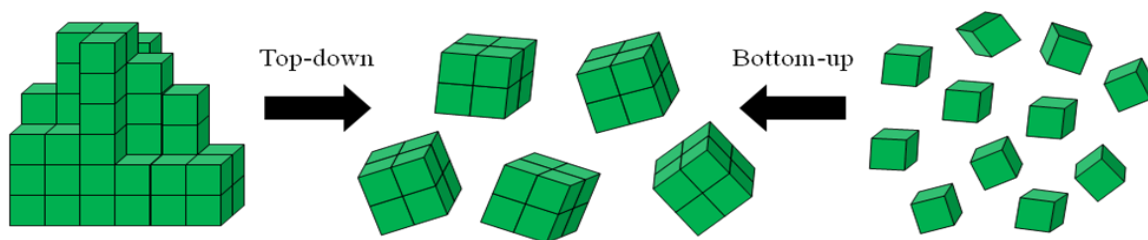


Figure 1.5 Top-down versus bottom-up approaches to micronization

## 1.4 Particle Formation Using Supercritical CO<sub>2</sub>

A supercritical fluid is any substance existing at a temperature above its critical temperature ( $T_c$ ) and a pressure above its critical pressure ( $P_c$ ). Supercritical fluids have diffusivities ( $\sim 10^{-3}$  cm<sup>2</sup>/s) higher than those of traditional liquid solvents, viscosities ( $\sim 10^{-4}$  g/cm·s) lower than traditional solvents, and densities that can be varied drastically by small changes in pressure, all of which make them unique reaction media (Eckert et al. 1996; Gupta and Shim 2007). Supercritical fluids have been used for a wide variety of applications, such as food processing, dry cleaning, chromatography, power generation, and oxidation of hazardous waste. In addition, supercritical fluids have found utility for the production of pharmaceutical micro- and nanoparticles due to a number of unique and advantageous properties.

### 1.4.1 Supercritical CO<sub>2</sub>

Supercritical carbon dioxide (CO<sub>2</sub>) is the most commonly used supercritical fluid for pharmaceutical applications because it is nontoxic, nonflammable, inexpensive, naturally abundant, and has mild critical parameters ( $T_c = 31.1$  °C,  $P_c = 73.8$  bar). A pressure versus temperature phase diagram for CO<sub>2</sub>, highlighting the supercritical fluid region, is shown in Figure 1.6.

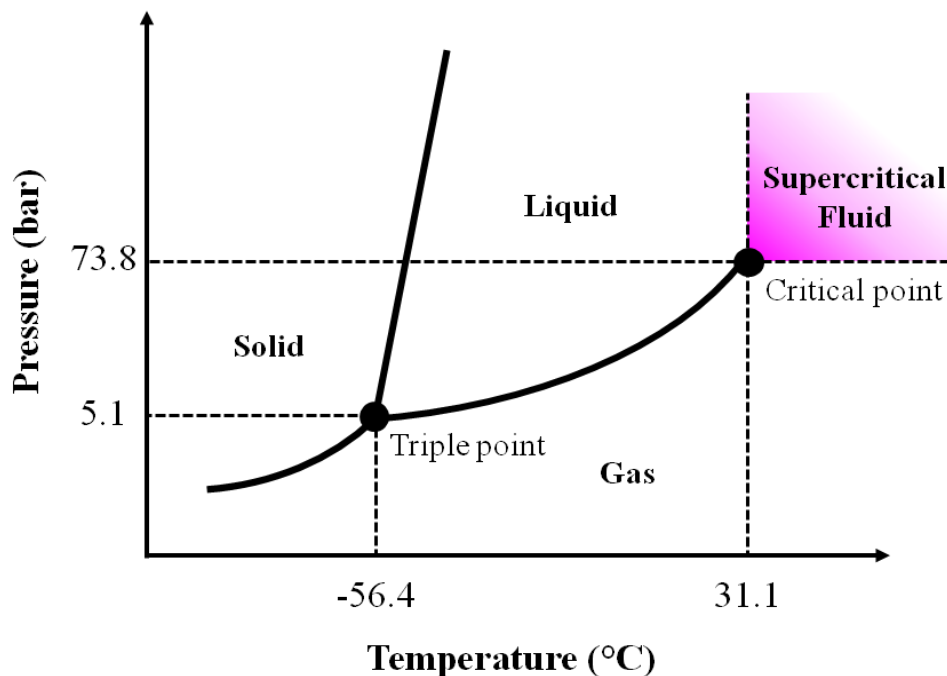


Figure 1.6 Pressure versus temperature phase diagram for CO<sub>2</sub>

#### 1.4.2 Solubility in Supercritical CO<sub>2</sub>

The efficacy of supercritical CO<sub>2</sub>-based processes for producing pharmaceutical micro- and nanoparticles is extremely dependent on the API's solubility in supercritical CO<sub>2</sub>. The solvent strength of supercritical CO<sub>2</sub> can be qualitatively described by the solubility parameter,  $\delta$ , which is the square root of the cohesive energy density,

$$\delta^2 = \left( \frac{\Delta E}{v} \right)_T \approx \left( \frac{\partial E}{\partial v} \right)_T = T \left( \frac{\partial P}{\partial T} \right)_v - P \quad (6)$$

where  $E$  is the internal energy,  $v$  is the molar volume,  $T$  is temperature, and  $P$  is pressure. The molar volume, or density, of supercritical CO<sub>2</sub> is highly pressure and temperature dependent, as shown in Figure 1.7 (Gupta and Shim 2007).

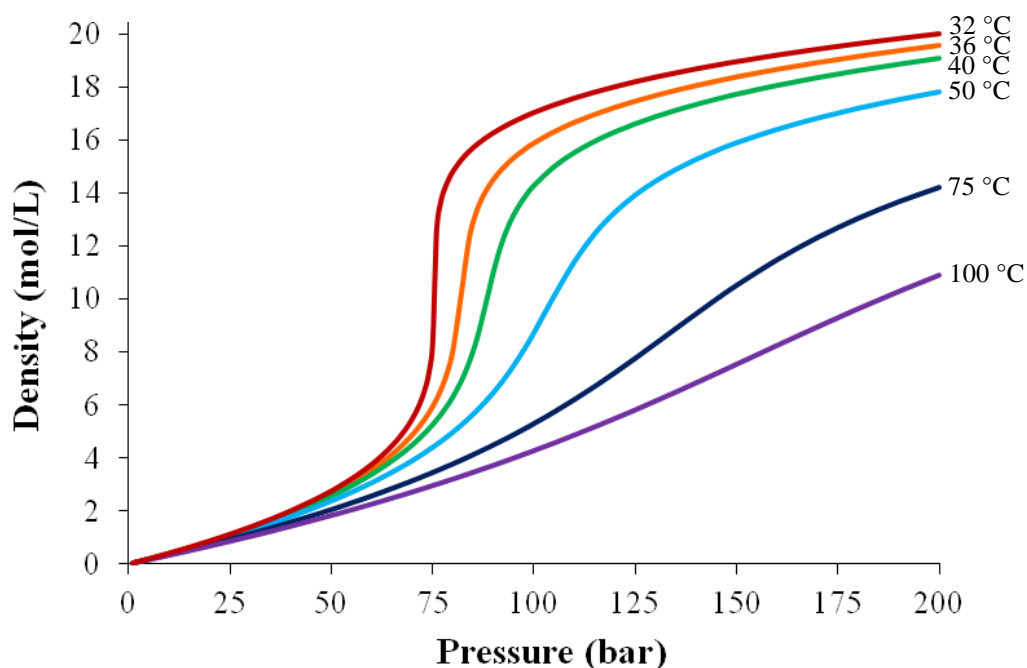


Figure 1.7 Pressure and temperature dependence of CO<sub>2</sub> density ( — 32 °C, — 36 °C, — 40 °C, — 50 °C, — 75 °C, — 100 °C)

Accordingly, the solubility of solutes in supercritical CO<sub>2</sub> is also highly pressure and temperature dependent. Solubility in supercritical CO<sub>2</sub> increases with pressure at a constant temperature due to greater attractive forces between the solute and CO<sub>2</sub> (Gupta and Shim 2007). The effect of temperature on solubility in supercritical CO<sub>2</sub> is less straightforward. Below a certain crossover pressure, defined as the pressure at which isotherms at various near-critical temperatures tend to converge (Chimowitz and Pennisi 1986), solubility decreases with increasing temperature due to the decreasing density of supercritical CO<sub>2</sub>. Above the crossover pressure, the increasing vapor pressure of the solid solute dominates causing an increase in solubility with temperature (Chimowitz 2005). To illustrate this behavior, the solubility of itraconazole, a poorly water-soluble antifungal drug generally considered to be insoluble in supercritical CO<sub>2</sub>, is shown in

Figure 1.8 (Al-Marzouqi et al. 2006). From Figure 1.8, it is clear that the crossover pressure for itraconazole is approximately 250 bar.

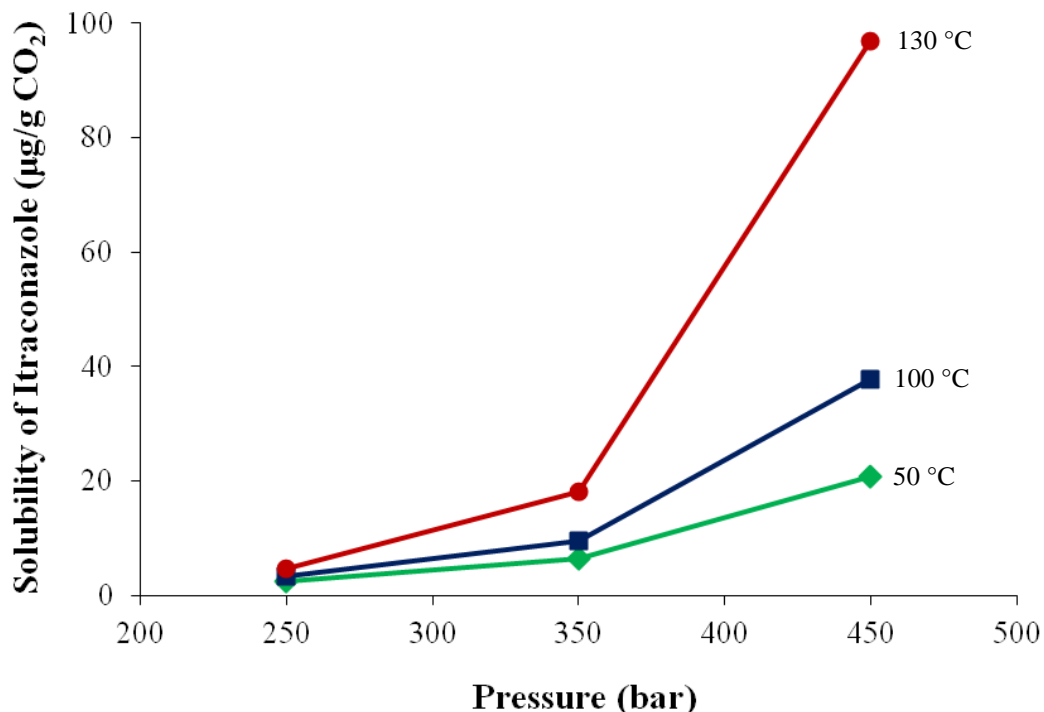


Figure 1.8 Solubility of itraconazole in supercritical CO<sub>2</sub> at 50 °C (◆), 100 °C (■), and 130 °C (●)

#### 1.4.3 Micronization Using Supercritical CO<sub>2</sub>

A number of supercritical CO<sub>2</sub>-based processes have been developed for the production of pharmaceutical micro- and nanoparticles. Supercritical CO<sub>2</sub> has been used as a solvent in rapid expansion of supercritical solutions (RESS), a cosolvent in depressurization of an expanded liquid organic solution (DELLOS) and supercritical assisted atomization (SAA), and an antisolvent in precipitation with compressed antisolvent (PCA), gas antisolvent (GAS), aerosol solvent extraction system (ASES),

solution-enhanced dispersion by supercritical fluids (SEDS), and supercritical antisolvent (SAS). A number of reviews on supercritical CO<sub>2</sub>-based micronization technologies have been published in the literature (Tom and Debenedetti 1991; Jung and Perrut 2001; Shariati and Peters 2003; Martín and Cocero 2008; Yasuji et al. 2008).

The two most common supercritical CO<sub>2</sub>-based pharmaceutical microparticle formation technologies are RESS and SAS. The RESS process utilizes the high solvating power of supercritical CO<sub>2</sub> to solubilize a bulk drug and recrystallize it as fine particles. A drug-containing supercritical CO<sub>2</sub> solution is expanded through a nozzle to ambient conditions causing rapid phase change from the supercritical state to the gaseous, solute supersaturation, and particle crystallization. The advantage of the RESS technique is the purity of the final product, with no concerns of residual solvent. In contrast to the RESS technique, the SAS technique relies on the weak solubilizing power of supercritical CO<sub>2</sub> for many pharmaceuticals. In the SAS technique, a bulk drug is dissolved in a liquid organic solvent and this solution sprayed into a high pressure chamber containing supercritical CO<sub>2</sub>, as shown in Figure 1.9. Diffusion of CO<sub>2</sub> into the organic phase and evaporation of the organic phase into the CO<sub>2</sub> synergistically cause supersaturation and particle crystallization. Excess solvent is removed by flushing with additional supercritical CO<sub>2</sub>. The complementarity of the RESS and SAS techniques facilitates applicability to a wide range of pharmaceutical compounds, those both soluble and insoluble in supercritical CO<sub>2</sub>.



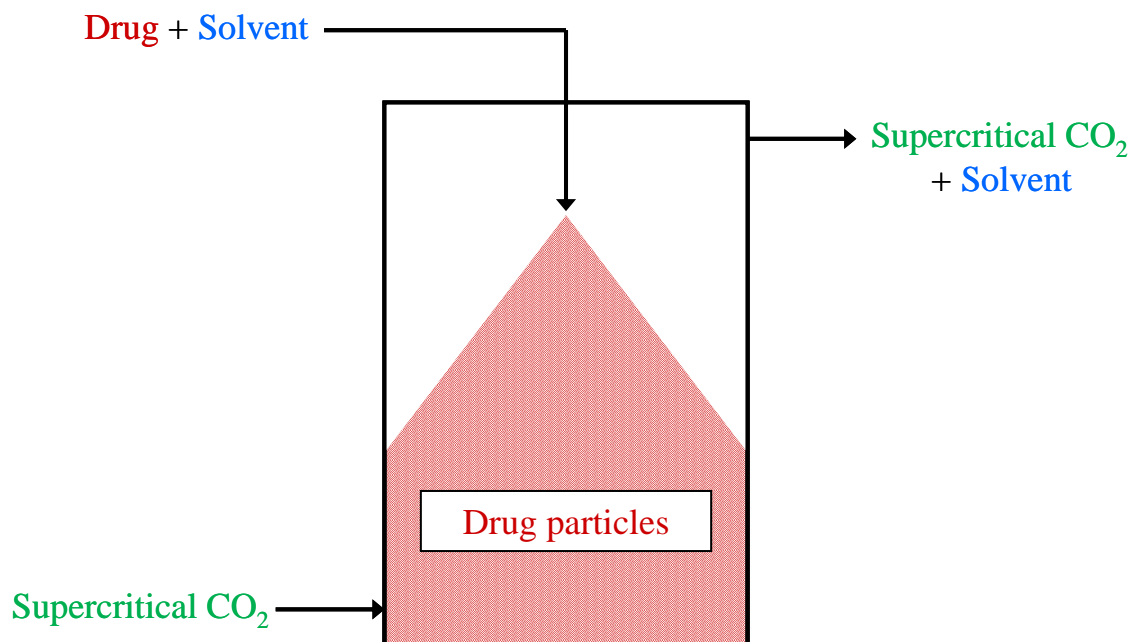


Figure 1.9 Schematic of the SAS process

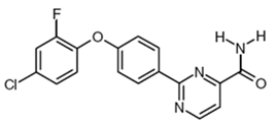
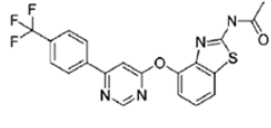
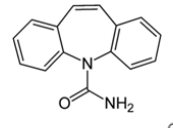
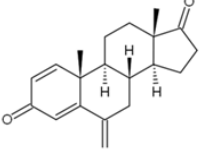
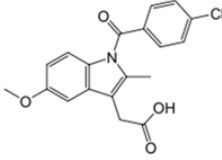
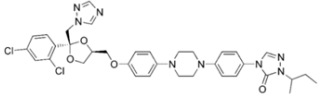
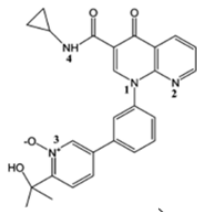
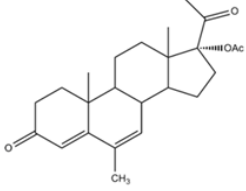
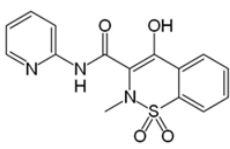
## 1.5 Pharmaceutical Cocrystal Engineering

Cocrystals can be loosely defined as crystalline structures containing two or more compounds in a stoichiometric relationship and existing in the solid state under ambient conditions (Shan and Zaworotko 2008). The components in a cocrystal interact by hydrogen bonding or other directional noncovalent forces. Cocrystals date at least as far back as 1844, to Friedrich Wöhler's study of quinhydrone (Wöhler 1844), but have experienced a renewed interest within the past 10 years (Childs and Zaworotko 2009). Cocrystals have found utility in the electronics, textiles, paper, photographic, and chemical processing industries (Stahly 2009), but their recent popularity has focused primarily on their pharmaceutical applications (Vishweshwar et al. 2006; Sekhon 2009; Schultheiss and Newman 2009; Qiao et al. 2011).

### 1.5.1 Physical Property Enhancement Through Cocrystallization

The unique properties afforded by multi-component crystalline solids have demonstrated significant potential in pharmaceutical formulation by improving the stability, mechanical properties, and dissolution of certain APIs. Cocrystallization can minimize polymorphism as it did for a carbamazepine–saccharin cocrystal which exhibits only two polymorphic forms compared to the four polymorphic forms and host of solvates characteristic of pure carbamazepine (Hickey et al. 2007; Shan and Zaworotko 2008; Porter III et al. 2008). Cocrystallization can improve humidity resistance by reducing the number of available hydrogen bond donors and acceptors present in a crystal lattice (Trask et al. 2005; Trask et al. 2006). Mechanical properties critical for effective drug tableting have also been improved through cocrystallization (Sun and Hou 2008; Karki et al. 2009; Rahman et al. 2011; Chow et al. 2012). Despite these other benefits, dissolution enhancement is the most common motivation for pharmaceutical cocrystallization (Blagden et al. 2007; Shiraki et al. 2008; Good and Rodríguez-Hornedo 2009; Babu and Nangia 2011). Cocrystals engineered for this purpose contain a poorly water-soluble API and a water-soluble, pharmaceutically acceptable former. Table 1.1 lists a number of poorly water-soluble APIs whose solubility and/or dissolution has been enhanced through cocrystallization.

Table 1.1 Cocrystals of poorly water-soluble APIs

API	Aqueous Solubility	Structure	Former(s)	Reference
2-[4-(4-chloro-2-fluorophenoxy)phenyl]pyrimidine-4-carboxamide	< 0.1 µg/mL		glutaric acid	McNamara et al. 2006
AMG 517	≤ 7.0 µg/mL		11 different carboxylic acids and amides	Stanton et al. 2009
Carbamazepine	17.7 µg/mL		13 different compounds	Fleischman et al. 2003
Exemestane	6.83 µg/mL		maleic acid	Shiraki et al. 2008
Indomethacin	2.5-4.0 µg/mL		saccharin	Basavoju et al. 2008
Itraconazole	≤ 5.0 µg/mL		fumaric acid succinic acid malic acid tartaric acid	Remenar et al. 2003
L-883555	7.5 µg/mL		L-tartaric acid	Variankaval et al. 2006
Megestrol acetate	2.0 µg/mL		saccharin	Shiraki et al. 2008
Piroxicam	19.8 µg/mL		50 cocrystals from 23 carboxylic acids	Childs and Hardcastle 2007

The advantages of cocrystallization as a dissolution enhancement technique are numerous. The complex chemical structures characteristic of poorly water-soluble drugs usually contain multiple hydrogen bond capable functionalities, which in combination with the variety of water-soluble generally regarded as safe (GRAS) substances which can serve as cocrystal formers, provide flexibility in engineering cocrystals with enhanced dissolution. Cocrystals represent a new, patentable chemical form of a drug and can therefore offer intellectual property protection to manufacturers (Trask 2007). Since the components in a cocrystal interact by hydrogen bonding in a stoichiometric way, cocrystals may be amenable to a degree of structural predictability as opposed to experimental optimization. The design and prediction of cocrystals is a rapidly growing field of research with a number of investigators using thermodynamic considerations (Nehm et al. 2006; Schartman 2009; Ter Horst et al. 2009), ternary phase diagrams (Chiarella et al. 2007; Chadwick et al. 2009), hydrogen bonding motifs (Aakeröy and Salmon 2005; Aakeröy et al. 2006), and computer models (Issa et al. 2008; Karamertzanis et al. 2009).

### 1.5.2 Methods for Cocrystallization

Traditionally, cocrystals were prepared by either grinding or solution-based methods which induce supersaturation by cooling, solvent evaporation, or the addition of a liquid antisolvent. The solid-state grinding of two components with hydrogen bonding complementarities has been shown to produce cocrystals, some of which were unachievable by solution-based methods due to solubility and solvent competition (Patil et al. 1984; Toda et al. 1987; Hollingsworth et al. 1994). In other cases, the presence of a

liquid solvent can facilitate cocrystal formation by enhancing molecular reactivity through mobility in solution. In the last few years, numerous other techniques, including heating (Lu et al. 2008; Berry et al. 2008; Yamashita et al. 2012), hot melt extrusion (Dhumal et al. 2010; Kelly et al. 2012), sonication (Bučar and MacGillivray 2007; Sander et al. 2010; Aher et al. 2010), membrane crystallization (Di Profio et al. 2011), spray-drying (Alhalaweh and Velaga 2010), supercritical CO<sub>2</sub>-based processes (Padrela et al. 2009; Padrela et al. 2010), and CO<sub>2</sub>-expanded liquid crystallization (Shikhar et al. 2011), have been used to produce pharmaceutical cocrystals. The aim of these new methods is to reduce organic solvent use, decrease particle size, and improve scalability. Due to the variety of production methods available, cocrystal discovery is largely still a trial and error process which requires a combination of former, solvent, and production method screening.

## **1.6 Crystallization in CO<sub>2</sub>-Expanded Liquids**

### **1.6.1 Gas-Expanded Liquids**

Gas-expanded liquids (GXLs) are an environmentally benign class of solvents which can offer an alternative media for performing separations, extractions, reactions, and other applications (Eckert et al. 2004; Jessop and Subramaniam 2007). GXLs are formed by the dissolution of a gas, often CO<sub>2</sub>, into a liquid organic solvent. In general, CO<sub>2</sub> is a poor solvent compared to organic solvents such as acetone and methanol, such that a range of solvation properties can be achieved depending on the amount of dissolved CO<sub>2</sub> (Eckert et al. 2004). The amount of dissolved CO<sub>2</sub> in an organic solvent is tunable by simple changes in the applied CO<sub>2</sub> pressure. The mole fraction of CO<sub>2</sub> in the

liquid phase at a given pressure can vary greatly depending on the solvent and temperature, as shown in Figure 1.10 (Chang et al. 1997).

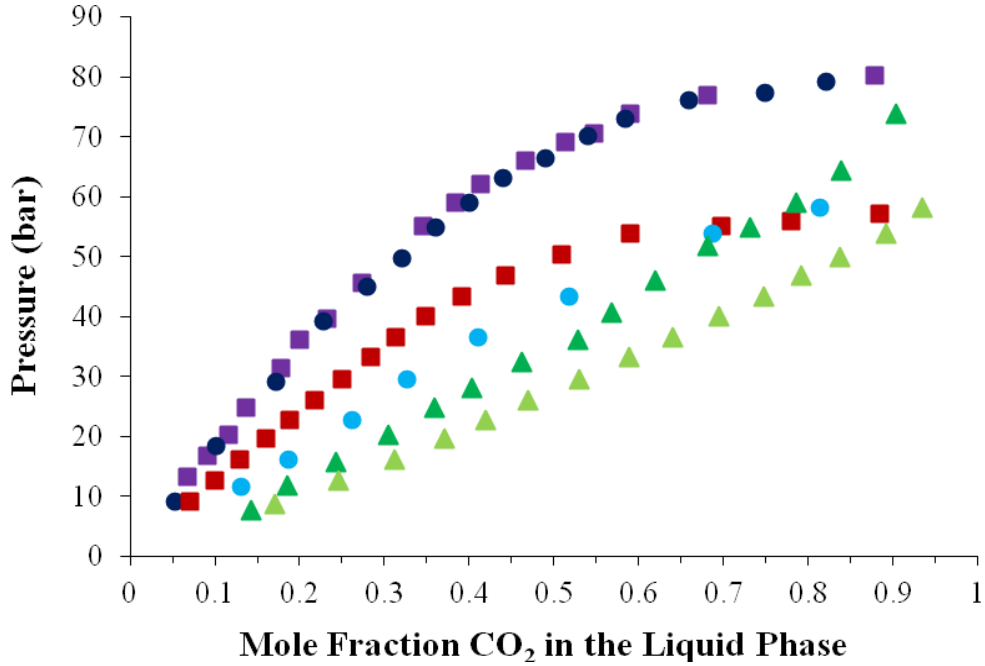


Figure 1.10 Vapor liquid equilibria for CO<sub>2</sub>-organic solvent mixtures: Methanol at 40 °C (■), ethanol at 40 °C (●), methanol at 25 °C (■), ethanol at 25 °C (●), acetone at 40 °C (▲), and acetone at 25 °C (▲)

### 1.6.2 Modeling VLE Behavior Using the Peng-Robinson Equation of State

The vapor-liquid equilibrium (VLE) behavior of CO<sub>2</sub>-expanded liquids (CXLs) is often modeled using the Peng-Robinson equation of state,

$$P = \frac{RT}{v-b} - \frac{a(T)}{v(v+b) + b(v-b)} \quad (7)$$

where  $P$  is pressure,  $R$  is the gas constant (8.314 J/mol·K),  $T$  is temperature,  $v$  is the molar volume, and  $a$  and  $b$  are the equation of state parameters (Peng and Robinson 1976). The parameter  $a$  is temperature dependent and can be found from,

$$a(T) = 0.45724 \frac{\alpha(T_r, \omega) R^2 T_c^2}{P_c} \quad (8)$$

$$\alpha(T_r, \omega) = \left[ + (0.37464 + 1.54226\omega - 0.26992\omega^2)(1 - T_r^{1/2})^2 \right] \quad (9)$$

where  $T_r$  is the reduced temperature,  $T_c$  is the critical temperature,  $P_c$  is the critical pressure, and  $\omega$  is the acentric factor. The parameter  $b$  is a function of the critical properties of a compound,

$$b = 0.07780 \frac{RT_c}{P_c} \quad (10)$$

The multicomponent nature of CXLs requires the use of binary mixing rules for calculating the equation of state parameters  $a$  and  $b$ ,

$$a = \sum_i \sum_j x_i x_j a_{ij} \quad (11)$$

$$a_{ij} = (1 - \delta_{ij}) a_i^{1/2} a_j^{1/2} \quad (12)$$

$$b = \sum_i x_i b_i \quad (13)$$

where  $x_i$  is the mole fraction of component  $i$  and  $\delta_{ij}$  is a binary interaction parameter found through the regression of experimental VLE data.

### 1.6.3 Tunable Properties of CO<sub>2</sub>-Expanded Liquids

The utility of CXLs comes not only from the ability to tune and predict the amount of CO<sub>2</sub> in an organic solvent, but the resultant changes in physicochemical properties of the CO<sub>2</sub>-solvent system. As CO<sub>2</sub> pressure is increased, the increasing amount of solubilized CO<sub>2</sub> in the solvent leads to an expansion in volume and a significant change in properties including solvent density, viscosity, diffusivity, surface

tension, polarity, dielectric constant, and solvating power (Eckert et al. 2004; Saunders 2011). Figure 1.11 shows the volumetric expansion of methanol at 25 °C as CO<sub>2</sub> pressure is applied and the corresponding change in the solubility parameter (Bezanehtak et al. 2002; Li and Maroncelli 2006). When the solubility parameters of a given solute and solvent are similar, they are predicted to be mutually and athermally soluble (Hancock et al. 1997). Therefore, the tunability of solvent strength in CXL systems provides a unique opportunity for controlling solute solubilization and crystallization. For example, Jessop et al. used CO<sub>2</sub> pressure to reversibly dissolve and precipitate fluorinated compounds in liquid hydrocarbons (Jessop et al. 2002). Solvent tunability is also the basis of an important pharmaceutical crystallization technique called gas antisolvent (GAS) crystallization.

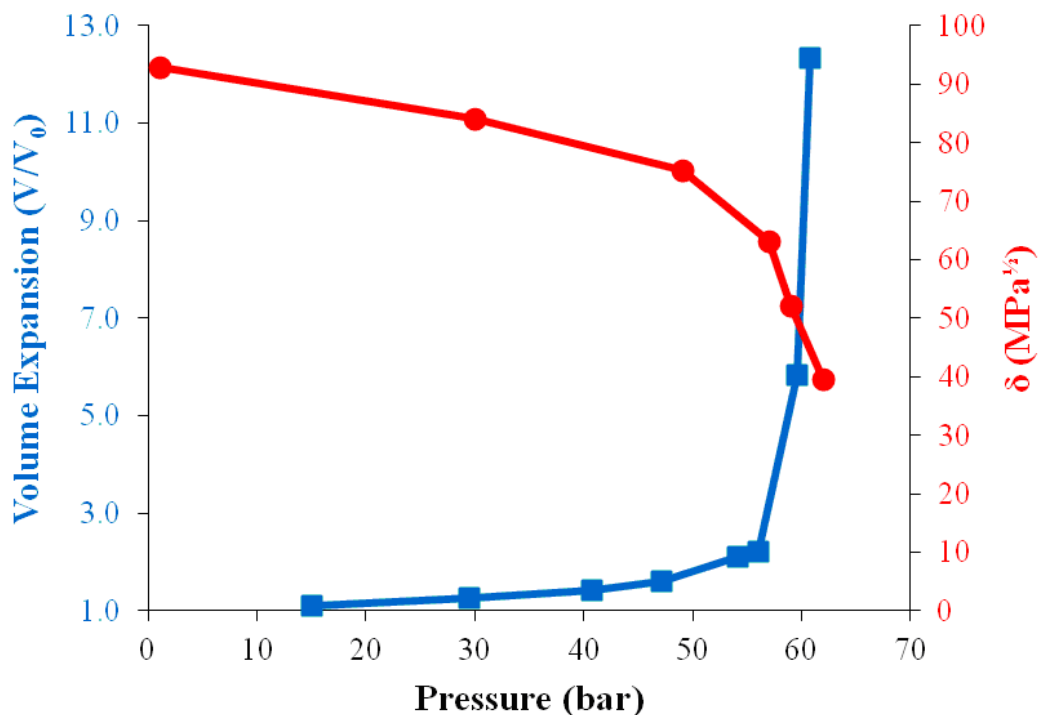


Figure 1.11 Volumetric expansion ( $V/V_0$ ) of methanol as a function of CO<sub>2</sub> pressure at 25 °C (■) and solubility parameter ( $\delta$ ) of CO<sub>2</sub>-expanded methanol (●)



#### 1.6.4 Gas Antisolvent Crystallization

GAS crystallization is one of the most common applications of GXLs. GAS crystallization involves the dissolution of a gas, commonly CO<sub>2</sub>, into a solute-containing and CO<sub>2</sub>-miscible liquid organic solvent. The solubilization of CO<sub>2</sub> in the organic solvent decreases its solvating power, eventually triggering crystallization of the solute. For example, the solubility of acetaminophen in CO<sub>2</sub>-expanded ethanol at 22 °C, 42 °C, and 44 °C as a function of dissolved CO<sub>2</sub> in the liquid phase is shown in Figure 1.12 (Wubbolts et al. 2004).

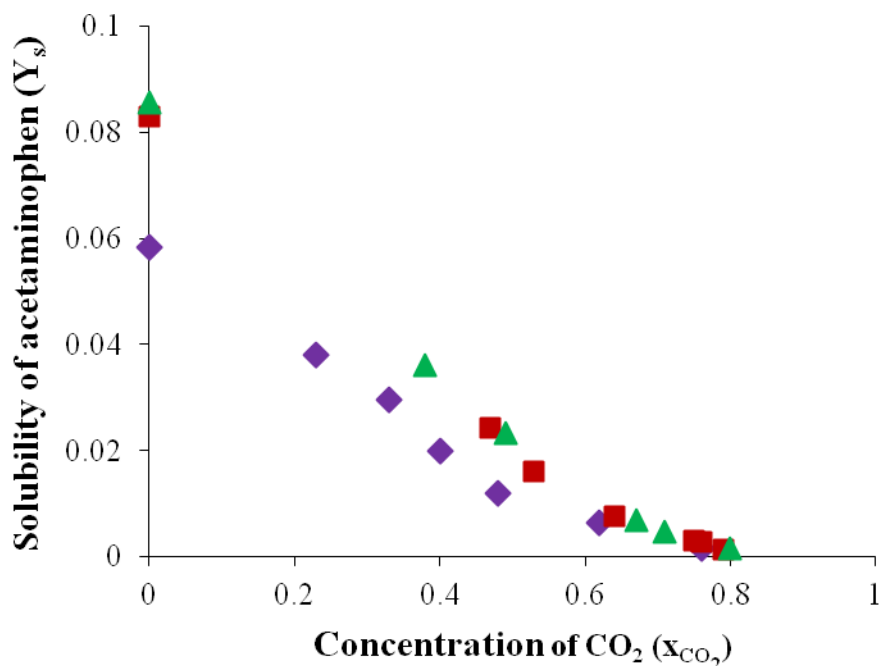


Figure 1.12 Solubility of acetaminophen in CO<sub>2</sub>-expanded ethanol at 22 °C (◆), 42 °C (■), and 44 °C (▲)

APIs which have been recrystallized by GAS crystallization include beclomethasone-17,21-dipropionate (Bakhbakhi et al. 2006), chlorpropamide (Yeo et al.

2003), griseofulvin (De Gioannis et al. 2004), indomethacin (Warwick et al. 2000), paracetamol (Fusaro and Mazzotti 2004), phenanthrene (Berends et al. 1996), phenylbutazone (Park and Yeo 2008a), theophylline (Roy et al. 2011), and tolbutamide (Subra-Paternault et al. 2007). Judicious selection of the organic solvent and GAS crystallization operating conditions such as temperature, CO<sub>2</sub> addition rate, stirring, and solute concentration can facilitate tailoring of dissolution relevant properties such as particle size, particle morphology, crystallinity, and crystal habit.

Incorporation of multiple solutes in GAS crystallization has focused on fractionation, composite production, and very limitedly, crystal growth manipulation. Starting from an equimolar solution of phenanthrene and naphthalene in toluene, greater than 98.5% pure phenanthrene could be precipitated by CO<sub>2</sub> pressurization while naphthalene with 13% phenanthrene was collected from the liquid phase following expansion (Bertucco et al. 1998). Drug/polymer composites, including hydrocortisone/polyvinylpyrrolidone (PVP), insulin/polyethylene glycol (PEG), and insulin/poly L-lactide (PLA), have been developed for controlled release formulations by co-precipitation using the GAS technique (Elvassore et al. 2001; Corrigan and Crean 2002). The crystal growth orientation preference of caffeine could be manipulated by addition of  $\alpha$ -D-glucose penta acetate, a growth retardant, during GAS recrystallization (Park and Yeo 2008b). These few examples illustrate the many opportunities for engineering multicomponent pharmaceutical formulations by controlled crystallization using the GAS technique.

## 1.7 Summary of Chapters

The objective of this work was to demonstrate the applicability of tunable solvent systems to the development of novel particulate formulations which enhance the deliverability and dissolution of poorly water-soluble APIs. This objective was accomplished through (1) the preparation of drug/excipient mixtures by supercritical antisolvent-drug excipient mixing (SAS-DEM) and (2) the preparation of itraconazole–dicarboxylic acid cocrystals by GAS cocrystallization.

### 1.7.1 Chapter 2

The two poorly water-soluble APIs used in this work, rifampicin and itraconazole, as well as the excipients, stabilizers, formers, solvents, and antisolvents were introduced. A description of the equipment, schematic diagrams of the processes, procedures of operation, and process conditions for each of the crystallization techniques used in this work, including SAS, SAS-DEM, liquid antisolvent cocrystallization, and GAS cocrystallization, were given. Finally, descriptions of the equipment and techniques used to characterize the drug products produced in this work were also provided.

### 1.7.2 Chapter 3

Rifampicin was crystallized in the presence of inhalable lactose particles using a SAS-DEM technique to create rifampicin/lactose microparticle composites intended to improve the effectiveness of pulmonary tuberculosis treatments by increasing the respirable fraction of rifampicin. The effects of solvent, rifampicin concentration, and rifampicin to lactose loading were examined. Changes in the crystalline structure of

rifampicin, expected to improve the aqueous solubility of rifampicin, following SAS crystallization from both dimethyl sulfoxide (DMSO) and methanol were observed by powder X-ray diffraction (PXRD). Differences in particle size and morphology resulting from solvent selection were discussed with respect to the operating conditions employed and mixture critical points (MCPs). Microparticle composite mixtures of rifampicin and lactose with varying rifampicin contents were prepared by SAS-DEM and characterized for composition, homogeneity, particle size and surface morphology, crystallinity, thermal behavior, and chemical interactions.

### 1.7.3 Chapter 4

Itraconazole microflakes were simultaneously crystallized and deposited on the surface of spray dried lactose excipient particles by a SAS-DEM technique to enhance itraconazole dissolution by preventing microflake agglomeration. The effects of itraconazole to lactose loading and addition of stabilizers, sodium dodecyl sulfate (SDS) and Pluronic F-127, on particle formation and drug dissolution were studied. Itraconazole was observed to retain its crystalline structure following SAS crystallization from dichloromethane (DCM), thus allowing improvements in dissolution to be attributed to decreases in particle size resulting in an increased specific surface area as predicted by the Noyes-Whitney equation. The effectiveness of microflake deposition on lactose during crystallization as a means of preventing agglomeration was compared to physical mixing with the excipient. Changes in particle size and morphology due to stabilization were observed by scanning electron microscopy (SEM). Finally, effects of synergism for

particle stabilization during SAS crystallization and deagglomeration through the SAS-DEM technique were investigated through their simultaneous use.

#### 1.7.4 Chapter 5

Itraconazole and L-malic acid were individually dissolved in tetrahydrofuran (THF) and recrystallized by pressurization with CO<sub>2</sub>. The recrystallized components were compared with the original for changes in particle size and morphology and crystallinity. Subsequently, itraconazole and L-malic acid were simultaneously dissolved in THF and recrystallized by pressurization with CO<sub>2</sub> to assess the potential for cocrystal formation in a CO<sub>2</sub>-expanded liquid. The itraconazole/L-malic acid cocrystal product prepared by GAS cocrystallization was compared to that produced using a traditional liquid antisolvent, *n*-heptane, for crystallinity, thermal behavior, composition, homogeneity, particle size and surface morphology, and dissolution behavior. Additional discussion on the effects that cocrystallization might have on equilibrium solubility was provided through the application of thermodynamic equilibria.

#### 1.7.5 Chapter 6

Based on the results of Chapter 5, a less soluble, more crystalline former, succinic acid, was studied for its potential to form cocrystals with itraconazole by GAS cocrystallization. The itraconazole–succinic acid cocrystals prepared by GAS cocrystallization were again compared to those produced using a traditional liquid antisolvent, *n*-heptane, for crystallinity, chemical interactions, thermal behavior, composition, homogeneity, particle size and surface morphology, and dissolution

behavior. Thermal analysis of a number of itraconazole and succinic acid physical mixtures of varying composition revealed the presence of a binary eutectic and provided insight into the extent of cocrystallization achievable by the two methods employed. Supersaturation invoked during solvent removal by flushing with supercritical CO<sub>2</sub> was hypothesized to promote additional cocrystallization, thus producing a product with a qualitatively greater fraction of cocrystals, and thus higher dissolution rate, than that achievable via a traditional liquid antisolvent technique.

## Chapter 2

### Materials and Methods

#### 2.1 Materials

##### 2.1.1 Active Pharmaceutical Ingredients

Rifampicin ( $C_{43}H_{58}N_4O_{12}$ ) is a first line anti-tuberculosis drug that interrupts messenger RNA (mRNA) transcription in *Mycobacterium tuberculosis* by binding to the  $\beta$ -subunit of the DNA-dependent RNA polymerase enzyme complex (Rifampin 2008). The chemical structure of rifampicin and a 3-D depiction of the drug are given in Figure 2.1. The complex structure of rifampicin allows various possibilities for hydrogen bonding, conformational exchanges, and ionization states which give rise to different crystal packings including two crystalline anhydrous forms (forms I and II), a monohydrate, dihydrate, pentahydrate, numerous solvates, as well as two amorphous forms (forms I and II). Rifampicin is freely soluble in chloroform and dimethyl sulfoxide (DMSO), soluble in ethyl acetate, methanol (MeOH), and tetrahydrofuran (THF), and only slightly soluble in acetone and water, leading to its classification as a borderline BCS class II biopharmaceutical (Agrawal et al. 2004). Commercial forms of rifampicin include Rimactane® (Novartis Pharmaceuticals) tablets (450 mg), capsules (150 mg, 300 mg, and 450 mg), and syrup (20 mg/mL), and Rifater® (Sanofi-Aventis) tablets which contain the rifampicin (120 mg) in combination with isoniazid (50 mg) and pyrazinamide

(300 mg). Rifampicin (CAS no. 13292-46-1) powder was purchased from Sigma-Aldrich (St. Louis, MO). The purity was  $\geq 97\%$  (HPLC), as determined by the manufacturer.

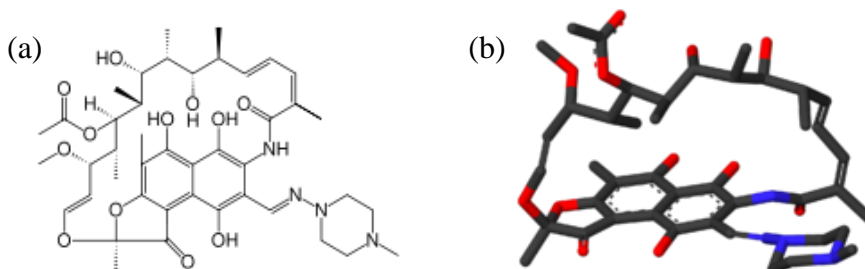


Figure 2.1 (a) Chemical structure and (b) 3-D depiction of rifampicin

Itraconazole ( $C_{35}H_{38}Cl_2N_8O_4$ ) is an antifungal agent that interacts with 14- $\alpha$  demethylase, a cytochrome P-450 enzyme necessary to convert lanosterol to ergosterol, an essential component of the fungal cell membrane. By inhibiting ergosterol synthesis, itraconazole increases fungal cell permeability resulting in leakage of cellular contents. The chemical structure of itraconazole and a 3-D depiction of the drug are given in Figure 2.2. Itraconazole is a weak base ( $pK_a = 3.7$ ), known to form salts and cocrystals. Itraconazole is practically insoluble in water and dilute acidic solutions ( $\sim 1$  ng/mL at pH = 7,  $\sim 5$   $\mu$ g/mL at pH = 1), freely soluble in dichloromethane (DCM), sparingly soluble in THF, and very slightly soluble in alcohol. Itraconazole exhibits high membrane permeability and is commonly used as a model BCS class II biopharmaceutical. The commercial form of itraconazole, Sporanox<sup>®</sup> capsules produced by Janssen Pharmaceutica, coat the drug (100 mg) in its amorphous form on 0.4-0.5 mm diameter sucrose spheres. Other inactive ingredients in Sporanox capsules are hydroxypropyl methylcellulose (HPMC), poly(ethylene glycol) (PEG) 20,000, and starch. Itraconazole



BP micronized (CAS no. 84625-61-6) was purchased from Hawkins Pharmaceutical Group (Minneapolis, MN).

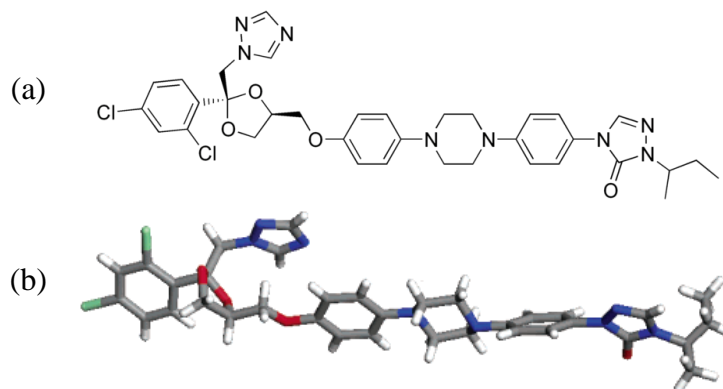


Figure 2.2 (a) Chemical structure and (b) 3-D depiction of itraconazole

### 2.1.2 Excipients, Stabilizers, and Formers

Pharmaceutical grade micronized  $\alpha$ -lactose monohydrate (Lactochem® Microfine) was received as a gift sample from Friesland Foods Domo (The Netherlands). The particle size distribution of Lactochem® Microfine, as reported by the manufacturer, is shown in Figure 2.3. Lactose monohydrate powder is currently in use as an inactive ingredient for inhalable delivery in FDA approved drug products.

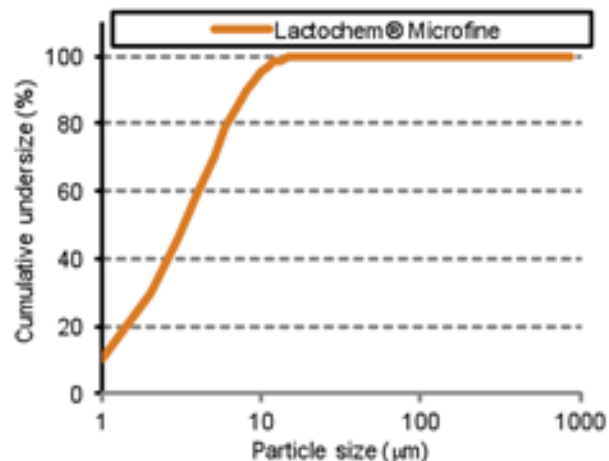


Figure 2.3 Particle size distribution of Lactochem® Microfine (as reported by the manufacturer)

Spray dried lactose monohydrate NF (FastFlo® 316, average size ~ 100 µm) was obtained as a gift sample from Foremost, Inc. (Baraboo, WI). According to the manufacturer, the spray dried lactose is a mixture of crystalline and amorphous lactose, containing 4.5-5.5% water. Lactose monohydrate powder is also FDA approved as an excipient for oral delivery via tablets and capsules.

Sodium dodecyl sulfate (SDS, sodium lauryl sulfate, SLS) is an anionic surfactant approved for use in oral tablets and capsules. The chemical structure of SDS is shown in Figure 2.4. SDS (CAS no. 151-21-3) was purchased from Spectrum Chemical Manufacturing Corporation (Gardena, CA).

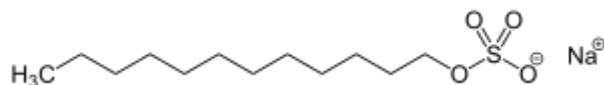


Figure 2.4 Chemical structure of sodium dodecyl sulfate (SDS)

Pluronic® F-127 (Poloxamer 407, Lutrol® F 127) is a hydrophilic tri-block copolymer consisting of a central hydrophobic poly(propylene oxide) (PPO) block surrounded by two hydrophilic poly(ethylene oxide) (PEO) blocks, as shown in Figure 2.5. The hydrophobicity/philicity of block copolymers is controlled by the lengths of the PPO and PEO blocks. For Pluronic F-127,  $x \sim 98$  and  $y \sim 57$ . Pluronic F-127 has been used as an inactive ingredient in FDA approved oral tablets. Pluronic F-127 was obtained as a gift sample from BASF Corporation (Parsippany, NJ).

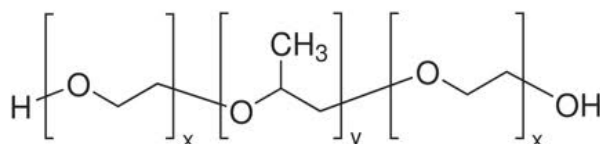


Figure 2.5 Chemical structure of Pluronic® F-127 ( $x \sim 98$  and  $y \sim 57$ )

L-malic acid ( $\text{pK}_{\text{a}1} = 3.4$ ,  $\text{pK}_{\text{a}2} = 5.2$ ) and succinic acid ( $\text{pK}_{\text{a}1} = 4.2$ ,  $\text{pK}_{\text{a}2} = 5.6$ ) are water-soluble dicarboxylic acids. Their structures and 3-D representations are shown in Figures 2.6 and 2.7, respectively. L-malic acid has one extra hydroxyl group compared to succinic acid, giving it an aqueous solubility of 558 g/L at 20 °C as compared to 58 g/L for succinic acid. Both compounds have been used as formers in pharmaceutical cocrystals and inactive ingredients in FDA approved drug products formulated as tablets for oral delivery. L-malic acid (CAS no. 6915-15-7) and succinic acid (CAS no. 110-15-6) were purchased from Sigma-Aldrich (St. Louis, MO).

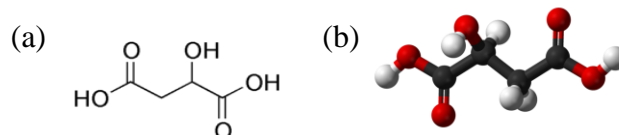


Figure 2.6 (a) Chemical structure and (b) 3-D representation of L-malic acid

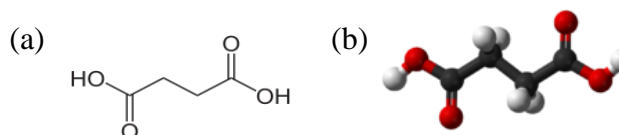


Figure 2.7 (a) Chemical structure and (b) 3-D representation of succinic acid

### 2.1.3 Solvents and Antisolvents

The solvents and antisolvents used in this work are listed in Table 2.1. They represent a range of Class II, solvents whose use should be limited because of their inherent toxicity, and Class III, solvents which may be regarded as less toxic and of lower risk to human health, as classified by the International Conference on Harmonisation of Technical Requirements for Registration of Pharmaceuticals for Human Use (ICH) guidelines. Either ACS or HPLC grade DMSO (CAS no. 67-68-5), MeOH (CAS no. 67-56-1), DCM (CAS no. 75-09-2), THF (CAS no. 109-99-9), and *n*-heptane (CAS no. 142-82-5) were purchased from BDH Chemicals (West Chester, PA), EMD Chemicals Inc. (Gibbstown, NJ), Fisher Scientific Co. (Fair Lawn, NJ), or Mallinckrodt Baker Inc. (Phillipsburg, NJ). Bone-dry carbon dioxide (99.8% purity, < 10 ppb H<sub>2</sub>O) was purchased from Airgas (Opelika, AL).

Table 2.1 Solvents and antisolvents

Solvent	Formula	Class	Concentration Limit (ppm)
Dimethyl sulfoxide (DMSO)	(CH <sub>3</sub> ) <sub>2</sub> SO	III	5,000
Methanol (MeOH)	CH <sub>3</sub> OH	II	3,000
Dichloromethane (DCM)	CH <sub>2</sub> Cl <sub>2</sub>	II	600
Tetrahydrofuran (THF)	(CH <sub>2</sub> ) <sub>4</sub> O	II	720
<i>n</i> -Heptane	C <sub>7</sub> H <sub>16</sub>	III	5,000
Carbon Dioxide	CO <sub>2</sub>	--	--

## 2.2 Crystallization Technologies

### 2.2.1 Supercritical Antisolvent Crystallization

The SAS crystallization apparatus consists of a compressed CO<sub>2</sub> gas cylinder, Isotemp 3006 chiller (Fisher Scientific Inc., Pittsburgh, PA), high pressure P-series pump (Thar Technologies Inc., Pittsburgh, PA), preheater consisting of a water bath and Isotemp immersion circulator (Fisher Scientific Inc., Pittsburgh, PA), high pressure stirred vessel, high pressure Series 1500 liquid pump (Chrom Tech Inc., Apple Valley, MN), and back pressure regulator (Stra-Val Machine Co., Garfield, NJ), as shown in Figure 2.8. A 450 mL stainless steel high pressure vessel was brought to the desired pressure by filling with CO<sub>2</sub> and maintained at  $40 \pm 2$  °C using a Digi-Sense temperature controller (Eutech Instruments, Singapore), BriskHeat heating tape (Cole-Parmer, Vernon Hills, IL), and a thermocouple (Omega Engineering Inc., Stamford, CT). Pressure was measured on a  $0\text{-}345 \pm 2$  bar pressure gauge (McDaniel Controls Inc., Boutte, LA). The pressure was then maintained while flowing CO<sub>2</sub> at 20 g/min using a back pressure regulator. Following equilibration, the drug solution was sprayed into the vessel at 1.0 mL/min through a 75 μm diameter and 15 cm in length PEEKsil nozzle (SGE Analytical Science, Austin, TX). Mass transfer was enhanced by the action of two 45° pitched 4-

blade impellers run at 400 rpm by a BDC 2000 motor (Caframo, Wiarton, Ontario) for the duration of the experiment. The particles were retained in the vessel by a 0.22  $\mu\text{m}$  polytetrafluoroethylene bonded to high density polyethylene membrane filter (Millipore Inc., Billerica, MA) affixed to the CO<sub>2</sub> outlet line inside the vessel. Following injection of the drug solution, the vessel was flushed with excess supercritical CO<sub>2</sub> at a flow rate of 20 g/min for a minimum of 60 minutes to remove any residual solvent. The vessel was then depressurized and the powder collected. Powder samples were stored in airtight glass vials for further analysis.

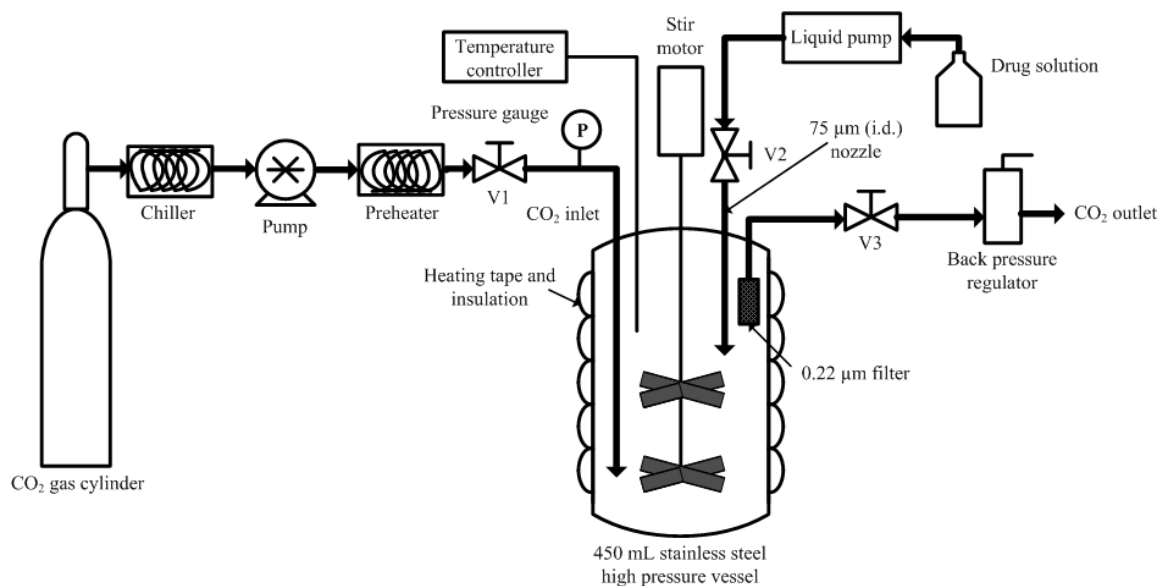


Figure 2.8 Schematic of apparatus for SAS crystallization

## 2.2.2 Supercritical Antisolvent-Drug Excipient Mixing

For supercritical antisolvent-drug excipient mixing (SAS-DEM), a mass of excipient (lactose) was placed in the vessel prior to pressurization. The vessel was then sealed, pressurized, and heated following the procedure outlined in subsection 2.2.1. The

lactose particles were fluidized in the vessel by the action of the impellers, again run at 400 rpm. Following fluidization of the excipient particles, the drug solution was sprayed into the vessel using the same 75  $\mu\text{m}$  diameter PEEKsil nozzle. The vessel was then flushed with excess supercritical  $\text{CO}_2$  at a flow rate of 20 g/min for a minimum of 60 minutes to remove any residual solvent, depressurized, and the powder collected and stored exactly as outlined in subsection 2.2.1. The presence of the excipient particles during drug crystallization is expected to curb particle growth, prevent particle agglomeration, enhance drug product stability, and reduce downstream processing.

### 2.2.3 Liquid Antisolvent Cocrystallization

Itraconazole (250 mg) and either L-malic acid (250 mg) or succinic acid (100 mg) were dissolved in 10 mL of THF, using moderate stirring and heat. The solution was then filtered through a 0.2  $\mu\text{m}$  pore size nylon filter (Whatman Inc., Florham Park, NJ) to remove any undissolved material. *n*-Heptane (20-50 mL) was then added dropwise to the solution, with continuous stirring, to induce cocrystallization. The suspension was centrifuged and the supernatant removed. The cocrystals were then washed with additional *n*-heptane and the centrifugation and supernatant removal process carried out an additional 3 times to ensure full removal of the THF. The cocrystals were allowed to dry overnight. The dried powder was collected and stored in an airtight glass vial for further analysis.

## 2.2.4 Gas Antisolvent Cocrystallization

A schematic of the GAS cocrystallization apparatus (Version 1.0) is shown in Figure 2.9. The 37 mL stainless steel vessel (Thar Technologies, Inc., Pittsburgh, PA) is equipped with multiple sapphire windows for observation. Fiber optic lighting (41720-Series Illuminator, Cole-Parmer, Vernon Hills, IL) was used, through the smaller sapphire windows on the sides of the vessel, to enhance visual observation of the process through the larger sapphire window on the base of the vessel. The same chiller, pump, preheater, pressure gauge, temperature controller, heating tape, thermocouple, and back pressure regulator described in subsection 2.2.1 were also used for GAS cocrystallization. Temperature was maintained at  $40 \pm 2$  °C. Due to size constraints of the vessel, the impeller was replaced with a magnetic stir bar and the vessel placed on an Isotemp magnetic stir plate (Fisher Scientific Inc., Pittsburgh, PA) (not shown in Figure 2.9). Immediate solvent removal following pressurization was facilitated by placing the outlet line, containing a 2  $\mu$ m stainless steel frit (Valco Instruments Company Inc., Houston, TX) for powder retention, at the base of the crystallization vessel.

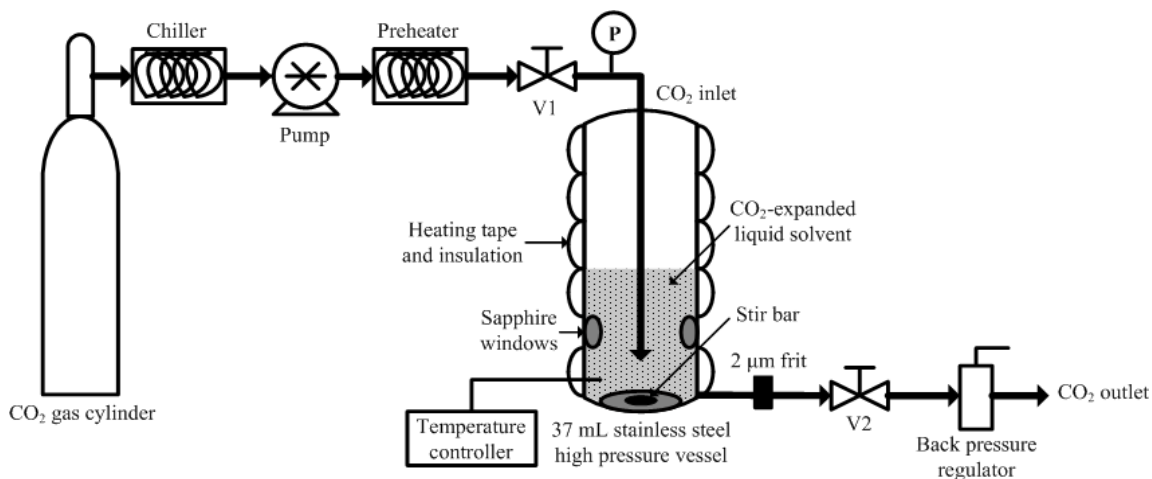


Figure 2.9 Schematic of GAS cocrystallization apparatus (Version 1.0)



Itraconazole (250 mg) and L-malic acid (250 mg) were dissolved in 10 mL of THF, using moderate stirring and heat. The solution was then filtered through a 0.2  $\mu\text{m}$  pore size nylon filter to remove any undissolved material and injected into the GAS cocrystallization vessel previously described. Due to the outlet pressure of the compressed  $\text{CO}_2$  cylinder ( $\sim 65$  bar), pressurization for GAS cocrystallization was accomplished in two regimes, as shown in Figure 2.10. With valve V2 closed, pressure was initially increased stepwise at 6.89 bar/min by opening and closing valve V1. Upon reaching the outlet pressure of the  $\text{CO}_2$  cylinder,  $\text{CO}_2$  was pumped into the vessel at a  $\text{CO}_2$  flow rate of 1 g/min and the pressure recorded. Upon reaching 103 bar, valve V2 was opened and supercritical  $\text{CO}_2$  flushed through the vessel at a flow rate of 10 g/min for 60 minutes using a back pressure regulator to maintain the pressure at 103 bar. The vessel was then depressurized over a period of 30 minutes, and the powder collected and stored in an airtight glass vial for further analysis.

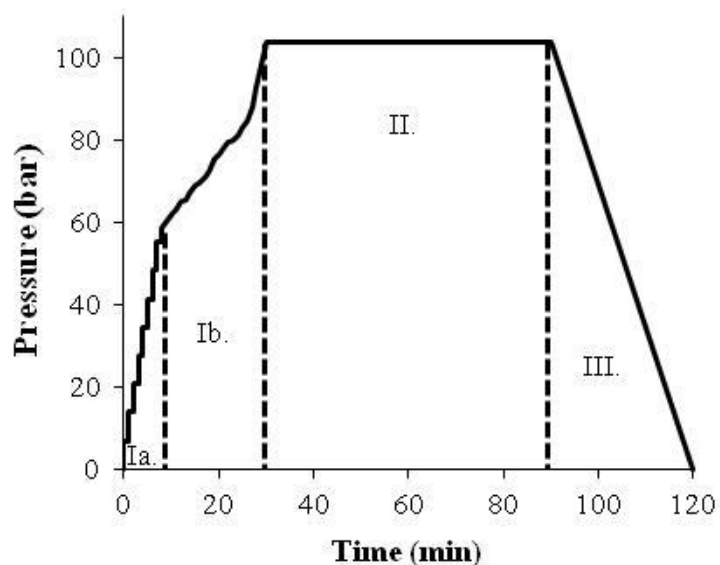


Figure 2.10 Pressure profile for GAS cocrystallization (Version 1.0) Ia. Pressurization at 6.89 bar/min, Ib. Pressurization by  $\text{CO}_2$  pumping at 1 g/min, II. Cocrystal drying at 103 bar, and III. Depressurization

Following itraconazole cocrystallization with L-malic acid, several modifications were made to the GAS cocrystallization apparatus, resulting in Version 2.0, as shown in Figure 2.11. A 0.22  $\mu\text{m}$  stainless steel filter was attached to the  $\text{CO}_2$  inlet line within the crystallization vessel which allowed  $\text{CO}_2$  to be sparged through the liquid solution, thus enhancing mass transfer as compared to magnetic stirring. A second stainless steel vessel was connected in series prior to the crystallization vessel to moderate  $\text{CO}_2$  pressurization by acting as a  $\text{CO}_2$  reservoir. The pressure inside each vessel was measured using a 0-345  $\pm 2$  bar pressure gauge. The temperature inside both vessels was maintained at  $40 \pm 2$   $^\circ\text{C}$  using a standard thermocouple and heating tape. The outlet line, which was relocated to the top of the crystallization vessel to prevent powder clogging and slow solvent flushing, was changed to contain a 0.5  $\mu\text{m}$  size frit.

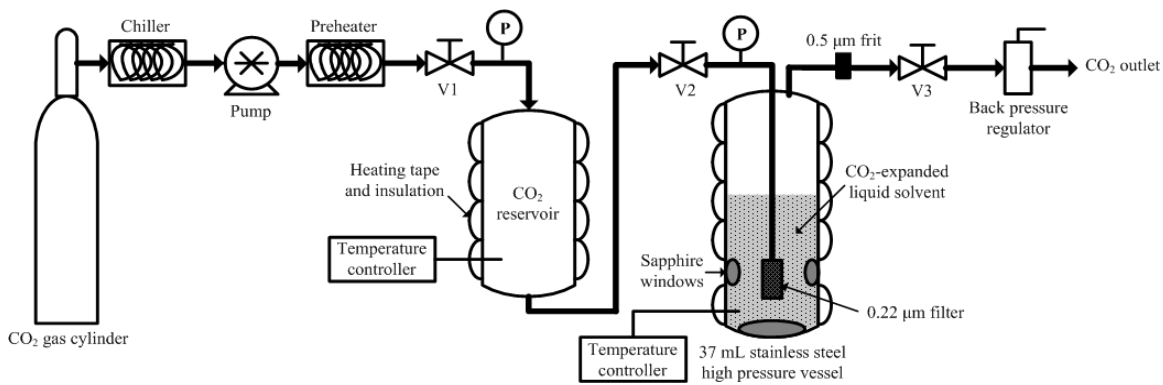


Figure 2.11 Schematic of apparatus for GAS cocrystallization (Version 2.0)

Itraconazole (250 mg) and succinic acid (100 mg) were dissolved in 10 mL of THF, using moderate stirring and heat. The solution was then filtered through a 0.2  $\mu\text{m}$  pore size nylon filter to remove any undissolved material and injected into the crystallization vessel. With valves V2 and V3 closed, compressed  $\text{CO}_2$  was chilled,

pumped with a piston pump, and preheated to 40 °C prior to entering the CO<sub>2</sub> reservoir. Upon filling the CO<sub>2</sub> reservoir to a sufficient pressure, valve V2 was slightly opened to allow a controlled flow of CO<sub>2</sub> into the crystallization vessel. Pressure was increased at a constant rate of approximately 4 bar/min over a period of 25 minutes until a final pressure of 103 bar was achieved, as shown in Figure 2.12. For solvent removal and CO<sub>2</sub> flushing, valve V3 was opened and a back pressure regulator was used to maintain the desired pressure (103 bar). Flushing with additional supercritical CO<sub>2</sub> was conducted for 60 minutes at a CO<sub>2</sub> flow rate of 5 g/min. The vessel was then depressurized over a period of approximately 30 minutes and the cocrystals collected and stored in an airtight glass vial for further analysis.

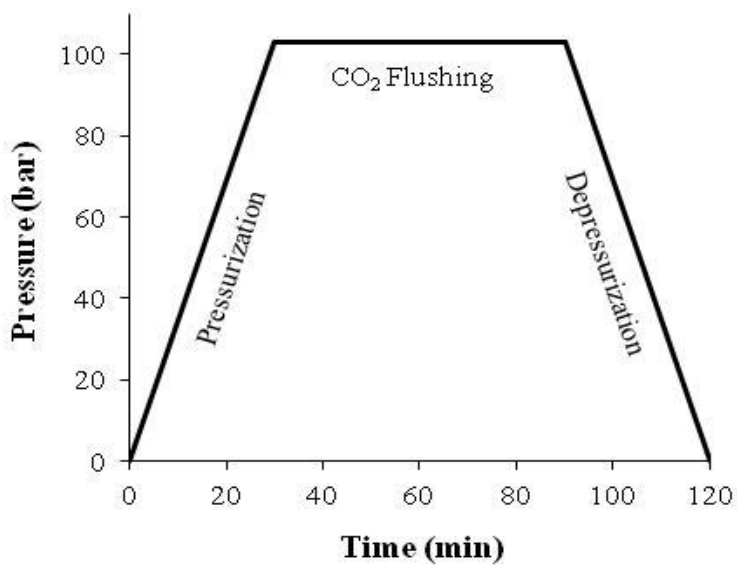


Figure 2.12 Pressure profile for GAS cocrystallization (Version 2.0)

## 2.3 Characterization Techniques

### 2.3.1 Scanning Electron Microscopy

Particle size and surface morphology were studied using an EVO 50 (Zeiss, UK) scanning electron microscope (SEM). Powder samples were sprinkled onto double-sided adhesive carbon tape on an aluminum stub. A thin coating (~15 nm) of gold was applied to the sample using an EMS 550X sputter coater (Hatfield, PA) prior to microscopy.

### 2.3.2 Powder X-ray Diffraction

Crystallinity and cocrystal formation were evaluated by powder X-ray diffraction (PXRD) using either a Rigaku (Rigaku Americas, The Woodlands, TX), Bruker D8 (Madison, WI), or Bruker D8 Advance diffractometer. The Rigaku and Bruker D8 diffractometers were equipped with a Cu  $K\alpha_1$  radiation source while the Bruker D8 Advance was equipped with a Co  $K\alpha_1$  radiation source. All diffractometers were operated at 40 kV and 40 mA. Diffraction patterns were collected from either 5-50° using a step size of 0.05° and a scan speed of 5°/min or 5°-40° using a step size of 0.01° and a count time of 0.1 sec/step. For comparison, the diffraction patterns found using Co  $K\alpha_1$  radiation ( $\lambda = 1.790 \text{ \AA}$ ) were converted to Cu  $K\alpha_1$  radiation diffraction patterns ( $\lambda = 1.542 \text{ \AA}$ ) using the Bragg equation,

$$n\lambda = 2d\sin(\theta) \tag{1}$$

to calculate the  $d$ -spacing.

### 2.3.3 Differential Scanning Calorimetry

Differential scanning calorimetry (DSC) was performed on either a Q200 Differential Scanning Calorimeter or Differential Scanning Calorimeter Autosampler System, both manufactured by TA Instruments (New Castle, DE). Approximately 5 mg of each sample was weighed in an aluminum pan and the thermographs recorded using a heating rate of 10 °C/min under a nitrogen purge.

### 2.3.4 Fourier Transform Infrared Spectroscopy

Fourier transform infrared (FTIR) spectroscopy was conducted on a Nicolet IR 100 (Thermo Scientific, USA). Each sample was mixed with 100-fold KBr for preparing the pellets. The final spectra consist of either 128 scans performed in the range of 400-4000  $\text{cm}^{-1}$  with 4  $\text{cm}^{-1}$  resolution or 64 scans performed in the range of 400-4000  $\text{cm}^{-1}$  with 2  $\text{cm}^{-1}$  resolution.

### 2.3.5 Drug Loading and Content Uniformity

Rifampicin content was determined by ultraviolet-visible (UV-Vis) spectrophotometry using a Jasco V680 UV spectrophotometer (Tokyo, Japan). A rifampicin calibration curve was constructed using standards of 10-50  $\mu\text{g/mL}$  in methanol and the absorption measured at  $\lambda = 475 \text{ nm}$ . Rifampicin/lactose composite compositions were determined by dissolving a known amount of sample (3-10 mg) in 10 mL of methanol and analyzing the rifampicin content by UV spectrophotometry. Since lactose is insoluble in methanol, the solutions were centrifuged and the rifampicin content of the supernatant analyzed. Itraconazole content was determined by UV spectrophotometry at  $\lambda$

= 261 nm. A known amount of sample was dissolved in acetonitrile and the itraconazole content analyzed by UV spectrophotometry. The effect of lactose and Pluronic F-127 on itraconazole absorbance was negligible.

As a measure of content uniformity for both APIs, the relative standard deviation (RSD) of drug content for five randomly selected samples was calculated from:

$$RSD = \frac{\sigma}{\bar{C}} \quad (2)$$

$$\sigma^2 = \frac{\sum_{i=1}^n (\bar{C} - C_i)^2}{n - 1} \quad (3)$$

where  $n$  is the total number of samples,  $\sigma^2$  is the variance,  $\sigma$  is the standard deviation,  $\bar{C}$  is the mean concentration determined experimentally, and  $C_i$  is concentration in sample  $i$ . RSDs of drug content up to 6% are acceptable according to FDA guidelines (Rohrs et al. 2006).

### 2.3.6 Dynamic Light Scattering

Particle size was determined by light obscuration using an Accusizer 780 AD particle size analyzer (Particle Sizing Systems, Santa Barbara, CA). Itraconazole samples were dispersed in deionized water with 0.2 wt. % SDS to form a saturated solution of drug, gently hand-shaken, and 0.5 mL of the dispersion was introduced to the flow cell for analysis. For mixtures containing lactose, care was taken to ensure the lactose was fully dissolved before performing analysis. The particle size distribution (PSD) is expressed as a number weighted average diameter, and the results are expressed as  $d_{50}$  and  $d_{90}$ , denoting the diameter of the 50<sup>th</sup> and 90<sup>th</sup> percentiles of the distribution, respectively. To verify the accuracy of the particle size measurements, latex standards of

0.8  $\mu\text{m}$ , 2  $\mu\text{m}$ , and 5  $\mu\text{m}$  were tested. Average diameters were measured as 0.8  $\mu\text{m}$ , 2.02  $\mu\text{m}$ , and 4.96  $\mu\text{m}$ , respectively.

### 2.3.7 Brunauer-Emmett-Teller Surface Area

Specific surface area was determined using a Nova 3000 surface area analyzer (Quantachrome Corporation, Boynton Beach, FL) to measure nitrogen sorption. The surface area per unit powder mass was calculated by fitting the Brunauer-Emmett-Teller (BET) equation.

### 2.3.8 Saturation Solubility

Saturation solubility studies were carried out according to the procedure described by Higuchi and Connors (Higuchi and Connors 1965). A formulation equivalent to 10 mg of itraconazole was added to 5 mL of water in a scintillation vial and sonicated for 30 minutes, five times a day for two days. Following 24 hours of equilibration, aliquots were withdrawn, filtered using a 0.22  $\mu\text{m}$  pore size nylon filter (Whatman International, England), and spectrophotometrically assayed for itraconazole content at  $\lambda = 261 \text{ nm}$ .

### 2.3.9 High Pressure Liquid Chromatography

A number of the characterization techniques subsequently described require determination of the itraconazole content in a liquid or solid sample, for which liquid chromatography was employed. A Waters (Milford, MA) HPLC system with a UV dual absorbance detector and Brownlee C18 column with inner diameter of 2.1 mm, length of 150 mm, particle size of 5  $\mu\text{m}$ , and pore size of 100  $\text{\AA}$  manufactured by PerkinElmer

(Waltham, MA) were used. A mobile phase of 0.01 M tetrabutylammonium hydrogen sulfate in water and acetonitrile (55:45% (v:v)) and flow rate of 0.3 mL/min were used. Pressure was approximately 97 bar. An itraconazole calibration curve was constructed using standards of 1-20 µg/mL in methanol. Itraconazole content was assayed at  $\lambda = 261$  nm. The concentration of the cocrystal formers (L-malic acid and succinic acid) were not able to be determined (on the C18 column) due to their elution with the mobile phase and the inability to differentiate their peak areas from those of the solvent or mobile phase components.

#### 2.3.10 Gas-Expanded Liquid Solubility

The amount of itraconazole in CO<sub>2</sub>-expanded THF was measured at CO<sub>2</sub> pressures of 0, 21, 41, 62, 83, and 103 bar and in the presence of L-malic acid. The GAS cocrystallization vessel shown in Figure 2.9 was slightly modified for the purpose of making such measurements. A three-way valve and 0.5 µm stainless steel frit were attached to the CO<sub>2</sub> inlet line just prior to its entrance into the vessel. The three-way valve allowed flow of CO<sub>2</sub> into the vessel through its left side and withdrawal of liquid sample through its right side. By using the same line for CO<sub>2</sub> pressurization and sample withdrawal, the line was flushed with CO<sub>2</sub> to remove any residual liquid sample between subsequent measurements. A 0.22 µm inlet solvent filter was also attached to the end of the CO<sub>2</sub> line within the vessel. The inlet solvent filter and frit prevented withdrawal of solid sample such that upon depressurization the itraconazole content in solution remained the same. Similar apparatus have been used in the literature for making solubility measurements in gas-expanded liquids (Chang and Randolph 1990; Warwick et



al. 2000; Cocero and Ferrero 2002). Itraconazole (500 mg) and L-malic acid (500 mg) were dissolved in 20 mL of THF, using moderate stirring and heat. The concentrations used for making these measurements were selected to reflect the concentrations used in forming the cocrystals (Warwick et al. 2000). The solution was filtered through a 0.2  $\mu\text{m}$  pore size nylon filter to remove any undissolved material and injected into the GAS cocrystallization vessel. An aliquot was also set aside for itraconazole content determination at 0 bar. The GAS cocrystallization vessel was subjected to the desired pressure, allowed to equilibrate for 30 minutes, and a sample withdrawn. Itraconazole content was analyzed by the HPLC method previously described. Although the itraconazole content measurements were made on a  $\text{CO}_2$ -free basis, their values are representative of the solubility in a  $\text{CO}_2$ -expanded THF phase since itraconazole solubility would only be enhanced upon depressurization.

#### 2.3.11 Dissolution Studies

Dissolution studies were carried out in either 900 mL of 0.1 N HCl with 0.3% SDS medium using a USP-II dissolution apparatus (Hansen Research, Chatsworth, CA) or 450 mL 0.1 N HCl with 0.3% SDS medium using a self-constructed dissolution apparatus. Temperature was maintained at  $37 \pm 2$  °C and stirring at 50 rpm in order to represent physiological conditions. A formulation equivalent to either 10 mg of the drug or 5 mg of the drug was sprinkled onto the top of the dissolution medium. Liquid samples were withdrawn at time intervals of 5, 10, 15, 20, 30, 45, 60, 75, 90, and 120 minutes, and filtered using 0.45  $\mu\text{m}$  or 0.2  $\mu\text{m}$  pore size nylon filters. Equivalent aliquots of dissolution medium were added following sample withdrawal to maintain a constant

volume. The samples were assayed for itraconazole content by UV spectrophotometry at 261 nm. Dissolution profiles were constructed to show the amount of drug dissolved as a function of time. The data presented represent a mean  $\pm$  standard error of 2 to 6 studies. The mean cumulative amount of itraconazole dissolved after 60 or 120 minutes is expressed as  $D_{60}$  or  $D_{120}$ , respectively.

#### 2.3.12 Physical Stability

The physical stability (shelf life) of the cocrystal samples was evaluated by placing powder samples, contained in glass vials, in a 90 °C/dry oven for 7, 14, and 28 days and assessing any changes in crystallinity by PXRD. All samples (including an untreated sample) were from the same batch and were analyzed at the same time, which allowed any changes in crystallinity to be attributed to thermal stress and not due to storage at ambient conditions.

## Chapter 3

### Preparation of Rifampicin/Lactose Microparticle Composites by a Supercritical Antisolvent-Drug Excipient Mixing Technique for Inhalation Delivery

#### **3.1 Rifampicin for the Treatment of Tuberculosis**

Tuberculosis (TB) is an airborne infectious disease caused by *Mycobacterium tuberculosis*. When inhaled, *Mycobacterium tuberculosis* is phagocytosed by the alveolar macrophages and will reside in the lungs until the immune system of the human host is compromised, thus triggering its activation and leading to an eventual symptomatic infection. The World Health Organization (WHO) estimates that one third of the world population is infected with latent TB, from which approximately 6 million people will develop active TB. In 2009, 1.7 million people died from TB, with the highest number of deaths occurring in Africa (WHO 2010). Current treatment for TB consists of frequent high dosing of combinations of oral anti-tuberculosis drugs, most commonly isoniazid, pyrazinamide, and rifampicin (Figure 3.1). This method of treatment, however, causes systemic toxicity and undesired side effects while the intensive regimen leads to patient noncompliance (Schreiber et al. 1999). To avoid systemic toxicity and maximize drug effectiveness, anti-tuberculosis drugs are also being formulated for direct delivery to the affected site, the deep regions of the lungs.

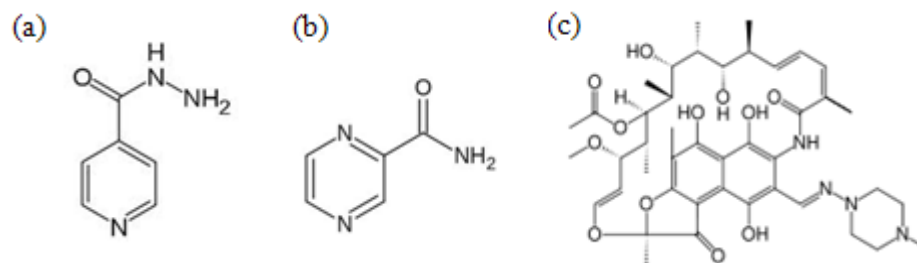


Figure 3.1 Chemical structures of (a) isoniazid, (b) pyrazinamide, and (c) rifampicin

The most common pulmonary delivery devices include nebulizers, metered dose inhalers, and dry powder inhalers (DPIs) (Groneberg et al. 2003). DPIs can effectively deliver an aerosolized fine powder of drug particles directly to the lung, do not use chlorofluorocarbon propellants, and have the advantage of keeping the drug in a dry, solid form which promotes stability (Prime et al. 1997). Recently, microparticle and nanoparticle systems have been incorporated into inhalation delivery (Gupta and Kompella 2006; Swai et al. 2009). Despite the ability of micro- and nanoparticles to penetrate deep within the lungs and their rapid uptake by the alveolar macrophages, their delivery remains challenging. Particle agglomeration prohibits deep lung penetration while unaggregated nanoparticles are exhaled due to their low inertia (Heyder and Rudolf 1984; Heyder et al. 1986). Therefore, micro- and nanoparticle inhalation therapies often combine the active pharmaceutical ingredient(s) (APIs) with pharmaceutically acceptable excipients or carriers. The blending of micro- and nanoparticle APIs with pharmaceutical excipients for use in DPIs can assist with processing properties such as flowability, promote dosing consistency, and provide a taste or sensation to assure the patient a dose has been received (Prime et al. 1997).

Rifampicin is the most common drug used in anti-tuberculosis therapies (Rifampin 2008; Becker et al. 2009). Despite being an effective drug molecule, treatment

of TB with rifampicin still faces a number of challenges. Firstly, the oral delivery of rifampicin can cause a number of serious side effects including hepatotoxicity (Changsan et al. 2009). Secondly, rifampicin exhibits concentration-dependent activity, meaning that its therapeutic activity is directly proportional to its concentration at the target site (Gumbo et al. 2007). Compounding this is the fact that rifampicin is a class II biopharmaceutical, and its dissolution is rate-limited by its poor aqueous solubility (Becker et al. 2009). Therefore, treatment of TB using rifampicin will be most effective when a high concentration of the drug can be delivered directly to and sustained at the alveolar macrophages.

Various researchers have sought to achieve this goal by creating rifampicin nanoparticles (Viçosa et al. 2011) and microparticles (Reverchon et al. 2002), encapsulating rifampicin in 200-300 nm liposome vesicles (Changsan et al. 2009) and biodegradable polymers such as poly(lactide-*co*-glycolide) (PLGA) (O'Hara and Hickey 2000; Suarez et al. 2001; Sung et al. 2009) and poly(L-lactide) (PLA) (Muttill et al. 2007; Patomchaiwivat et al. 2008; Son and McConville 2012), creating rifampicin composites through spray drying with pharmaceutical excipients such as mannitol (Mizoe et al. 2008) and lactose (Darbandi et al. 2008), increasing the aqueous solubility of rifampicin through cyclodextrin complexation (Tewes et al. 2008), and altering the crystal structure and particle morphology of rifampicin (Son and McConville 2011). The problem with many of these techniques is that the excipients used, such as PLGA, PLA, hydroxypropyl- $\beta$ -cyclodextrin (HP $\beta$ CD), and randomly methylated  $\beta$ -cyclodextrin (RAMEB), are not approved by the Food and Drug Administration (FDA) for inhalation delivery.

In this study, four rifampicin/lactose microparticle composite formulations were prepared using supercritical antisolvent-drug excipient mixing (SAS-DEM). Supercritical antisolvent (SAS) crystallization in the presence of excipients such as lactose has previously been shown to deagglomerate cohesive drug micro- and nanoparticles (Sanganwar et al. 2010). Furthermore, lactose monohydrate is an FDA approved excipient for inhalation delivery. Rifampicin micro- and nanoparticles were prepared from two solvents, DMSO and methanol, using SAS crystallization. The rifampicin micro- and nanoparticles were then crystallized in the presence of inhalation size appropriate ( $d_{90} = 10 \mu\text{m}$ ) lactose monohydrate particles and the effects of rifampicin concentration and rifampicin to lactose loading studied. Each of the rifampicin/lactose microparticle composites was characterized for composition, particle size and surface morphology, crystallinity, thermal behavior, and physicochemical properties. Pulmonary delivery of the rifampicin/lactose microparticle composites should reduce rifampicin particle loss during exhalation, improve aqueous solubility through increased surface area due to particle deagglomeration, and allow deep lung penetration of the rifampicin micro- and nanoparticles following lactose dissolution. In addition, the rifampicin/lactose microparticle composites produced in this single-step process should be suitable for direct use in a DPI without further processing.

## **3.2 SAS Crystallization of Rifampicin Micro- and Nanoparticles**

### **3.2.1 Scanning Electron Microscopy**

The SEM image of unprocessed rifampicin, as obtained from the supplier, featured rod-like structures with a mean particle size ranging from 20 to 200  $\mu\text{m}$ , as

shown in Figure 3.2a. Since this particle size range is inappropriate for inhalation delivery, which requires aerodynamic diameters from 1-5  $\mu\text{m}$ , SAS crystallization was invoked as a means of micronizing the rifampicin. The SAS technique has previously been used to precipitate rifampicin micro- and nanoparticles using a number of solvents and conditions (Reverchon et al. 2002). The solvent found most effective by Reverchon et al. was DMSO, which at 40  $^{\circ}\text{C}$  and 120 bar gave nanoparticles with mean diameters ranging from 0.4 to 1  $\mu\text{m}$ . These results were replicated in the current study (Figure 3.2b), where rifampicin was precipitated by the SAS process using a drug concentration of 10 mg/mL in DMSO at 124 bar and 40  $^{\circ}\text{C}$ . Despite the individual particles having an average diameter of approximately 1  $\mu\text{m}$ , their propensity for agglomeration, as illustrated by the flock of nanoparticles in Figure 3.2b, renders them unsuitable for effective pulmonary delivery to the alveolar macrophages.

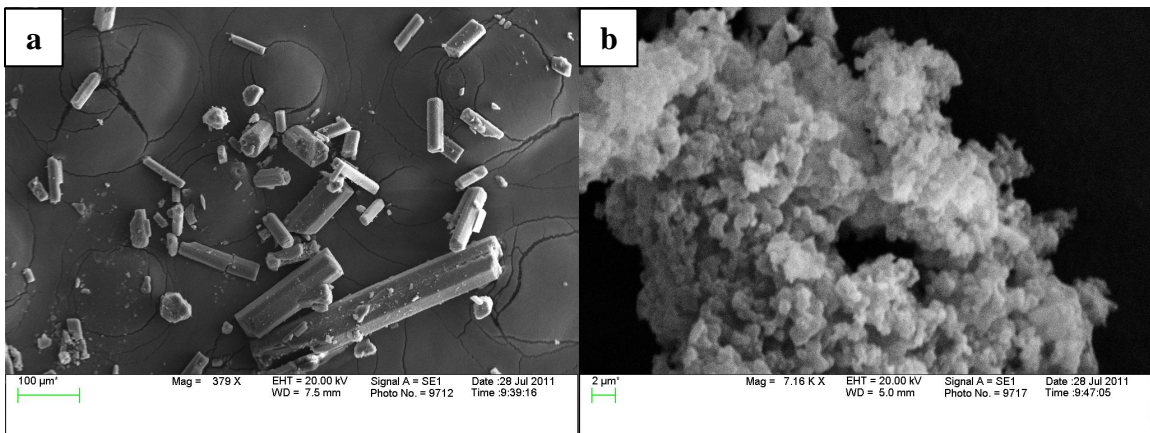


Figure 3.2 SEM images of (a) supplier rifampicin and (b) rifampicin nanoparticles precipitated from DMSO at 10 mg/mL, 124 bar, and 40  $^{\circ}\text{C}$

In order to overcome the van der Waals forces ( $F_{vdw}$ ) responsible for rifampicin nanoparticle agglomeration, it is desirable to incorporate an excipient, which can act as a

spacer between the drug particles, thus increasing the interparticle spacing ( $l$ ). The addition of an excipient can also assist with powder flowability for DPI delivery and maintenance of mixture homogeneity to ensure accurate dosing. The SAS-DEM process has already been found effective at reducing drug particle agglomeration, improving flowability, and maintaining homogeneity (RSD < 4%) (Sanganwar et al. 2010). Previous work, however, has focused on the micronization and deagglomeration of a poorly water-soluble drug, nevirapine, for oral formulations utilizing spray dried lactose particles of approximately 100  $\mu\text{m}$  in diameter. This current study is the first to use the SAS-DEM process with excipient particles less than 10  $\mu\text{m}$  in size. The lactose monohydrate excipient particles are shown in Figure 3.3 and had particle size distribution  $d_{90}$  and  $d_{50}$  values of 10  $\mu\text{m}$  and 5  $\mu\text{m}$ , respectively, as reported by the manufacturer (see Figure 2.3). The solubility of lactose in DMSO, however, made the solvent unsuitable for use in the SAS-DEM technique. In order to effectively deagglomerate the drug micro- and nanoparticles and create uniform drug/excipient composites using the SAS-DEM technique, the excipient must be insoluble in the solvent used.



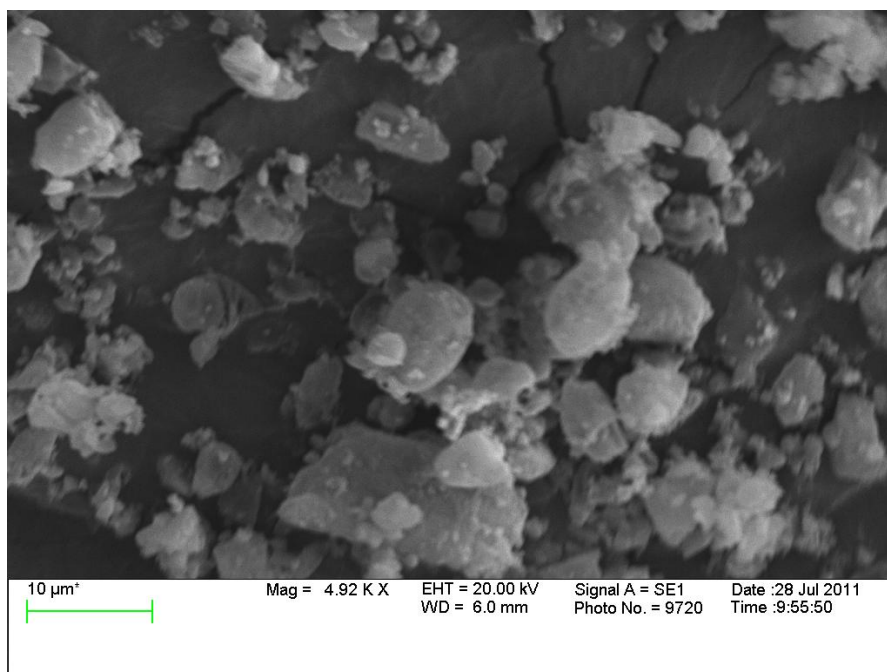


Figure 3.3 SEM image of supplier lactose monohydrate

Methanol was selected as an alternative solvent for rifampicin crystallization in the SAS-DEM process due to its inability to dissolve lactose. SAS crystallization of rifampicin from methanol using the same conditions as SAS crystallization from DMSO, namely 10 mg/mL, 124 bar, and 40 °C, gave larger microflakes, as seen in Figure 3.4a. Based on previous results with DMSO, it was assumed that lowering the drug concentration would decrease particle size to a range more appropriate for pulmonary delivery (Reverchon et al. 2002). Reducing the rifampicin concentration to 5 mg/mL in methanol gave a number of smaller particles and fewer large microflakes, as shown in Figure 3.4b.

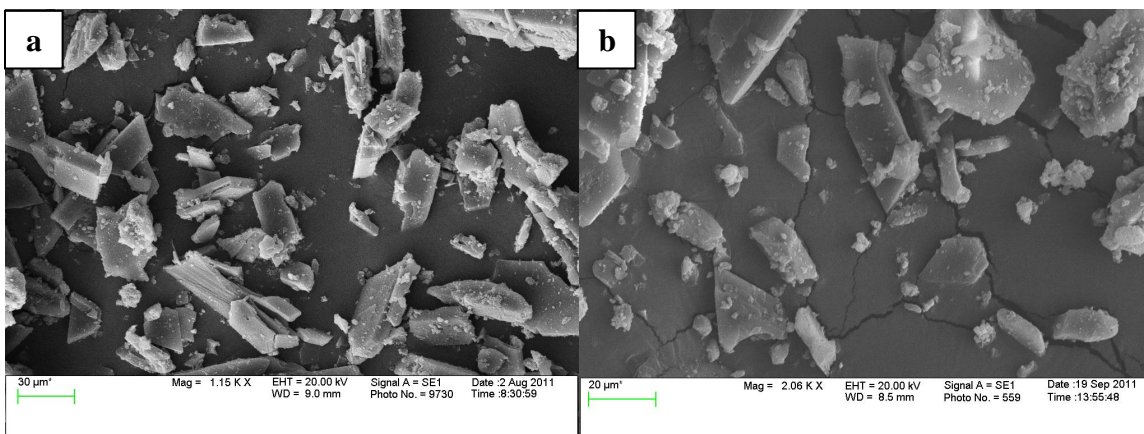


Figure 3.4 SEM images of (a) rifampicin microflakes crystallized from methanol at 10 mg/mL, 124 bar, and 40 °C and (b) rifampicin microparticles crystallized from methanol at 5 mg/mL, 124 bar, and 40 °C

The mechanism of particle formation during SAS crystallization is dependent upon the operating conditions (i.e. temperature and pressure) used with respect to the mixture critical point (MCP), or the pressure at which the mixture becomes supercritical. While MCPs for CO<sub>2</sub>-solvent mixtures are readily available from phase equilibria, the presence of a solute can influence the location of the MCP. For example, the presence of rifampicin shifted the MCP for CO<sub>2</sub>-DMSO from slightly above 90 bar to nearly 120 bar at 40 °C (Reverchon et al. 2002). When operating below the MCP, particle formation is a result of multiphase mixing, owing to the persistence of interfacial tension between the solvent and supercritical fluid, following jet break up of the solution stream into droplets. When operating above the MCP, particle formation is governed by gas plume formation, due to the disappearance of interfacial tension prior to jet break up, resulting in the rapid nucleation of nanoparticles (Figure 3.2b). Based on the results observed in Figure 3.4, it is hypothesized that conditions of 124 bar and 40 °C are below the MCP for CO<sub>2</sub>-methanol with rifampicin and that particle formation occurs in the liquid droplets

following jet break up. Under these conditions, a decrease in rifampicin concentration would mean less rifampicin molecules per droplet of solution, leading to a decrease in particle size.

Prior to carrying out SAS crystallization in the presence of lactose, the effect of spraying methanol on the lactose monohydrate particles was also studied. A quantity of lactose, 1000 mg, was placed in the SAS crystallization vessel, and pure methanol (no rifampicin) was sprayed into the vessel at 124 bar and 40 °C. Following flushing and depressurization, the lactose particles were collected and analyzed by SEM. The results are shown in Figure 3.5. By comparison with Figure 3.3, the unprocessed lactose monohydrate, there appeared to be no change in lactose particle size or surface morphology due to SAS processing.

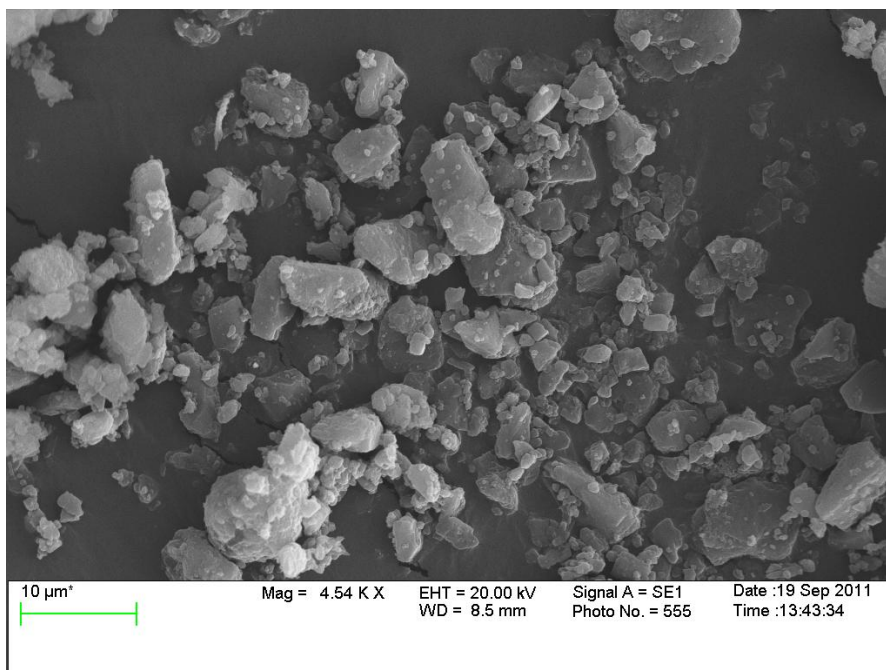


Figure 3.5 SEM image of lactose monohydrate following SAS processing with pure methanol (no rifampicin) at 124 bar and 40 °C

### 3.2.2 Powder X-ray Diffraction

In addition to particle size and surface morphology, solvent selection also affected the crystallinity of rifampicin. Rifampicin is known to be a polymorphic drug, featuring two crystalline forms, form I and form II, as well as a number of solvates, hydrates, and amorphs (Pelizza et al. 1977; Henwood et al. 2001). The PXRD patterns for the unprocessed rifampicin, SAS rifampicin precipitated from DMSO, and SAS rifampicin crystallized from methanol are shown in Figure 3.6. The unprocessed rifampicin PXRD pattern featured crystalline peaks at  $2\theta$  values of  $13.65^\circ$  and  $14.36^\circ$ , characteristic of rifampicin form I. The lack of any peaks in the rifampicin precipitated from DMSO indicates that processing has caused the rifampicin to lose its crystalline nature and become amorphous. This result correlates with previous literature which found rifampicin to be amorphous following SAS precipitation from DMSO since the speed of precipitation, resulting from operation above the MCP, prevents the rifampicin from reorganizing into a crystalline form (Reverchon et al. 2002). Rifampicin crystallized from methanol under the same conditions as that precipitated from DMSO showed a crystalline nature. The PXRD pattern matched that reported in the literature for a rifampicin dihydrate form previously obtained by crystallization from a number of solvents including benzene, ethyl acetate, and tetrahydrofuran (Henwood et al. 2001; Son and McConville 2011). It is suspected that trace water content in the methanol, certified as 0.007% by the manufacturer, contributed to the formation of rifampicin hydrates during SAS crystallization.

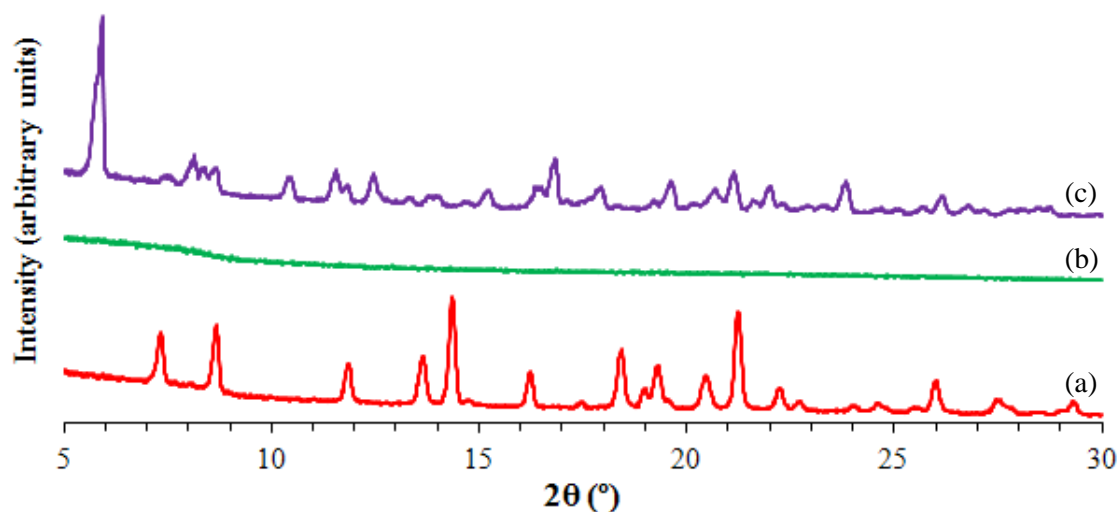


Figure 3.6 PXRD patterns (from bottom to top) for (a) rifampicin, (b) SAS rifampicin precipitated from DMSO, and (c) SAS rifampicin crystallized from methanol

Since rifampicin is reported to be approximately twice as soluble in DMSO (120 mg/mL) as it is in methanol (60 mg/mL), it would be expected that for identical concentrations of rifampicin (10 mg/mL), supersaturation would occur more quickly using methanol if the rifampicin-CO<sub>2</sub>-solvent systems displayed identical phase behavior (Reverchon et al. 2002). Therefore, differences in the speed of crystallization must result from the differing phase behaviors of the rifampicin-CO<sub>2</sub>-solvent systems. This again confirms the fact that the MCP for a rifampicin-CO<sub>2</sub>-methanol system is above that of a rifampicin-CO<sub>2</sub>-DMSO system.

Changes in the crystalline form of rifampicin may have several implications when considering clinical applications. Rifampicin dihydrate has been shown to have improved aqueous solubility ( $1.28 \pm 0.01$  mg/mL) compared to rifampicin form I ( $0.59 \pm 0.05$  mg/mL), especially in acidic environments (Henwood et al. 2001; Son and McConville

2011). Delivery of rifampicin dihydrate to the alveolar macrophages, where the endosomal pH is 5.2, may increase rifampicin efficacy (O'Hara and Hickey 2000). The stability of the dihydrate form, however, will need to be studied. While relative humidity during storage should actually preserve the dihydrate form, excessive heat during storage could cause dehydration and conversion to amorphous rifampicin (Henwood et al. 2001).

### **3.3 Rifampicin/Lactose Microparticle Composites by SAS-DEM**

Rifampicin micro- and nanoparticles were crystallized in the presence of micronized  $\alpha$ -lactose monohydrate particles using the SAS-DEM technique (refer to subsection 2.2.2 for details). A known mass of lactose (~1000 mg) was placed in the SAS crystallization vessel shown in Figure 2.8 prior to pressurization. The vessel was brought to 124 bar and 40 °C, as before, to achieve supercritical CO<sub>2</sub> conditions. Stirring was maintained at 400 rpm and antisolvent (CO<sub>2</sub>) flow at 20 g/min, allowing the lactose particles to become suspended in the vessel. Varying volumes of 1 mg/mL and 5 mg/mL rifampicin in methanol solutions were sprayed into the vessel to prepare rifampicin/lactose microparticle composites ranging in rifampicin composition from 1-25 wt. %. Following injection of the drug solution, the vessel was flushed with excess supercritical CO<sub>2</sub> at a flow rate of 20 g/min for a minimum of 60 minutes to remove any residual solvent. The vessel was then depressurized and the rifampicin/lactose composite powders were collected indiscriminately from the sides and base of the crystallization vessel using a spatula and/or brush. Powders were stored in airtight glass vials at -20 °C until analysis.

Table 3.1 summarizes the experiments performed, the rifampicin loading in the final composite as determined by UV spectrophotometry, RSD of rifampicin content for each composite, and the maximum and minimum concentrations observed in the RSD analysis. Run 1 used a rifampicin concentration of 1 mg/mL while runs 2-4 used a concentration of 5 mg/mL. Yield was not calculated for the experiments, but it should be noted that the amount of rifampicin sprayed into the vessel was slightly more than the amount determined by UV analysis in the final rifampicin/lactose composite. For example, in the experiments using a concentration of 5 mg/mL in methanol, approximately 75% of the rifampicin sprayed crystallized in the vessel while approximately 25% remained in solution. This loss of rifampicin was also visually confirmed, due to its bright orangish-red color, in the methanol/CO<sub>2</sub> effluent stream.

Table 3.1 Rifampicin loading, relative standard deviation (RSD), and maximum and minimum concentrations observed in RSD analysis for rifampicin/lactose microparticle composites produced by SAS-DEM

Run	Rifampicin Loading (wt. %)	RSD (%)	Maximum Concentration (µg/mL)	Minimum Concentration (µg/mL)
1	1.2	5.7	12.9	11.2
2	7.2	4.5	37.4	34.2
3	14.0	5.2	73.1	63.9
4	25.7	2.3	79.4	75.7

Drug content homogeneity is a critical factor when considering the rifampicin/lactose composites for delivery via a DPI. The bright orangish-red color of rifampicin with contrasting white color of lactose facilitated visual observation of homogeneity. The 1.2 wt. % rifampicin composite was predominately white with a hint

of light orange, while the 7.2-25.7 wt. % rifampicin composites ranged from light orange to light pink to a dark rose color with increasing rifampicin content, as shown in Figure 3.7. Differences in the composition of the powder on the sides of the vessel versus the base of the vessel were not studied, since the powder was collected indiscriminately from both locations. Nonetheless, the inherent spatula mixing encountered during collection was sufficient to achieve composites who's RSD of drug content, as shown in Table 3.1, conformed to the FDA acceptability guidelines of up to 6% (Rohrs et al. 2006). In support of the narrow RSDs, the maximum and minimum concentrations observed in the RSD analysis for each composite were also included in Table 3.1. Even with light microscopy, differentiation of drug versus lactose particles was unachievable, indicating the absence of large pure component domains.

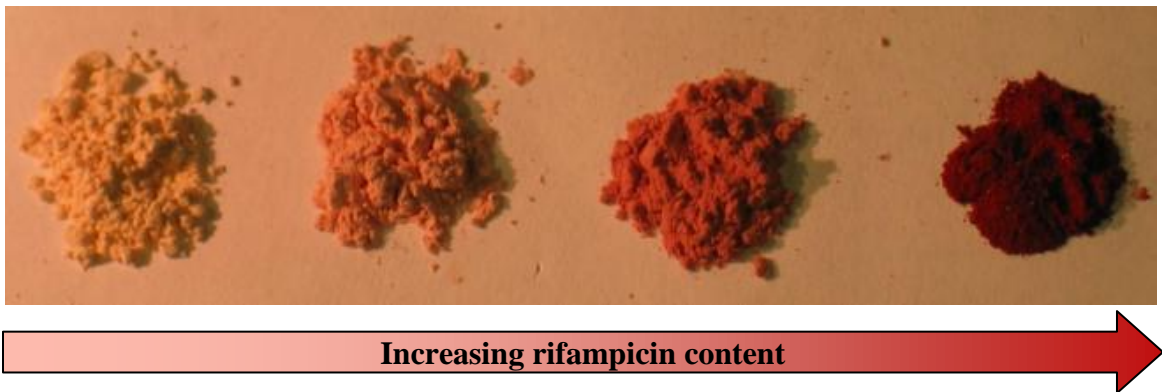


Figure 3.7 Visual observation of increasing rifampicin content in rifampicin/lactose composites



### **3.4 Characterization of Rifampicin/Lactose Microparticle Composites**

#### **3.4.1 Scanning Electron Microscopy**

An SEM image of each composite is shown in Figure 3.8. Due to the similar surface morphology and particle sizes of the crystallized rifampicin and lactose microfine, there are no distinguishable differences between the composites. An important observation gained from the SEM images, however, is the lack of large rifampicin microflakes as were observed in the SAS experiment which used a concentration of 5 mg/mL in methanol (Figure 3.4b). It is thought that the presence of the lactose particles had an effect on rifampicin particle growth during crystallization. In the images, nearly all particles seem to be less than 8  $\mu\text{m}$  in diameter with the majority of particles ranging between 1 and 5  $\mu\text{m}$ . The following subsections will elaborate upon the results obtained from a number of characterization techniques that were used to further study the nature of the interactions between the rifampicin and lactose.

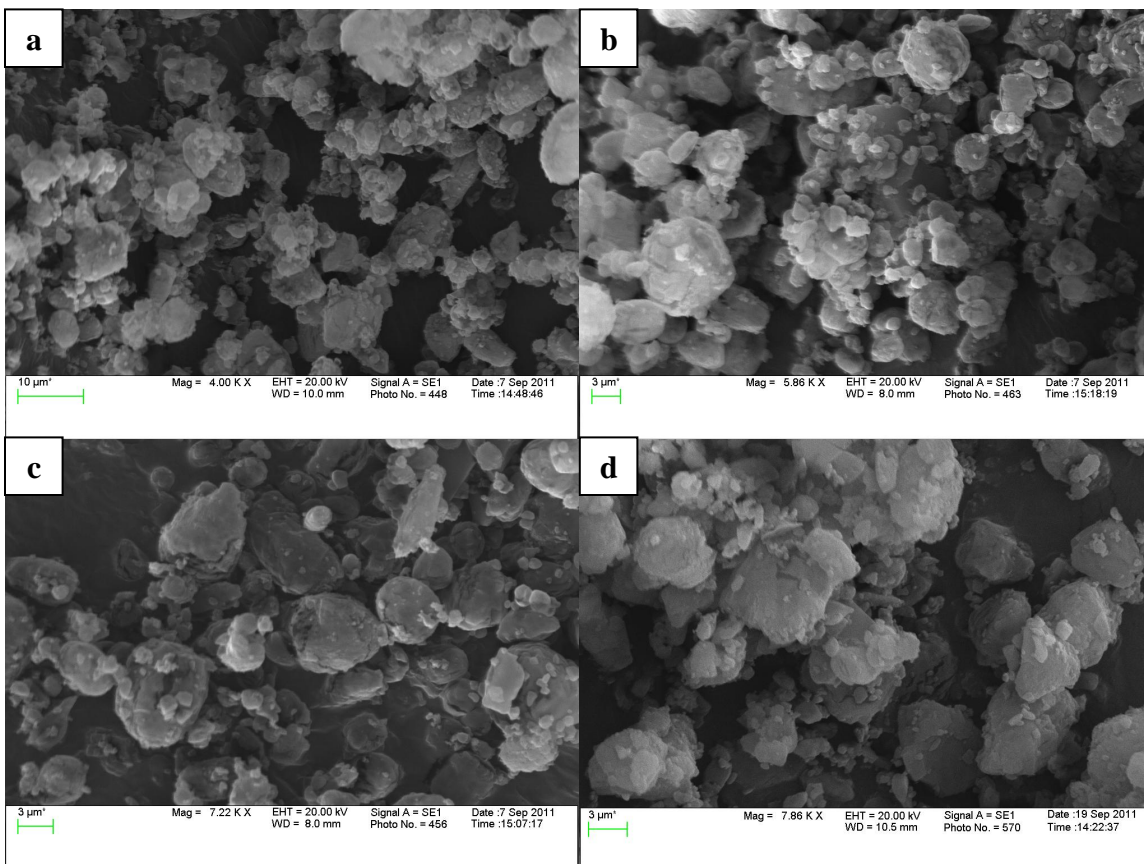


Figure 3.8 SEM images of composites obtained from SAS-DEM with (a) 1.2 wt. % rifampicin loading (run 1), (b) 7.2 wt. % rifampicin loading (run 2), (c) 14.0 wt. % rifampicin loading (run 3), and (d) 25.7 wt. % rifampicin loading (run 4)

### 3.4.2 Powder X-Ray Diffraction

The PXRD patterns for the SAS processed lactose monohydrate, rifampicin/lactose composites produced by SAS-DEM, and SAS rifampicin are shown in Figure 3.9. The SAS processed lactose monohydrate is highly crystalline, despite a slight decrease in the degree of crystallinity compared to the unprocessed lactose monohydrate (pattern not shown) due to its contact with methanol and supercritical CO<sub>2</sub> in the SAS process. From the composites' PXRD patterns it appears that both the lactose and rifampicin retained their individual crystalline structures during processing. Due to the

low concentration of rifampicin in the composite, its peaks are not apparent in the patterns for runs 1 and 2, but as rifampicin loading is increased (runs 3 and 4) its characteristic crystalline peaks, namely the peak at a  $2\theta$  value of  $5.9^\circ$ , become more prominent. The slight shift ( $0.2^\circ$  or less) that appears between the  $19.9^\circ$  peak in the lactose monohydrate pattern and that same peak in each of the processed composites is likely due to a small change in the alignment of the sample as opposed to a change in the  $d$ -spacing of the crystal lattice since that same shift occurs for each peak in the pattern. Since each of the components retained its individual crystalline structure during processing, it appears that changes in the composite bioavailability due to cocrystallization of the two components during shelf storage should be avoided.

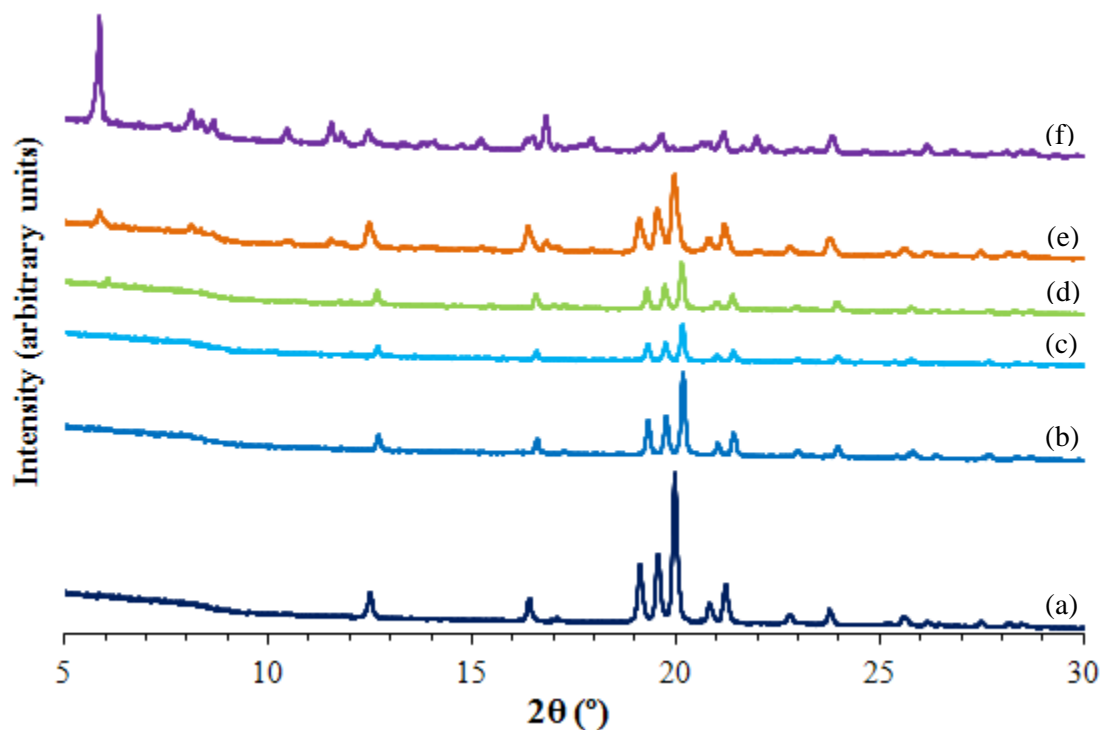


Figure 3.9 PXR D patterns (from bottom to top) for (a) SAS processed lactose monohydrate, (b) SAS-DEM composite with 1.2 wt. % rifampicin loading, (c) SAS-DEM composite with 7.2 wt. % rifampicin loading, (d) SAS-DEM composite with 14.0 wt. % rifampicin loading, (e) SAS-DEM composite with 25.7 wt. % rifampicin loading, and (f) SAS rifampicin

### 3.4.3 Differential Scanning Calorimetry

DSC was conducted to study the thermal behavior of the raw materials and processed samples. Thermographs from 90 °C to 230 °C for rifampicin, SAS processed rifampicin, the SAS-DEM rifampicin/lactose composites, and lactose monohydrate are shown in Figure 3.10. The lack of a melting endotherm from 180-197 °C, as is characteristic of rifampicin form II, supports the PXR D results (Figure 3.6) that the unprocessed rifampicin is form I, which is known to directly decompose at 255-266 °C (Agrawal et al. 2004). In contrast to the supplier rifampicin, the rifampicin crystallized from methanol by the SAS process at 5 mg/mL, 124 bar, and 40 °C shows a desolvation

endotherm up to 110 °C, characteristic of rifampicin dihydrate, and a broad exotherm from 188 °C to 214 °C, characteristic of amorphous rifampicin. This thermograph shows that upon heating, the rifampicin dihydrate formed by SAS crystallization from methanol undergoes dehydration and converts to amorphous rifampicin. The DSC thermograph for lactose monohydrate shows an endothermic transition at 149 °C, representing the loss of crystalline water, and an endothermic peak at 209 °C representing the melting  $\alpha$ -lactose monohydrate (Gombás et al. 2002). The thermographs for the SAS-DEM composites show several deviations from the lactose monohydrate thermograph. Melting of  $\alpha$ -lactose occurs at a higher temperature ( $\sim$  217 °C) in the composites, attributed to a change in the crystalline versus amorphous content of the lactose caused by exposure to methanol and supercritical CO<sub>2</sub> during SAS processing. Also, a second melting endotherm emerges at  $\sim$  225 °C, corresponding to the melting of  $\beta$ -lactose, which becomes more prominent as the rifampicin loading is increased. It appears that exposure to methanol in the SAS process, the duration of which increases with rifampicin loading, causes a polymorphic change in the crystalline form of the lactose.

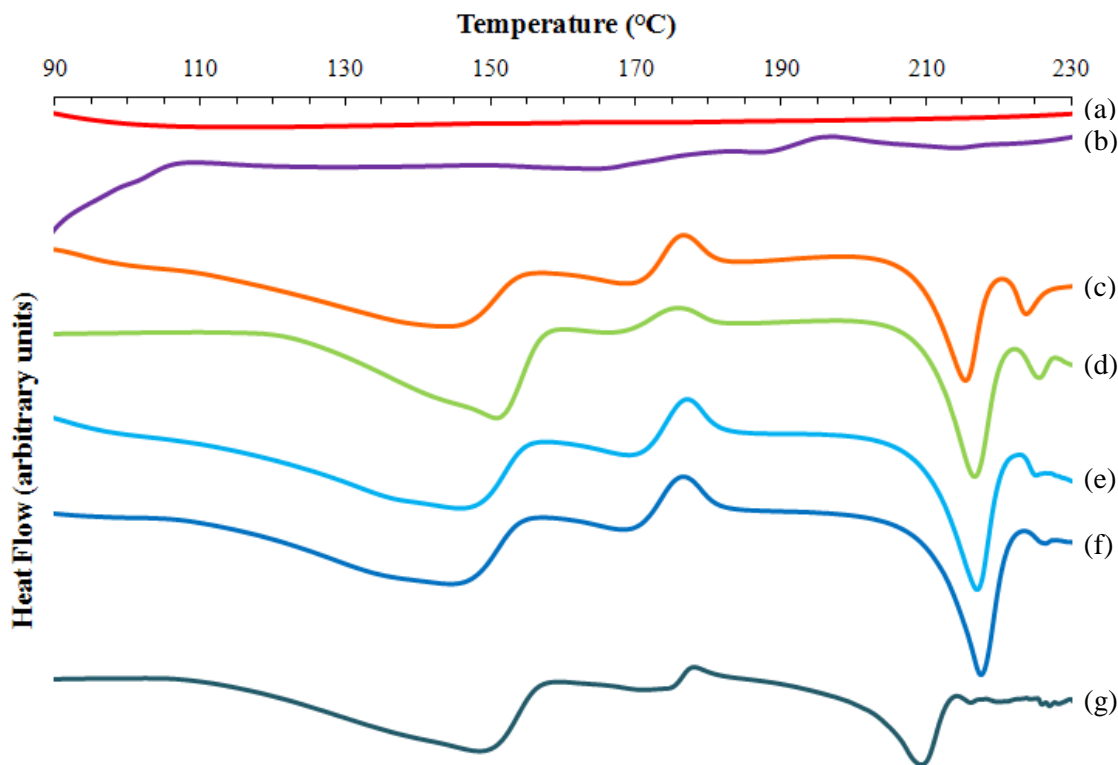


Figure 3.10 DSC thermographs (from top to bottom) for (a) rifampicin, (b) SAS rifampicin, (c) SAS-DEM composite with 25.7 wt. % rifampicin loading, (d) SAS-DEM composite with 14.0 wt. % rifampicin loading, (e) SAS-DEM composite with 7.2 wt. % rifampicin loading, (f) SAS-DEM composite with 1.2 wt. % rifampicin loading, and (g) lactose monohydrate

#### 3.4.4 Fourier Transform Infrared Spectroscopy

FTIR spectroscopy was performed on each of the raw materials and processed samples to determine the nature of any chemical interactions between the rifampicin and lactose. The FTIR spectra are presented in Figure 3.11. The spectrum for the supplier rifampicin is superimposable with the spectrum previously given in the literature for rifampicin form I. The spectrum for the SAS processed rifampicin, however, matches the spectrum reported in the literature for amorphous rifampicin (Agrawal et al. 2004). A key difference is the broad OH band from  $3728\text{-}3082\text{ cm}^{-1}$  in the SAS processed rifampicin,

which indicates amorphousness, compared to the sharp peak at  $3483\text{ cm}^{-1}$  in the supplier rifampicin spectrum, which is characteristic of rifampicin form I. Based on these results, it is proposed that in addition to rifampicin dihydrate, the SAS processed rifampicin also contains amorphous rifampicin. The spectra for the various SAS-DEM composites closely match the spectrum for lactose monohydrate with the rifampicin peaks, at  $1718\text{ cm}^{-1}$  for example, becoming more intense as rifampicin loading is increased. The key observation is that there are no peak shifts in the SAS-DEM composite spectra indicating a chemical interaction between rifampicin and lactose. The SAS-DEM composite spectra are effectively a summation of the SAS processed rifampicin and lactose monohydrate spectra, taking into account the composite composition. This observation means that while the lactose particles are effectively deagglomerating the rifampicin microparticles, the two are only loosely associated. Therefore, upon inhalation and exposure to the aqueous biological membranes of the throat and lung, the lactose particles should readily dissolve while the rifampicin microparticles travel to the deep regions of the lungs. A similar phenomenon was observed for rifampicin/mannitol carrier systems (Mizoe et al. 2008). While this current study demonstrated the viability of the single-step SAS-DEM process for producing homogeneous rifampicin/lactose microparticle composites, further analyses focused on determining the potential clinical relevance of such composites is needed. The next step will be to assess the *in vitro* aerosol performance of the composite powders using a cascade impactor and to determine the fine particle fraction of rifampicin.

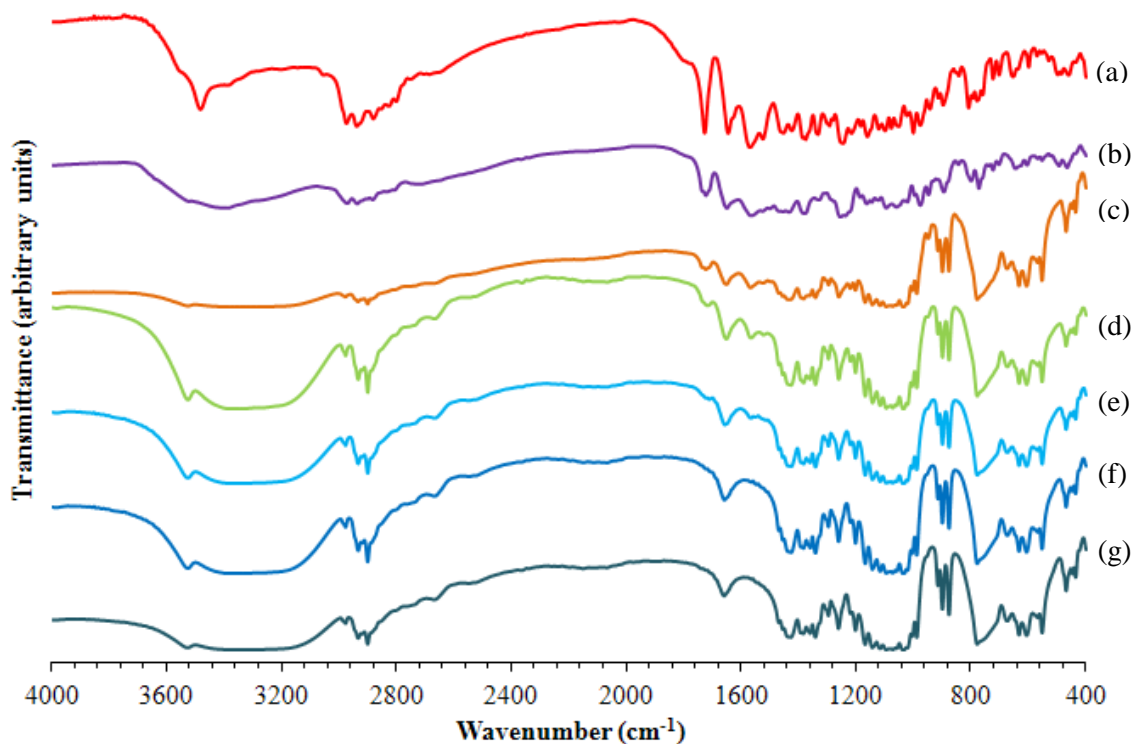


Figure 3.11 FTIR spectra (from top to bottom) for (a) rifampicin, (b) SAS rifampicin, (c) SAS-DEM composite with 25.7 wt. % rifampicin loading, (d) SAS-DEM composite with 14.0 wt. % rifampicin loading, (e) SAS-DEM composite with 7.2 wt. % rifampicin loading, (f) SAS-DEM composite with 1.2 wt. % rifampicin loading, and (g) lactose monohydrate

### 3.5 Conclusions

In this study, rifampicin was recrystallized from methanol in the presence of lactose monohydrate microparticles using the SAS-DEM technique to produce microparticle composites suitable for the pulmonary treatment of TB. Compositional analysis and SEM imaging revealed homogeneous rifampicin/lactose composite mixtures of inhalation size appropriate (1-5  $\mu\text{m}$ ) microparticles ranging in rifampicin content from 1.2 wt. % to 25.7 wt. %. Characterization by PXRD showed a change in the crystalline form of rifampicin from form I to rifampicin dihydrate following SAS crystallization



from methanol. Further characterization by PXRD, DSC, and FTIR showed that the rifampicin and lactose retained their individual crystal structures, thermal behavior, and physicochemical properties during SAS-DEM processing, thus confirming a physical mixture of the two. The rifampicin/lactose microparticle composite powders produced in this study are hypothesized to provide effective delivery of rifampicin to the alveolar macrophages by utilization of a DPI delivery system for the treatment of TB, but a confirmation is necessary.

## Chapter 4

### Simultaneous Production and Deagglomeration of Itraconazole Microflakes by Supercritical Antisolvent-Drug Excipient Mixing

#### 4.1 Dissolution Enhancement of Itraconazole

Systemic fungal infections are a major health concern, and can even become life-threatening, for immunocompromised patients (Silva 2010). Immunocompromised patients, including those who have HIV or AIDS, are pregnant, are undergoing chemotherapy or radiation therapy for cancer, or have a genetic disorder, lack the basic cellular defenses to fight off fungal infections. For these patients, as well as healthy patients suffering from localized fungal infections such as athlete's foot or ringworm, an azole antifungal agent is commonly prescribed. Azole antifungal agents interact with 14- $\alpha$  demethylase, the enzyme necessary to convert lanosterol to ergosterol. Depletion of ergosterol in the fungal cell membrane disrupts the cell structure, thereby inhibiting fungal growth. Some of the more common azole antifungal compounds are shown in Figure 4.1. Ketoconazole and miconazole are imidazoles, containing a 1,3-C<sub>3</sub>H<sub>3</sub>N<sub>2</sub> heterocyclic ring, while fluconazole and itraconazole are triazoles, containing 1,2,4-C<sub>2</sub>H<sub>2</sub>N<sub>3</sub> heterocyclic rings. For the oral treatment of systemic fungal infections, itraconazole is a potent CYP450 3A4 inhibitor with minimal toxicity. The formulation challenge with itraconazole is to increase its aqueous solubility to achieve a predictable release with nominal variability.

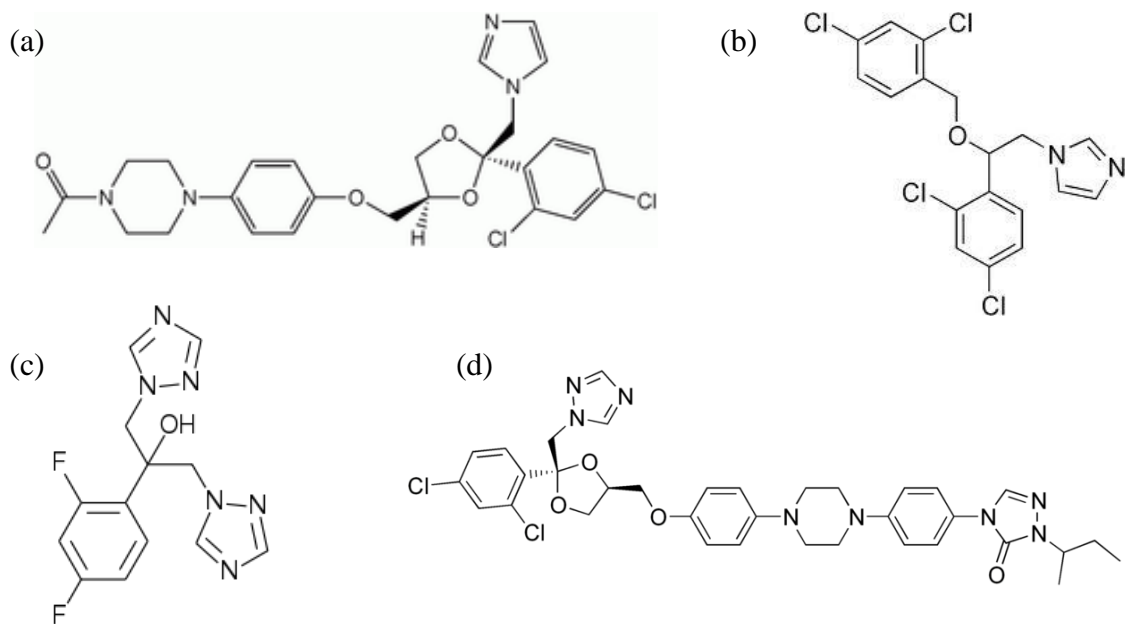


Figure 4.1 Chemical structures of azole antifungal agents (a) ketoconazole, (b) miconazole, (c) fluconazole, and (d) itraconazole

Strategies for enhancing the dissolution of itraconazole for oral formulations have included hydrochloride salt formation (Tao et al. 2009), solid dispersions with water-soluble polymers and surfactants including polyethylene glycol (PEG), hydroxypropylmethylcellulose (HPMC), polyvinylpyrrolidone (PVP), Eudragit E100, and poloxamer 188 (Six et al. 2004; Liu et al. 2006; El Maghraby and Alomrani 2009; Engers et al. 2010), complexation with  $\beta$ -cyclodextrin and chemically modified derivatives (De Chasteigner et al. 1996; Peeters et al. 2002; Al-Marzouqi et al. 2006), micronization (Barrett et al. 2008), loading of itraconazole onto mesoporous silica micro- and nanoparticle carriers (Mellaerts et al. 2008; Van Speybroeck et al. 2010; Kinnari et al. 2011), and cocrystal formation with water-soluble dicarboxylic acids (Remenar et al. 2003; Shevchenko et al. 2012). While hydrochloride salt formation was effective at increasing the aqueous solubility of itraconazole, the addition of a dispersing agent was

necessary to prevent salt nanoparticle agglomeration during dissolution (Tao et al. 2009). The drawback of both solid dispersions and complexation with  $\beta$ -cyclodextrins is low drug loadings. For example, the maximum miscibility of itraconazole with Eudragit E100 is 13 wt. % drug loading while the bulky structure of itraconazole sterically hinders cyclodextrin complexation giving a maximum association of 6.8 wt. % drug (De Chasteigner et al. 1996; Six et al. 2004). Cocrystallization of itraconazole will be the focus of Chapters 5 and 6, and thus will not be discussed here. Therefore, itraconazole micronization and subsequent stabilization by deposition on pharmaceutical carriers appears to be one of the most promising approaches for achieving commercially relevant formulations of itraconazole with enhanced dissolution.

In an effort to reduce organic solvent use, many itraconazole formulation techniques have exploited supercritical CO<sub>2</sub> as an antisolvent for particle formation due to the drug's insolubility in supercritical CO<sub>2</sub> at moderate conditions (< 50 °C, < 250 bar), as shown in Figure 1.8 (Al-Marzouqi et al. 2006; Hassan et al. 2007; Barrett et al. 2008). Itraconazole has been recrystallized from acetone, dimethyl formamide (DMF), THF, and DCM using a SAS process at conditions of 25-40 °C and 90-190 bar (Barrett et al. 2008). Decreases in particle size led to increases in itraconazole dissolution, which were preserved by dissolving PEG in solution to create less agglomerated itraconazole/PEG composite microparticles. However, a noticeable delay in the release of itraconazole while the PEG carrier dissolved, which would delay the therapeutic action of the drug, was evident for the composite particles (Barrett et al. 2008). Therefore, it is proposed that micronization of itraconazole by SAS crystallization and simultaneous deposition on the surface of a larger carrier particle using the single-step SAS-DEM

technique will increase the dissolution of itraconazole while allowing for immediate release of the drug.

In this study, itraconazole microflakes were prepared from DCM using SAS crystallization. The microflakes were then crystallized in the presence of spray dried lactose excipient particles ( $d \sim 100 \mu\text{m}$ ) using the SAS-DEM technique and the effects of itraconazole to lactose loading on drug dissolution studied. The effects of two stabilizers, sodium dodecyl sulfate (SDS) and Pluronic F-127, on particle formation and drug dissolution within the SAS-DEM process were also examined. The drug powders were characterized for particle size and surface morphology, surface area, composition, dissolution behavior, and physical properties. This study extends the SAS-DEM process to a new drug/excipient combination while the addition of stabilizers to affect particle formation is a novel element. The powders produced by the single-step SAS-DEM process should be suitable for direct compression into an oral tablet without further processing.

#### **4.2 SAS Crystallization of Itraconazole Microflakes**

Figure 4.2a shows an SEM image of the micronized itraconazole drug as obtained from the supplier. The drug particles are rod-like structures ranging in size from 1-10  $\mu\text{m}$ . In an effort to enhance itraconazole dissolution by decreasing particle size and increasing surface area, the drug was recrystallized using SAS crystallization. Itraconazole was dissolved in DCM at 10 mg/mL and the solution sprayed at 1.0 mL/min into the SAS crystallization vessel (Figure 2.8) at 116 bar and 40 °C, following the procedure outlined in subsection 2.2.1. Figure 4.2b shows an SEM image of the itraconazole microflakes

produced by SAS crystallization. In contrast to the supplier drug, the SAS-produced drug appeared as thin rectangular flakes. The shape of the flakes can be attributed to preferential growth of the crystal lattice in a dominating direction. As observed under SEM (Figures 4.2b and 4.3), the primary particle length and width varied between 1  $\mu\text{m}$  and 25  $\mu\text{m}$ , while thickness was generally in the submicron range.

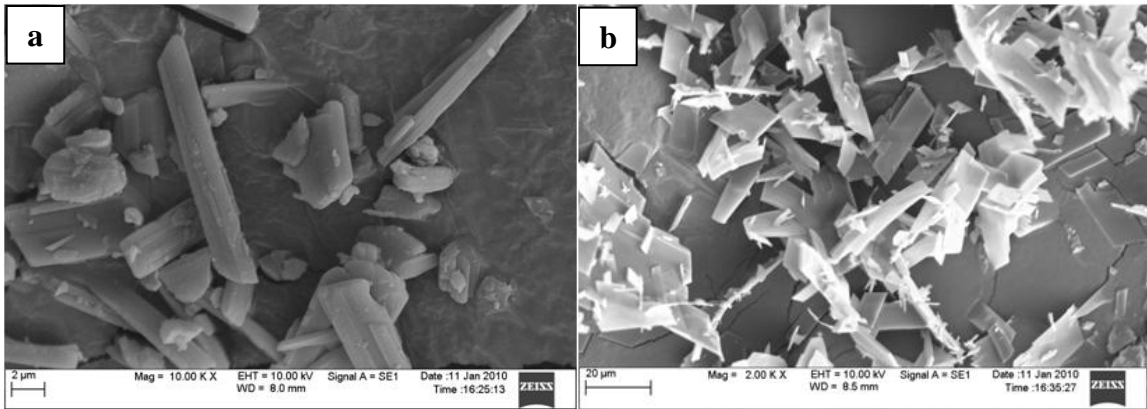


Figure 4.2 SEM images of (a) supplier (micronized) itraconazole and (b) SAS-produced itraconazole microflakes

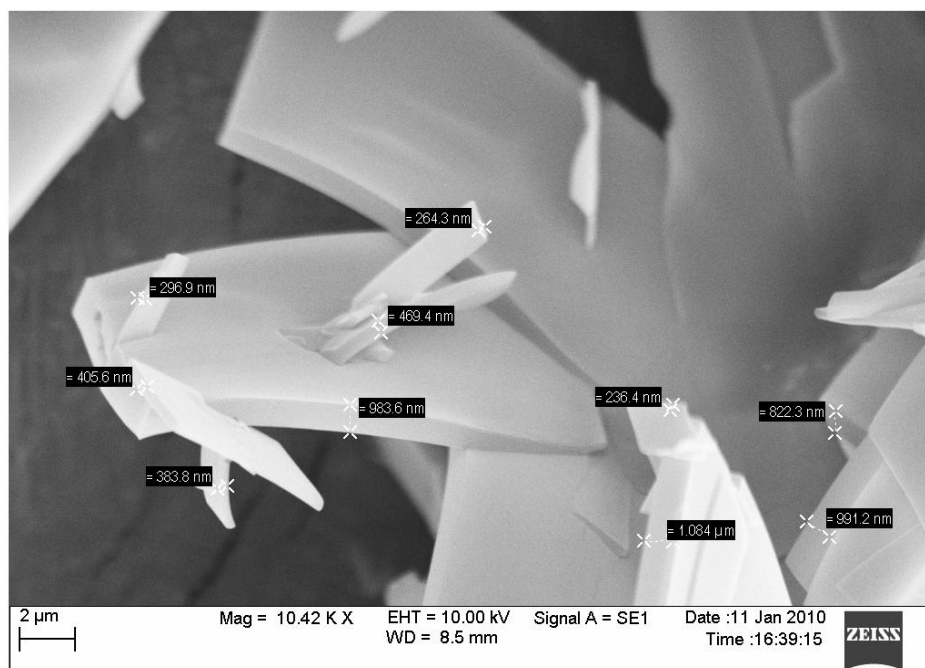


Figure 4.3 SEM image of SAS itraconazole microflakes with dimensions

As previously discussed for the SAS crystallization of rifampicin in subsection 3.2.1, the selection of operating conditions with respect to the MCP dictate the mechanism of particle formation in a SAS crystallization process. Although the conditions employed in this work were above the MCP for the CO<sub>2</sub>-DCM system, the formation of itraconazole microflakes suggests that jet break up is the dominating mechanism of particle formation and that operation is below the MCP when the effects of itraconazole are considered.

The particle size distributions (PSDs) of the micronized itraconazole and SAS itraconazole microflakes were determined by light obscuration and are given in Table 4.1. The particle size is expressed as a number weighted distribution, which is useful for determining the size of the primary particles in agglomerated systems. The itraconazole microflakes produced by SAS crystallization featured smaller particle sizes and a more

narrow distribution as compared to the micronized itraconazole. The specific surface areas of the two itraconazole samples, as determined by Brunauer-Emmett-Teller (BET) sorption, are also reported in Table 4.1 and were found to be similar. This result points towards the tendency of the itraconazole microflakes to agglomerate in the dry state. The PSDs were determined by dispersing the microflakes in water, with the aid of a stabilizer (SDS), such that the PSD of the individual microflakes was determined. In contrast, the surface areas of the powders were taken in the dry state where the individual microflakes are agglomerated, as observed under SEM (Figure 4.2b), such that the specific surface area represents that of the microflake agglomerates and not the individual microflakes. The individual microflakes are hypothesized to possess a greater specific surface area, not recognizable by BET sorption in the dry state, as compared to the supplier itraconazole. This hypothesis was confirmed by comparing the dissolution behavior of the supplier itraconazole and SAS itraconazole microflakes.

Table 4.1 Particle size distribution (PSD) and specific surface area of supplier (micronized) itraconazole and SAS itraconazole microflakes

Sample	Particle size distribution		Specific surface area (m <sup>2</sup> /g)
	d <sub>50</sub> (μm)	d <sub>90</sub> (μm)	
Micronized itraconazole	1.55 ± 0.49	10.31 ± 2.30	2.008
SAS itraconazole microflakes	0.94 ± 0.05	5.09 ± 0.39	2.105

Figure 4.4 shows the dissolution profiles for the supplier itraconazole and SAS itraconazole microflakes. The dissolution rate of the microflakes was found to be about 2.5-fold higher ( $D_{60} = 65\%$ ) than the dissolution rate of the supplier drug ( $D_{60} = 24\%$ ). The higher dissolution rate of the microflakes is attributed to a decrease in particle size



and increase in surface area. As described by the Noyes-Whitney equation (see subsection 1.3.1), particle size reduction leads to increased surface area which results in an enhanced dissolution rate. Just as with the particle size measurements, the aqueous stabilized dissolution medium acts to break-up the agglomerates into individual microflakes, leading to increased surface area and enhanced dissolution.

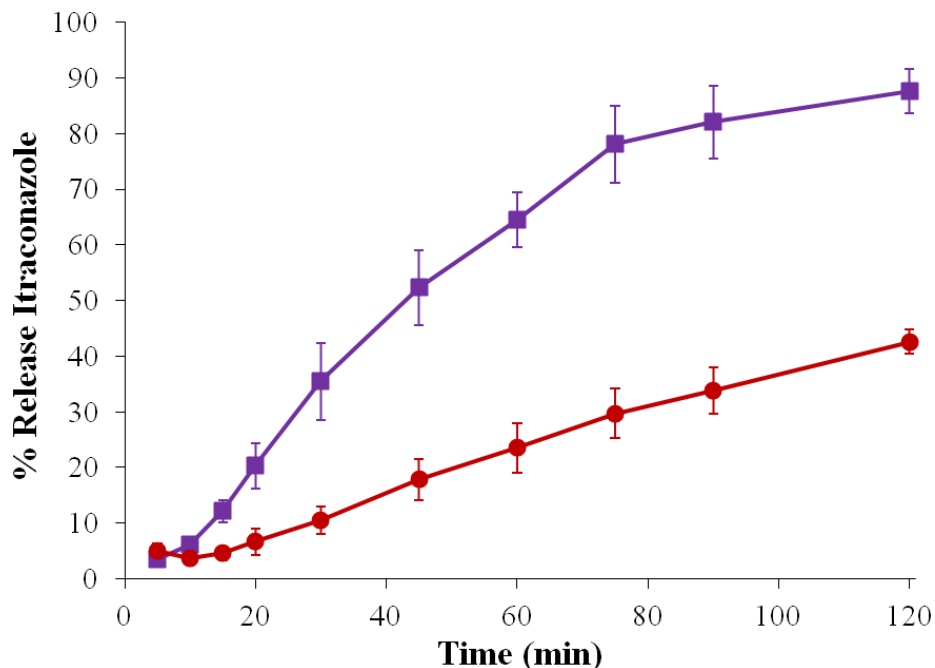


Figure 4.4 Dissolution profiles for supplier (micronized) itraconazole (●) and SAS itraconazole microflakes (■)

In addition to dissolution rate, an increase in the saturation solubility of an API is also achievable by decreasing the particle size. The saturation solubility ( $S$ ) of a micronized API is described by the Freundlich-Ostwald equation,

$$S = S_{\infty} \exp\left(\frac{2\gamma MW}{r\rho RT}\right) \quad (1)$$

where  $S_{\infty}$  is the saturation solubility of an infinitely large API crystal,  $\gamma$  is the solid-liquid interfacial tension,  $MW$  is the molecular weight of the API,  $r$  is the particle radius,  $\rho$  is the density,  $R$  is the gas constant, and  $T$  is the temperature. Saturation solubility enhancements as high as 50% have been observed for APIs when particle size is decreased to the submicron region (Kesisoglou et al. 2007). As determined by a saturation solubility study following the procedure of Higuchi and Connors (1965), the aqueous solubility of the SAS itraconazole microflakes (0.247 mg/mL) was slightly higher than that of the supplier itraconazole (0.187 mg/mL). This increase in saturation solubility also contributes to the increase in dissolution rate observed for the SAS itraconazole microflakes in Figure 4.4.

### **4.3 SAS-DEM Mixtures of Itraconazole and Lactose**

The deagglomeration of itraconazole microflakes by simple mixing with pharmaceutical excipients would prove challenging due to their irregular shape and cohesion. It was presumed based on previous work from our laboratory that the SAS-DEM process would be more effective at deagglomerating the microflakes than simple blending (Sanganwar and Gupta 2008; Sanganwar et al. 2010). The SAS-DEM process employs pharmaceutical carriers on which the drug microparticles or nanoparticles are deposited while they are produced by the SAS process. The drug/excipient mixtures thus obtained offer a number of pharmaceutical advantages including enhanced dissolution of poorly water-soluble drugs due to increased surface area and wettability by deposition onto hydrophilic or porous excipients, enhanced flow properties of the micronized drug particles due to deposition of the particles onto freely flowable excipient particles, and

reduction of handling toxicity due to dilution of the highly potent drug particles with excipients.

To prevent microflake agglomeration in the dry state, itraconazole was again crystallized by SAS crystallization, this time in the presence of spray dried lactose excipient particles (SAS-DEM). An SEM image of the spray dried lactose particles is shown in Figure 4.5. The lactose particles are mostly spherical in shape, ranging in size from 25-100  $\mu\text{m}$ , with a variety of surface pores appropriate for drug microflake deposition. A desired amount of lactose (500-2000 mg) was placed inside the SAS crystallization vessel shown in Figure 2.8. The SAS crystallization vessel was then sealed, pressurized with  $\text{CO}_2$  to 116 bar, and heated to 40  $^\circ\text{C}$ . The stirrer was run at 400 rpm for the duration of each experiment. While maintaining the flow of  $\text{CO}_2$  through the vessel at 20 g/min, varying volumes of 10 mg/mL itraconazole in DCM solutions were sprayed into the vessel at a flow rate of 1.0 mL/min. Following flushing with excess supercritical  $\text{CO}_2$ , the itraconazole and lactose mixtures were collected and analyzed. Three itraconazole and lactose mixtures with itraconazole loadings of 6 wt. %, 23 wt. % and 40 wt. %, as determined by HPLC, were prepared.

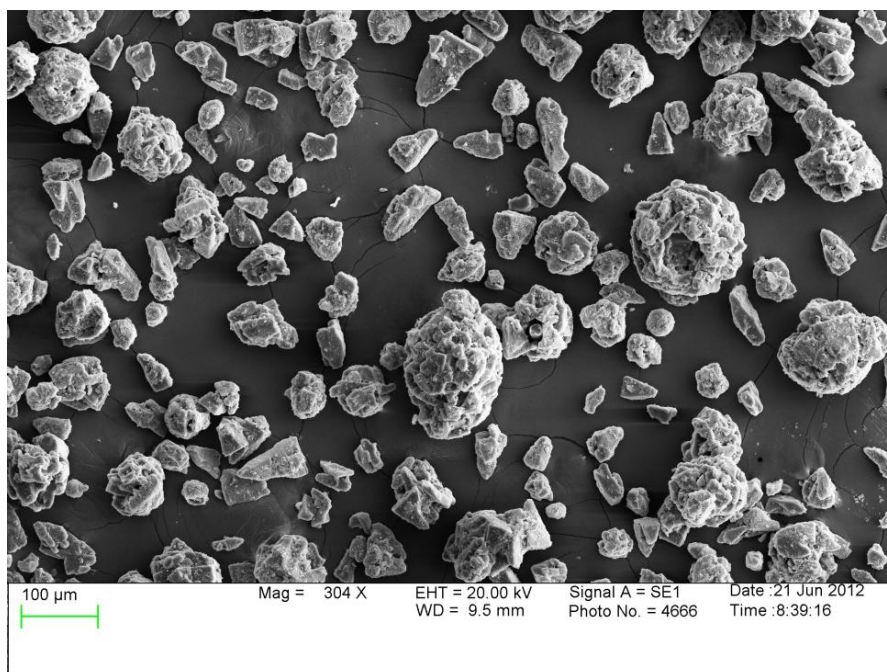


Figure 4.5 SEM image of spray dried lactose excipient particles

Figure 4.6 is an SEM image of a SAS-DEM itraconazole and lactose mixture with 6 wt. % itraconazole loading. It is clear that individual itraconazole microflakes are indeed depositing on the surface of the excipient lactose particles. The rectangular shape of the itraconazole microflakes allows for greater contact area between the drug microflakes and the lactose surface, thus enhancing their interaction. Figure 4.7 shows the dissolution of a SAS-DEM itraconazole and lactose mixture with 6 wt. % itraconazole loading as compared to the SAS itraconazole microflakes and supplier itraconazole. By depositing the itraconazole microflakes on the lactose particles during SAS crystallization, the individual itraconazole microflakes are more rapidly dispersed, despite coming to the same equilibrium solubility as the SAS itraconazole microflakes after approximately 2 hours. It was observed that upon introducing the SAS-DEM itraconazole and lactose mixture to the dissolution medium, the lactose particles

immediately dissolved, facilitating dispersion of the individual, deagglomerated itraconazole microflakes into the dissolution medium.

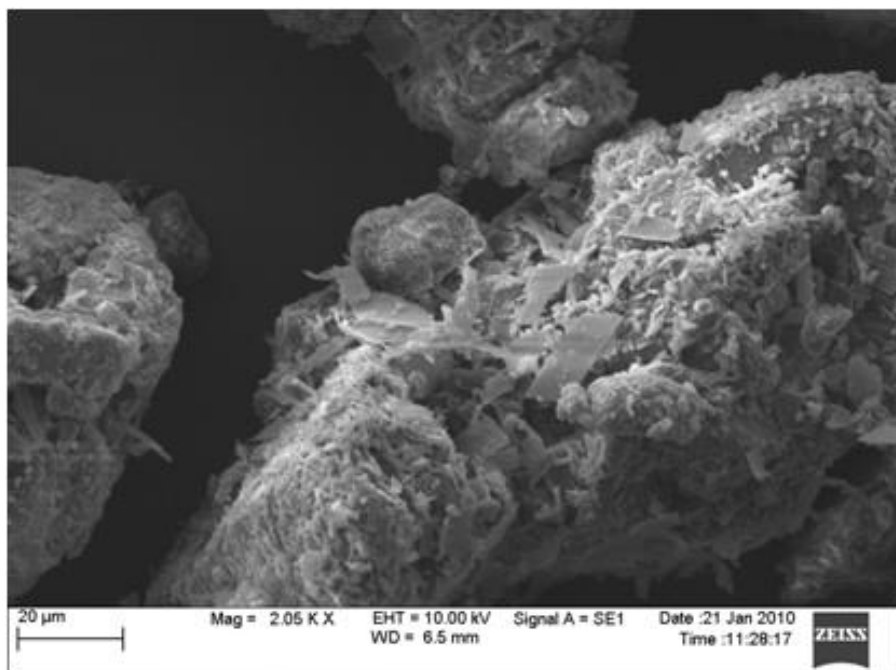


Figure 4.6 SEM image of SAS-DEM mixture with 6 wt. % itraconazole loading

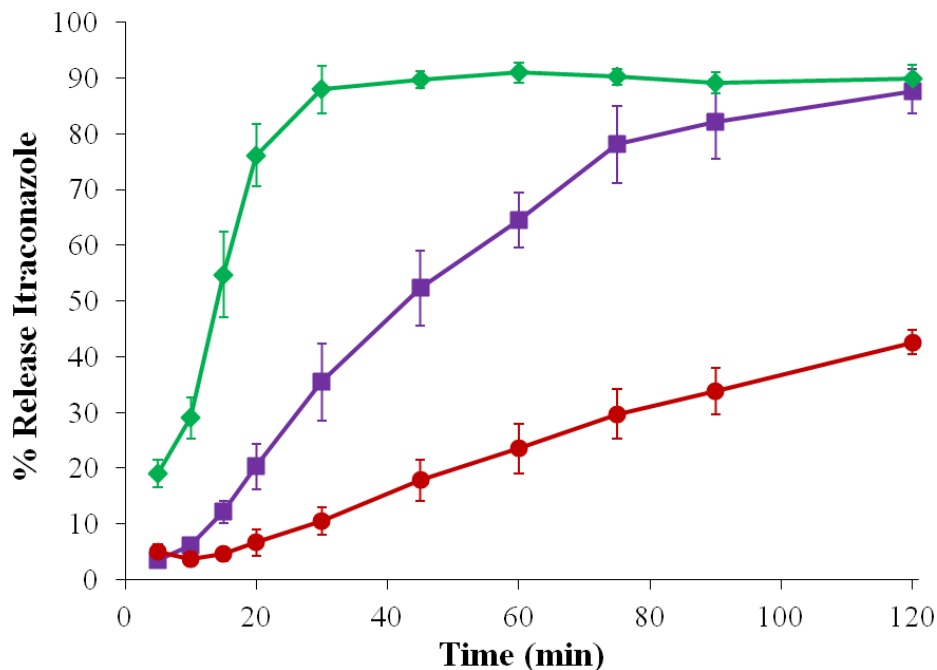


Figure 4.7 Dissolution profiles for supplier itraconazole (●), SAS itraconazole microflakes (■), and SAS-DEM mixture with 6 wt. % itraconazole loading (◆)

As stated in section 4.1, low drug loadings were a primary drawback of the solid dispersion and cyclodextrin complexation routes of dissolution enhancement for itraconazole. Low drug loadings require the use of significant amounts of excipients. For example, at 6 wt. % drug loading, a typical dosage of 100 mg of itraconazole would require the use of 1667 mg of lactose leading to a total tablet mass of approximately 1800 mg. The use of large amounts of excipients results in an inconvenient dosage platform (e.g. a large tablet) which can cause patient noncompliance. As such, the effects of itraconazole to lactose loading in the SAS-DEM process were studied. Figure 4.8 shows the dissolution profiles for SAS-DEM itraconazole and lactose mixtures with 6 wt. % itraconazole loading, 23 wt. % itraconazole loading, and 40 wt. % itraconazole loading as well as a physical mixture of itraconazole and lactose with 25 wt. % itraconazole loading.

The physical mixture was prepared by spatula mixing SAS itraconazole microflakes and lactose for approximately 2 minutes.

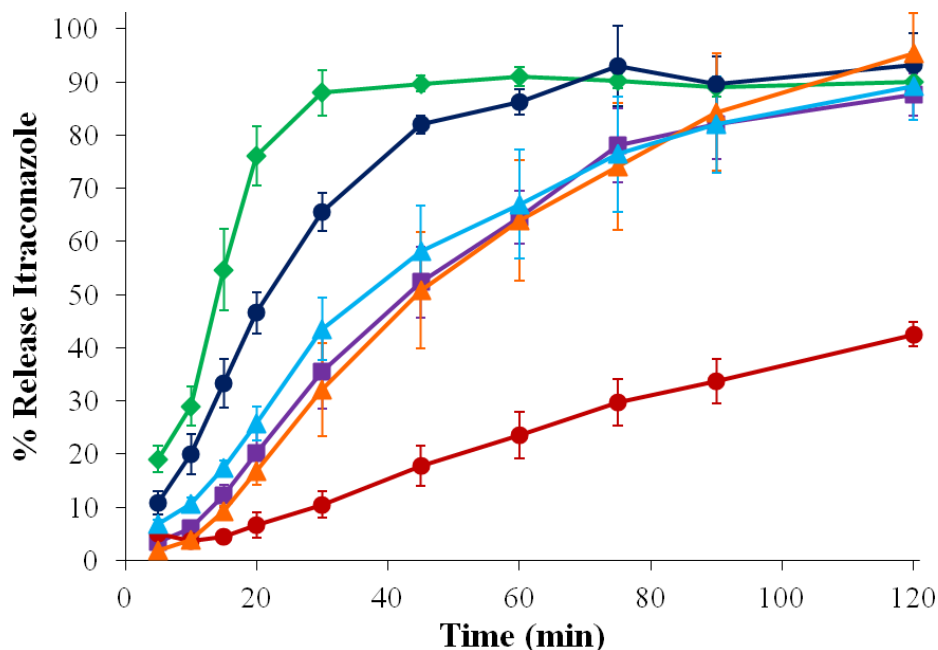


Figure 4.8 Dissolution profiles for supplier itraconazole (●), SAS itraconazole microflakes (■), SAS-DEM mixture with 6 wt. % itraconazole loading (◆), SAS-DEM mixture with 23 wt. % itraconazole loading (●), physical mixture with 25 wt. % itraconazole loading (▲), and SAS-DEM mixture with 40 wt. % itraconazole loading (▲)

As seen in Figure 4.8, the dissolution rate of itraconazole decreases as its loading is increased in the SAS-DEM process. The  $D_{60}$  values for SAS-DEM mixtures with itraconazole loadings of 6 wt. %, 23 wt. %, and 40 wt. % were 91%, 86%, and 64%, respectively. This decrease is attributed to microflake saturation on the lactose surface and excess microflake agglomeration. At low drug loadings, the itraconazole microflakes deposit on the surface of the lactose particles (Figure 4.6) and are individually dispersed following exposure to the dissolution medium. As drug loading is increased, the surface

of the lactose particles becomes saturated with microflakes while the excess microflakes agglomerate, as shown in Figure 4.9. While the deposited microflakes are still readily dispersed, the agglomerated microflakes take longer to separate, thus delaying the dissolution. While the SAS-DEM process shows strong potential for dissolution enhancement at low drug loadings, its effectiveness at higher drug loadings is minimal due to deposition limitations.

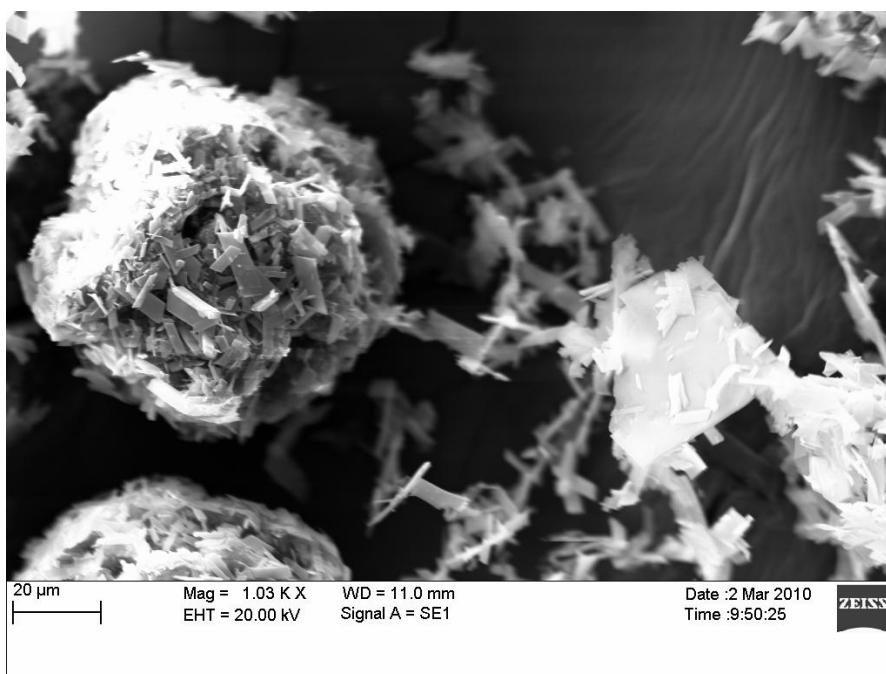


Figure 4.9 SEM image of SAS-DEM mixture with 23 wt. % itraconazole loading

Another important observation gained from Figure 4.8 is that a SAS-DEM mixture with 23 wt. % itraconazole loading possesses significantly faster dissolution ( $D_{60} = 86\%$ ) than a physical mixture with 25 wt. % itraconazole loading ( $D_{60} = 66\%$ ). The physical mixture of itraconazole and lactose showed comparable dissolution to that of the SAS drug microflakes, indicating that simple drug mixing is not effective in



deagglomerating the itraconazole microflakes. These results prove that crystallization in the presence of an excipient is an efficient and effective means of preventing the agglomeration of cohesive drug particles.

The PSDs of the SAS-DEM itraconazole and lactose mixtures are given in Table 4.2. The results represent the size distribution of the itraconazole particles after eliminating lactose from the samples by dissolving out in water. The microflakes obtained from the SAS-DEM process at 6 wt. % itraconazole loading are significantly smaller than the SAS itraconazole microflakes crystallized in the absence of lactose (see Table 4.1). This result shows that deposition of the microflakes on lactose during crystallization curbs particle growth, in addition to preventing particle agglomeration. As itraconazole loading is increased, a smaller percentage of the microflakes come into contact with the already saturated lactose surface, giving PSDs similar to that observed during SAS crystallization without lactose. These results are in contrast to previous work in which nevirapine, due to its recrystallization into tiny rectangular particles, showed continual deposition and no excess drug agglomeration as the drug loading was increased to sufficiently high values (Sanganwar et al. 2010).

Table 4.2 PSDs of SAS-DEM itraconazole and lactose mixtures

Sample	$d_{50}$ ( $\mu\text{m}$ )	$d_{90}$ ( $\mu\text{m}$ )
SAS-DEM: 6 wt. % itraconazole	$0.82 \pm 0.06$	$3.49 \pm 0.84$
SAS-DEM: 23 wt. % itraconazole	$1.73 \pm 0.83$	$6.28 \pm 0.86$
SAS-DEM: 40 wt. % itraconazole	$0.90 \pm 0.05$	$6.75 \pm 0.61$

#### **4.4 SAS-DEM Mixtures of Itraconazole and Lactose with Stabilizers**

The attractive forces responsible for particle agglomeration (see subsection 1.3.2) can be minimized by either kinetic or thermodynamic stabilization. Kinetic stabilization is accomplished through the addition of energy, in the form of mixing or ultrasound, which provides the particles with excess kinetic energy to compensate their increased surface energy (Thorat and Dalvi 2012). Thermodynamic stabilization involves the addition of a stabilizer or stabilizing medium which adsorbs to the particle surfaces and thus reduces the number of available surface groups to participate in particle–particle interactions (agglomeration). Since high energy mixing is already a part of the SAS-DEM process via two 4-blade 45° pitched impellers run at 400 rpm, additional stabilization was investigated via the thermodynamic route.

In antisolvent crystallization, the stabilizer can be added in either the solvent or antisolvent phases. The efficiency of thermodynamic stabilization is dependent on the solubility of the stabilizer in the solvent and antisolvent phases and the strength of particle–stabilizer interactions versus the stabilizer–solvent and stabilizer–antisolvent interactions. Thermodynamic stabilization is typically accomplished through two main mechanisms, electrostatic and steric (Thorat and Dalvi 2012). Electrostatic stabilization is achieved through strong adsorption of charged ionic surfactants or polymers on a particle surface due to van der Waals attraction between the particle surface and repeating monomer units of the polymer chain (Thorat and Dalvi 2012). Adsorption of an anionic stabilizer such as sodium dodecyl sulfate (SDS), at concentrations below the critical micelle concentration (CMC), on a particle surface gives the particle surface a negative charge, thus preventing agglomeration by increasing the energy barrier through repulsion

between adjacent particles (Dalvi and Dave 2009). Steric stabilizers are typically non-ionic polymers and amphiphilic block copolymers, such as Pluronic F-127 (Figure 2.5). Pluronic F-127 (poloxamer 407) was previously found effective at stabilizing the liquid antisolvent crystallization of itraconazole from THF using water as the antisolvent. Addition of the stabilizer in the aqueous phase gave a  $d_{50}$  of 620 nm, while addition of the stabilizer in the organic phase gave a  $d_{50}$  of 290 nm, keeping all other conditions constant (Matteucci et al. 2006). Direct addition of Pluronic F-127 in the organic phase along with itraconazole allows more controlled crystallization as the polymer chains are more available to the crystallizing drug particles since they do not need to diffuse across the interface from the bulk antisolvent phase to the organic phase. Additional discussion on the mechanisms of particle stabilization in antisolvent crystallization is included in Appendix A.

It was postulated that the addition of stabilizers, either electrostatic or steric, within the SAS-DEM process could decrease microflake agglomeration and allow for improved drug deposition at higher drug loadings. To date, itraconazole particles have been stabilized by hydroxypropyl methylcellulose (HPMC), Pluronic F-68, Pluronic F-127 (poloxamer 407), polyethylene glycol (PEG) 4000 and 6000, polystyrene-block-polyethylene oxide, polyvinylpyrrolidone (PVP), sodium alginate, SDS, and Tween (polysorbate) 80 (Sinswat et al. 2005; Matteucci et al. 2006; Wulsten et al. 2009; Bhakay et al. 2011; Liu et al. 2011; Thorat and Dalvi 2012). The two stabilizers investigated in this work were the anionic surfactant SDS and copolymer Pluronic F-127. The stabilizers were dissolved along with itraconazole in 1 wt. % and 10 wt. % ratios. Since SDS is insoluble in dichloromethane, it was dissolved first in methanol and then added to the

itraconazole in dichloromethane solution. In both cases, the stabilizer-containing drug solution was sprayed into the high pressure vessel following the procedures outlined in subsections 2.2.1 and 2.2.2. Initial experiments were conducted in the absence of lactose to examine the effect of each stabilizer on particle size and morphology.

#### 4.4.1 Electrostatic Stabilization with Sodium Dodecyl Sulfate

At 1 wt. % concentration, SDS was not an effective deagglomerating agent, as a large number of drug agglomerates were observed under SEM. At 10 wt. %, particle deagglomeration did occur as seen in Figure 4.10, but the size of the individual itraconazole microflakes increased. This increase in size is attributed to changes in supersaturation caused by the addition of methanol to the drug solution.

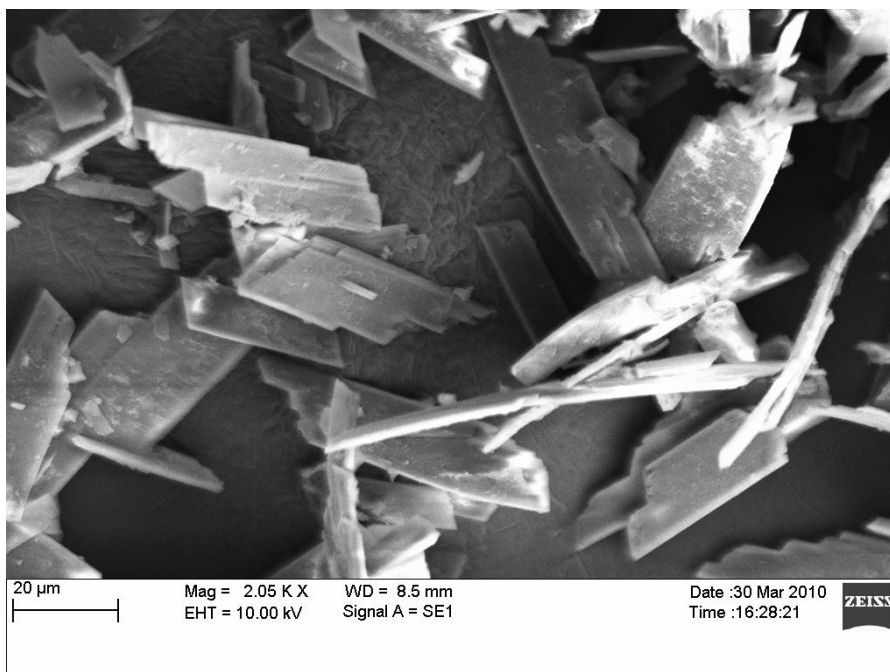


Figure 4.10 SEM image of itraconazole microflakes stabilized with 10 wt. % SDS

The dissolution profiles for the SAS itraconazole microflakes stabilized with SDS are shown in Figure 4.11. The microflake agglomeration observed by SEM for the 1 wt. % SDS stabilized microflakes explains the 20 minute delay in release observed in the dissolution profile. Furthermore, the increase in microflake size, attributed to changes in supersaturation from the addition of methanol, explains why the SDS stabilized microflakes reach a saturation solubility intermediate to that of the larger supplier drug particles and smaller unstabilized SAS microflakes. Since electrostatic stabilization with SDS appeared to have a counterproductive effect on itraconazole dissolution, steric stabilization was investigated using Pluronic F-127.

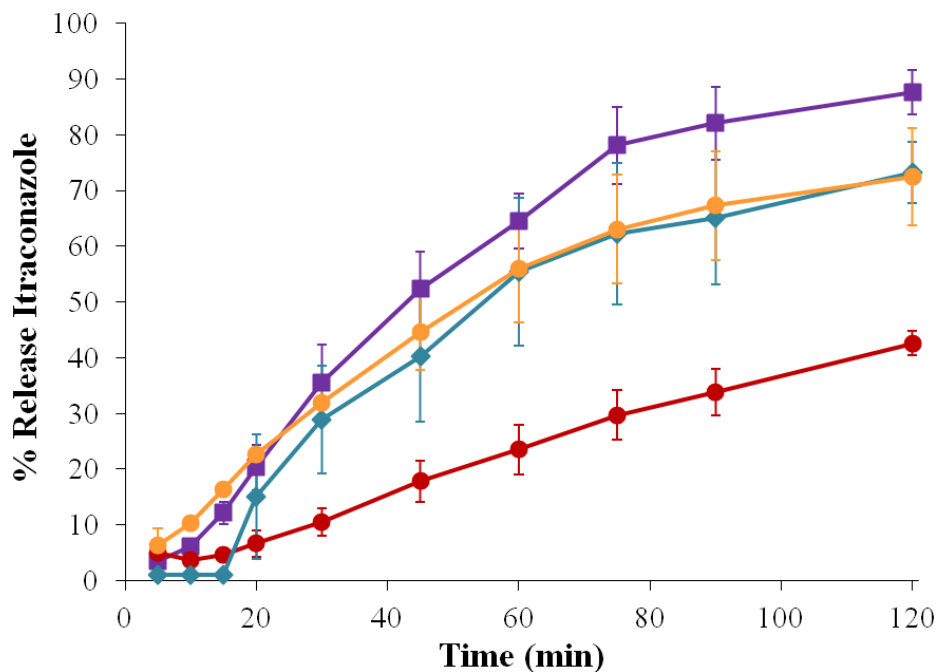


Figure 4.11 Dissolution profiles for supplier itraconazole (●), SAS itraconazole microflakes (■), SAS itraconazole microflakes stabilized with 1 wt. % SDS (◆), and SAS itraconazole microflakes stabilized with 10 wt. % SDS (●)

#### 4.4.2 Steric Stabilization with Pluronic F-127

Figure 4.12 shows an SEM image of the SAS itraconazole microflakes stabilized with 10 wt. % Pluronic F-127. When stabilized with Pluronic F-127, the individual microflakes attach to one another to form loosely aggregated sheet-like structures. Similar observations were reported for danazol and naproxen drug particles crystallized with Pluronic F-127 from methanol (Rogers et al. 2004). To confirm that the microflakes were only loosely aggregated, a sample was suspended in a saturated drug solution with 0.3% SDS to dissolve the Pluronic F-127, leaving behind the itraconazole microflakes. The resulting suspension was analyzed by light obscuration and a PSD smaller than that of the unstabilized SAS itraconazole microflakes was observed ( $d_{50} = 0.82 \pm 0.01 \mu\text{m}$ ,  $d_{90} = 3.45 \pm 0.19 \mu\text{m}$ ). The sheet-like microflake aggregates, which range up to several hundred microns in size as observed by SEM, are easily broken apart when exposed to an aqueous medium, as confirmed by the PSD.

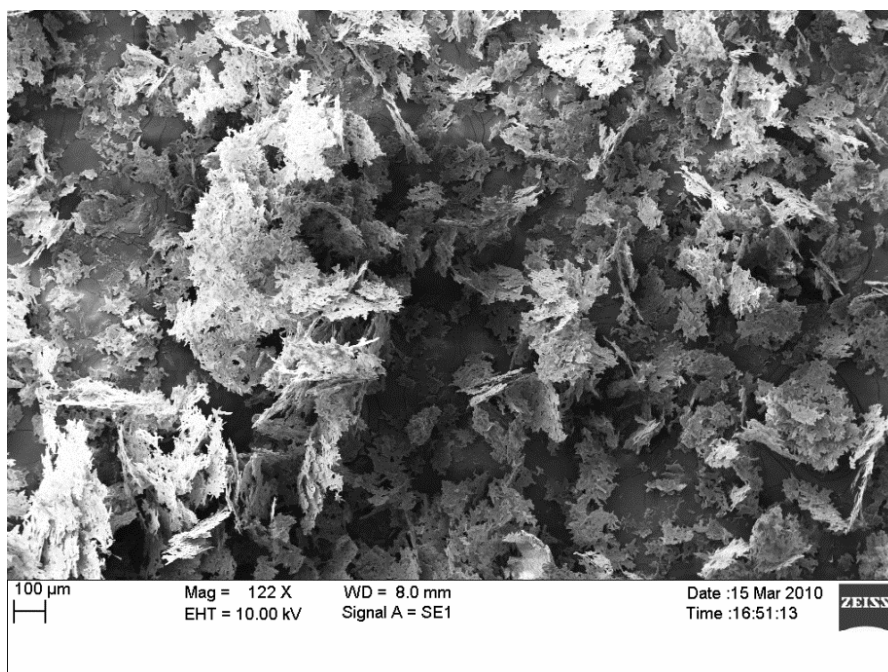


Figure 4.12 SEM image of itraconazole microflakes stabilized with 10 wt. % Pluronic F-127

Figure 4.13 shows the dissolution profiles for the Pluronic F-127 stabilized itraconazole microflakes, as well as a physical mixture of itraconazole microflakes with 10 wt. % Pluronic F-127. There is no significant increase in dissolution for the 1 wt. % Pluronic F-127 stabilized microflakes, but at 10 wt. % stabilizer, the dissolution increased two-fold ( $D_{30} = 78\%$ ) compared to the unstabilized SAS microflakes ( $D_{30} = 35\%$ ). This improvement is attributed to a decrease in particle size, stemming from the ability of the individual microflakes to dissociate from the sheet-like aggregates when exposed to an aqueous medium, and an improvement in wettability from the presence of the surfactant.

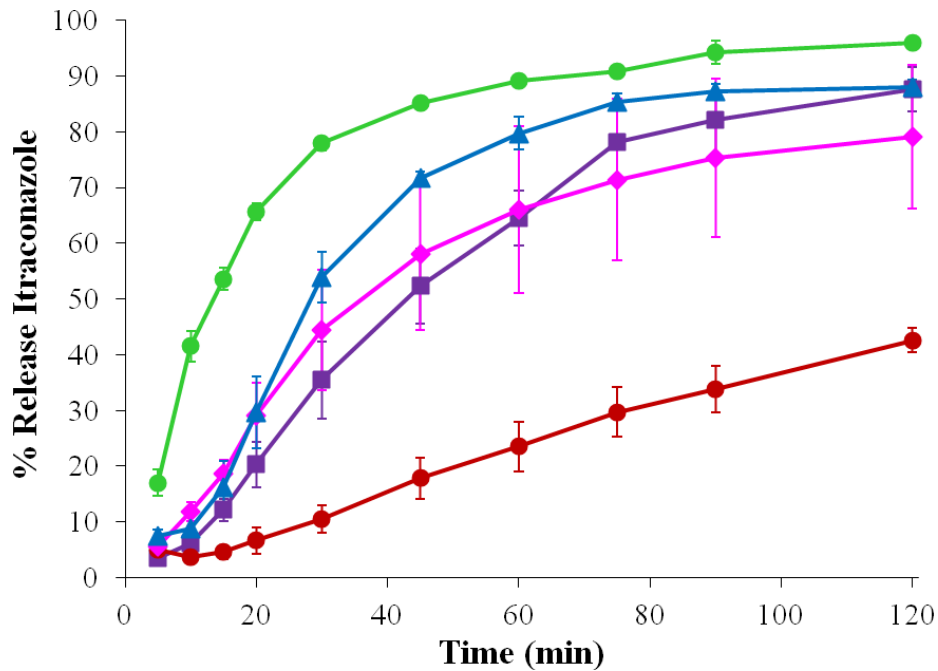


Figure 4.13 Dissolution profiles for supplier itraconazole (●), SAS itraconazole microflakes (■), SAS itraconazole microflakes stabilized with 1 wt. % Pluronic F-127 (◆), physical mixture of SAS itraconazole microflakes with 10 wt. % Pluronic F-127 (▲), and SAS itraconazole microflakes with 10 wt. % Pluronic F-127 (●)

From Figure 4.13, there is also an increase in dissolution when Pluronic F-127 is sprayed in solution with itraconazole during SAS crystallization compared to when the stabilizer is physically mixed with the drug microflakes in the dry state. Figure 4.14 shows the mechanism of adsorption for a block copolymer, such as Pluronic F-127, onto the surface of a hydrophobic drug particle. The central hydrophobic block adsorbs onto the surface of the drug particle, while the hydrophilic chains extend into the aqueous solution (dissolution medium), promoting wettability. The fact that stabilization is more effective when the stabilizer is incorporated during crystallization indicates that the interaction between the stabilizer and drug is solvent-facilitated. While in solution, the polymer chains have increased mobility, allowing the polymer to better orient into the



structure illustrated in Figure 4.14. The reader is again referred to Appendix A for additional discussion on particle stabilization.

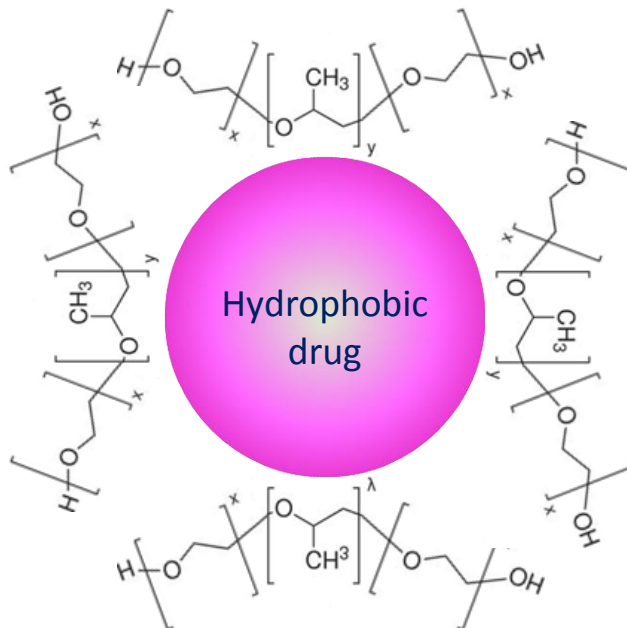


Figure 4.14 Adsorption of Pluronic F-127 on the surface of a hydrophobic drug particle

Figure 4.15 shows an SEM image of the SAS-DEM product when itraconazole microflakes stabilized with 10 wt. % Pluronic F-127 are crystallized in the presence of lactose. The sheet-like aggregates of itraconazole microflakes deposit on the surface of the lactose particles until saturation, at which point the excess drug microflakes form additional sheet-like aggregates which are expected to break apart when exposed to an aqueous medium.

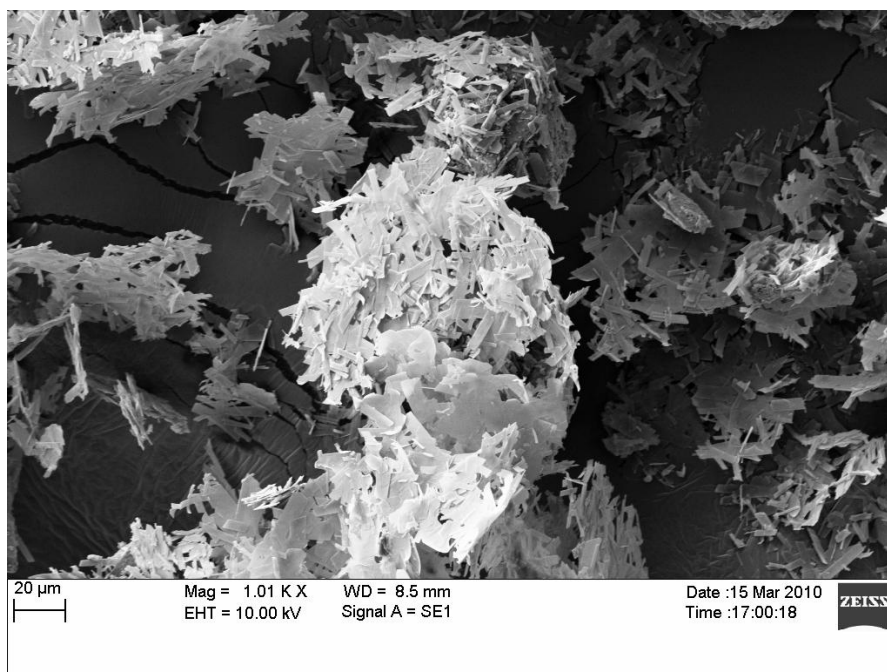


Figure 4.15 SEM image of SAS-DEM mixture with 50 wt. % itraconazole loading stabilized with 10 wt. % Pluronic F-127

Figure 4.16 compares the dissolution of the supplier itraconazole, SAS itraconazole microflakes, a SAS-DEM mixture of itraconazole and lactose with 40 wt. % itraconazole loading, and a SAS-DEM mixture of itraconazole stabilized with 10 wt. % Pluronic F-127 and lactose with 50 wt. % itraconazole loading. The Pluronic F-127 stabilized SAS-DEM product shows superior dissolution, even with a high drug loading. The  $D_{60}$  values for a SAS-DEM product with 10 wt. % Pluronic F-127 and 15 wt. % itraconazole loading, and a SAS-DEM product with 10 wt. % Pluronic F-127 and 50 wt. % drug loading were 78% and 85%, respectively. Through the incorporation of a steric stabilizer during SAS itraconazole crystallization, dissolution has become independent of drug loading, at least up to a drug loading of 50 wt. %. This independence of drug loading is further confirmed by the PSDs reported in Table 4.3.

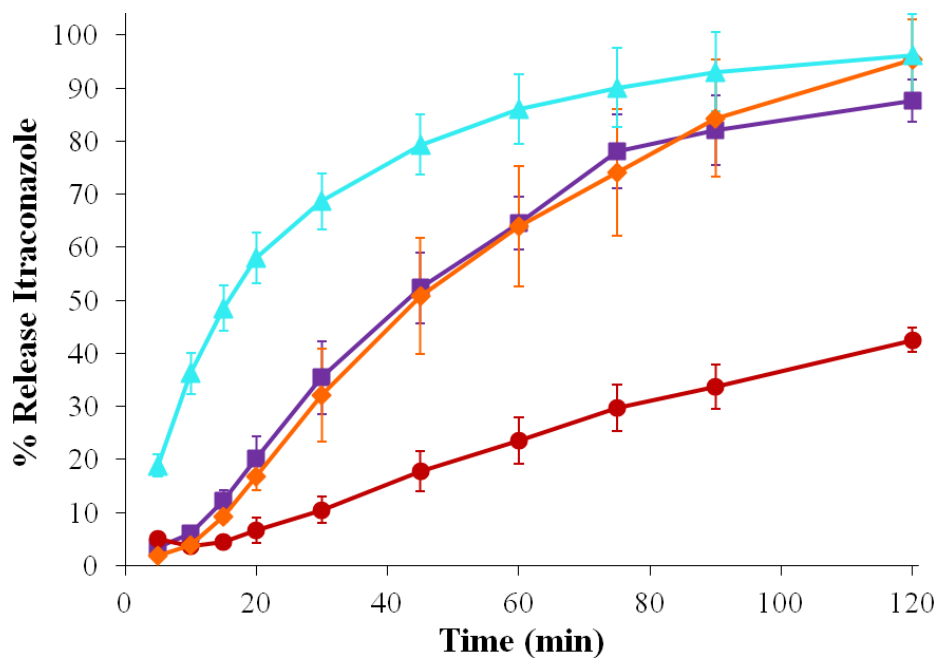


Figure 4.16 Dissolution profiles for supplier itraconazole (●), SAS itraconazole microflakes (■), SAS-DEM mixture with 40 wt. % itraconazole (◆), and SAS-DEM mixture with 50 wt. % itraconazole stabilized with 10 wt. % Pluronic F-127 (▲)

Table 4.3 PSDs of SAS-DEM itraconazole and lactose mixtures with Pluronic F-127

Sample	d <sub>50</sub> (μm)	d <sub>90</sub> (μm)
SAS-DEM: 15 wt. % itraconazole + 10 wt. % Pluronic F-127	0.85 ± 0.03	2.66 ± 0.13
SAS-DEM: 50 wt. % itraconazole + 10 wt. % Pluronic F-127	0.86 ± 0.03	4.32 ± 0.15

The itraconazole content uniformity of the SAS-DEM mixtures was assessed by the relative standard deviation (RSD) of the spectrophotometrically assayed itraconazole loading. The results presented in Table 4.4 show RSDs of less than 5% for all SAS-DEM mixtures, indicating that the itraconazole is uniformly dispersed by the SAS-DEM process, independent of itraconazole loading.

Table 4.4 Relative standard deviation (RSD) of itraconazole content for SAS-DEM mixtures at various drug loadings

Mean Itraconazole Loading (wt. %)	RSD (%)
SAS-DEM Itraconazole + Lactose	
6	1.17
23	4.24
40	1.28
SAS-DEM Itraconazole + 10 wt. % Pluronic F-127 + Lactose	
50	3.95

## 4.5 Characterization of Itraconazole Products

### 4.5.1 Powder X-ray Diffraction

Figure 4.17 shows the PXRD patterns for the supplier itraconazole, SAS itraconazole microflakes, itraconazole microflakes stabilized with 10 wt. % SDS, and itraconazole microflakes stabilized with 10 wt. % Pluronic F-127. Itraconazole exhibited intense characteristic crystalline peaks at  $2\theta$  values of  $14.35^\circ$ ,  $17.46^\circ$ ,  $20.31^\circ$ , and  $23.41^\circ$ . In general, the SAS processed itraconazole samples show a slight decrease in crystallinity, denoted by less intense peaks, compared to the supplier itraconazole. This decrease is attributed to the rapid rate of crystallization in the SAS process, which prevents complete crystal lattice reorganization. The PXRD patterns for the SAS itraconazole microflakes and itraconazole microflakes stabilized with SDS matched the pattern for itraconazole, indicating maintenance of the drug's crystalline structure during SAS processing. The PXRD pattern for the itraconazole microflakes stabilized with Pluronic F-127 also shows characteristic peaks, indicating a crystalline nature. The decrease in the intensity of the  $17.46^\circ$  peak may be due to association of Pluronic F-127 on a specific crystal surface. It was reported in the literature that when itraconazole and

Pluronic F-127 were crystallized by antisolvent crystallization from dichloromethane into an aqueous solution, the drug maintained its crystallinity (Sinswat et al. 2005). Itraconazole also maintained its crystallinity during SAS-DEM processing with lactose (data not shown). Similarly, it was reported in a previous study from our laboratory that the SAS-DEM process with lactose did not alter the crystallinity of nevirapine (Sanganwar et al. 2010).

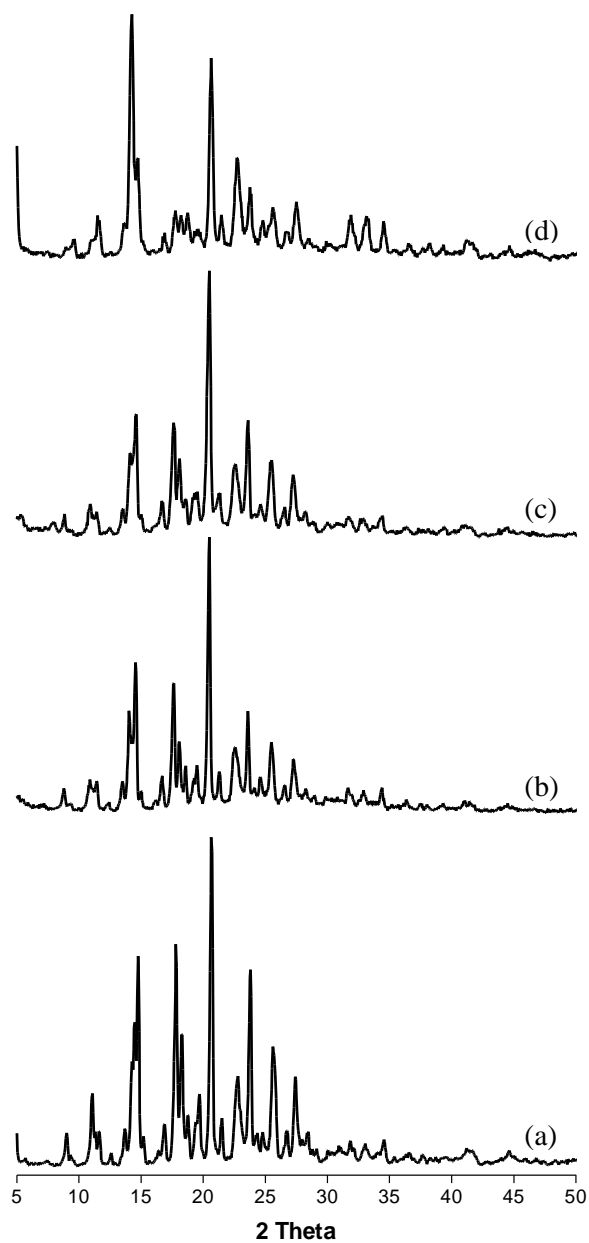


Figure 4.17 PXRD patterns for (a) supplier itraconazole, (b) SAS itraconazole microflakes, (c) itraconazole microflakes stabilized with 10 wt. % SDS, and (d) itraconazole microflakes stabilized with 10 wt. % Pluronic F-127

#### 4.5.2 Differential Scanning Calorimetry

Figure 4.18 shows DSC thermographs for the supplier itraconazole, SAS itraconazole microflakes, SDS, itraconazole microflakes stabilized with 10 wt. % SDS, Pluronic F-127, itraconazole microflakes stabilized with 10 wt. % Pluronic F-127, lactose, SAS-DEM mixture of itraconazole (40 wt. %) and lactose, and SAS-DEM mixture of itraconazole (15 wt. %) and lactose stabilized with 10 wt. % Pluronic F-127. Itraconazole exhibited the typical behavior of an anhydrous crystalline drug, with a well defined melting endotherm at 170 °C. The SAS itraconazole microflakes exhibited an identical melting endotherm, confirming that there is no change in crystallinity by the SAS process. The thermograph for SDS featured two endothermic transitions at 100 °C and 193 °C, while Pluronic F-127 exhibited a single endothermic transition at 57 °C. The stabilized drug microflakes showed small endothermic transitions corresponding to the presence of 10 wt. % stabilizer, but also featured the typical itraconazole melting endotherm at 170 °C, indicating that the crystalline nature of the drug was not affected by the addition of either stabilizer. This result further confirms the hypothesis that the stabilizers are adsorbed onto the surface of the itraconazole crystals, as opposed to being incorporated into the drug's crystalline lattice. The endothermic transitions observed for lactose (monohydrate) between 130 °C and 160 °C represent the loss of crystalline water, as previously confirmed by TGA (Gombás et al. 2002). The itraconazole and lactose mixture produced by SAS-DEM features the loss of crystalline water from the lactose as well as the melting of crystalline itraconazole. It is interesting to note that upon incorporation of Pluronic F-127 into the SAS-DEM process the loss of crystalline water from the lactose monohydrate occurs at 138 °C instead of 144 °C, indicating a possible

interaction between Pluronic F-127 and lactose, an idea that will be further explored by FTIR. From the DSC results it was concluded that the melting behavior of itraconazole, corresponding to the crystalline nature of the drug, was not affected by SAS crystallization, the addition of stabilizers, or by mixing with lactose in the SAS-DEM process.



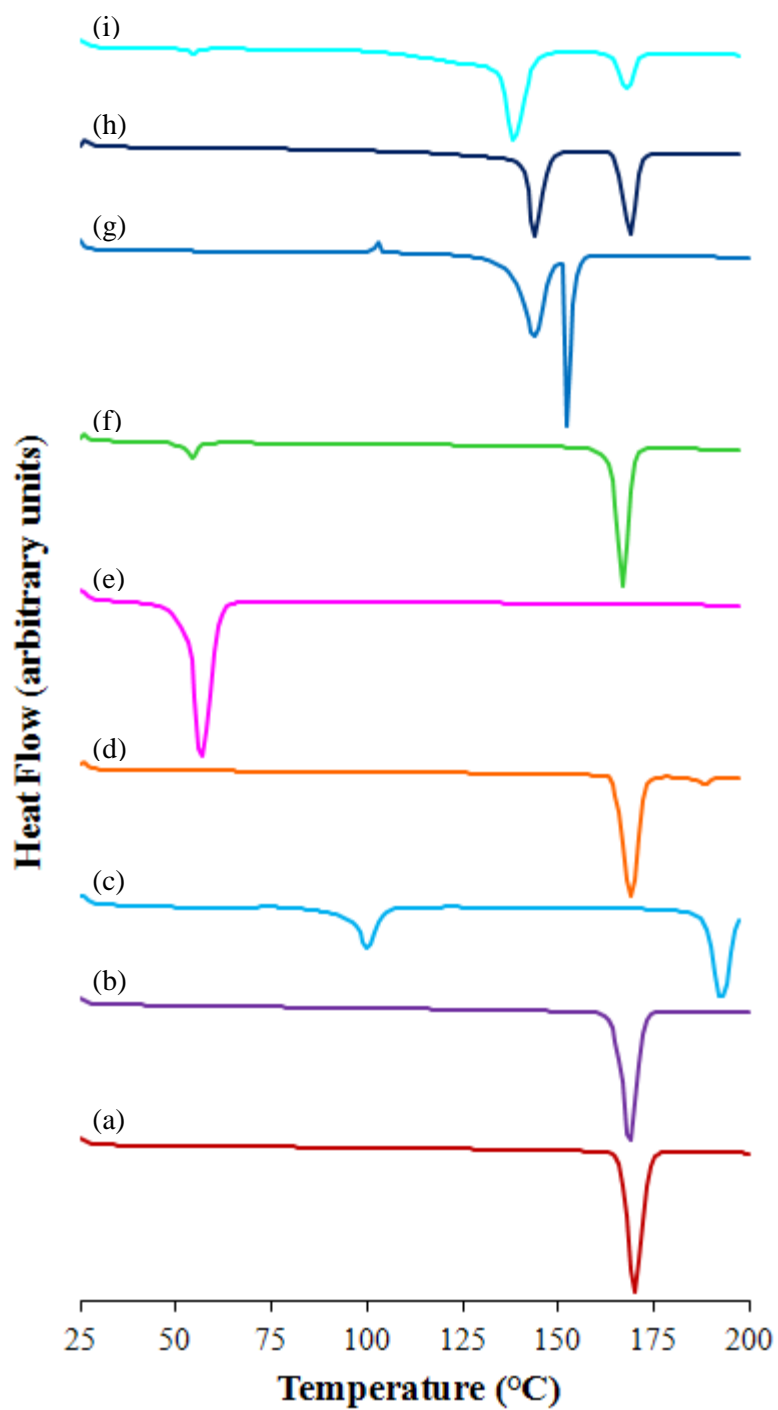


Figure 4.18 DSC thermographs (from bottom to top) for (a) itraconazole, (b) SAS itraconazole microflakes, (c) SDS, (d) itraconazole microflakes stabilized with 10 wt. % SDS, (e) Pluronic F-127, (f) itraconazole microflakes stabilized with 10 wt. % Pluronic F-127, (g) lactose, (h) SAS-DEM mixture of itraconazole (40 wt. %) and lactose, and (i) SAS-DEM mixture of itraconazole (15 wt. %) and lactose stabilized with 10 wt. % Pluronic F-127

#### 4.5.3 Fourier Transform Infrared Spectroscopy

Figure 4.19 shows the FTIR spectra for the supplier itraconazole, SAS itraconazole microflakes, itraconazole microflakes stabilized with 10 wt. % SDS, itraconazole microflakes stabilized with 10 wt. % Pluronic F-127, SAS-DEM mixture of itraconazole (40 wt. %) and lactose, and SAS-DEM mixture of itraconazole (15 wt. %) and lactose stabilized with 10 wt. % Pluronic F-127. The spectra of the SAS microflakes, stabilized SAS microflakes, and SAS-DEM mixtures are similar to that of the supplier drug, with no peak shifts due to the process or component interaction. These results indicate that there are no significant changes in the physicochemical properties of itraconazole and there is no chemical interaction between the drug, excipient, and stabilizers during the SAS-DEM process.

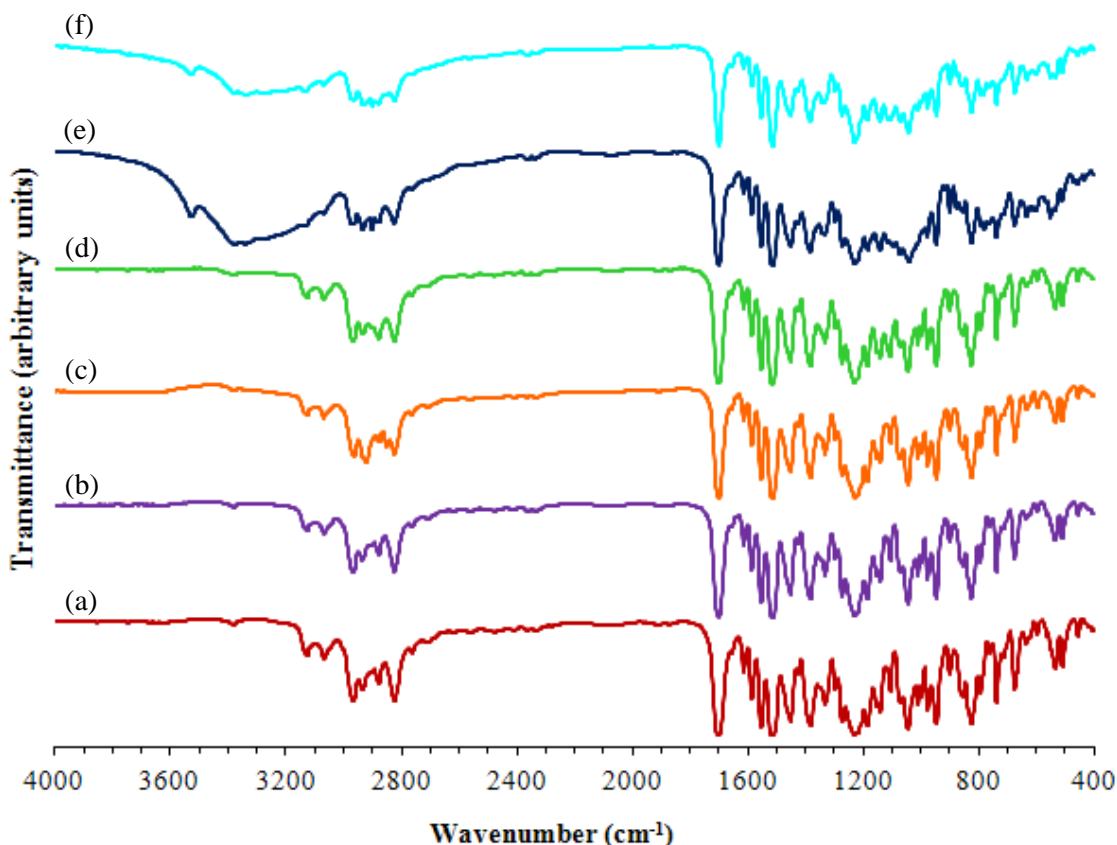


Figure 4.19 FTIR spectra (from bottom to top) for (a) itraconazole, (b) SAS itraconazole microflakes, (c) itraconazole microflakes stabilized with 10 wt. % SDS, (d) itraconazole microflakes stabilized with 10 wt. % Pluronic F-127, (e) SAS-DEM mixture of itraconazole (40 wt. %) and lactose, and (f) SAS-DEM mixture of itraconazole (15 wt. %) and lactose stabilized with 10 wt. % Pluronic F-127

#### 4.6 Conclusions

In this study, itraconazole was recrystallized from dichloromethane in the presence of spray dried lactose excipient particles using the SAS-DEM technique to prevent agglomeration and enhance dissolution. While the SAS crystallized itraconazole microflakes showed enhanced dissolution due to a decrease in particle size and increase in surface area, the microflakes were prone to agglomeration in the dry state. Crystallization in the presence of lactose using the SAS-DEM technique curbed particle growth, prevented agglomeration, and further enhanced dissolution, at low drug loadings

(6 wt. %). At higher drug loadings, the surface of the lactose excipient particles became saturated with microflakes, allowing the excess microflakes to agglomerate and decreasing the dissolution rate. Incorporation of a hydrophilic tri-block copolymer stabilizer, Pluronic F-127, during SAS crystallization altered particle morphology, creating loosely aggregated sheets of microflakes which were easily dispersed when exposed to an aqueous medium. Stabilization within the SAS-DEM process allowed for improved itraconazole dissolution, even at high drug loadings (50 wt. %). Characterization by PXRD showed that the crystalline structure of itraconazole was not significantly altered by SAS recrystallization or by the addition of a stabilizer. DSC and FTIR revealed no change in physicochemical properties of the drug due to processing or the addition of a stabilizer.

## Chapter 5

### Formation of Itraconazole/L-malic Acid Cocrystals in a CO<sub>2</sub>-Expanded Liquid

#### 5.1 Crystallization in CO<sub>2</sub>-Solvent Systems

Crystallization is defined as the evolution of a crystalline state from a solution or melt (Blagden et al. 2007). It is estimated that over 70% of all solid materials are produced by crystallization (Lu and Rohani 2009). Crystallization is a major technological process for particle formation in the pharmaceutical industry. Each crystalline form of an API may possess its own mechanical, thermal, physical, and chemical properties which will influence its solubility, bioavailability, hygroscopicity, melting point, stability, compressibility, and other performance properties. Control over the crystal form of an API is the most direct way to influence its physicochemical properties. The form of an API can be altered by dissolving the API in a liquid organic solvent and recrystallizing the API by inducing supersaturation through cooling, solvent evaporation, or the addition of an antisolvent. The use of a compressed-fluid antisolvent for crystallization offers advantages including single-step processing of particulate pharmaceuticals with controlled characteristics and the ability to recover both the solute and organic solvent through efficient separation of the compressed-fluid antisolvent by depressurization (Jarmer et al. 2005).

In just the last few years, pharmaceutical cocrystals have been prepared using compressed CO<sub>2</sub>-based processes. Padrela et al. (2009) investigated the formation of

indomethacin–saccharin cocrystals using the cocrystallization with supercritical solvent (CSS), supercritical antisolvent (SAS), and atomization and antisolvent (AAS) techniques. While cocrystal formation was not obtainable with CSS due to the low solubility of indomethacin in supercritical CO<sub>2</sub>, indomethacin–saccharin cocrystals were formed using both SAS and AAS (Padrela et al. 2009). In a subsequent study, Padrela et al. utilized a supercritical fluid enhanced atomization (SEA) process to produce cocrystals of six different APIs (Padrela et al. 2010). While Shikhar et al. (2011) used a GAS technique to simultaneously form and complex carbamazepine–nicotinamide cocrystals with  $\gamma$ -cyclodextrin, the focus of this study was on the cocrystals' complexation with the cyclodextrin and not on the mechanism of cocrystallization. These preliminary studies have demonstrated that cocrystal formation is most probable when the drug and former are dissolved in a liquid organic solvent and cocrystallized using compressed CO<sub>2</sub> as an antisolvent or atomizing agent.

The two most common CO<sub>2</sub>-based antisolvent crystallization techniques are supercritical antisolvent (SAS) (see subsection 1.4.3) and gas antisolvent (GAS) (see subsection 1.6.4). SAS crystallization is characterized by high supersaturations and rapid crystallization kinetics, dictated primarily by the interfacial tension between the solvent and antisolvent phases, which is controlled by temperature and pressure. In contrast, the rates of supersaturation and crystallization in the GAS technique are controlled by the rate of addition of the antisolvent (CO<sub>2</sub>), which allows for greater process control. It is typically understood that a slower growth rate will favor cocrystallization, since cocrystals are often a thermodynamically metastable phase, while rapid growth will cause

recrystallization of the thermodynamically stable pure compounds and/or prevent crystallization thus producing an amorphous product.

In this study, GAS crystallization was investigated as a means of producing pharmaceutical cocrystals. The compounds used in this study were the poorly water-soluble drug itraconazole and water-soluble former L-malic acid. In a previous work, cocrystallization of itraconazole with L-malic acid gave a dissolution profile rivaling that of the commercial amorphous form of the drug (Remenar et al. 2003). Itraconazole and L-malic acid were simultaneously dissolved in a liquid organic solvent, tetrahydrofuran (THF). The solution was then pressurized with CO<sub>2</sub>, which reduced the solvating power of THF and caused precipitation of an itraconazole/L-malic acid cocrystal product. Upon near complete precipitation, the pressure was maintained and the liquid solvent removed by flushing with supercritical CO<sub>2</sub>. The cocrystals produced by this method (GAS cocrystallization) were compared to cocrystals produced using a solution-based method, with *n*-heptane as the antisolvent. The itraconazole/L-malic acid cocrystals produced by each method were characterized by powder X-ray diffraction (PXRD), differential scanning calorimetry (DSC), scanning electron microscopy (SEM), high pressure liquid chromatography (HPLC), and dissolution studies.

## **5.2 Recrystallization from CO<sub>2</sub>-Expanded Tetrahydrofuran**

The vapor-liquid equilibria for CO<sub>2</sub> + THF mixtures at various temperatures have been reported by a number of researchers (Im et al. 2004; Li et al. 2007; Knez et al. 2008; Kodama et al. 2010). Tetrahydrofuran is a moderately polar aprotic solvent and Lewis base, capable of hydrogen bonding through donation of an electron pair from its

heterocyclic oxygen atom. As such, tetrahydrofuran is an excellent solvent for a wide range of compounds, and may offer advantages for cocrystal formation through intermediate hydrogen bonding. In contrast, CO<sub>2</sub> is a nonpolar molecule which exhibits poor solvency for polar or heavy molecules. As shown in Figure 5.1, CO<sub>2</sub> shows high solubility in THF, with its solubilization causing a substantial volumetric expansion (Li et al. 2007; Kodama et al. 2010). The THF/CO<sub>2</sub> solvent/antisolvent system was selected for use based on the ability to control solvency by tuning the mole fraction of dissolved CO<sub>2</sub> through changes in the applied CO<sub>2</sub> pressure.

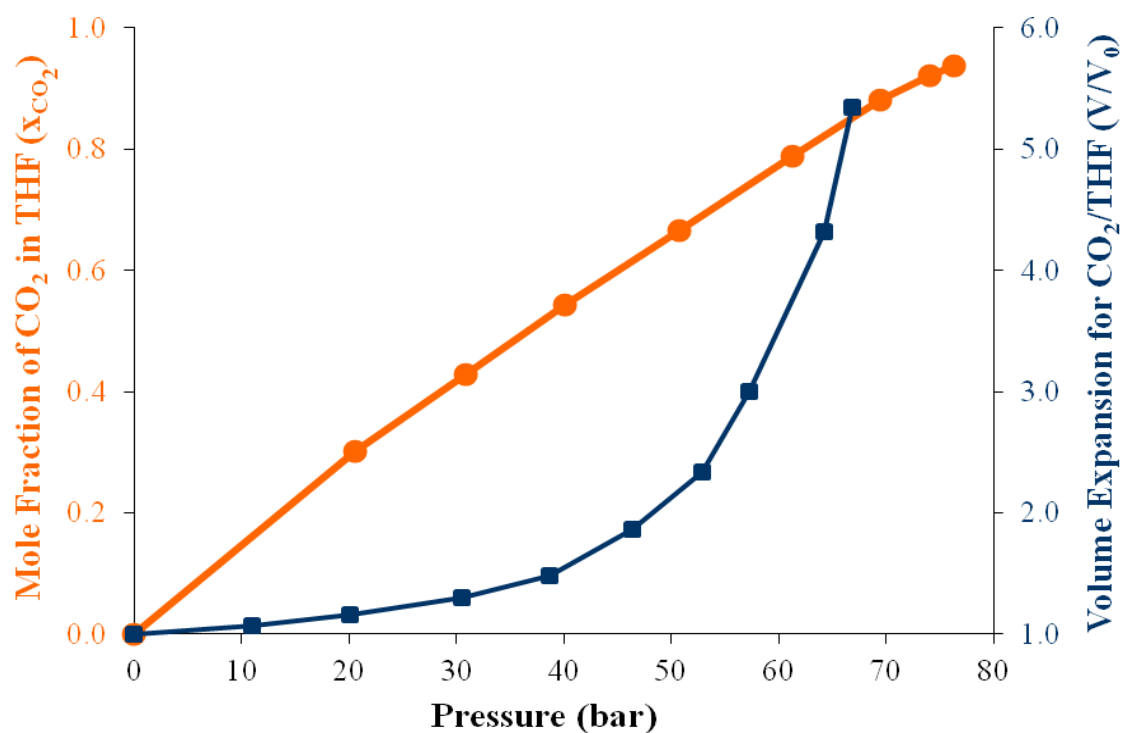


Figure 5.1 Mole fraction of CO<sub>2</sub> ( $x_{CO_2}$ ) in THF at 40 °C (●) and volume expansion ( $V/V_0$ ) of a CO<sub>2</sub>/THF mixture at 40 °C (■)



Two possible methods of CO<sub>2</sub> pressurization have been employed in GAS processes. The CO<sub>2</sub> can either be directly bubbled through solution (Roy et al. 2011) or the headspace above the solution pressurized and CO<sub>2</sub> dissolution governed by diffusion (Tai and Cheng 1998). For the current study, CO<sub>2</sub> was directly bubbled into solution by submerging the CO<sub>2</sub> inlet line in the initial solution, as shown in Figure 2.9. This method of CO<sub>2</sub> pressurization was selected to minimize equilibration time, such that the precipitation events could be directly correlated to the reading on the pressure gauge and there was no diffusion-limited delay. CO<sub>2</sub> pressurization initially proceeded stepwise by opening and closing the CO<sub>2</sub> inlet valve until the outlet pressure of the CO<sub>2</sub> cylinder was reached and the valve was fully open. CO<sub>2</sub> was then pumped at a constant flow rate (1 g/min) and the pressure recorded at various time points to create the pressure profile shown in Figure 2.10. A slow rate of CO<sub>2</sub> addition was used to prevent recrystallization of the pure components and facilitate cocrystal formation. A final pressure of 103 bar was selected to ensure that the CO<sub>2</sub> was in the supercritical phase. Flushing with supercritical CO<sub>2</sub> is known to produce pharmaceutical powders significantly lower in residual solvent than evaporative methods, in a shorter time (Ruchatz et al. 1997; Falk and Randolph 1998; Elvassore et al. 2001). The residual solvent content of the drug products was not analyzed in this work. However, previous literature has shown that in a GAS crystallization process, a sufficient volume of CO<sub>2</sub> (650 mL) is capable of removing residual THF from a precipitate initially containing 12 mL of the solvent (Barrett et al. 2008). Therefore, the flushing method employed in this study, using a CO<sub>2</sub> flow rate of 10 g/min for 60 minutes or approximately 930 mL, should be suitable for removing the

initial 10 mL of THF and producing a drug powder which meets the FDA standards for maximum allowed residual solvent (720 ppm for THF) (Table 2.1).

### 5.2.1 Scanning Electron Microscopy

To determine how CO<sub>2</sub>-recrystallization might affect pure component morphology and crystallinity, each of the pure components was recrystallized by dissolving in THF and recrystallizing under the same conditions used for cocrystallization, namely the pressure profile given in Figure 2.10. An SEM image of the supplier (micronized) itraconazole, the same as used in Chapter 4, is given in Figure 5.2a. The drug features rod-like structures and smaller irregularly shaped particles. Recrystallization of pure itraconazole from THF with CO<sub>2</sub> as an antisolvent causes the drug to form thin microflakes, as shown in Figure 5.2b, similar to those produced by SAS crystallization in Chapter 4. Both SAS crystallization from DCM and GAS crystallization from THF with CO<sub>2</sub> as the antisolvent show crystal growth of itraconazole in a preferential direction, giving the recrystallized drug its rectangular microflake morphology. The supplier L-malic acid, as shown in Figure 5.2c, consisted of irregularly shaped particles with an uneven surface microstructure that appears to be the result of fusion of smaller particles. A less dramatic change in morphology as compared to itraconazole occurs following CO<sub>2</sub>-recrystallization of L-malic acid. Recrystallization of L-malic acid produces smaller particles, as shown in Figure 5.2d, which appear to be fragments of the supplier L-malic acid.

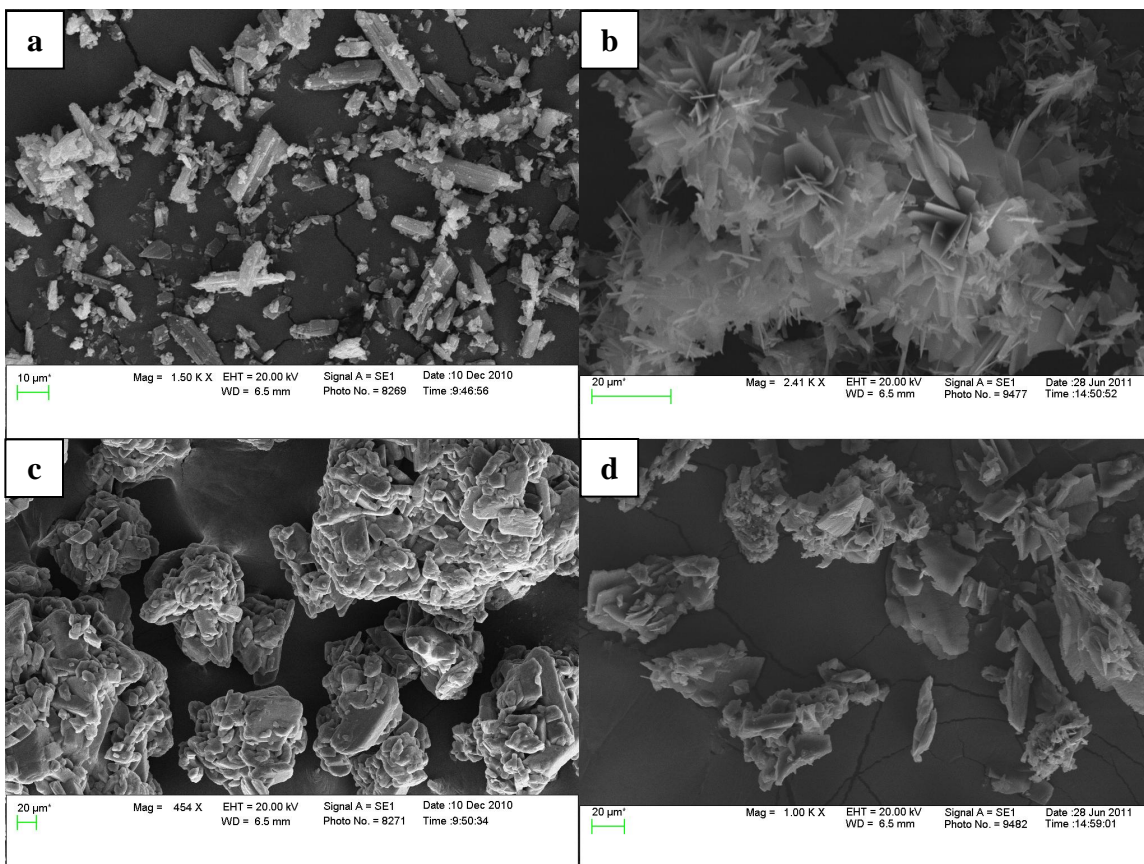


Figure 5.2 SEM images of (a) supplier itraconazole, (b) CO<sub>2</sub>-recrystallized itraconazole, (c) supplier L-malic acid, and (d) CO<sub>2</sub>-recrystallized L-malic acid

### 5.2.2 Powder X-Ray Diffraction

The PXRD patterns for the supplier and recrystallized itraconazole and supplier and recrystallized L-malic acid are given in Figures 5.3 and 5.4, respectively. Itraconazole exhibited characteristic crystalline peaks at  $2\theta$  values of 18.0°, 20.8°, 23.9°, and 25.8°. L-Malic acid also exhibited highly crystalline peaks, with the most intense peaks occurring at  $2\theta$  values of 19.6°, 24.7°, 29.7° and 38.0°. The PXRD patterns of the recrystallized components were superimposable with their respective supplier components, confirming preservation of the crystal lattice and  $d$ -spacing following GAS recrystallization from THF. There was, however, a loss of crystallinity in each of the

recrystallized components, as denoted by a decrease in the peak intensities compared to the supplier materials. Using the intensities of the four most intense peaks previously mentioned for each component, an average loss in crystallinity was calculated from the ratio of the recrystallized peak intensity to the supplier peak intensity. Itraconazole exhibited an approximately 10% decrease in crystallinity following GAS recrystallization while L-malic acid exhibited an approximately 50% decrease. Loss of itraconazole crystallinity during GAS processing has been previously documented in the literature and is attributed to the rapid nucleation of particles preventing reorganization of the molecules into the crystalline form (Barrett et al. 2008). The high solubility of L-malic acid in THF likely inhibits its recrystallization. Hydrogen bonding between THF and L-malic acid will disrupt the former's crystal lattice, leading to the precipitation of amorphous L-malic acid.

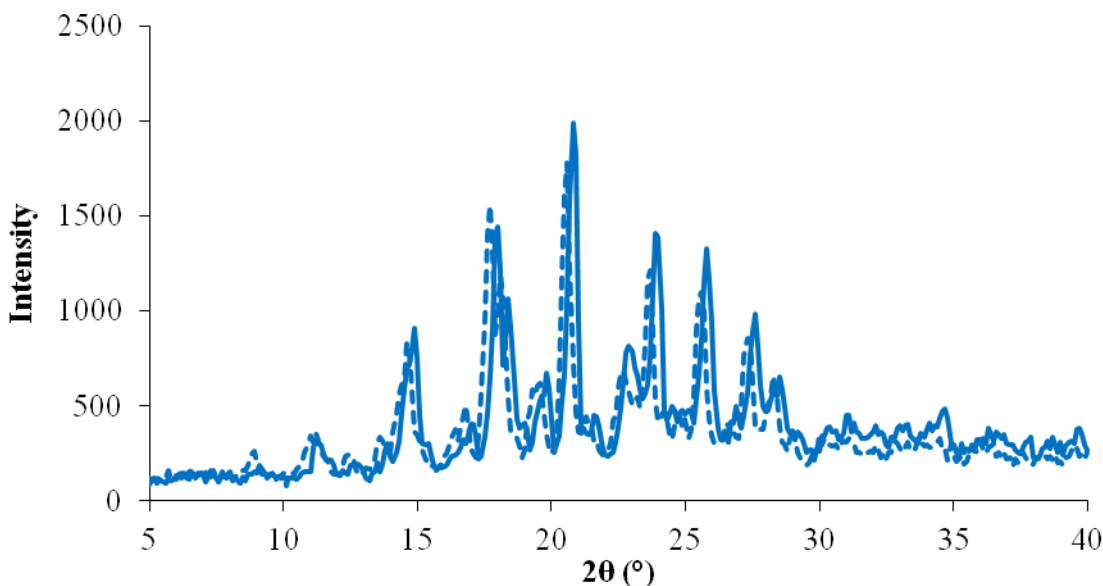


Figure 5.3 PXRD patterns of supplier itraconazole (—) and CO<sub>2</sub>-recrystallized itraconazole (.....)

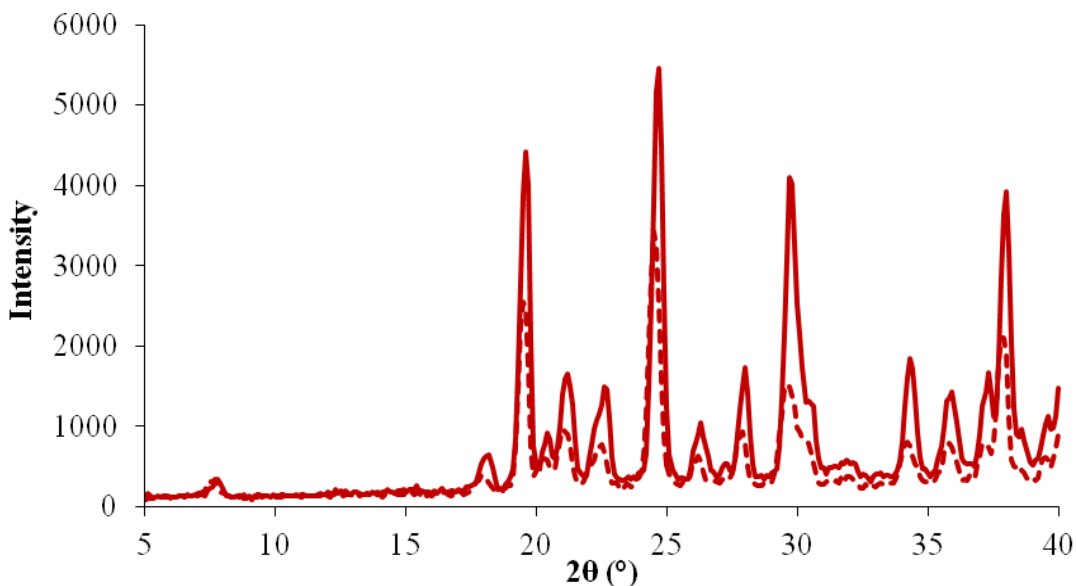


Figure 5.4 PXRD patterns of supplier L-malic acid (—) and  $\text{CO}_2$ -recrystallized L-malic acid (.....)

### 5.3 GAS Cocrystallization of Itraconazole and L-Malic Acid

Solute crystallization in a GAS process is governed by the rate of  $\text{CO}_2$  addition or the pressure versus time profile (Figure 2.10) (Thiering et al. 2000). For cocrystal formation, matching the rates of drug and former crystallization in accordance with cocrystal stoichiometry is critical. For example, to form cocrystals by grinding, the necessary drug and former amounts are dictated by the stoichiometry of the expected cocrystal. To form the same cocrystal using a  $\text{CO}_2$  antisolvent method, the starting quantities of drug and former are based on the pressure dependent solubilities of the two components such that their simultaneous crystallization will occur stoichiometrically, but the starting quantities are likely nonstoichiometric. Similar challenges in matching solubility were encountered when using the cocrystallization with supercritical solvent (CSS) technique to produce indomethacin–saccharin cocrystals (Padrela et al. 2009). In

CSS, the drug and former must have sufficient and ideally equal solubility in supercritical CO<sub>2</sub>, such that upon depressurization their crystallization is stoichiometric. Cocrystal formation using a CO<sub>2</sub> antisolvent method such as GAS is thus a complex thermodynamic problem, for which thermodynamic modeling will need to be employed. Although a strategy for calculating the appropriate amounts of drug and former based on thermodynamic modeling of their pressure-dependent solubilities in a CO<sub>2</sub>-expanded solvent is outlined in Appendix B, the method of preparation employed in this study was to provide the more soluble compound (L-malic acid) in stoichiometric excess such that the precipitating amount cocrystallized with itraconazole and the excess remained in solution and was flushed out. As previously reported in the literature, itraconazole–dicarboxylic acid cocrystals have 2:1 stoichiometry dictated by the geometric fit of the dicarboxylic acid former between two antiparallel oriented itraconazole molecules, as shown for an itraconazole–succinic acid cocrystal in Figure 5.5 (Remenar et al. 2003). The proposed cocrystal structure for itraconazole–dicarboxylic acid cocrystals involves the formation of two hydrogen bonds between the pyridine nitrogens of two itraconazole molecules and the terminal hydroxyl groups of a single dicarboxylic acid molecule. Itraconazole–dicarboxylic acid cocrystals have been known to favor geometric fit over acid-base chemistry, which would predict interaction with the strongest base of itraconazole, piperazine (Morissette et al. 2004). The starting quantities of itraconazole (250 mg) and L-malic acid (250 mg) were provided in an approximate stoichiometric ratio of 2:10 despite the expected cocrystal stoichiometry of 2:1 to account for the increased solubility of L-malic acid in THF.

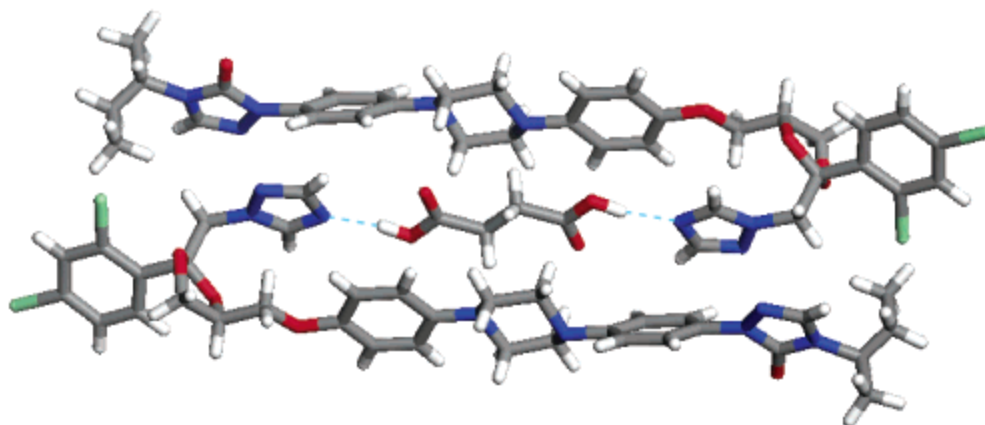


Figure 5.5 Chemical structure of a 2:1 itraconazole–succinic acid cocrystal

Figure 5.6 gives a visualization of the GAS cocrystallization process as it was observed through the sapphire window on the base of the crystallization vessel. Figure 5.6a shows the clear solution of dissolved itraconazole and L-malic acid in THF. This solution was filtered prior to its injection into the vessel to remove any undissolved material. Undissolved solutes could cause a seeding effect, promoting crystallization of one or both of the pure components instead of cocrystallization (Braga and Grepioni 2004). From visual observation, the onset of crystallization was observed around 41 bar (Figure 5.6b), while crystallization stagnated after 70 bar (Figure 5.6c). Upon reaching 103 bar, the outlet valve was opened and additional CO<sub>2</sub> was flushed through the vessel to remove the THF and dry the cocrystal powder (Figure 5.6d).

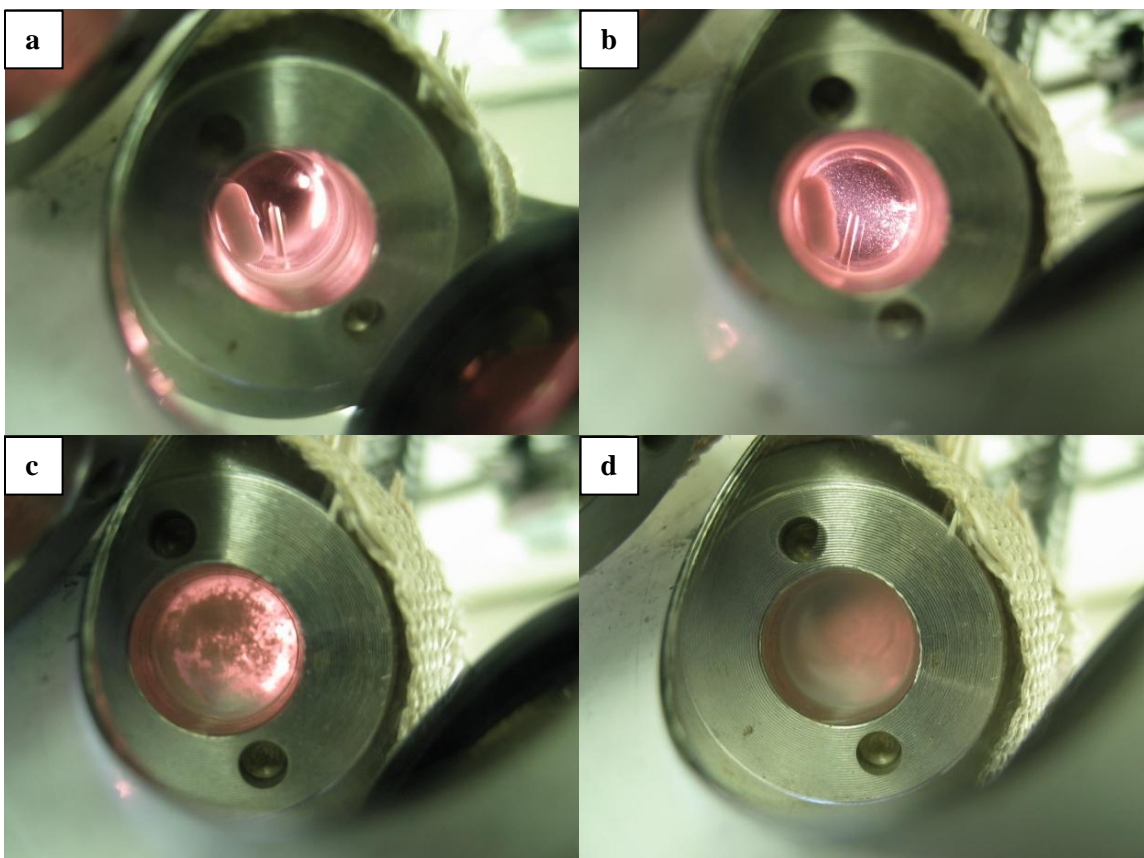


Figure 5.6 Visualization of the GAS cocrystallization process: (a) Clear solution of dissolved itraconazole and L-malic acid in THF, (b) onset of particle crystallization around 41 bar, (c) near complete crystallization around 70 bar, and (d) dry powder following supercritical CO<sub>2</sub> flushing at 103 bar

In order to better quantify the process of crystallization, the amount of itraconazole in solution at various pressures was determined. These measurements were conducted by dissolving 500 mg of itraconazole in 20 mL of THF at 40 °C and in the presence of 500 mg of L-malic acid, since co-solutes with high solubility, such as L-malic acid, are known to significantly influence phase behavior in GAS crystallization processes (Dixon and Johnston 1991; Foster et al. 1997; Warwick et al. 2000). Figure 5.7 illustrates the amount of itraconazole in solution per gram of THF (CO<sub>2</sub>-free basis) as pressure is increased. Corresponding with the visual results seen in Figure 5.6,



itraconazole crystallization begins at around 40 bar, where a dramatic decrease in the amount of itraconazole in solution, caused by catastrophic precipitation, is observed. Itraconazole crystallization concludes around 103 bar, where a small amount (3.9 mg/g THF) is left in solution. As pressure is increased, the solubility of itraconazole approaches a limiting value corresponding to its solubility in pure supercritical CO<sub>2</sub> (Bungert et al. 1998). At 40 °C and 103 bar, the amount of itraconazole crystallized from solution was approximately 85% of that originally dissolved. The combination of high itraconazole and CO<sub>2</sub> solubility in THF and the low solubility of itraconazole in CO<sub>2</sub> renders the system suitable for GAS development (Bungert et al. 1998). Since L-malic acid was provided in excess, the itraconazole crystallization curve shown in Figure 5.7 effectively demonstrates the process of cocrystallization as CO<sub>2</sub> pressure is increased.

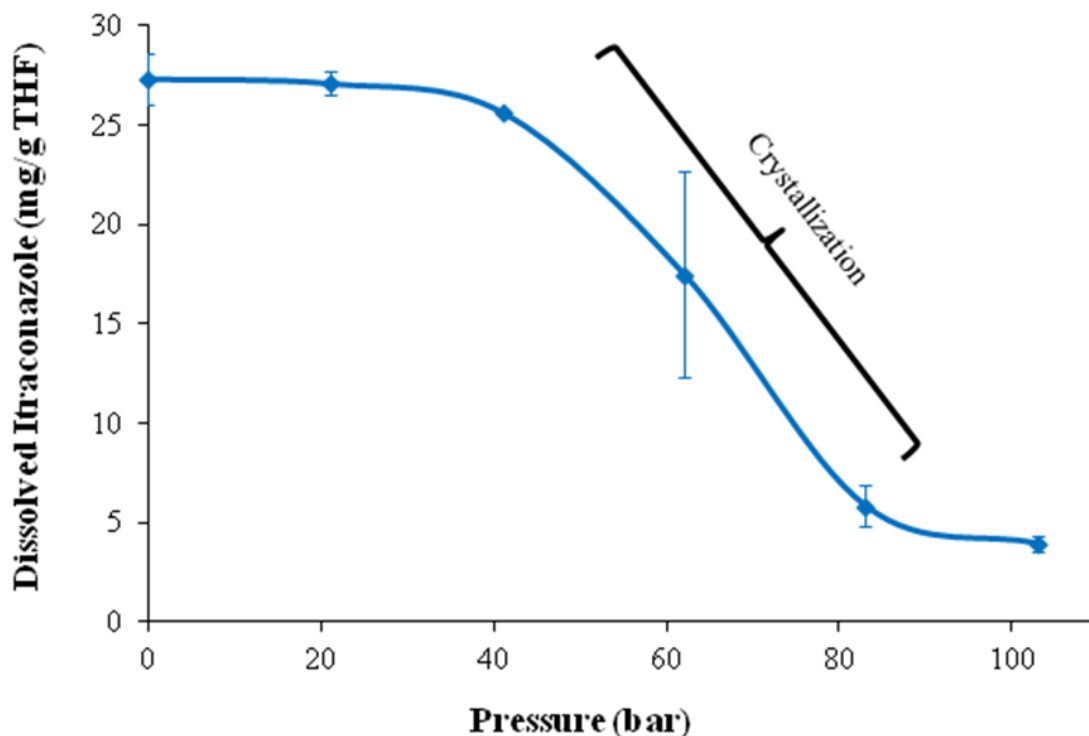


Figure 5.7 Itraconazole concentration in THF (CO<sub>2</sub>-free basis) at 40 °C and in the presence of L-malic acid as a function of pressure

## 5.4 Characterization of Cocrystal Products

### 5.4.1 Powder X-ray Diffraction

To confirm cocrystal formation, the product obtained from simultaneous dissolution and crystallization of itraconazole and L-malic acid should exhibit a PXRD pattern which does not match either of the pure component patterns and is not a summation of their individual patterns, which would indicate a mere physical mixture of the two components. Figure 5.8 shows the PXRD patterns for the products obtained using both liquid antisolvent cocrystallization with *n*-heptane and GAS cocrystallization with CO<sub>2</sub>. The cocrystal product obtained by GAS cocrystallization shows discernable peaks at  $2\theta$  values of 8.7°, 17.0°, 17.6°, 21.2°, and 22.5°. The PXRD peaks correspond well with

those previously reported in the literature for an itraconazole/L-malic acid cocrystal (Remenar et al. 2003). The lack of pure component peaks in the cocrystal product indicates the absence of crystalline itraconazole or L-malic acid. The PXRD results thus confirm that itraconazole/L-malic cocrystals are obtainable by GAS cocrystallization.

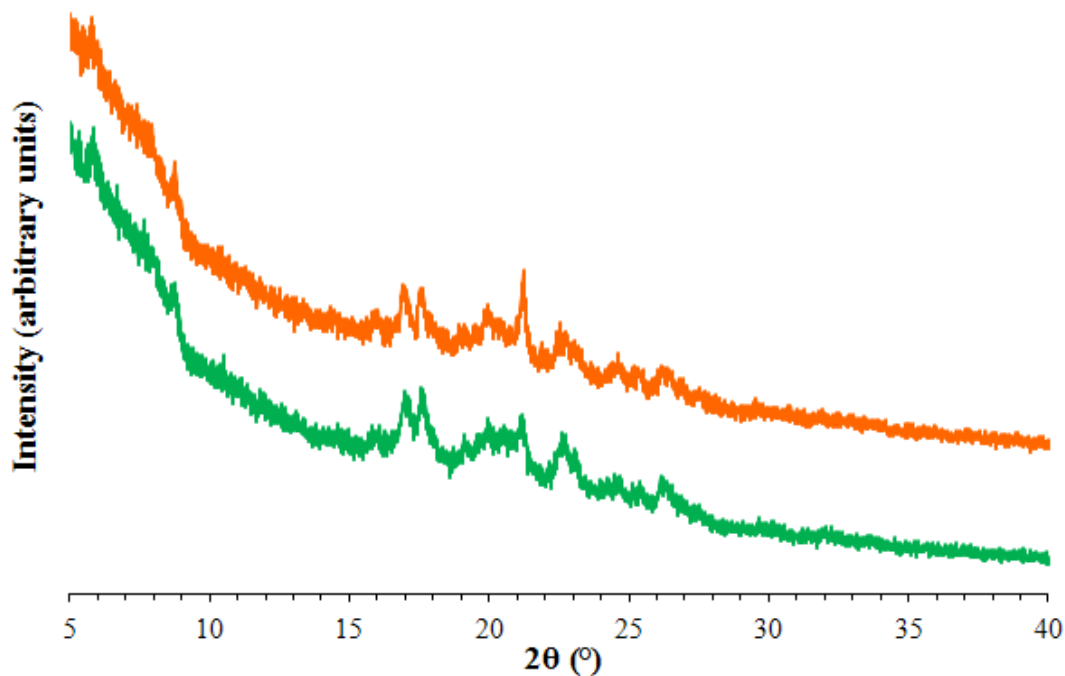


Figure 5.8 PXRD patterns of itraconazole/L-malic acid cocrystals produced using a liquid antisolvent, *n*-heptane, ( — ) and itraconazole/L-malic acid cocrystals produced by GAS cocrystallization ( — )

The degree of crystallinity of the cocrystals compared to that of the pure drug and former is significantly less as indicated by diminished peak intensities. Similar results have been observed for salts and cocrystals of the antibacterial drug norfloxacin (Basavoju et al. 2006). Due to the catastrophic nature of itraconazole crystallization, in both methods of preparation, the growth of well defined crystallographic faces is limited. Therefore, while the cocrystal products show some crystalline nature, it is suspected that

some quantity of uncrystallized amorphous itraconazole and/or L-malic acid may also be present in the final product. Two theories of crystallization have been proposed to describe the formation of this mixed amorphous and cocrystal product. The first theory considers that precipitation produces a fully amorphous product which subsequently cocrystallizes to some extent in the CO<sub>2</sub>-expanded liquid media. The second theory considers that precipitation directly produces a cocrystalline phase but that the speed of crystal nucleation prevents organization of all molecules, and thus, amorphous product is also precipitated. Since the reactor outlet was immediately opened upon reaching the desired pressure (103 bar) and the solvent removed from the vessel, any amorphous to crystalline transformation following precipitation would be facilitated primarily by supercritical CO<sub>2</sub>. The literature regarding itraconazole processing in supercritical CO<sub>2</sub> supports the transformation of crystalline itraconazole to a mixed product containing some amorphous itraconazole, but not crystallization of amorphous itraconazole. Based on these considerations it is suspected that the crystallinity of the itraconazole product is dictated during precipitation, not subsequently. While amorphous itraconazole has been known to dissolve faster than the drug in its crystalline form (Six et al. 2004), concerns about the stability of a mixed cocrystalline and amorphous product and the effect on shelf life will need to be explored in future studies.

#### 5.4.2 Differential Scanning Calorimetry

As an alternative means of assessing cocrystal formation, DSC analysis was conducted. The DSC thermographs for the supplier itraconazole, supplier L-malic acid, itraconazole/L-malic acid cocrystals produced from *n*-heptane, and itraconazole/L-malic

acid cocrystals produced by GAS cocrystallization are given in Figure 5.9. Itraconazole and L-malic acid showed well defined melting points at 169.2 °C and 106.3 °C, respectively. The cocrystals produced from *n*-heptane exhibited a well defined melting point at 150.7 °C, while the cocrystals produced by GAS cocrystallization exhibited a well defined melting point at 136.9 °C. A distinct cocrystal melting point between those of the two pure components is in agreement with previous reports in the literature for a number of cocrystals (McNamara et al. 2006; Basavoju et al. 2008; Padrela et al. 2010). The lack of residual itraconazole and L-malic acid peaks in both of the cocrystal thermographs indicate the absence of either of the pure crystalline components. The differing melting points of the two cocrystal products are attributed to differing quantities and/or compositions of amorphous material in the final product.

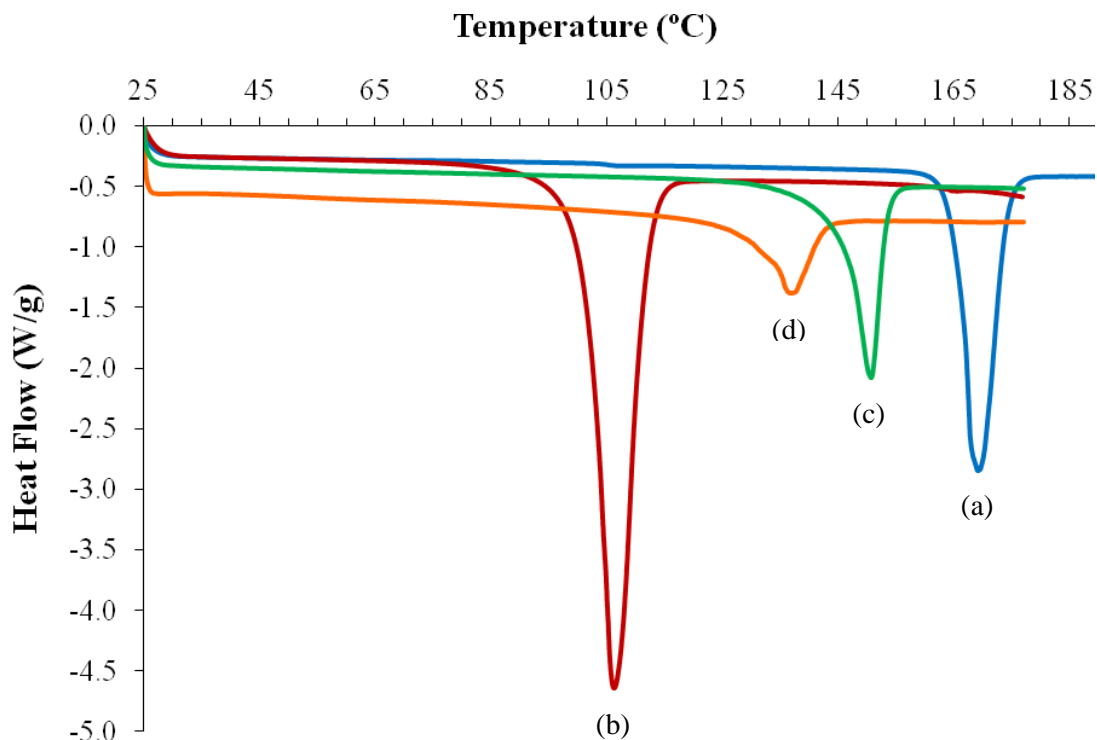


Figure 5.9 DSC thermographs for (a) itraconazole, (b) L-malic acid, (c) itraconazole/L-malic acid cocrystals from *n*-heptane, and (d) itraconazole/L-malic acid cocrystals produced by GAS cocrystallization

The thermograph for a 1:1 by mass physical mixture of itraconazole and L-malic acid, taken on a different machine at a later date, demonstrated a number of interesting features, as shown in Figure 5.10. Endothermic transitions were observed at 83.9 °C, 103.1 °C, 154.6 °C, and 165.5 °C. The endothermic transitions at 103.1 °C and 165.5 °C are attributed to the melting of pure L-malic acid and itraconazole, respectively. The distinct endothermic peak at 83.9 °C is suspected to be a eutectic melt, formed by heating the physical mixture of itraconazole and L-malic acid. Eutectic melts occur at temperatures lower than the pure component melting points, and can be present for both cocrystal and non-cocrystal forming binary mixtures (Mohammad et al. 2011). The

endothermic transition at 154.6 °C corresponds to the melting point of an itraconazole/L-malic acid cocrystal (154.4 °C) as reported in the literature (Almarsson et al. 2007). It is suspected that cocrystal formation may have resulted from recrystallization of the eutectic melt upon further heating. *In situ* cocrystal formation during DSC heating has been reported for some organic physical mixtures of binary eutectic systems when they are heated beyond their eutectic melting point (Lu et al. 2008; Padrela et al. 2009). Despite the ability of DSC to produce itraconazole/L-malic acid cocrystals, it is not suspected that this phenomenon is responsible for the cocrystal melting points observed in Figure 5.9. The lack of crystalline pure components in the cocrystal products, which prevent the formation of a crystalline eutectic, also prevent recrystallization of the eutectic melt to form cocrystals.

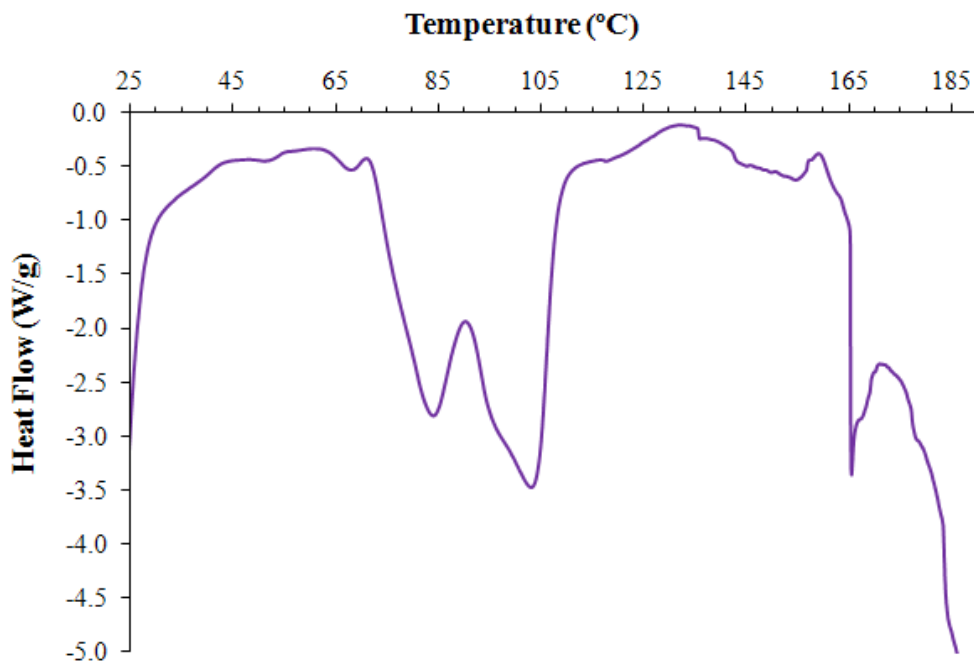


Figure 5.10 DSC thermograph for a 1:1 by mass physical mixture of itraconazole and L-malic acid

Enthalpies of fusion ( $\Delta H_f$ ) were also calculated from the DSC thermographs shown in Figure 5.9 and are reported in Table 5.1. The lower enthalpies of fusion for the cocrystals, as compared to the pure components, are typical cocrystal behavior, especially for cocrystals prepared by CO<sub>2</sub>-based processes. Cocrystals formed by CO<sub>2</sub>-based crystallization processes have previously been found to have lower enthalpies of fusion than single crystals of the same composition prepared by slow evaporation from solution due to their polycrystalline nature and surface imperfections in the crystal lattice (Padrela et al. 2009). The speed at which catastrophic precipitation occurred as *n*-heptane was added dropwise to solution and during pressurization in the GAS process limits the extent of cocrystallization and prevents the formation of a perfect cocrystal lattice. The lower the enthalpy of fusion, the easier it is for the crystals to turn into liquid. Likewise, during dissolution, a lower enthalpy of fusion can promote dissociation of the cocrystal and allow interaction of the components with the dissolution medium, thereby enhancing drug release.

Table 5.1 Summary of melting temperatures ( $T_m$ ) and enthalpies of fusion ( $\Delta H_f$ )

Sample	$T_m$ (°C)	$\Delta H_f$ (J/g)
Itraconazole	169.2	94.5
L-malic acid	106.3	196.6
Cocrystals from <i>n</i> -heptane	150.7	63.1
Cocrystals from GAS	136.9	38.3



### 5.4.3 Scanning Electron Microscopy

Figures 5.11a and 5.11b show the itraconazole/L-malic acid cocrystals produced using *n*-heptane as an antisolvent, and Figures 5.11c and 5.11d show the cocrystals produced by GAS cocrystallization. Both methods produce a visually homogeneous cocrystal phase with consistent particle morphology distinctly different from either of the pure components. The particles produced from *n*-heptane have an irregular shape but relatively smoother surface and smaller size while the particles produced by GAS cocrystallization are spherically shaped, appear fibrous, and have a larger particle size. It is suspected that the differences in particle morphology and size result from differences in the methods of production. When using the liquid antisolvent technique, crystallization occurs in the discrete droplets of *n*-heptane as it is mixed into the THF. The irregular shape of the resultant particles is thus caused by the complete miscibility of the *n*-heptane with THF while particle size is minimized due to the limited persistence of the discrete *n*-heptane droplets. In the GAS technique, the particles crystallize in the homogeneous CO<sub>2</sub>-expanded THF and particle growth continues until complete crystallization has been achieved or the outlet line is opened.

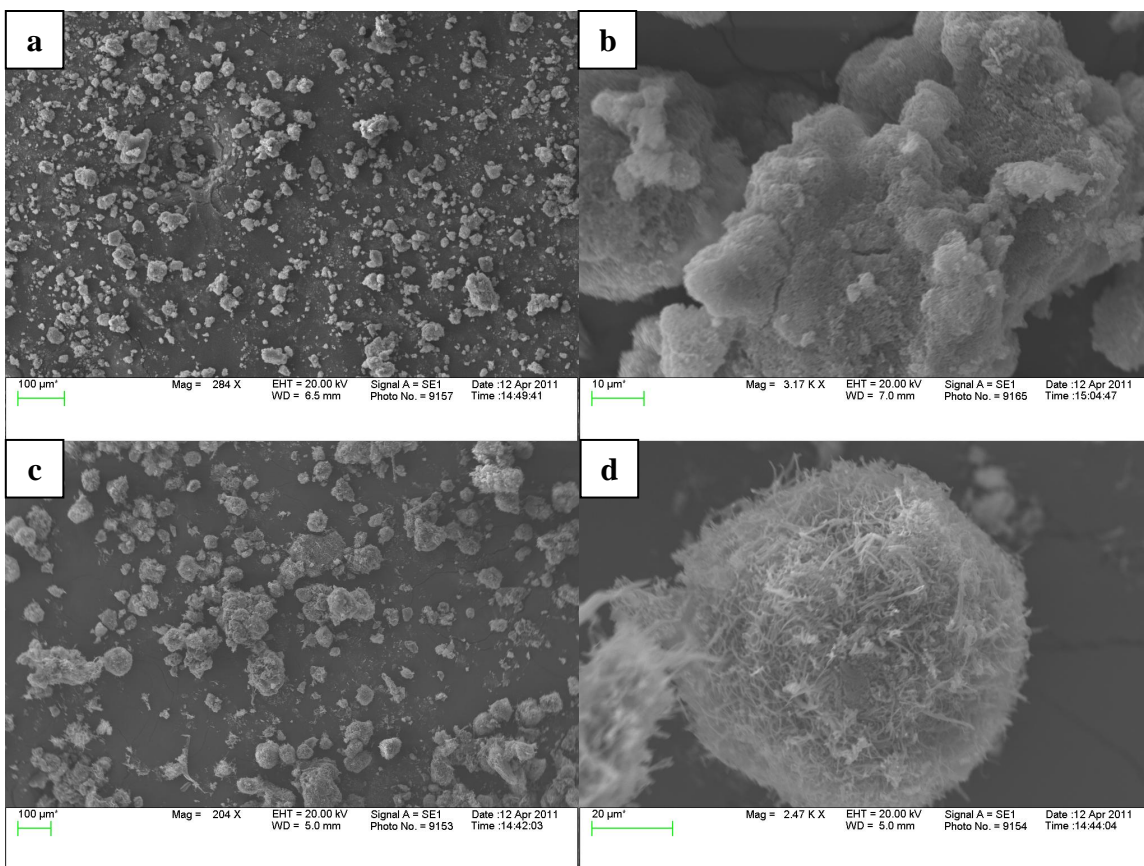


Figure 5.11 SEM images of (a and b) itraconazole/L-malic acid cocrystals obtained from *n*-heptane and (c and d) itraconazole/L-malic acid cocrystals produced by GAS cocrystallization

#### 5.4.4 Compositional Analysis

The powders produced by each method were characterized for composition by dissolving a sample of known mass in methanol, performing HPLC, and assaying the itraconazole content spectrophotometrically at  $\lambda = 261$  nm. The powder produced by GAS cocrystallization was determined to have an approximately 2:4 molar ratio of itraconazole to L-malic acid while the powder produced from *n*-heptane was found to have an approximately 2:6 molar ratio. The differences in cocrystal product composition are thought to be caused by differences in the rate and extent of supersaturation resulting

from the dropwise addition of *n*-heptane versus pressurization with CO<sub>2</sub>. Without in-depth single crystal X-ray diffraction, rationalizing the hydrogen bonding interactions and cocrystal stoichiometry based on the cocrystal composition as determined by HPLC analysis alone would be inappropriate. Furthermore, single crystal X-ray diffraction has shown that the cocrystal interactions between itraconazole and dicarboxylic acid formers give 2:1 drug to former stoichiometry, suggesting that the powders produced in this work likely contain excess amorphous pure components in addition to the cocrystals. This result is further supported by the lack of well defined crystal faces, as was noted by the absence of intense crystalline peaks in the cocrystals' PXRD patterns (Figure 5.8) and by the decreased enthalpies of fusion in the DSC thermographs (Table 5.1). Similar partial cocrystal formation was also proposed for indomethacin–saccharin cocrystals produced by the CSS technique (Padrela et al. 2009).

However, to further confirm the compositional homogeneity of the produced cocrystal powder, the relative standard deviation (RSD) of the itraconazole content in five identically prepared samples was determined. The RSDs for the cocrystal powder produced by each method are shown in Table 5.2. The powders produced by each method display good itraconazole content uniformity, with RSDs less than 4%. These results indicate that GAS cocrystallization is a viable technique for producing a homogeneous cocrystal powder which conforms to FDA drug content guidelines (Rohrs et al. 2006).

Table 5.2 RSD of itraconazole content in cocrystal products

Cocrystal Preparation Method	RSD (%)
<i>n</i> -heptane antisolvent	3.6
GAS cocrystallization	3.5

#### 5.4.5 Dissolution Studies

Dissolution testing was conducted to assess the potential impact that cocrystallization with L-malic acid, and more specifically, the GAS cocrystallization technique, may have on improving itraconazole dissolution. Cocrystallization with L-malic acid has previously been shown to improve itraconazole dissolution compared to the pure drug as well as cocrystals with other dicarboxylic acids including succinic acid and L-tartaric acid (Remenar et al. 2003). The dissolution profiles for the supplier itraconazole, itraconazole/L-malic cocrystals produced from *n*-heptane and by GAS cocrystallization, and a 1:1 by mass physical mixture of the two components are given in Figure 5.12. The dissolution profile for the supplier (micronized) drug correlates well with that reported in Chapter 4 (see Figure 4.4), with slight differences resulting from the dissolution apparatus, namely smaller impellers. The physical mixture had slightly improved dissolution over the supplier itraconazole. This result is thought to occur from particle size reduction caused by grinding the itraconazole with the L-malic acid. It is unlikely that the presence of L-malic acid had a significant solubilization effect on itraconazole since its concentration was only 0.006 mg/mL. The itraconazole/L-malic cocrystals prepared by each method, *n*-heptane antisolvent and GAS cocrystallization, showed improved dissolution over the supplier drug. As shown in Table 5.3, the cocrystals from *n*-heptane and GAS cocrystallization had  $D_{60}$  values of 37.4% and 48.2%, respectively, compared to the supplier itraconazole  $D_{60}$  of 21.7%. Likewise, the cocrystals from *n*-heptane and GAS cocrystallization had  $D_{120}$  values of 58.2% and 73.7%, respectively, compared to the supplier itraconazole  $D_{120}$  of 40.6%.

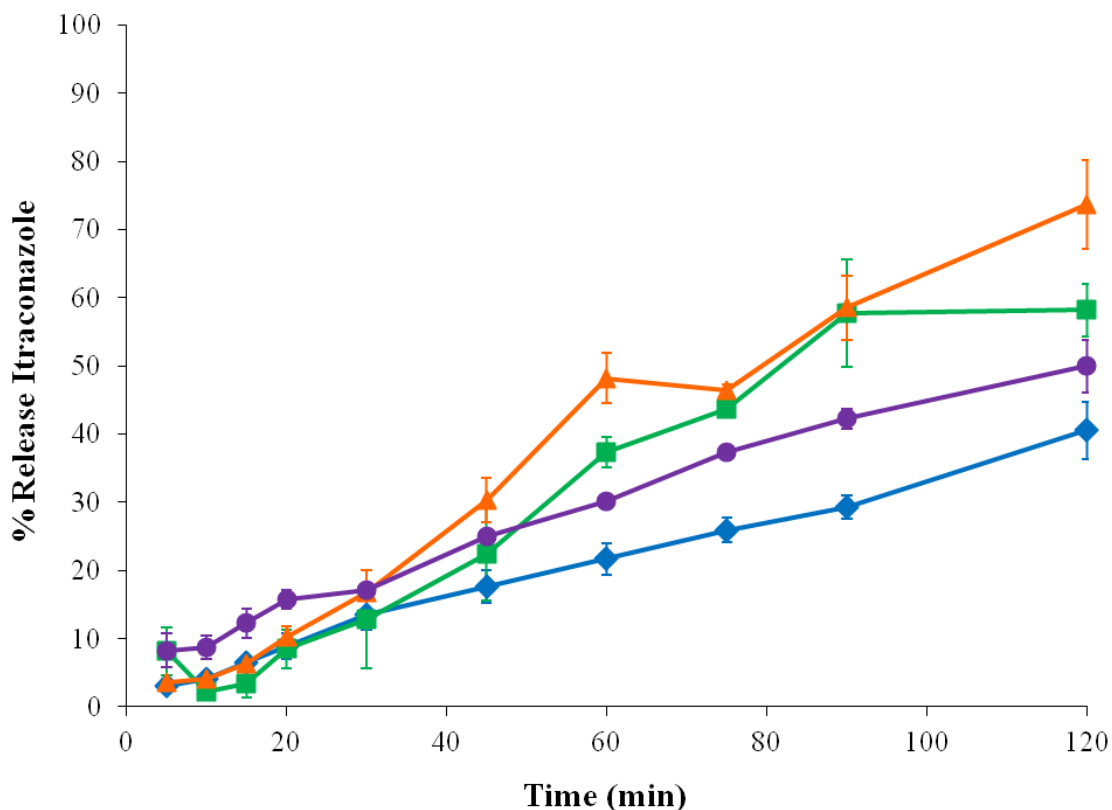


Figure 5.12 Dissolution profiles for itraconazole (◆), a 1:1 by mass physical mixture of itraconazole and L-malic acid (●), itraconazole/L-malic acid cocryystals produced from *n*-heptane (■), and itraconazole/L-malic acid cocryystals produced by GAS cocrySTALLIZATION (▲)

Table 5.3 Mean cumulative dissolved itraconazole after 60 ( $D_{60}$ ) and 120 ( $D_{120}$ ) minutes for various formulations (mean  $\pm$  standard error)

Sample	$D_{60}$ (%)	$D_{120}$ (%)
Supplier itraconazole	$21.7 \pm 2.3$	$40.6 \pm 4.2$
Physical mixture	$30.2 \pm 0.1$	$50.0 \pm 3.9$
Cocryystals from <i>n</i> -heptane	$37.4 \pm 2.3$	$58.2 \pm 3.9$
Cocryystals from GAS	$48.2 \pm 3.6$	$73.7 \pm 6.6$

Both cocryystals exhibited improved dissolution compared to the supplier itraconazole due to both the presence of amorphous itraconazole and the intimate

association of itraconazole with the water-soluble former, L-malic acid, to form a cocrystal structure. The improvements in dissolution suggest that the cocrystals maintain their cocrystal structure upon exposure to the dissolution medium. Dissociation of the cocrystal would result in a dissolution profile similar to that of the supplier drug, as was the case for exemestane and maleic acid cocrystals (Shiraki et al. 2008). The differences in dissolution of the two cocrystals are thought to result from their amorphous itraconazole content, as well as their differing particle structures. The fibrous structure of the cocrystals produced by GAS cocrystallization (Figure 5.11d) allowed greater water permeation and improved dissolution. There is still, however, room for improvement in the dissolution profile.

Since the dissolution profiles in Figure 5.12 do not appear to reach an equilibrium solubility, additional investigation into the effects that cocrystallization might have on itraconazole solubility was performed using literature data and thermodynamic equations. The effects of itraconazole solid form on equilibrium solubility were studied by Almarsson et al. in 0.1 N HCl medium at 25 °C. The itraconazole equilibrium solubilities, taken as the value where the dissolution profile plateaued, of crystalline itraconazole, itraconazole/L-malic acid cocrystals, and Sporanox® (amorphous) itraconazole were determined to be 0.03 mg/mL, 0.43 mg/mL, and 0.51 mg/mL, respectively (Almarsson et al. 2007). At the equilibrium solubility, the fugacity of itraconazole in the liquid and solid phases is equal,

$$f_{itz}^L = f_{itz}^S \quad (1)$$

The theoretical solubility, or mole fraction of dissolved itraconazole in the liquid phase ( $x_{itz}^L$ ) is,

$$x_{itz}^L = \frac{f_{itz}^S}{\gamma_{itz} f_{itz}^{0L}} \quad (2)$$

where  $f_{itz}^S$  is the fugacity of pure solid itraconazole,  $f_{itz}^{0L}$  is the standard-state fugacity of the pure hypothetical subcooled liquid itraconazole, and  $\gamma_{itz}$  is the liquid phase activity coefficient. The fugacity ratio for pure crystalline itraconazole is given by,

$$\ln \left[ \frac{f_{itz}^{0L}}{f_{itz}^S} \right] = \frac{MW_{itz} \Delta H_{f,itz}}{RT_{m,itz}} \left( \frac{T_{m,itz}}{T} - 1 \right) \quad (3)$$

where  $MW_{itz}$  is the molecular weight of itraconazole,  $T_{m,itz}$  is the melting temperature of itraconazole,  $\Delta H_{f,itz}$  is the enthalpy of melting for itraconazole,  $T$  is the temperature, and  $R$  is the gas constant (Prausnitz et al. 1998). The physical properties of itraconazole, as determined experimentally in subsection 5.4.2, are given in Table 5.4. Using the equilibrium solubility of 0.03 mg/mL ( $x_{itz}^L = 1.55 \times 10^{-6}$ ) as reported by Almarsson et al.,  $\gamma_{itz} = 100$  for a dissolution temperature of 25 °C (298 K). For amorphous itraconazole,  $\gamma_{itz}$  changes less than 0.1% compared to that calculated for crystalline itraconazole on the basis of a simple two-suffix Margules equation (Matteucci et al. 2007).

Table 5.4 Physical properties of itraconazole

$MW_{itz}$ (g/mol)	$T_{m,itz}$ (K)	$\Delta H_{f,itz}$ (J/g)
705.64	442.35	94.5

When engaging in cocrystallization, the physical properties used for calculating the fugacity ratio of itraconazole can be taken as those of the cocrystal, summarized in Table 5.5. The fugacity ratio for itraconazole when it is cocrystallized with L-malic acid was calculated using,

$$\ln \left[ \frac{f_{itz-co}^{0L}}{f_{itz-co}^S} \right] = \frac{MW_{itz} \Delta H_{f,itz/mal}}{RT_{m,itz/mal}} \left( \frac{T_{m,itz/mal}}{T} - 1 \right) \quad (4)$$

where  $MW_{itz}$  is the molecular weight of itraconazole,  $T_{m,itz/mal}$  is the melting temperature of an itraconazole/L-malic acid cocrystal,  $\Delta H_{f,itz/mal}$  is the enthalpy of melting for an itraconazole/L-malic acid cocrystal,  $T$  is the temperature, and  $R$  is the gas constant. Using an equilibrium solubility of 0.43 mg/mL ( $x_{itz}^L = 2.22 \times 10^{-5}$ ),  $\gamma_{itz-co} = 78$  for a dissolution temperature of 25 °C (298 K). From this calculation it is clear that the activity coefficient of itraconazole in the liquid phase changes when the drug is cocrystallized. An area of future exploration, however, will be to determine the validity of applying equation (4) to multicomponent crystals.

Table 5.5 Physical properties of an itraconazole/L-malic acid cocrystal (Almarsson et al. 2007)

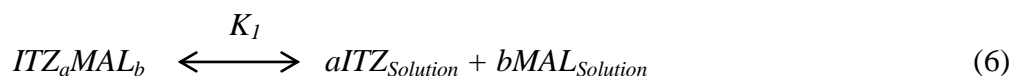
$MW_{itz}$ (g/mol)	$T_{m,itz/mal}$ (K)	$\Delta H_{f,itz/mal}$ (J/g)
705.64	427.51	73.98

The dissolution of itraconazole (*ITZ*) can be described as an equilibrium between the drug in its solid and dissolved forms,





where  $K_0$  is the equilibrium constant. It is based on this equilibrium that the solid-liquid fugacity equality, equation (1), can be applied and the physical properties of the drug used to calculate the liquid phase activity coefficient. Release of itraconazole from a cocrystal into solution, however, is slightly more complex. When the solid cocrystal  $ITZ_aMAL_b$  dissolves, it also dissociates into its constituent components,



such that the solid cocrystal is in equilibrium with both dissolved drug and former. Incorporating this equilibrium into the fugacity relations used to predict solubility will be an area of future work, as outlined in Chapter 8.

## 5.5 Conclusions

In this study, cocrystallization of itraconazole and L-malic acid in CO<sub>2</sub>-expanded THF was investigated as a means of improving itraconazole dissolution. As confirmed by PXRD, both itraconazole and L-malic acid were successfully recrystallized from THF by pressurization with CO<sub>2</sub> with no changes in their respective crystal lattices. Simultaneous dissolution and crystallization of itraconazole and L-malic acid by GAS cocrystallization from THF produced a mixed product of some itraconazole/L-malic acid cocrystals as well as uncocrystallized amorphous components, as determined by HPLC analysis of the itraconazole content. The cocrystals produced by both methods displayed enhanced dissolution compared to the supplier drug, with the cocrystals produced by GAS cocrystallization showing the best dissolution, attributed to the presence of amorphous

itraconazole and an increase in surface area from the particle's microporous structure as observed under SEM.

## Chapter 6

### Formation of Itraconazole–Succinic Acid Cocrystals by Gas Antisolvent Cocrystallization

#### 6.1 Gas Antisolvent Cocrystallization

The commercial adoption of pharmaceutical cocrystalline forms will rely on the development of scalable, environmentally benign processes capable of producing sufficient quantities of cocrystals which conform to the existing standards of purity and reproducibility. Traditional cocrystal production has been accomplished by grinding, neat or solvent facilitated, or solution-based methods which induce supersaturation by cooling, solvent evaporation, or the addition of a liquid antisolvent. The mechanical stress invoked during grinding and associated heat evolution can affect the stability of certain APIs while the large amounts of organic solvent used in solution-based methods are environmentally undesirable. Recently, supercritical CO<sub>2</sub>-based processes, which minimize organic solvent use, have also been used for cocrystal production (Padrela et al. 2009; Padrela et al. 2010; Shikhar et al. 2011; Ober et al. 2012). Cocrystal production by GAS cocrystallization reduces the thermal and mechanical stress applied to the API compared to grinding processes, reduces organic solvent use compared to traditional solution-based methods by replacing the antisolvent with environmentally benign CO<sub>2</sub>, allows facile recycling of the original organic solvent by simple depressurization, and has

the potential to produce cocrystal powders lower in residual solvent compared to solvent evaporative methods.

A number of unique advantages and opportunities exist when using GAS cocrystallization for pharmaceutical cocrystal engineering. The molecular recognition events that occur during cocrystal formation are influenced by and can be manipulated with the environment in which they are occurring. For example, the use of a supercritical enhanced atomization (SEA) process generated a novel theophylline and saccharin cocrystal previously undiscovered through a thermal cocrystal screening method (Lu et al. 2008; Padrela et al. 2010). Furthermore, the influence of operating conditions in CO<sub>2</sub> antisolvent processes on the crystal structure of recrystallized APIs has been well documented (Yeo et al. 2003; Bakhbakhi et al. 2006; Subra-Paternault et al. 2007; Park and Yeo 2008b; Rodrigues et al. 2011; Roy et al. 2011). GAS recrystallization of beclomethasone-17,21-dipropionate from acetone gave a more crystalline product, as indicated by increased peak intensities, compared to GAS recrystallization from methanol or ethanol (Bakhbakhi et al. 2006). Recrystallization of theophylline using both the GAS and SAS techniques resulted in changes in the crystal lattice of the drug, as evidenced by new peaks in the PXRD patterns (Roy et al. 2011). These few examples illustrate the crystal engineering flexibility of GAS cocrystallization and justify further exploration into its potential in developing pharmaceutical cocrystals.

In this study, succinic acid was investigated as an alternative former for enhancing the dissolution of itraconazole through cocrystallization. The lower solubility in THF and relatively higher degree of crystallinity of succinic acid, as compared to L-malic acid, are expected to promote additional crystallization and prevent amorphous

precipitation. Itraconazole and succinic acid were simultaneously dissolved in THF and cocrystallization invoked by pressurization with CO<sub>2</sub>. The itraconazole–succinic acid cocrystals produced by GAS cocrystallization were again compared to those produced using a liquid antisolvent, *n*-heptane. The itraconazole–succinic acid cocrystals produced by each method were characterized by powder X-ray diffraction (PXRD), Fourier transform infrared (FTIR) spectroscopy, high pressure liquid chromatography (HPLC), differential scanning calorimetry (DSC), scanning electron microscopy (SEM), and dissolution studies.

## **6.2 Cocrystal Formation by GAS Cocrystallization**

Itraconazole and succinic acid both exhibit very low solubility in supercritical CO<sub>2</sub>, making CO<sub>2</sub> antisolvent techniques ideal for their crystallization (Al-Marzouqi et al. 2006; Payne and Kerton 2010). The liquid solvent used in this work, THF, is a polar aprotic solvent capable of dissolving both itraconazole and succinic acid and previously shown to facilitate itraconazole–dicarboxylic acid cocrystal formation (Datta and Grant 2004). Itraconazole has been reported to be sparingly soluble in THF, while succinic acid shows high solubility in the solvent (Schütz et al. 1997; Al-Badr and El-Subbagh 2009). Cocrystallization using CO<sub>2</sub>-expanded THF requires that itraconazole and succinic acid crystallize at similar and ideally stoichiometric rates. If the less soluble component, itraconazole, was to crystallize first, then cocrystallization would likely not occur. Since itraconazole and succinic acid solubility are complex functions of CO<sub>2</sub> pressure, solvent expansion, and co-solvent effects in a quaternary component system, the approach taken in this work was to prevent itraconazole recrystallization by providing a stoichiometric

excess of succinic acid. A stoichiometric excess of former has been previously employed in the preparation of itraconazole–dicarboxylic acid cocrystals by liquid antisolvent and thermal crystallization techniques (Remenar et al. 2006; Almarsson et al. 2007).

The proposed cocrystal structure for itraconazole and succinic acid involves the formation of two hydrogen bonds between the triazoles of two itraconazole molecules and the hydroxyl groups of a single succinic acid molecule. This hydrogen bonding scheme allows a single succinic acid molecule to tether two antiparallel oriented itraconazole molecules and thus fill a void space between the molecules, as shown in Figure 5.5. The starting quantities of itraconazole (250 mg) and succinic acid (100 mg) were provided in an approximate stoichiometric ratio of 2:4.8 despite the expected cocrystal stoichiometry of 2:1.

Product yield is an important consideration in crystallization processes. Materials left behind in solution can inhibit solvent recycling and lead to increased costs, especially when working with expensive pharmaceutical compounds. By using excess succinic acid for cocrystal formation the amount of uncocrystallized itraconazole, the more expensive compound, can be minimized. In both types of cocrystallization, liquid and CO<sub>2</sub> antisolvent, crystallization is dictated by supersaturation which is primarily a function of the concentration of material and choice of solvent and antisolvent. In practice, however, the yield is also affected by powder collection from the crystallization beaker or vessel, in which some crystallized material is inevitably left behind. In this work, the liquid antisolvent technique gave a product yield of 69.4% while the CO<sub>2</sub> antisolvent technique gave a product yield of 75.4%. It is expected that both of these yields would increase

upon scale-up, where a smaller percentage of the crystallized material would be left behind.

### **6.3 Characterization of Cocrystallization**

#### **6.3.1 Powder X-ray Diffraction**

The PXRD patterns for itraconazole, succinic acid, a 1:1 by mass physical mixture of the two, and the itraconazole–succinic acid cocrystals produced by liquid antisolvent and GAS cocrystallization are shown in Figure 6.1. Due to the intense crystalline nature of succinic acid, each pattern has been shown on its own scale, but the numerical intensities of each scale are equivalent. Itraconazole exhibited characteristic crystalline peaks at  $2\theta$  values of  $17.0^\circ$ ,  $20.6^\circ$ ,  $21.1^\circ$ ,  $23.9^\circ$ ,  $27.6^\circ$ ,  $29.8^\circ$ , and  $31.8^\circ$ , in correspondence with the literature (Al-Badr and El-Subbagh 2009). Succinic acid exhibited characteristic crystalline peaks at  $2\theta$  values of  $23.3^\circ$ ,  $29.9^\circ$ ,  $30.4^\circ$ ,  $31.2^\circ$ , and  $36.9^\circ$ , also in correspondence with the literature (Krishnan et al. 2007). The physical mixture exhibited crystalline peaks characteristic of both itraconazole and succinic acid. The itraconazole–succinic acid cocrystals produced by both methods exhibited intense crystalline peaks at  $2\theta$  values of  $7.1^\circ$ ,  $10.6^\circ$ ,  $18.9^\circ$ ,  $20.2^\circ$ ,  $21.2^\circ$ ,  $23.4^\circ$ ,  $28.6^\circ$ , and  $31.1^\circ$ .

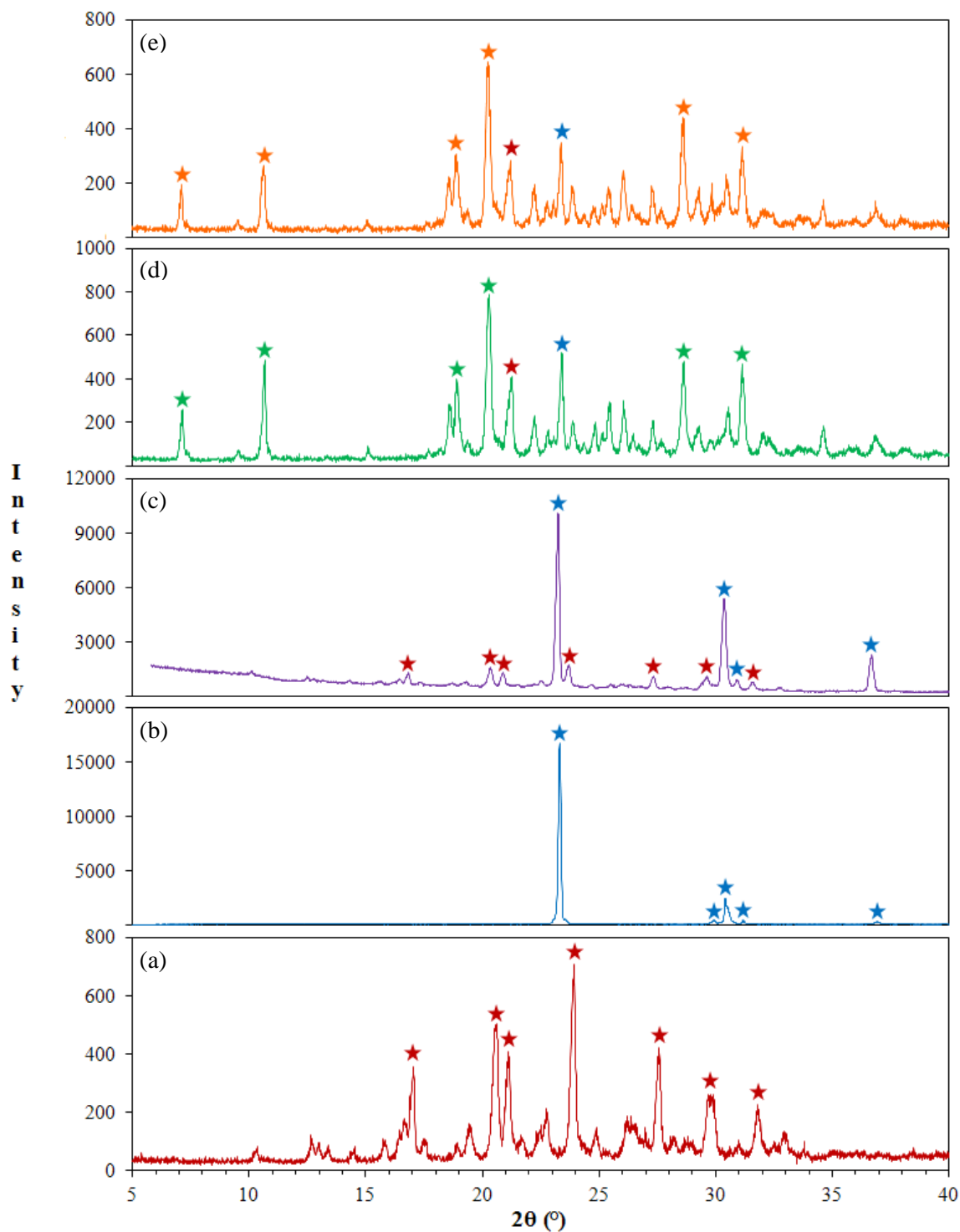


Figure 6.1 PXR D patterns for (a) itraconazole, (b) succinic acid, (c) a 1:1 by mass physical mixture of itraconazole and succinic acid, (d) itraconazole–succinic acid cocrystals from *n*-heptane, and (e) itraconazole–succinic acid cocrystals produced by GAS cocrystallization (★ = characteristic peak)



The PXRD patterns in Figure 6.1 clearly demonstrate the formation of a new phase following simultaneous crystallization of itraconazole and succinic acid using either *n*-heptane or CO<sub>2</sub> as the antisolvent. Cocrystal formation was confirmed by the presence of characteristic itraconazole–succinic acid cocrystal peaks at 7.1°, 10.6°, 18.9°, 20.2°, 28.6°, and 31.1°, according to previous literature (Remenar et al. 2003; Almarsson et al. 2007). The two additional crystalline peaks denoted in the cocrystal patterns correspond to two of the most intensely crystalline peaks of pure itraconazole (21.2°) and pure succinic acid (23.4°). A recent study showed that the intensity of characteristic cocrystal peaks could be used to quantitatively determine the amount of cocrystalline phase in a sample also containing the pure components (Padrela et al. 2012). While quantitative PXRD analysis would be inappropriate without using identical masses of sample, the presence of pure component peaks in the cocrystal patterns indicate that there is likely uncocrystallized components in the final cocrystal products obtained in this work. The degree of crystallinity of the cocrystals, as indicated by peak intensity, was slightly less for the cocrystals crystallized using CO<sub>2</sub> compared to the liquid antisolvent. It is thought that the higher diffusivity of pressurized CO<sub>2</sub>, as compared to *n*-heptane, promotes rapid mass transfer between the solvent and antisolvent phases which facilitates cocrystallization but inhibits crystal lattice organization.

### 6.3.2 Fourier Transform Infrared Spectroscopy

Infrared spectroscopy was conducted to examine the nature of any interactions between itraconazole and succinic acid in the cocrystals. The FTIR spectra for itraconazole, succinic acid, a 1:1 by mass physical mixture of the two, and the

itraconazole–succinic cocrystals formed by liquid antisolvent and GAS cocrystallization are shown in Figure 6.2. The characteristic peaks of itraconazole occurred at 3384, 3126, 3068, 2962, 1699, 1510, and 1450  $\text{cm}^{-1}$ , in correspondence with the literature (Nesseem 2001). The characteristic peaks of succinic acid occurred at 2931, 2650, 1693, 1417, 1311, and 1201  $\text{cm}^{-1}$ , also in correspondence with the literature (Krishnan et al. 2008). Table 6.1 summarizes the vibrational frequencies of relevant hydrogen bonding functional groups in an itraconazole–succinic acid cocrystal. The O–H stretch of succinic acid occurred at 2650  $\text{cm}^{-1}$  for the pure former. The frequency of this stretch was decreased to 2630  $\text{cm}^{-1}$  in the itraconazole–succinic acid cocrystals prepared by each method. The C–N and C=N stretches in itraconazole occurred at 1431 and 1614  $\text{cm}^{-1}$  for the pure drug. The frequency of the C–N stretch for the cocrystals formed by both methods increased to 1437  $\text{cm}^{-1}$  while the frequency of the C=N stretch was unaffected (within the resolution limits of the scan).

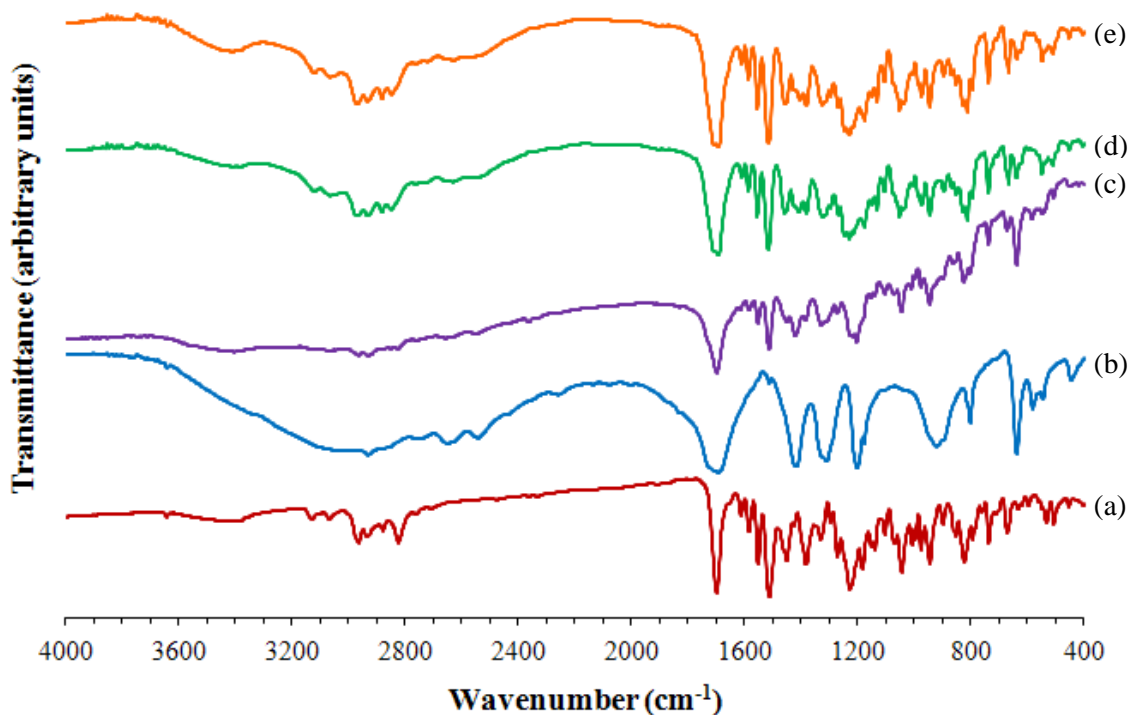


Figure 6.2 FTIR spectra for (a) itraconazole, (b) succinic acid, (c) a 1:1 by mass physical mixture of itraconazole and succinic acid, (d) itraconazole–succinic acid cocrystals from *n*-heptane, and (e) itraconazole–succinic acid cocrystals produced by GAS cocrystallization

Table 6.1 Relevant hydrogen bonding functional groups in an itraconazole–succinic acid cocrystal

Functional Group	Wavenumber (cm <sup>-1</sup> )			
	Itraconazole	Succinic Acid	Cocrystals from <i>n</i> -heptane	Cocrystals by GAS cocrystallization
O–H stretch	--	2650	2630	2630
C–N stretch	1431	--	1437	1437
C=N stretch	1614	--	1610	1612

Despite incomplete crystal lattice organization, it appears that the expected trimeric 2:1 itraconazole–succinic acid cocrystal structure has been obtained using both

cocrystal preparation techniques. The transition of the O–H stretch of succinic acid from  $2650\text{ cm}^{-1}$  to  $2630\text{ cm}^{-1}$  suggests that this group is participating in a strong hydrogen bond in the cocrystal structure. A similar decrease was observed for the O–H stretching frequency of the carboxylic acid group of indomethacin which is thought to participate in hydrogen bonding with saccharin to form the indomethacin–saccharin cocrystal (Basavoju et al. 2008). Although the C–N and C=N groups of itraconazole are likely participating in a hydrogen bond with succinic acid, their vibrational frequencies are less affected by the interaction due to their aromatic impaired flexibility. For the itraconazole–succinic acid cocrystal, it appears that the use of compressed  $\text{CO}_2$  has not resulted in the formation of any unique hydrogen bond interactions but has given the same cocrystal obtainable by a traditional liquid antisolvent technique.

### 6.3.3 Compositional Analysis

The composition of the cocrystal powder produced by each method was determined by HPLC. The powder produced using *n*-heptane was found to contain 71.4% itraconazole by mass, or a 2:4.8 molar ratio of drug to former, while the powder produced using  $\text{CO}_2$  as the antisolvent was found to contain 65.5% itraconazole by mass, or a 2:6.2 molar ratio. Considering that the cocrystal structure has a 2:1 itraconazole to succinic acid molar ratio, these ratios indicate the presence of excess uncocrystallized material in the final cocrystal powder. Without a reliable method to differentiate uncocrystallized itraconazole and succinic acid from cocrystallized, we cannot say with certainty which method, if either, leads to a greater fraction of cocrystals in the final product. It is thought, however, that the method of cocrystal preparation may play a role in

determining the composition of the final cocrystal powder. For example, when using a liquid antisolvent technique unprecipitated components remain in solution and are discarded following centrifugation. When the liquid solvent is removed by flushing with supercritical CO<sub>2</sub>, the remaining solvent becomes supersaturated with the unprecipitated component(s) causing either additional cocrystallization or possibly recrystallization of the pure drug and/or former which subsequently become part of the final cocrystal product. These differences in solvent removal also rationalize why higher yields may be achieved with the CO<sub>2</sub> antisolvent technique, and provide a basis for future studies examining the optimal amount of former to direct cocrystallization while maximizing cocrystal product purity in GAS cocrystallization (Appendix B).

The RSD of the itraconazole content in the cocrystal powder produced using *n*-heptane was 2.7% while that of the powder produced using CO<sub>2</sub> was 4.9%. Both methods are capable of producing drug powders which conform to the FDA standard for drug content homogeneity, less than 6.0% RSD (Rohrs et al. 2006). The RSDs show that despite the likely presence of uncocrystallized materials in the final cocrystal powder, there are not significant regions of heterogeneity.

#### 6.3.4 Differential Scanning Calorimetry

The thermal behavior of the pure components, several physical mixtures of varying compositions, and cocrystals were studied by DSC. The DSC thermographs for itraconazole, succinic acid, and the itraconazole–succinic acid cocrystals formed by liquid antisolvent using *n*-heptane and GAS cocrystallization are shown in Figure 6.3. Itraconazole exhibited a well-defined melting endotherm at 169.4 °C ( $\Delta H_f = 85.3$  J/g).

Succinic acid also showed a defined melting point at 191.3 °C ( $\Delta H_f = 168.0$  J/g), but underwent decomposition above 200° C. The itraconazole–succinic acid cocrystals formed by liquid antisolvent and GAS cocrystallization showed broad endothermic events between 145 °C and 165 °C.

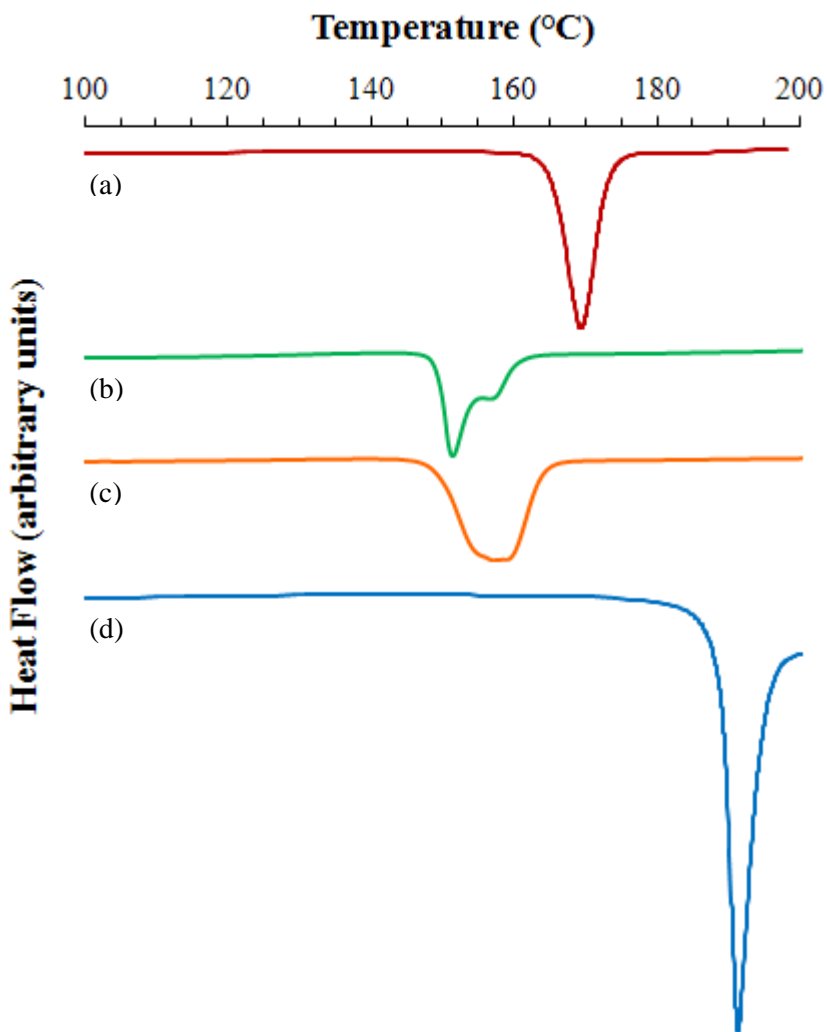


Figure 6.3 DSC thermographs (from top to bottom) for (a) itraconazole, (b) itraconazole–succinic acid cocrystals from *n*-heptane, (c) itraconazole–succinic acid cocrystals formed by GAS cocrystallization, and (d) succinic acid

To interpret the thermal behavior of the cocrystal systems, a number of physical mixtures of itraconazole and succinic acid were prepared by simple spatula mixing and analyzed by DSC. A summary of the compositions prepared, characterized by their mole fraction of itraconazole, is given in Table 6.2. The DSC thermographs for each of the physical mixtures as well as those for itraconazole and succinic acid are presented in Figure 6.4. The 0.67 itraconazole mole fraction physical mixture, which corresponds to the well known 2:1 stoichiometry for an itraconazole–succinic acid cocrystal, exhibited an endothermic melting point at 162.1 °C, corresponding to the melting point reported in the literature (160.3 °C) for an itraconazole–succinic acid cocrystal (Almarsson et al. 2007). Therefore, it appears that itraconazole–succinic acid cocrystal formation is achievable by heating stoichiometric amounts of drug and former. While there may also be some cocrystal formation for a physical mixture of 0.46 itraconazole mole fraction, as the mole fraction of itraconazole is decreased the mixture melting point shifts to a lower temperature. As is most pronounced for the 0.14 itraconazole mole fraction mixture, a eutectic melting point for the binary mixture of itraconazole and succinic acid occurs at 150.2 °C. The eutectic melt is then followed by melting of excess pure succinic acid as the mole fraction of succinic acid is increased. Nearly identical thermal behavior has been observed for a physical mixture of urea and sulfamethazine which also forms a eutectic but does not cocrystallize upon heating (Lu et al. 2008).

Table 6.2 Physical mixtures of itraconazole and succinic acid for DSC analysis

Mass of itraconazole	Mass of succinic acid	Mole fraction itraconazole ( $x_{itz}$ )	Mole fraction succinic acid ( $x_{succ}$ )
282 mg	23.6 mg	0.67	0.33
500 mg	100 mg	0.46	0.54
250 mg	100 mg	0.30	0.70
100 mg	100 mg	0.14	0.86
100 mg	250 mg	0.06	0.94

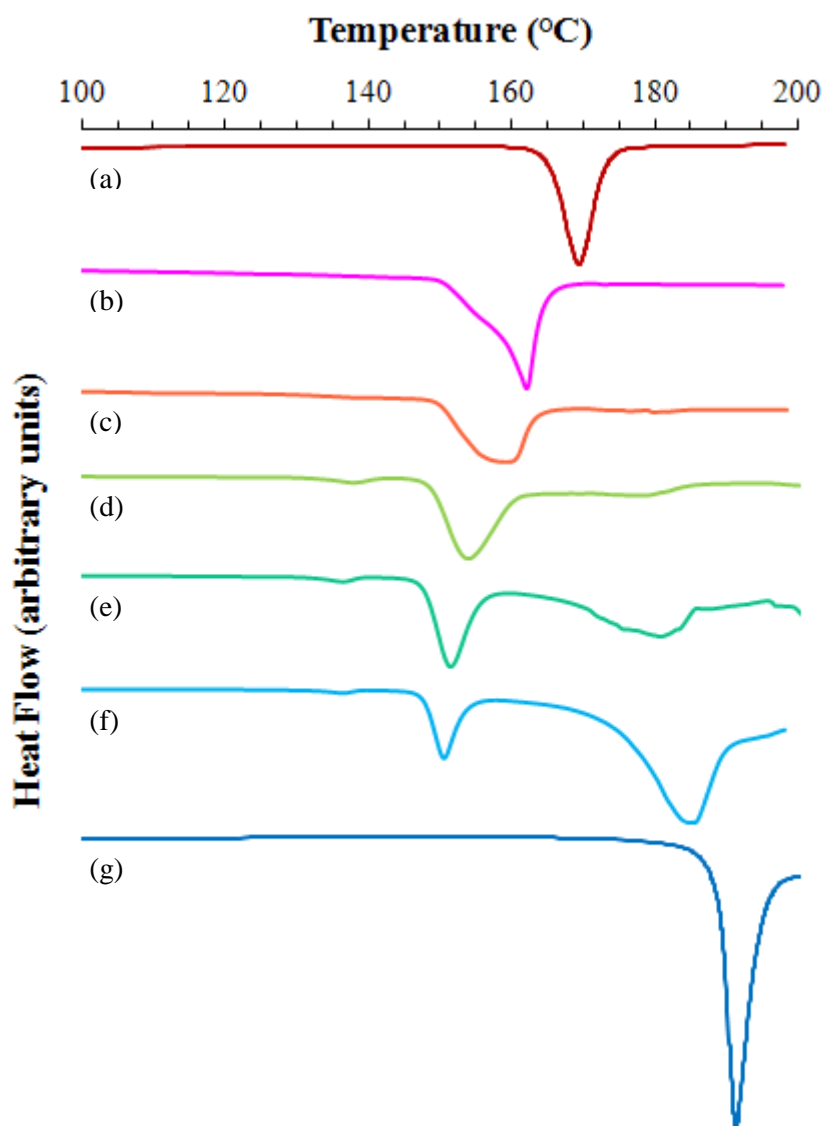


Figure 6.4 DSC thermographs (from top to bottom) for (a) itraconazole, physical mixtures of itraconazole and succinic acid with itraconazole mole fractions ( $x_{itz}$ ) of (b) 0.67, (c) 0.46, (d) 0.30, (e) 0.14, and (f) 0.06, and (g) succinic acid



By studying the thermal behaviors of a number of physical mixtures of itraconazole and succinic acid, insight into the cocrystal thermal behaviors observed in Figure 6.3 was gained. The cocrystals produced by liquid antisolvent using *n*-heptane display a clear eutectic melting point at 151.3 °C followed by some cocrystal melting closer to 160 °C. The eutectic melting results from the presence of pure uncocrystallized components. The itraconazole–succinic acid cocrystals produced by GAS cocrystallization demonstrate less eutectic melting, but more cocrystal melting as compared to those produced by the liquid antisolvent technique. Considering that both techniques began with identical amounts of itraconazole and succinic acid, the DSC results show that GAS cocrystallization produces a cocrystal product with a qualitatively greater fraction of cocrystals. From these results it appears that during removal of the liquid solvent with supercritical CO<sub>2</sub>, supersaturation may be promoting additional cocrystallization, and therefore maximizing the yield of cocrystals.

## **6.4 Dissolution Enhancement by GAS Cocrystallization**

### **6.4.1 Scanning Electron Microscopy**

SEM images of the pure components and cocrystals are shown in Figure 6.5. Itraconazole, as obtained from the supplier, featured rod-like structures and smaller particles with average sizes ranging from 2 to 20 μm, as shown in Figure 6.5a. Succinic acid, as obtained from the supplier, featured smooth semi-spherical particles with average sizes ranging from 50 μm to several hundred microns, as shown in Figure 6.5b. The itraconazole–succinic acid cocrystals formed by the liquid antisolvent technique with *n*-heptane were thin flakey structures, as shown in Figure 6.5c. Some of the flakes featured

a hexagonal shape while others had less defined edges and a more irregular shape. Slow growth of itraconazole–succinic acid single cocrystals from a 10/2/1 1,2-dichloroethane/ethyl acetate/1,4-dioxane solution also produced hexagonal plates (Remenar et al. 2003). Spherical agglomerates of radiating plates were also evident. Cocrystallization using CO<sub>2</sub> as the antisolvent gave thin irregularly shaped flakes, as shown in Figure 6.5d. Many of these flakes were oriented in rosette structures, with flattened radial agglomeration around a focal point.

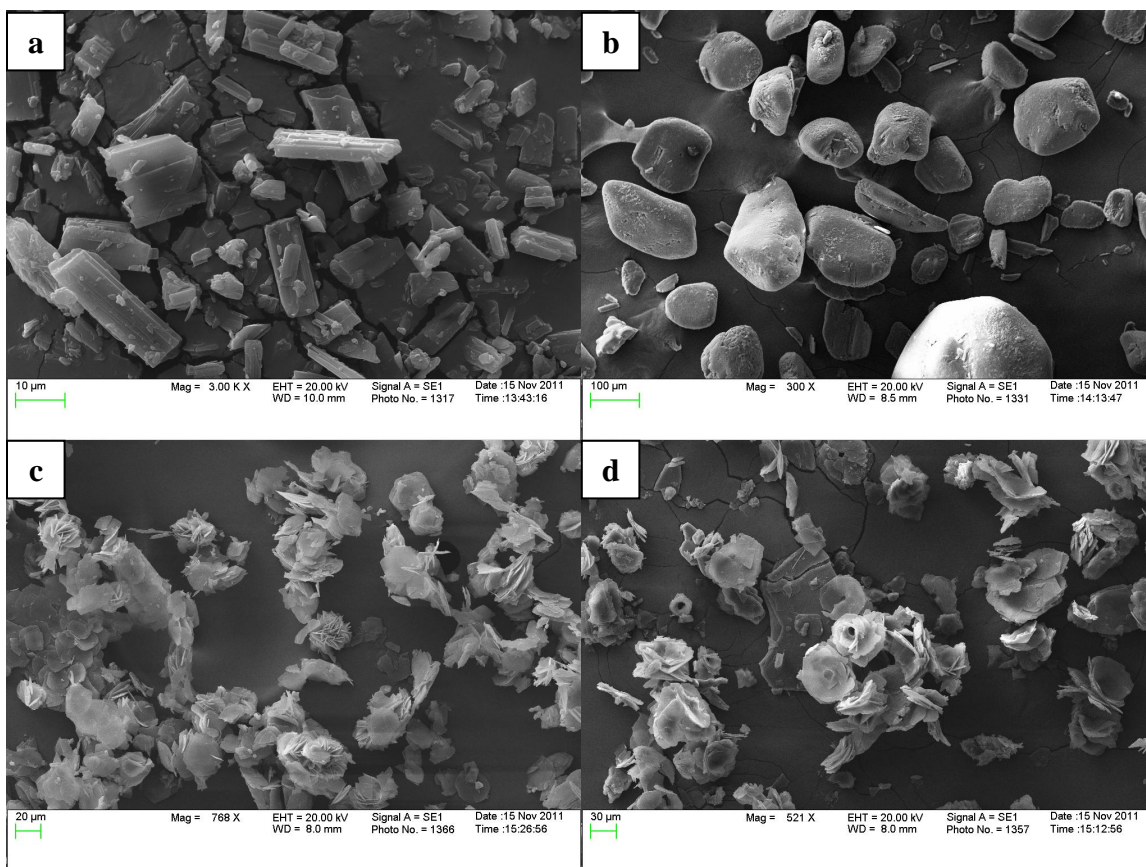


Figure 6.5 SEM images of (a) itraconazole, (b) succinic acid, (c) itraconazole–succinic acid cocrystals formed by liquid antisolvent (*n*-heptane), and (d) itraconazole–succinic acid cocrystals formed by GAS cocrystallization

#### 6.4.2 Dissolution Studies

Dissolution studies were conducted to assess the potential clinical relevance of an itraconazole–succinic acid cocrystal and to determine how differences in the extent of cocrystallization and particle agglomeration (i.e. spherulites vs. rosettes) resulting from the different methods of cocrystal preparation might affect clinically relevant drug properties such as dissolution rate. The dissolution profiles for itraconazole, a 1:1 by mass physical mixture of itraconazole and succinic acid, and the itraconazole–succinic acid cocrystals formed by liquid and CO<sub>2</sub> antisolvent are shown in Figure 6.6. Itraconazole, despite being purchased in micronized form, exhibited poor dissolution achieving less than 30% release in 2 hours. The dissolution profile of the physical mixture is nearly an upward linear shift of the pure itraconazole dissolution profile. This shift is likely caused by a decrease in itraconazole particle size from grinding the itraconazole and succinic acid together with a mortar and pestle to create the mixture. The itraconazole–succinic acid cocrystals prepared by both methods show significantly faster dissolution than the physical mixture, thereby demonstrating their clinical relevance for potentially improving itraconazole bioavailability. The itraconazole–succinic acid cocrystals produced using CO<sub>2</sub> as an antisolvent have the fastest release profile, achieving 92% release in 2 hours. The itraconazole–succinic acid cocrystals produced using *n*-heptane have significantly slower release, achieving only 50% release in 2 hours.

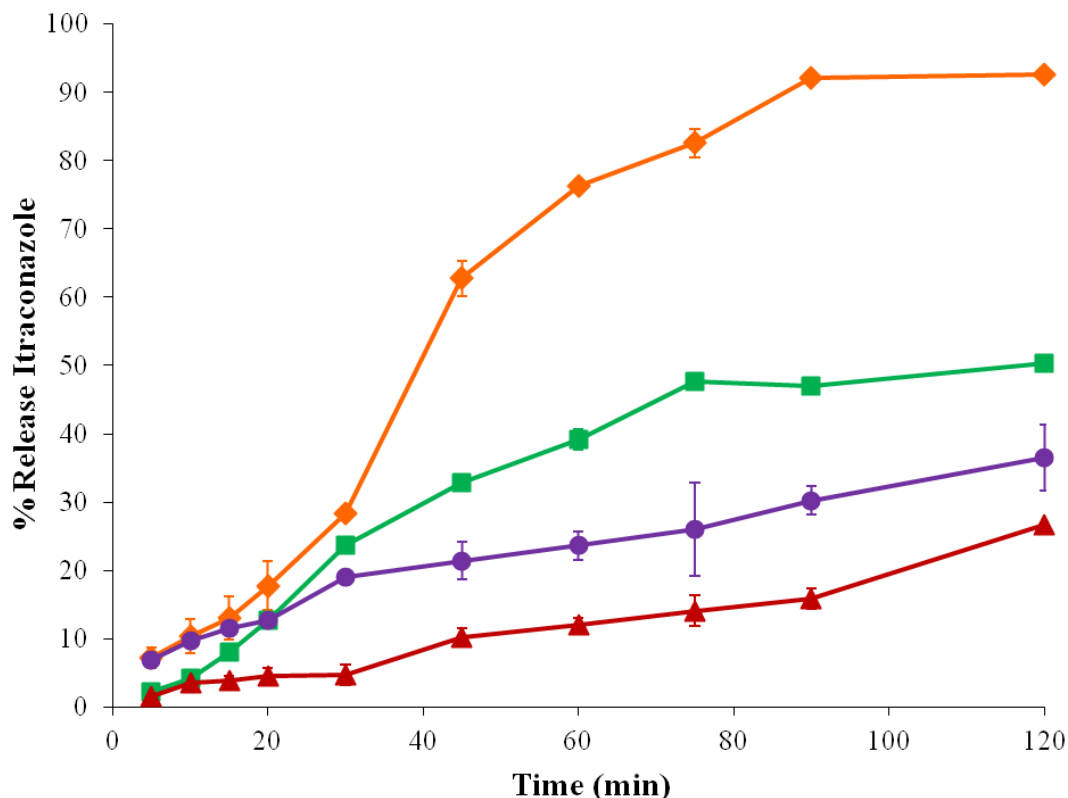


Figure 6.6 Dissolution profiles for itraconazole (▲), a 1:1 by mass physical mixture of itraconazole and succinic acid (●), itraconazole–succinic acid cocrystals produced from *n*-heptane (■), and itraconazole–succinic acid cocrystals formed by GAS cocrystallization (◆)

Despite the cocrystals produced by each method having similar crystal and chemical structures as determined by PXRD and FTIR, it appears that morphological and compositional differences resulting from the method of preparation can have a strong effect on drug dissolution. Both methods of cocrystal preparation gave thin flakes, a morphology previously observed in itraconazole crystallization (Sathigari et al. 2011). The flakes, characterized by a length, width, and height, cannot be sized by conventional means (light scattering) and determining a particle size distribution would have little value. Furthermore, since the particles are not submicron, particle size is not expected to

have a significant influence on the dissolution rate. Based on a prior publication (Sathigari et al. 2011) in which the specific surface area of  $\sim 20 \times 5 \times 1$  ( $l \times w \times h$ )  $\mu\text{m}$  itraconazole flakes was determined, it is expected that the cocrystal products produced by both methods would have nearly identical specific surface areas of  $\sim 2 \text{ m}^2/\text{g}$ . Therefore, it is not expected that particle size or surface area is responsible for the enhanced dissolution of the itraconazole–succinic acid cocrystals produced by GAS cocrystallization.

While primary particle size and shape was similar for both methods of cocrystal preparation, agglomeration tendencies differed with respect to the antisolvent employed. The spherulite structures obtained during liquid antisolvent cocrystallization (Figure 6.5c) were nearly identical to those obtained in the literature for antisolvent crystallization of theophylline (Subra et al. 2005). The formation of such agglomerates was attributed to the existence of two phases of solvent and antisolvent with crystallization occurring in discrete antisolvent droplets. It is suspected that the spherulite structures formed using the liquid antisolvent process actually inhibit itraconazole dissolution by blocking aqueous permeation to the center of the particle through the formation of a surface tension “skin” between adjacent radiating plates. The rosette structures observed when using  $\text{CO}_2$  as an antisolvent (Figure 6.5d) are thought to result from initial flake nucleation followed by subsequent flake attachment. Rosettes have been known to possess improved flowability, a property critical for effective tableting of pharmaceuticals, over other types of particle morphologies such as needles (Booij and Lefferts 2005). It also appears that the open central cavity of the rosette structures facilitates dissolution by allowing increased water permeation. These results suggest that cocrystal morphology, which can be altered by the

method of preparation and within a preparation method (i.e. CO<sub>2</sub> antisolvent) by such factors as the pressure profile, can have a dramatic effect on drug dissolution.

The dissolution of itraconazole is pH dependent, especially around a pH of 1.0 due to itraconazole's second pK<sub>a</sub> of ~1.5. While the amount of succinic acid used, ≤ 5 mg in 450 mL of dissolution medium, is not enough to affect the solution pH, the effect of uncocrystallized components on itraconazole dissolution is worth considering. From the DSC results it was determined that the cocrystal product produced using the liquid antisolvent technique contained uncocrystallized itraconazole and succinic acid which underwent eutectic melting similar to the physical mixture. While eutectic melting also occurred for the cocrystal product formed by GAS cocrystallization, it was to a lesser extent likely due to lesser quantities of uncocrystallized components present. Therefore, it is suspected that the dissolution profile of the cocrystals produced by liquid antisolvent represents the dissolution of some cocrystallized itraconazole and some uncocrystallized itraconazole, while the dissolution profile for the cocrystals produced by CO<sub>2</sub> antisolvent represents the dissolution of itraconazole–succinic acid cocrystals with a significantly lesser amount of uncocrystallized itraconazole. Future studies will seek to quantify the amounts of cocrystallized and uncocrystallized itraconazole in a mixed product and work to maximize cocrystallization.

#### 6.4.3 Stability Studies

The dissolution benefits of a cocrystal are only realizable if the cocrystal structure is stable. Thermal stress is commonly used for accelerated stability studies, whereby correlation with an Arrhenius equation can predict the chemical and physical stability of

a formulation during shelf storage at ambient conditions. For this study, the cocrystals were stored at 90 °C with no humidity (dry) for 7, 14, and 28 days and changes in crystallinity assessed by PXRD. The effects of thermal stress on the crystallinity of the itraconazole–succinic acid cocrystals produced by liquid antisolvent and GAS cocrystallization are shown in Figures 6.7 and 6.8, respectively. There were no new peaks, no peak shifts, and no polymorphic transformations observed in any of the samples. Most notably, the cocrystals produced by both methods maintained their structures and did not convert back to the free drug and former.

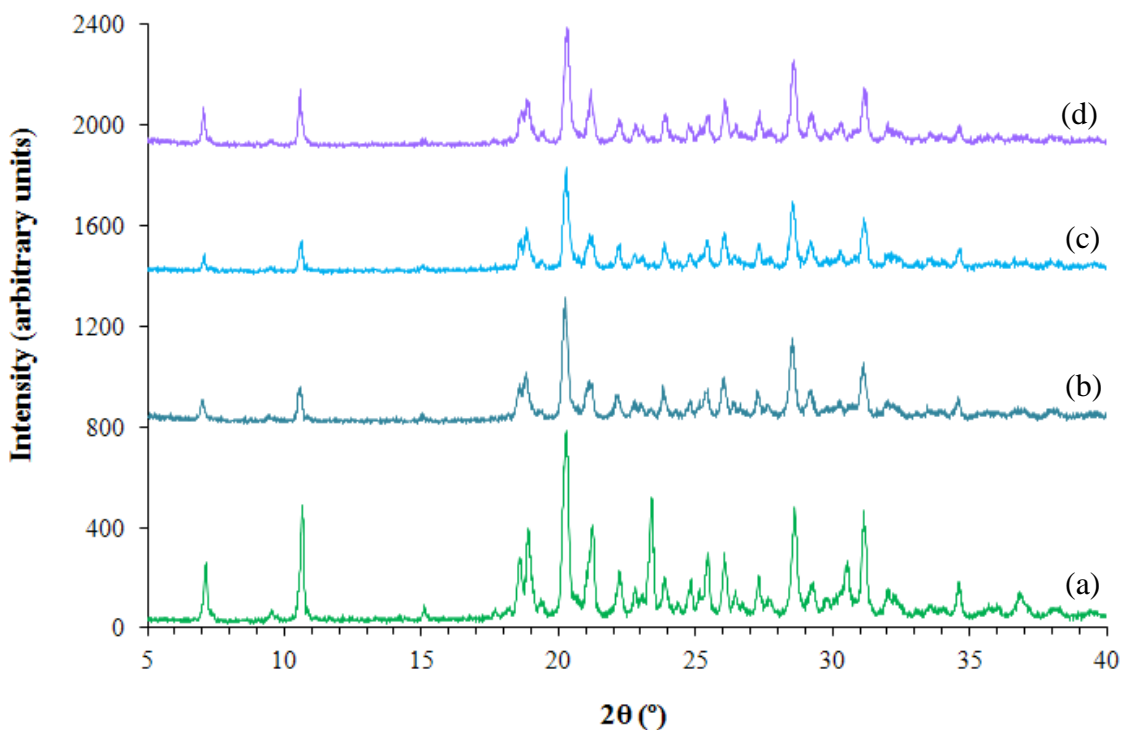


Figure 6.7 PXRD patterns for itraconazole–succinic acid cocrystals formed by liquid antisolvent using *n*-heptane after (a) 0 days at 90 °C, (b) 7 days at 90 °C, (c) 14 days at 90 °C, and (d) 28 days at 90 °C

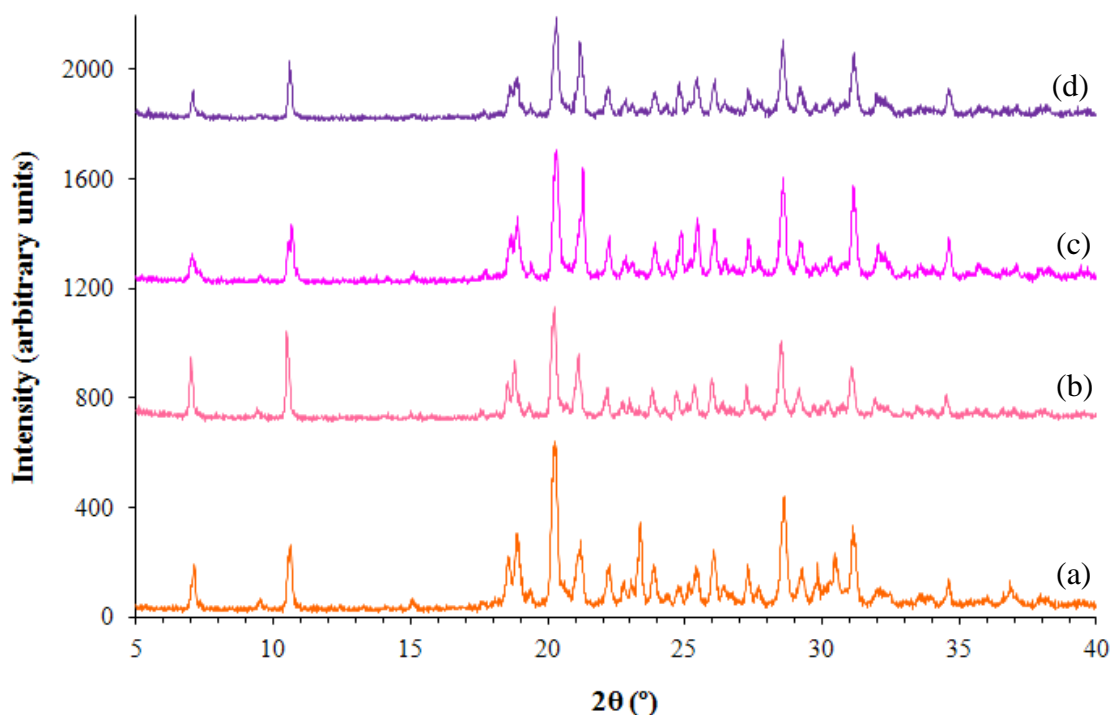


Figure 6.8 PXR D patterns for itraconazole–succinic acid cocrystals formed by GAS cocrystallization after (a) 0 days at 90 °C, (b) 7 days at 90 °C, (c) 14 days at 90 °C, and (d) 28 days at 90 °C

While the temperature used for the stability studies (90 °C) is significantly below the eutectic and cocrystal melting points, it was selected based on previous literature studying the stability of itraconazole formulations (Sanganwar and Gupta 2008) and is sufficiently above those encountered during pharmaceutical manufacturing processes such as milling or tableting. Cocrystal dissociation and molecular demixing in the solid state was previously observed for a 1:1 caffeine–theophylline cocrystal at a temperature below its eutectic melting point (201 °C). In this study, PXR D analysis revealed a transformation from the cocrystal PXR D pattern to that of the two pure components after heating to 170 °C (Eddleston et al. 2012).



Decreases in crystallinity, signified by decreases in peak intensity, were noticeable in all thermally treated samples, but there was not a definitive correlation between the duration of thermal exposure and the decrease in crystallinity. It is thought that an increase in thermal energy may cause some fraction of the cocrystal's hydrogen bonds to break, due to temperature-dependent proton disorder (Parkin et al. 2007), leading to a less crystalline structure. Nonetheless, the dissolution rate enhancement of the itraconazole–succinic acid cocrystals produced by GAS cocrystallization is expected to be preserved during shelf storage due to maintenance of the cocrystal structure under thermal stress as shown in Figure 6.8.

## 6.5 Conclusions

The feasibility of GAS cocrystallization for producing itraconazole–succinic acid cocrystals from THF was compared to a traditional liquid antisolvent process using *n*-heptane. Itraconazole–succinic acid cocrystals of similar crystallinity and chemical structure were produced by both methods. While PXRD and FTIR analysis support previous literature findings of a 2:1 itraconazole to succinic acid trimeric cocrystal structure formed by hydrogen bonding between the triazoles of 2 itraconazole molecules and the hydroxyl groups of a single succinic acid molecule, compositional analysis and DSC have revealed the presence of some fraction of uncocrystallized components which undergo eutectic melting when heated. The itraconazole–succinic acid cocrystals produced by both methods appear to have potential clinical relevance, with the cocrystals formed by GAS cocrystallization achieving over 90% dissolution in less than 2 hours. Furthermore, the cocrystals appeared stable against dissociation under accelerated

stability conditions for up to 4 weeks, suffering only moderate decreases in crystallinity thought to be attributed to the energetic breaking of some fraction of the cocrystal's hydrogen bonds. Through the preparation of itraconazole–succinic acid cocrystals, this work has shown the potential for inexpensive and environmentally benign CO<sub>2</sub> to replace traditional liquid antisolvents, offering advantages for cocrystal production scale-up.

## Chapter 7

### Conclusions

Through the development of two novel single-step processes which exploit the tunable solvent power of CO<sub>2</sub>-based solvent systems, this work has enhanced the deliverability and dissolution of two poorly water-soluble APIs, rifampicin and itraconazole. In a technique termed supercritical antisolvent-drug excipient mixing (SAS-DEM), drug crystallization in the presence of fluidized excipient particles was shown to curb particle growth, prevent drug particle agglomeration, and create homogenous drug/excipient mixtures, all in a single-step. Decreases in the solvating power of the liquid organic solvent THF by pressurization with CO<sub>2</sub> was shown to facilitate itraconazole–dicarboxylic acid cocrystal formation in a technique termed gas antisolvent (GAS) cocrystallization. In addition to enhancing poorly water-soluble drug deliverability and dissolution and reducing organic solvent use in favor of environmentally benign CO<sub>2</sub>, the SAS-DEM process was found more effective at cohesive particle deagglomeration than physical mixing, while GAS cocrystallization allowed for homogeneous crystal nucleation not achievable with traditional crystallization techniques.

The aqueous solubility of rifampicin was enhanced by SAS crystallization from methanol, which caused a change in the crystalline form of the drug from form I to rifampicin dihydrate, as determined by PXRD. Operating at conditions below the MCP, the growth of the recrystallized rifampicin dihydrate microflakes was limited when

crystallization was conducted in the presence of  $\alpha$ -lactose monohydrate particles, creating rifampicin microparticles of a size suitable for efficient delivery to the alveolar macrophages. Characterization of the rifampicin/lactose microparticle composites by PXRD, DSC, and FTIR showed that physical mixtures of the drug and excipient, with excellent drug content homogeneity, were obtained by the SAS-DEM process.

The dissolution rate of itraconazole was enhanced by increasing the specific surface area through SAS crystallization of itraconazole microflakes from DCM. Crystallization in the presence of excipient lactose particles was found more effective at deagglomerating the microflakes and enhancing the dissolution rate than physically mixing the microflakes with lactose, for comparable drug loadings. At high drug loadings, steric stabilization using Pluronic F-127 was found more effective at enhancing dissolution than electrostatic stabilization using SDS, although the ineffectiveness of SDS may be due to changes in supersaturation caused by the addition of methanol. Pluronic F-127 did not effect the crystallinity of itraconazole, as verified by PXRD, but is thought to associate on the surface, thus improving the drug's wettability.

Characterization by PXRD showed that individual dissolution and GAS crystallization of itraconazole and L-malic acid from THF had no effect on the drug or former's crystal lattice. GAS cocrystallization of itraconazole and L-malic acid produced a primarily amorphous product, indicating some interaction of the two components in solution. The inability of this system to form a crystalline structure under the GAS cocrystallization conditions investigated is attributed to the high solubility of L-malic acid in THF. Alternatively, GAS cocrystallization of itraconazole with succinic acid from THF gave a thermally stable, crystalline product which featured rapid dissolution.

Characterization by DSC revealed the presence of an itraconazole/succinic acid eutectic, and pointed towards a greater extent of cocrystallization for the itraconazole–succinic acid cocrystals produced by GAS cocrystallization as compared to those produced using *n*-heptane as the antisolvent.

Some general observations regarding the effectiveness of particle engineering, excipient mixing, stabilization, and solid form selection for formulation enhancement can be drawn from this work. The rapid kinetics of mass transfer, homogeneity of crystal nucleation, and effective removal of solvent make CO<sub>2</sub> antisolvent techniques such as SAS and GAS ideal for the particle size reduction of drug molecules insoluble in compressed CO<sub>2</sub>. Simultaneous crystallization in the presence of excipients offered formulation enhancements over traditional drug/excipient physical mixing. While excipient mixing and chemical stabilization were both effective in overcoming particle cohesiveness, the two approaches displayed only minimal synergism. When enhancing dissolution through changes in the solid form or crystal structure of a molecule, a quantitative characterization of the relative amounts of each possible phase and their stability is necessary to ensure reproducible performance.

Areas of future exploration stemming from this body of work include the application of thermodynamic models to predict solute crystallization and cocrystal dissolution and investigation into novel cocrystalline forms such as particulates with monolayer cocrystal coverage and ternary cocrystal lattices (A<sub>a</sub>B<sub>b</sub>C<sub>c</sub>), as discussed in Chapter 8.

## Chapter 8

### Future Directions

As alluded to throughout this dissertation, there are a number of areas of future exploration stemming from this work. Two areas already mentioned are the thermodynamic modeling of GAS cocrystallization and prediction of cocrystal solubility based on physical parameters of the cocrystal. Two additional future directions are the development of immediate release formulations through monolayer cocrystal formation by sequential GAS crystallization and the investigation of thermodynamically stable ternary cocrystal lattices ( $A_aB_bC_c$ ) which utilize the physical property enhancements of multiple formers through competitive cocrystallization. The following paragraphs will briefly describe these four areas of future exploration.

As outlined extensively in Appendix B, the development of a thermodynamically rigorous model for predicting the pressure-dependent solubilities of drug and former in a  $\text{CO}_2$ -expanded liquid will be a critical component of moving forward with the GAS cocrystallization technique. Not only will the development of such a model allow calculation of the initial amounts of drug and former needed for stoichiometrically matching their rates of crystallization, but it will also maximize cocrystal formation and minimize excess pure component impurities. Thermodynamic modeling is also expected to reduce screening by providing an efficient means for choosing an appropriate former, solvent, and set of operating conditions.

As discussed in Chapter 5, the dissociation of a cocrystal during dissolution prevents application of the solid-liquid equilibrium fugacity relation for calculating solubility. While the physical properties of a cocrystal are readily obtainable, a fundamental relation for determining solubility is needed. It is postulated that the dissociation constant ( $K_1$ ), in combination with the solid ( $f^S_{cocrystal}$ ) and liquid ( $f^L_{cocrystal}$ ) fugacities and physical properties of the cocrystal may provide a means for determining solubility, but additional investigation is needed.

The deposition of itraconazole on the surface of larger excipient particles has been proven effective for creating immediate release formulations of the drug. For example, Sporanox® capsules coat amorphous itraconazole on ~0.5 mm sucrose spheres, while the formulations explored in Chapter 4 deposited crystalline itraconazole microflakes on ~100  $\mu\text{m}$  lactose particles. An area of future exploration could be the development of immediate release itraconazole formulations through surface cocrystallization by sequential GAS crystallization. Through an understanding of pressure dependent drug and former solubilities in a GXL system, the crystallization of former particles and sequential crystallization of drug could promote cocrystal formation at the surface of the already crystallized former particles. It is postulated that by engaging only the surface molecules of the former particles in cocrystallization, a monolayer of itraconazole cocrystals, which would display extremely rapid release, could be formed.

Cocrystallization has been shown to improve a number of drug properties including solubility, stability, and mechanical properties. For some drugs, more than one of these properties can be improved depending on the choice of former. For example, cocrystallization of theophylline with oxalic acid improved the drug's physical stability

by avoidance of hydrate formation while cocrystallization with nicotinamide improved the drug's solubility but increased hygroscopicity. A future direction for pharmaceutical cocrystallization may be the incorporation of multiple formers in a single crystal lattice to simultaneously improve multiple drug properties. Competitive cocrystallization resulting from the introduction of multiple formers should lead to the formation of the thermodynamically most stable cocrystalline structure, whether that structure involves only one or multiple formers. It is suspected that for drugs which form similar cocrystal structures with different formers, such as the trimeric structures formed between itraconazole and dicarboxylic acid formers, that the formation of ternary cocrystal lattices ( $A_aB_bC_c$ ) which exploit the physical property enhancements of multiple formers is possible.



## References

- Aakeröy, C. B. and D. J. Salmon. 2005. Building co-crystals with molecular sense and supramolecular sensibility. *CrystEngComm* 7(72): 439-448.
- Aakeröy, C. B., N. Schultheiss, J. Desper, and C. Moore. 2006. Balancing intermolecular hydrogen-bond interactions for the directed assembly of binary 1:1 co-crystals. *New Journal of Chemistry* 30(10): 1452-1460.
- Agrawal, S., Y. Ashokraj, P. V. Bharatam, O. Pillai, R. Panchagnula. 2004. Solid-state characterization of rifampicin samples and its biopharmaceutic relevance. *European Journal of Pharmaceutical Sciences* 22(2-3): 127-144.
- Aher, S., R. Dhumal, K. Mahadik, A. Paradkar, and P. York. 2010. Ultrasound assisted cocrystallization from solution (USSC) containing a non-congruently soluble cocrystal component pair: Caffeine/maleic acid. *European Journal of Pharmaceutical Sciences* 41(5): 597-602.
- Al-Badr, A. A. and H. I. El-Subbagh. 2009. Itraconazole: Comprehensive profile. *Profiles of Drug Substances, Excipients and Related Methodology* 34: 193-264.
- Alhalaweh, A. and S. P. Velaga. 2010. Formation of cocrystals from stoichiometric solutions of incongruently saturating systems by spray drying. *Crystal Growth & Design* 10(8): 3302-3305.
- Almarsson, Ö., M. B. Hickey, M. L. Peterson, M. J. Zaworotko, B. Moulton, and N. Rodríguez-Hornedo. 2007. Pharmaceutical co-crystal compositions. US Patent 7,927,613.
- Al-Marzouqi, A. H., I. Shehatta, B. Jobe, and A. Dowaidar. 2006. Phase solubility and inclusion complex of itraconazole with  $\beta$ -cyclodextrin using supercritical carbon dioxide. *Journal of Pharmaceutical Sciences* 95(2): 292-304.
- Ansel, H. C., L. V. Allen Jr., and N. G. Popovich. 1999. Pharmaceutical Dosage Forms and Drug Delivery Systems, 7th Ed. Baltimore: Lippincott Williams & Wilkins.
- Babu, N. J. and A. Nangia. 2011. Solubility advantage of amorphous drugs and pharmaceutical cocrystals. *Crystal Growth & Design* 11(7): 2662-2679.

- Bakhbakhi, Y., P. A. Charpentier, and S. Rohani. 2006. Experimental study of the GAS process for producing microparticles of beclomethasone-17,21-dipropionate suitable for pulmonary delivery. *International Journal of Pharmaceutics* 309(1-2): 71-80.
- Banerjee, R., P. M. Bhatt, N. V. Ravindra, and G. R. Desiraju. 2005. Saccharin salts of active pharmaceutical ingredients, their crystal structures, and increased water solubilities. *Crystal Growth & Design* 5(6): 2299-2309.
- Barrett, A. M., F. Dehghani, and N. R. Foster. 2008. Increasing the dissolution rate of itraconazole processed by gas antisolvent techniques using polyethylene glycol as a carrier. *Pharmaceutical Research* 25(6): 1274-1289.
- Basavoju, S., D. Boström, and S. P. Velaga. 2006. Pharmaceutical cocrystal and salts of norfloxacin. *Crystal Growth & Design* 6(12): 2699-2708.
- Basavoju, S., D. Boström, and S. P. Velaga. 2008. Indomethacin–saccharin cocrystal: Design, synthesis and preliminary pharmaceutical characterization. *Pharmaceutical Research* 25(3): 530-541.
- Bauer, J., S. Spanton, R. Henry, J. Quick, W. Dziki, W. Porter, and J. Morris. 2001. Ritonavir: An extraordinary example of conformational polymorphism. *Pharmaceutical Research* 18(6): 859-866.
- Becker, C., J. B. Dressman, H. E. Junginger, S. Kopp, K. K. Midha, V. P. Shah, S. Stavchansky, and D. M. Barends. 2009. Biowaiver monographs for immediate release solid oral dosage forms: Rifampicin. *Journal of Pharmaceutical Sciences* 98(7): 2252-2267.
- Berends, E. M., O. S. L. Bruinsma, J. de Graauw, and G. M. van Rosmalen. 1996. Crystallization of phenanthrene from toluene with carbon dioxide by the GAS process. *AIChE Journal* 42(2): 431-439.
- Bernstein, J. 2002. Polymorphism in Molecular Crystals. Oxford: Oxford University Press.
- Berry, D. J., C. C. Seaton, W. Clegg, R. W. Harrington, S. J. Coles, P. N. Horton, M. B. Hursthouse, R. Storey, W. Jones, T. Frišćić, and N. Blagden. 2008 Applying hot-stage microscopy to co-crystal screening: A study of nicotinamide with seven active pharmaceutical ingredients. *Crystal Growth & Design* 8(5): 1697-1712.
- Bertucco, A., M. Lora, and I. Kikic. 1998. Fractional crystallization by gas antisolvent technique: Theory and experiments. *AIChE Journal* 44(10): 2149-2158.

- Bezanehtak, K., G. B. Combes, F. Dehghani, N. R. Foster, and D. L. Tomasko. 2002. Vapor-liquid equilibrium for binary systems of carbon dioxide + methanol, hydrogen + methanol, and hydrogen + carbon dioxide at high pressures. *Journal of Chemical & Engineering Data* 47(2): 161-168.
- Bhakay, A., M. Merwade, E. Bilgili, and R. N. Dave. 2011. Novel aspects of wet milling for the production of microsuspensions and nanosuspensions of poorly water-soluble drugs. *Drug Development and Industrial Pharmacy* 37(8): 963-976.
- Blagden, N., M. de Matas, P. T. Gavan, and P. York. 2007. Crystal engineering of active pharmaceutical ingredients to improve solubility and dissolution rates. *Advanced Drug Delivery Reviews* 59(7): 617-630.
- Booij, J. and A. G. Lefferts. 2005. Agglomerates by crystallization. US Patent 6,979,735.
- Braga, D. and F. Grepioni. 2004. Reactions between or within molecular crystals. *Angewandte Chemie International Edition* 43(31): 4002-4011.
- Brewster, M. E. and T. Loftsson. 2007. Cyclodextrins as pharmaceutical solubilizers. *Advanced Drug Delivery Reviews* 59(7): 645-666.
- Bruner, L. and S. Tolloczko. 1900. Über die auflösegeschwindigkeit fester körper. *Z. Phys. Chem.* 35: 283-290.
- Brunner, E. 1904. Reaktionsgeschwindigkeit in heterogenen systemen. *Z. Phys. Chem.* 47: 56-102.
- Buçar, D.-K. and L. R. MacGillivray. 2007. Preparation and reactivity of nanocrystalline cocrystals formed via sonocrystallization. *Journal of the American Chemical Society* 129(1): 32-33.
- Bungert, B., G. Sadowski, and W. Arlt. 1998. Separations and material processing in solutions with dense gases. *Industrial & Engineering Chemistry Research* 37(8): 3208-3220.
- Chadwick, K., R. Davey, G. Sadiq, W. Cross, and R. Pritchard. 2009. The utility of a ternary phase diagram in the discovery of new co-crystal forms. *CrystEngComm* 11(3): 412-414.
- Challa, R., A. Ahuja, J. Ali, and R. K. Khar. 2005. Cyclodextrins in drug delivery: An updated review. *AAPS PharmSciTech* 6(2): 329-357.
- Chang, C. J., C.-Y. Day, C.-M. Ko, and K.-L. Chiu. 1997. Densities and P-x-y diagrams for carbon dioxide dissolution in methanol, ethanol, and acetone mixtures. *Fluid Phase Equilibria* 131(1-2): 243-258.

- Chang, C. J. and A. D. Randolph. 1990. Solvent expansion and solute solubility predictions in gas-expanded liquids. *AIChE Journal* 36(6): 939-942.
- Changsan, N., H.-K. Chan, F. Separovic, and T. Srichana. 2009. Physicochemical characterization and stability of rifampicin liposome dry powder formulations for inhalation. *Journal of Pharmaceutical Sciences* 98(2): 628-639.
- Chiarella, R. A., R. J. Davey, and M. L. Peterson. 2007. Making co-crystals—the utility of ternary phase diagrams. *Crystal Growth & Design* 7(7): 1223-1226.
- Childs, S. L. and K. I. Hardcastle. 2007. Cocrystals of piroxicam with carboxylic acids. *Crystal Growth & Design* 7(7): 1291-1304.
- Childs, S. L. and M. J. Zaworotko. 2009. The reemergence of cocrystals: The crystal clear writing is on the wall. Introduction to virtual special issue on pharmaceutical cocrystals. *Crystal Growth & Design* 9(10): 4208-4211.
- Chimowitz, E. H. 2005. Introduction to Critical Phenomena in Fluids. Oxford: Oxford University Press.
- Chimowitz, E. H. and K. J. Pennisi. 1986. Process synthesis concepts for supercritical gas extraction in the crossover region. *AIChE Journal* 32(10): 1665-1676.
- Chow, S. F., M. Chen, L. Shi, A. H. L. Chow, and C. C. Sun. 2012. Simultaneously improving the mechanical properties, dissolution performance, and hygroscopicity of ibuprofen and flurbiprofen by cocrystallization with nicotinamide. *Pharmaceutical Research* 29(7): 1854-1865.
- Cocero, M. J. and S. Ferrero. 2002. Crystallization of  $\beta$ -carotene by a GAS process in batch, Effect of operating conditions. *Journal of Supercritical Fluids* 22(3): 237-245.
- Corrigan, O. I. and A. M. Crean. 2002. Comparative physicochemical properties of hydrocortisone–PVP composites prepared using supercritical carbon dioxide by the GAS anti-solvent recrystallization process, by coprecipitation and by spray drying. *International Journal of Pharmaceutics* 245(1-2): 75-82.
- Dalvi, S. V. and R. N. Dave. 2009. Controlling particle size of a poorly water-soluble drug using ultrasound and stabilizers in antisolvent precipitation. *Industrial & Engineering Chemistry Research* 48(16): 7581-7593.
- Darbandi, M. A., N. A. Rouholamini, K. Gilani, and H. Tajerzadeh. 2008. The effect of vehicles on spray drying of rifampicin inhalable microparticles: In vitro and in vivo evaluation. *DARU* 16(3): 128-135.
- Datta, S. and D. J. W. Grant. 2004. Crystal structures of drugs: advances in determination, prediction and engineering. *Nature Reviews Drug Discovery* 3(1): 42-57.

- De Chasteigner, S., H. Fessi, J.-P. Devissaguet, and F. Puisieux. 1996. Comparative study of the association of itraconazole with colloidal drug carriers. *Drug Development Research* 38(2): 125-133.
- De Gioannis, B., P. Jestin, and P. Subra. 2004. Morphology and growth control of griseofulvin recrystallized by compressed carbon dioxide as antisolvent. *Journal of Crystal Growth* 262(1-4): 519-526.
- Dhumal, R. S., A. L. Kelly, P. York, P. D. Coates, and A. Paradkar. 2010. Cocrystallization and simultaneous agglomeration using hot melt extrusion. *Pharmaceutical Research* 27(12): 2725-2733.
- Di Profio, G., V. Grosso, A. Caridi, R. Caliendo, A. Guagliardi, G. Chita, E. Curcio, and E. Drioli. 2011. Direct production of carbamazepine–saccharin cocrystals from water/ethanol solvent mixtures by membrane-based crystallization technology. *CrystEngComm* 13(19): 5670-5673.
- Dixon, D. J. and K. P. Johnston. 1991. Molecular thermodynamics of solubilities in gas antisolvent crystallization. *AIChE Journal* 37(10): 1441-1449.
- Eckert, C. A., B. L. Knutson, and P. G. Debenedetti. 1996. Supercritical fluids as solvents for chemical and materials processing. *Nature* 383: 313-318.
- Eckert, C. A., C. L. Liotta, D. Bush, J. S. Brown, and J. P. Hallett. 2004. Sustainable reactions in tunable solvents. *Journal of Physical Chemistry B* 108(47): 18108-18118.
- Eddleston, M. D., G. O. Lloyd, and W. Jones. 2012. Cocrystal dissociation and molecular demixing in the solid state. *Chemical Communications* 48: 8075-8077.
- El Maghraby, G. M. and A. H. Alomrani. 2009. Synergistic enhancement of itraconazole dissolution by ternary system formation with pluronic F68 and hydroxypropylmethylcellulose. *Scientia Pharmaceutica* 77(2): 401-417.
- Elvassore, N., A. Bertucco, and P. Caliceti. 2001. Production of insulin-loaded poly (ethylene glycol)/poly (L-lactide) (PEG/PLA) nanoparticles by gas antisolvent techniques. *Journal of Pharmaceutical Sciences* 90(10): 1628-1636.
- Engers, D., J. Teng, J. Jimenez-Novoa, P. Gent, S. Hossack, C. Campbell, J. Thomson, I. Ivanisevic, A. Templeton, S. Byrn, and A. Newman. 2010. A solid-state approach to enable early development compounds: selection and animal bioavailability studies of an itraconazole amorphous solid dispersion. *Journal of Pharmaceutical Sciences* 99(9): 3901-3922.
- Falk, R. F. and T. W. Randolph. 1998. Process variable implications for residual solvent removal and polymer morphology in the formation of gentamycin-loaded poly (L-lactide) microparticles. *Pharmaceutical Research* 15(8): 1233-1237.

- Fleischman, S. G., S. S. Kuduva, J. A. McMahon, B. Moulton, R. D. B. Walsh, N. Rodríguez-Hornedo, and M. J. Zaworotko. 2003. Crystal engineering of the composition of pharmaceutical phases: Multiple-component crystalline solids involving carbamazepine. *Crystal Growth & Design* 3(6): 909-919.
- Foster, N. R., S. L. J. Yun, A. Dillow, P. A. Wells, and F. P. Lucien. 1997. A fundamental study of the gas anti-solvent process. *The 4th International Symposium on Supercritical Fluids*, p. 27.
- Fusaro, F., M. Mazzotti, and G. Muhrer. 2004. Gas antisolvent recrystallization of paracetamol from acetone using compressed carbon dioxide as antisolvent. *Crystal Growth & Design* 4(5): 881-889.
- Gombás, Á., P. Szabó-Révész, M. Kata, G. Regdon Jr., and I. Erős. 2002. Quantitative determination of crystallinity of  $\alpha$ -lactose monohydrate by DSC. *Journal of Thermal Analysis and Calorimetry* 68(2): 503-510.
- Good, D. J. and N. Rodríguez-Hornedo. 2009. Solubility advantage of pharmaceutical cocrystals. *Crystal Growth & Design* 9(5): 2252-2264.
- Groneberg, D. A., C. Witt, U. Wagner, K. F. Chung, and A. Fischer. 2003. Fundamentals of pulmonary drug delivery. *Respiratory Medicine* 97(4): 382-387.
- Gumbo, T., A. Louie, M. R. Deziel, W. Liu, L. M. Parsons, M. Salfinger, and G. L. Drusano. 2007. Concentration-dependent *Mycobacterium tuberculosis* killing and prevention of resistance by rifampin. *Antimicrobial Agents and Chemotherapy* 51(11): 3781-3788.
- Gupta, R. B. and U. B. Kompella. 2006. Nanoparticle Technology for Drug Delivery. New York: Taylor & Francis Group.
- Gupta, R. B. and J.-J. Shim. 2007. Solubility in Supercritical Carbon Dioxide. Boca Raton: Taylor & Francis Group.
- Hancock, B. C., P. York, and R. C. Rowe. 1997. The use of solubility parameters in pharmaceutical dosage form design. *International Journal of Pharmaceutics* 148(1): 1-21.
- Harnby, N. 2000. An engineering view of pharmaceutical powder mixing. *Pharmaceutical Science & Technology Today* 3(9): 303-309.
- Hassan, H. A., A. H. Al-Marzouqi, B. Jobe, A. A. Hamza, and G. A. Ramadan. 2007. Enhancement of dissolution amount and in vivo bioavailability of itraconazole by complexation with  $\beta$ -cyclodextrin using supercritical carbon dioxide. *Journal of Pharmaceutical and Biomedical Analysis* 45(2): 243-250.

- Henwood, S. Q., W. Liebenberg, L. R. Tiedt, A. P. Lötter, and M. M. de Villiers. 2001. Characterization of the solubility and dissolution properties of several new rifampicin polymorphs, solvates, and hydrates. *Drug Development and Industrial Pharmacy* 27(10): 1017-1030.
- Heyder, J., J. Gebhart, G. Rudolf, C. F. Schiller, and W. Stahlhofen. 1986. Deposition of particles in the human respiratory tract in the size range 0.005-15  $\mu\text{m}$ . *Journal of Aerosol Science* 17(5): 811-825.
- Heyder, J. and G. Rudolf. 1984. Mathematical models of particle deposition in the human respiratory tract. *Journal of Aerosol Science* 15(6): 697-707.
- Hickey, M. B., M. L. Peterson, L. A. Scoppettuolo, S. L. Morrisette, A. Vetter, H. Guzmán, J. F. Remenar, Z. Zhang, M. D. Tawa, S. Haley, M. J. Zaworotko, and Ö. Almarsson. 2007. Performance comparison of a co-crystal of carbamazepine with marketed product. *European Journal of Pharmaceutics and Biopharmaceutics* 67(1): 112-119.
- Higuchi, T. and K. A. Connors. 1965. Phase-solubility techniques. *Advances in Analytical Chemistry and Instrumentation* 4(2): 117-212.
- Hollingsworth, M. D., M. E. Brown, B. D. Santarsiero, J. C. Huffman, and C. R. Goss. 1994. Template-directed synthesis of 1:1 layered complexes of  $\alpha,\omega$ -dinitriles and urea: Packing efficiency versus specific functional group interactions. *Chemistry of Materials* 6(8): 1227-1244.
- Hu, J., K. P. Johnston, and R. O. Williams III. 2004. Nanoparticle engineering processes for enhancing the dissolution rates of poorly water soluble drugs. *Drug Development and Industrial Pharmacy* 30(3): 233-245.
- Im, J., W. Bae, J. Lee, and H. Kim. 2004. Vapor-liquid equilibria of the binary carbon dioxide-tetrahydrofuran mixture system. *Journal of Chemical & Engineering Data* 49(1): 35-37.
- Issa, N., P. G. Karamertzanis, G. W. A. Welch, and S. L. Price. 2009. Can the formation of pharmaceutical cocrystals be computationally predicted? I. Comparison of lattice energies. *Crystal Growth & Design* 9(1): 442-453.
- Jarmer, D. J., C. S. Lengsfeld, K. S. Anseth, and T. W. Randolph. 2005. Supercritical fluid crystallization of griseofulvin: Crystal habit modification with a selective growth inhibitor. *Journal of Pharmaceutical Sciences* 94(12): 2688-2702.
- Jessop, P. G., M. M. Olmstead, C. D. Ablan, M. Grabenauer, D. Sheppard, C. A. Eckert, and C. L. Liotta. 2002. Carbon dioxide as a solubility "switch" for the reversible dissolution of highly fluorinated complexes and reagents in organic solvents: Application to crystallization. *Inorganic Chemistry* 41(13): 3463-3468.

- Jessop, P. G. and B. Subramaniam. 2007. Gas-expanded liquids. *Chemical Reviews* 107(6): 2666-2694.
- Jung, J. and M. Perrut. 2001. Particle design using supercritical fluids: Literature and patent survey. *Journal of Supercritical Fluids* 20(3): 179-219.
- Kale, K., K. Hapgood, and P. Stewart. 2009. Drug agglomeration and dissolution – What is the influence of powder mixing? *European Journal of Pharmaceutics and Biopharmaceutics* 72(1): 156-164.
- Karamertzanis, P. G., A. V. Kazantsev, N. Issa, G. W. A. Welch, C. S. Adjiman, C. C. Pantelides, and S. L. Price. 2009. Can the formation of pharmaceutical cocrystals be computationally predicted? 2. Crystal structure prediction. *Journal of Chemical Theory and Computation* 5(5): 1432-1448.
- Karki, S., T. Frišćić, L. Fábián, P. R. Laity, G. M. Day, and W. Jones. 2009. Improving mechanical properties of crystalline solids by cocrystal formation: New compressible forms of paracetamol. *Advanced Materials* 21(38-39): 3905-3909.
- Kelly, A. L., T. Gough, R. S. Dhumal, S. A. Halsey, and A. Paradkar. 2012. Monitoring ibuprofen–nicotinamide cocrystal formation during solvent free continuous cocrystallization (SFCC) using near infrared spectroscopy as a PAT tool. *International Journal of Pharmaceutics* 426(1-2): 15-20.
- Kesisoglou, F., S. Panmai, and Y. Wu. 2007. Nanosizing – oral formulation development and biopharmaceutical evaluation. *Advanced Drug Delivery Reviews* 59(7): 631-644.
- Kinnari, P., E. Mäkilä, T. Heikkilä, J. Salonen, J. Hirvonen, and H. A. Santos. 2011. Comparison of mesoporous silicon and non-ordered mesoporous silica materials as drug carriers for itraconazole. *International Journal of Pharmaceutics* 414(1-2): 148-156.
- Knez, Ž., M. Škerget, L. Ilič, and C. Lütge. 2008. Vapor–liquid equilibrium of binary CO<sub>2</sub>–organic solvent systems (ethanol, tetrahydrofuran, *ortho*-xylene, *meta*-xylene, *para*-xylene). *Journal of Supercritical Fluids* 43(3): 383-389.
- Kodama, D., T. Yagihashi, T. Hosoya, and M. Kato. 2010. High pressure vapor–liquid equilibria for carbon dioxide + tetrahydrofuran mixtures. *Fluid Phase Equilibria* 297(2): 168-171.
- Krishnan, S., C. J. Raj, S. M. N. Priya, R. Robert, S. Dinakaran, and S. J. Das. 2008. Optical and dielectric studies on succinic acid single crystals. *Crystal Research and Technology* 43(8): 845-850.
- Krishnan, S., C. J. Raj, R. Robert, A. Ramanand, and S. J. Das. 2007. Growth and characterization of succinic acid single crystals. *Crystal Research and Technology* 42(11): 1087-1090.



- Krycer, I. and J. A. Hersey. 1980. Fine powder mixing in a vibratory ball mill. *International Journal of Pharmaceutics* 6(2): 119-129.
- Leuner, C. and J. Dressman. 2000. Improving drug solubility for oral delivery using solid dispersions. *European Journal of Pharmaceutics and Biopharmaceutics* 50(1): 47-60.
- Li, H. and M. Maroncelli. 2006. Solvation and solvatochromism in CO<sub>2</sub>-expanded liquids. 1. Simulations of the solvent systems CO<sub>2</sub> + cyclohexane, acetonitrile, and methanol. *Journal of Physical Chemistry B* 110(42): 21189-21197.
- Li, J., M. Rodrigues, A. Paiva, H. A. Matos, E. G. de Azevedo. 2007. Vapor-liquid equilibria and volume expansion of the tetrahydrofuran/CO<sub>2</sub> system: Application to a SAS-atomization process. *Journal of Supercritical Fluids* 41(3): 343-351.
- Linsenbühler, M. and K.-E. Wirth. 2005. An innovative dry powder coating process in non-polar liquids producing tailor-made micro-particles. *Powder Technology* 158(1-3): 3-20.
- Lipinski, C. A. 2001. Avoiding investment in doomed drugs, is poor solubility an industry wide problem? *Current Drug Discovery* 4: 17-19.
- Lipinski, C. 2002. Poor aqueous solubility—an industry wide problem in drug discovery. *American Pharmaceutical Review* 5: 82-85.
- Liu, D., X. Fei, S. Wang, T. Jiang, and D. Su. 2006. Increasing solubility and dissolution rate of drugs via eutectic mixtures: itraconazole-poloxamer 188 system. *Asian Journal of Pharmaceutical Sciences* 1(3-4): 213-221.
- Liu, P., X. Rong, J. Laru, B. van Veen, J. Kiesvaara, J. Hirvonen, T. Laaksonen, and L. Peltonen. 2011. Nanosuspensions of poorly soluble drugs: Preparation and development by wet milling. *International Journal of Pharmaceutics* 411(1-2): 215-222.
- Löbenberg, R. and G. L. Amidon. 2000. Modern bioavailability, bioequivalence and biopharmaceutics classification system. New scientific approaches to international regulatory standards. *European Journal of Pharmaceutics and Biopharmaceutics* 50(1): 3-12.
- Loftsson, T. and M. E. Brewster. 1996. Pharmaceutical applications of cyclodextrins. 1. Drug solubilization and stabilization. *Journal of Pharmaceutical Sciences* 85(10): 1017-1025.
- Lu, E., N. Rodríguez-Hornedo, and R. Suryanarayanan. 2008. A rapid thermal method for cocrystal screening. *CrystEngComm* 10(6): 665-668.
- Lu, J. and S. Rohani. 2009. Polymorphism and crystallization of active pharmaceutical ingredients (APIs). *Current Medicinal Chemistry* 16(7): 884-905.

- Martín, A. and M. J. Cocero. 2008. Micronization processes with supercritical fluids: Fundamentals and mechanisms. *Advanced Drug Delivery Reviews* 60(3): 339-350.
- Matteucci, M. E., B. K. Brettmann, T. L. Rogers, E. J. Elder, R. O. Williams III, and K. P. Johnston. 2007. Design of potent amorphous drug nanoparticles for rapid generation of highly supersaturated media. *Molecular Pharmaceutics* 4(5): 782-793.
- Matteucci, M. E., M. A. Hotze, K. P. Johnston, and R. O. Williams III. 2006. Drug nanoparticles by antisolvent precipitation: Mixing energy versus surfactant stabilization. *Langmuir* 22(21): 8951-8959.
- McNamara, D. P., S. L. Childs, J. Giordano, A. Iarriccio, J. Cassidy, M. S. Shet, R. Mannion, E. O'Donnell, and A. Park. 2006. Use of a glutaric acid cocrystal to improve oral bioavailability of a low solubility API. *Pharmaceutical Research* 23(8): 1888-1897.
- Mellaerts, R., R. Mols, J. A. G. Jammaer, C. A. Aerts, P. Annaert, J. Van Humbeeck, G. Van den Mooter, P. Augustijns, and J. A. Martens. 2008. Increasing the oral bioavailability of the poorly water soluble drug itraconazole with ordered mesoporous silica. *European Journal of Pharmaceutics and Biopharmaceutics* 69(1): 223-230.
- Merisko-Liversidge, E. M. and G. G. Liversidge. 2008. Drug nanoparticles: Formulating poorly water-soluble compounds. *Toxicologic Pathology* 36(1): 43-48.
- Merisko-Liversidge, E., G. G. Liversidge, and E. R. Cooper. 2003. Nanosizing: a formulation approach for poorly-water-soluble compounds. *European Journal of Pharmaceutical Sciences* 18(2): 113-120.
- Meyer, K. and I. Zimmermann. 2004. Effect of glidants in binary powder mixtures. *Powder Technology* 139(1): 40-54.
- Miller, J. M., B. M. Collman, L. R. Greene, D. J. W. Grant, and A. C. Blackburn. 2005. Identifying the stable polymorph early in the drug discovery–development process. *Pharmaceutical Development and Technology* 10(2): 291-297.
- Mizoe, T., T. Ozeki, and H. Okada. 2008. Application of a four-fluid nozzle spray drier to prepare inhalable rifampicin-containing mannitol microparticles. *AAPS PharmSciTech* 9(3): 755-761.
- Mohammad, M. A., A. Alhalaweh, and S. P. Velaga. 2011. Hansen solubility parameter as a tool to predict cocrystal formation. *International Journal of Pharmaceutics* 407(1-2): 63-71.

- Morissette, S. L., Ö. Almarsson, M. L. Peterson, J. F. Remenar, M. J. Read, A. V. Lemmo, S. Ellis, M. J. Cima, and C. R. Gardner. 2004. High-throughput crystallization: Polymorphs, salts, co-crystals and solvates of pharmaceutical solids. *Advanced Drug Delivery Reviews* 56(3): 275-300.
- Muttill, P., J. Kaur, K. Kumar, A. B. Yadav, R. Sharma, and A. Misra. 2007. Inhalable microparticles containing large payload of anti-tuberculosis drugs. *European Journal of Pharmaceutical Sciences* 32(2): 140-150.
- Nehm, S. J., B. Rodríguez-Spong, and N. Rodríguez-Hornedo. 2006. Phase solubility diagrams of cocrystals are explained by solubility product and solution complexation. *Crystal Growth & Design* 6(2): 592-600.
- Nernst, W. 1904. Theorie der reaktionsgeschwindigkeit in heterogenen systemen. *Z. Phys. Chem.* 47: 52-55.
- Nesseem, D. I. 2001. Formulation and evaluation of itraconazole via liquid crystal for topical delivery system. *Journal of Pharmaceutical and Biomedical Analysis* 26(3): 387-399.
- Noyes, A. A. and W. R. Whitney. 1897. The rate of solution of solid substances in their own solutions. *Journal of the American Chemical Society* 19(12): 930-934.
- Ober, C. A., S. E. Montgomery, and R. B. Gupta. 2012. Formation of itraconazole/L-malic acid cocrystals by gas antisolvent cocrystallization. *Powder Technology, In Press*. <http://dx.doi.org/10.1016/j.powtec.2012.04.058>.
- O'Hara, P. and A. J. Hickey. 2000. Respirable PLGA microspheres containing rifampicin for the treatment of tuberculosis: Manufacture and characterization. *Pharmaceutical Research* 17(8): 955-961.
- Padrela, L., E. G. de Azevedo, and S. P. Velaga. 2012. Powder X-ray diffraction method for the quantification of cocrystals in the crystallization mixture. *Drug Development and Industrial Pharmacy* 38(8): 923-929.
- Padrela, L., M. A. Rodrigues, S. P. Velaga, A. C. Fernandes, H. A. Matos, and E. G. de Azevedo. 2010. Screening for pharmaceutical cocrystals using the supercritical fluid enhanced atomization process. *Journal of Supercritical Fluids* 53(1-3): 156-164.
- Padrela, L., M. A. Rodrigues, S. P. Velaga, H. A. Matos, and E. G. de Azevedo. 2009. Formation of indomethacin–saccharin cocrystals using supercritical fluid technology. *European Journal of Pharmaceutical Sciences* 38(1): 9-17.
- Park, S.-J. and S.-D. Yeo. 2008a. Recrystallization of phenylbutazone using supercritical fluid antisolvent process. *Korean Journal of Chemical Engineering* 25(3): 575-580.

- Park, S.-J. and S.-D. Yeo. 2008b. Recrystallization of caffeine using gas antisolvent process. *Journal of Supercritical Fluids* 47(1): 85-92.
- Parkin, A., C. C. Seaton, N. Blagden, and C. C. Wilson. 2007. Designing hydrogen bonds with temperature-dependent proton disorder: The effect of crystal environment. *Crystal Growth & Design* 7(3): 531-534.
- Patil, A. O., D. Y. Curtin, and I. C. Paul. 1984. Solid-state formation of quinhydrone from their components. Use of solid-solid reactions to prepare compounds not accessible from solution. *Journal of the American Chemical Society* 106(2): 348-353.
- Patomchaiwivat, V., O. Paeratakul, and P. Kulvanich. 2008. Formation of inhalable rifampicin–poly(L-lactide) microparticles by supercritical anti-solvent process. *AAPS PharmSciTech* 9(4): 1119-1129.
- Payne, S. M. and F. M. Kerton. 2010. Solubility of bio-sourced feedstocks in 'green' solvents. *Green Chemistry* 12(9): 1648-1653.
- Peeters, J., P. Neeskens, J. P. Tollenaere, P. Van Remoortere, and M. E. Brewster. 2002. Characterization of the interaction of 2-hydroxypropyl- $\beta$ -cyclodextrin with itraconazole at pH 2, 4, and 7. *Journal of Pharmaceutical Sciences* 91(6): 1414-1422.
- Pelizza, G., M. Nebuloni, P. Ferrari, and G. G. Gallo. 1977. Polymorphism of rifampicin. *II Farmaco; Edizione Scientifica* 32(7): 471-481.
- Peng, D.-Y. and D. B. Robinson. 1976. A new two-constant equation of state. *Industrial & Engineering Chemistry Fundamentals* 15(1): 59-64.
- Porter III, W. W., S. C. Elie, and A. J. Matzger. 2008. Polymorphism in carbamazepine cocrystals. *Crystal Growth & Design* 8(1): 14-16.
- Prausnitz, J. M., R. N. Lichtenthaler, and E. G. de Azevedo. 1998. Molecular Thermodynamics of Fluid-Phase Equilibria, 3rd Ed. Upper Saddle River: Prentice Hall.
- Prime, D., P. J. Atkins, A. Slater, and B. Sumby. 1997. Review of dry powder inhalers. *Advanced Drug Delivery Reviews* 26(1): 51-58.
- Qiao, N., M. Li, W. Schlindwein, N. Malek, A. Davies, and G. Trappitt. 2011. Pharmaceutical cocrystals: An overview. *International Journal of Pharmaceutics* 419(1-2): 1-11.
- Radtke, M. 2001. Pure drug nanoparticles for the formulation of poorly soluble drugs. *New Drugs* 3: 62-68.

Rahman, Z., C. Agarabi, A. S. Zidan, S. R. Khan, and M. A. Khan. 2011. Physico-mechanical and stability evaluation of carbamazepine cocrystal with nicotinamide. *AAPS PharmSciTech* 12(2): 693-704.

Remenar, J., M. MacPhee, M. L. Peterson, S. L. Morissette, and Ö. Almarsson. 2006. CIS-itraconazole crystalline forms and related processes, pharmaceutical compositions and methods. US Patent 7,078,526.

Remenar, J. F., S. L. Morissette, M. L. Peterson, B. Moulton, J. M. MacPhee, H. R. Guzmán, and Ö. Almarsson. 2003. Crystal engineering of novel cocrystals of a triazole drug with 1,4-dicarboxylic acids. *Journal of the American Chemical Society* 125(28): 8456-8457.

Reverchon, E. and R. Adami. 2006. Nanomaterials and supercritical fluids. *Journal of Supercritical Fluids* 37(1): 1-22.

Reverchon, E., I. De Marco, and G. D. Porta. 2002. Rifampicin microparticles production by supercritical antisolvent precipitation. *International Journal of Pharmaceutics* 243(1-2): 83-91.

Rifampin. 2008. *Tuberculosis* 88(2): 151-154.

Rodrigues, M. A., L. Padrela, V. Geraldés, J. Santos, H. A. Matos, and E. G. Azevedo. 2011. Theophylline polymorphs by atomization of supercritical antisolvent induced suspensions. *Journal of Supercritical Fluids* 58(2): 303-312.

Rogers, T. L., I. B. Gillespie, J. E. Hitt, K. L. Fransen, C. A. Crowl, C. J. Tucker, G. B. Kupperblatt, J. N. Becker, D. L. Wilson, C. Todd, C. F. Broomall, J. C. Evans, and E. J. Elder. 2004. Development and characterization of a scalable controlled precipitation process to enhance the dissolution of poorly water-soluble drugs. *Pharmaceutical Research* 21(11): 2048-2057.

Rohrs, B. R., G. E. Amidon, R. H. Meury, P. J. Secreast, H. M. King, and C. J. Skoug. 2006. Particle size limits to meet USP content uniformity criteria for tablets and capsules. *Journal of Pharmaceutical Sciences* 95(5): 1049-1059.

Roy, C., D. Vrel, A. Vega-González, P. Jestin, S. Laugier, and P. Subra-Paternault. 2011. Effect of CO<sub>2</sub>-antisolvent techniques on size distribution and crystal lattice of theophylline. *Journal of Supercritical Fluids* 57(3): 267-277.

Ruchatz, F., P. Kleinebudde, and B. W. Müller. 1997. Residual solvents in biodegradable microparticles. Influence of process parameters on the residual solvent in microparticles produced by the aerosol solvent extraction system (ASES) process. *Journal of Pharmaceutical Sciences* 86(1): 101-105.

Sander, J. R. G., D.-K. Bučar, R. F. Henry, G. G. Z. Zhang, and L. R. MacGillivray. 2010. Pharmaceutical nano-cocrystals: Sonochemical synthesis by solvent selection and use of a surfactant. *Angewandte Chemie* 122(40): 7442-7446.

Sanganwar, G. P. 2010. Environmentally benign mixing of nanoparticles. Ph.D. Dissertation, Auburn University, Auburn, AL.

Sanganwar, G. P. and R. B. Gupta. 2008. Enhancement of shelf life and handling properties of drug nanoparticles: Nanoscale mixing of itraconazole with silica. *Industrial & Engineering Chemistry Research* 47(14): 4717-4725.

Sanganwar, G. P., S. Sathigari, R. J. Babu, and R. B. Gupta. 2010. Simultaneous production and co-mixing of microparticles of nevirapine with excipients by supercritical antisolvent method for dissolution enhancement. *European Journal of Pharmaceutical Sciences* 39(1-3): 164-174.

Sastry, S. V., J. R. Nyshadham, and J. A. Fix. 2000. Recent technological advances in oral drug delivery – a review. *Pharmaceutical Science & Technology Today* 3(4): 138-145.

Sathigari, S. K., C. A. Ober, G. P. Sanganwar, R. B. Gupta, and R. J. Babu. 2011. Single-step preparation and deagglomeration of itraconazole microflakes by supercritical antisolvent method for dissolution enhancement. *Journal of Pharmaceutical Sciences* 100(7): 2952-2965.

Saunders, S. R. 2011. Use of gas-expanded liquids as tunable solvents for the preparation of well-defined nanomaterials. Ph.D. Dissertation, Auburn University, Auburn, AL.

Schartman, R. R. 2009. On the thermodynamics of cocrystal formation. *International Journal of Pharmaceutics* 365(1-2): 77-80.

Schreiber, J., G. Zissel, U. Greinert, M. Schlaak, and J. Müller-Quernheim. 1999. Lymphocyte transformation test for the evaluation of adverse effects of antituberculous drugs. *European Journal of Medical Research* 4(2): 67-71.

Schultheiss, N. and A. Newman. 2009. Pharmaceutical cocrystals and their physicochemical properties. *Crystal Growth & Design* 9(6): 2950-2967.

Schütz, S., I. Wengatz, M. H. Goodrow, S. J. Gee, H. E. Hummel, and B. D. Hammock. 1997. Development of an enzyme-linked immunosorbent assay for azadirachtins. *Journal of Agricultural and Food Chemistry* 45(6): 2363-2368.

Sekhon, B. S. 2009. Pharmaceutical co-crystals - a review. *ARS Pharmaceutica* 50(3): 99-117.

- Serajuddin, A. T. M. 1999. Solid dispersion of poorly water-soluble drugs: Early promises, subsequent problems, and recent breakthroughs. *Journal of Pharmaceutical Sciences* 88(10): 1058-1066.
- Serajuddin, A. T. M. 2007. Salt formation to improve drug solubility. *Advanced Drug Delivery Reviews* 59(7): 603-616.
- Shan, N. and M. J. Zaworotko. 2008. The role of cocrystals in pharmaceutical science. *Drug Discovery Today* 13(9-10): 440-446.
- Shariati, A. and C. J. Peters. 2003. Recent developments in particle design using supercritical fluids. *Current Opinion in Solid State and Materials Science* 7(4-5): 371-383.
- Shevchenko, A., L. M. Bimbo, I. Miroshnyk, J. Haarala, K. Jelínková, K. Syrjänen, B. van Veen, J. Kiesvaara, H. A. Santos, and J. Yliruusi. 2012. A new cocrystal and salts of itraconazole: Comparison of solid-state properties, stability and dissolution behavior. *International Journal of Pharmaceutics* 436(1-2): 403-409.
- Shikhar, A., M. M. Bommana, S. S. Gupta, and E. Squillante. 2011. Formulation development of carbamazepine–nicotinamide co-crystals complexed with  $\gamma$ -cyclodextrin using supercritical fluid process. *Journal of Supercritical Fluids* 55(3): 1070-1078.
- Shiraki, K., N. Takata, R. Takano, Y. Hayashi, and K. Terada. 2008. Dissolution improvement and the mechanism of the improvement from cocrystallization of poorly water-soluble compounds. *Pharmaceutical Research* 25(11): 2581-2592.
- Silva, R. F. 2010. Fungal infections in immunocompromised patients. *Jornal Brasileiro de Pneumologia* 36(1): 142-147.
- Sinswat, P., X. Gao, M. J. Yacaman, R. O. Williams III, and K. P. Johnston. 2005. Stabilizer choice for rapid dissolving high potency itraconazole particles formed by evaporative precipitation into aqueous solution. *International Journal of Pharmaceutics* 302(1-2): 113-124.
- Six, K., G. Verreck, J. Peeters, M. Brewster, and G. Van den Mooter. 2004. Increased physical stability and improved dissolution properties of itraconazole, a class II drug, by solid dispersions that combine fast- and slow-dissolving polymers. *Journal of Pharmaceutical Sciences* 93(1): 124-131.
- Son, Y.-J., and J. T. McConville. 2011. A new respirable form of rifampicin. *European Journal of Pharmaceutics and Biopharmaceutics* 78(3): 366-376.
- Son, Y.-J. and J. T. McConville. 2012. Preparation of sustained release rifampicin microparticles for inhalation. *Journal of Pharmacy and Pharmacology* 64(9): 1291-1302.

- Stahly, G. P. 2009. A survey of cocrystals reported prior to 2000. *Crystal Growth & Design* 9(10): 4212-4229.
- Stanton, M. K., S. Tufekcic, C. Morgan, and A. Bak. 2009. Drug substance and former structure property relationships in 15 diverse pharmaceutical co-crystals. *Crystal Growth & Design* 9(3): 1344-1352.
- Suarez, S., P. O'Hara, M. Kazantseva, C. E. Newcomer, R. Hopfer, D. N. McMurray, and A. J. Hickey. 2001. Respirable PLGA microspheres containing rifampicin for the treatment of tuberculosis: Screening in an infectious disease model. *Pharmaceutical Research* 18(9): 1315-1319.
- Subra, P., C.-G. Laudani, A. Vega-González, and E. Reverchon. 2005. Precipitation and phase behavior of theophylline in solvent–supercritical CO<sub>2</sub> mixtures. *Journal of Supercritical Fluids* 35(2): 95-105.
- Subra-Paternault, P., C. Roy, D. Vrel, A. Vega-Gonzalez, and C. Domingo. 2007. Solvent effect on tolbutamide crystallization induced by compressed CO<sub>2</sub> as antisolvent. *Journal of Crystal Growth* 309(1): 76-85.
- Sugimoto, M., T. Okagaki, S. Narisawa, Y. Koida, and K. Nakajima. 1998. Improvement of dissolution characteristics and bioavailability of poorly water-soluble drugs by novel cogrinding method using water-soluble polymer. *International Journal of Pharmaceutics* 160(1): 11-19.
- Sun, C. C. and H. Hou. 2008. Improving mechanical properties of caffeine and methyl gallate crystals by cocrystallization. *Crystal Growth & Design* 8(5): 1575-1579.
- Sung, J. C., D. J. Padilla, L. Garcia-Contreras, J. L. VerBerkmoes, D. Durbin, C. A. Peloquin, K. J. Elbert, A. J. Hickey, and D. A. Edwards. 2009. Formulation and pharmacokinetics of self-assembled rifampicin nanoparticle systems for pulmonary delivery. *Pharmaceutical Research* 26(8): 1847-1855.
- Swai, H., B. Semete, L. Kalombo, P. Chelule, K. Kisich, and B. Sievers. 2009. Nanomedicine for respiratory diseases. *Wiley Interdisciplinary Reviews: Nanomedicine and Nanobiotechnology* 1(3): 255-263.
- Tai, C. Y. and C.-S. Cheng. 1998. Supersaturation and crystal growth in gas anti-solvent crystallization. *Journal of Crystal Growth* 183(4): 622-628.
- Tao, T., Y. Zhao, J. Wu, and B. Zhou. 2009. Preparation and evaluation of itraconazole dihydrochloride for the solubility and dissolution rate enhancement. *International Journal of Pharmaceutics* 367(1-2): 109-114.
- Ter Horst, J. H., M. A. Deij, and P. W. Cains. 2009. Discovering new co-crystals. *Crystal Growth & Design* 9(3): 1531-1537.



- Tewes, F., J. Brillault, W. Couet, and J.-C. Olivier. 2008. Formulation of rifampicin–cyclodextrin complexes for lung nebulization. *Journal of Controlled Release* 129(2): 93-99.
- Thiering, R., F. Dehghani, A. Dillow, and N. R. Foster. 2000. The influence of operating conditions on the dense gas precipitation of model proteins. *Journal of Chemical Technology & Biotechnology* 75(1): 29-41.
- Thorat, A. A. and S. V. Dalvi. 2012. Liquid antisolvent precipitation and stabilization of nanoparticles of poorly water soluble drugs in aqueous suspensions: Recent developments and future perspective. *Chemical Engineering Journal* 181-182: 1-34.
- Toda, F., K. Tanaka, and A. Sekikawa. 1987. Host-guest complex formation by a solid-solid reaction. *Journal of the Chemical Society, Chemical Communications* (4): 279-280.
- Tom, J. W. and P. G. Debenedetti. 1991. Particle formation with supercritical fluids—a review. *Journal of Aerosol Science* 22(5): 555-584.
- Trask, A. V. 2007. An overview of pharmaceutical cocrystals as intellectual property. *Molecular Pharmaceutics* 4(3): 301-309.
- Trask, A. V., W. D. S. Motherwell, and W. Jones. 2005. Pharmaceutical cocrystallization: Engineering a remedy for caffeine hydration. *Crystal Growth & Design* 5(3): 1013-1021.
- Trask, A. V., W. D. S. Motherwell, and W. Jones. 2006. Physical stability enhancement of theophylline via cocrystallization. *International Journal of Pharmaceutics* 320(1-2): 114-123.
- Van Speybroeck, M., R. Mols, R. Mellaerts, T. D. Thi, J. A. Martens, J. Van Humbeeck, P. Annaert, G. Van den Mooter, and P. Augustijns. 2010. Combined use of ordered mesoporous silica and precipitation inhibitors for improved oral absorption of the poorly soluble weak base itraconazole. *European Journal of Pharmaceutics and Biopharmaceutics* 75(3): 354-365.
- Variankaval, N., R. Wenslow, J. Murry, R. Hartman, R. Helmy, E. Kwong, S.-D. Clas, C. Dalton, and I. Santos. 2006. Preparation and solid-state characterization of nonstoichiometric cocrystals of a phosphodiesterase-IV inhibitor and L-tartaric acid. *Crystal Growth & Design* 6(3): 690-700.
- Vasconcelos, T., B. Sarmiento, and P. Costa. 2007. Solid dispersions as strategy to improve oral bioavailability of poor water soluble drugs. *Drug Discovery Today* 12(23-24): 1068-1075.

- Viçosa, A., J.-J. Letourneau, F. Espitalier, and M. I. Ré. 2011. An innovative antisolvent precipitation process as a promising technique to prepare ultrafine rifampicin particles. *Journal of Crystal Growth* 342(1): 80-87.
- Vishweshwar, P., J. A. McMahon, J. A. Bis, and M. J. Zaworotko. 2006. Pharmaceutical co-crystals. *Journal of Pharmaceutical Sciences* 95(3): 499-516.
- Vogt, M., K. Kunath, and J. B. Dressman. 2008. Dissolution improvement of four poorly water soluble drugs by cogrinding with commonly used excipients. *European Journal of Pharmaceutics and Biopharmaceutics* 68(2): 330-337.
- Warwick, B., F. Dehghani, N. R. Foster, J. R. Biffin, and H. L. Regtop. 2000. Synthesis, purification, and micronization of pharmaceuticals using the gas antisolvent technique. *Industrial & Engineering Chemistry Research* 39(12): 4571-4579.
- Wöhler, F. 1844. *Justus Lieb. Ann. Chem.* 51: 153.
- World Health Organization. 2010. Fact Sheet: Tuberculosis. Geneva: World Health Organization.
- Wubbolts, F. E., O. S. L. Bruinsma, and G. M. van Rosmalen. 2004. Measurement and modelling of the solubility of solids in mixtures of common solvents and compressed gases. *Journal of Supercritical Fluids* 32(1-3): 79-87.
- Wulsten, E., F. Kiekens, F. van Dycke, J. Voorspoels, and G. Lee. 2009. Levitated single-droplet drying: Case study with itraconazole dried in binary organic solvent mixtures. *International Journal of Pharmaceutics* 378(1-2): 116-121.
- Yamashita, H., Y. Hirakura, M. Yuda, T. Teramura, and K. Terada. 2013. Detection of cocrystal formation based on binary phase diagrams using thermal analysis. *Pharmaceutical Research* 30(1): 70-80.
- Yasuji, T., H. Takeuchi, and Y. Kawashima. 2008. Particle design of poorly water-soluble drug substances using supercritical fluid technologies. *Advanced Drug Delivery Reviews* 60(3): 388-398.
- Yeo, S.-D., M.-S. Kim, and J.-C. Lee. 2003. Recrystallization of sulfathiazole and chlorpropamide using the supercritical fluid antisolvent process. *Journal of Supercritical Fluids* 25(2): 143-154.

## Appendix A

### Particle Stabilization in Antisolvent Crystallization

Some additional discussion on particle stabilization, outside the scope of the work presented in Chapter 4, is included in this Appendix. In crystallizing poorly water-soluble micro- and nanoparticulate pharmaceuticals, stabilization is most commonly employed to inhibit particle growth and prevent particle agglomeration. The type of stabilization employed, electrostatic or steric, is dependent upon characteristics of the drug, stabilizer, solvent, antisolvent, and their respective interactions. The following two sections discuss electrostatic and steric stabilization while the third section relates the mechanisms of stabilization back to the work done in Chapter 4 using itraconazole.

#### **A.1 Electrostatic Stabilization**

Electrostatic stabilization is achieved through the surface adsorption of charged ionic surfactants or polymers onto the drug particle surface, as shown in Figure A.1. The strength of surface adsorption is attributed to van der Waals attraction between the repeating monomer units of the polymer chain and the drug particle surface (Thorat and Dalvi 2012). Stabilization using ionic surfactants must be accomplished at surfactant concentrations below the critical micelle concentration (CMC). Above the CMC, the surfactant will form micelles as shown in Figure A.1, leaving the particles unprotected.

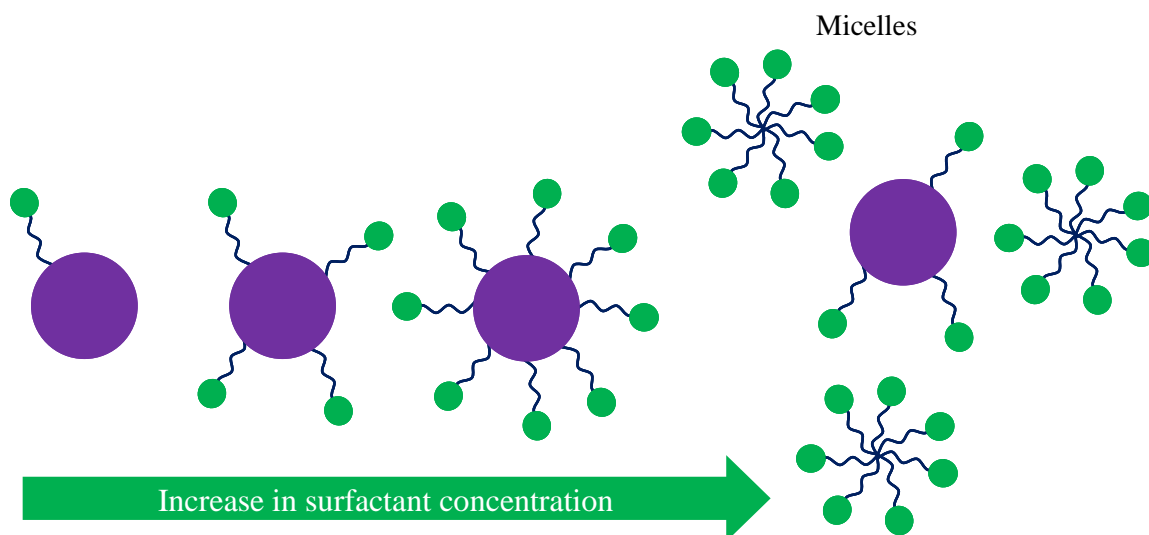


Figure A.1 Schematic of electrostatic stabilization for a poorly water-soluble drug particle in aqueous media

Electrostatic stabilization prevents particle agglomeration through repulsive forces between adjacent particles. The surface of a charged particle attracts a layer of counterions, termed the Stern layer, to preserve the electrical neutrality of the system, as shown in Figure A.2 for a negatively charged particle. The Stern layer is surrounded by a second layer, which is essentially a diffusion layer of ions (Wu et al. 2011). Together these two layers comprise the electric double layer (EDL), which when overlapped with the EDL of an adjacent particle is the source of particle–particle repulsion. The difference in charge between the bulk solution and the outer double layer, termed the zeta potential ( $\zeta$ ), is a measure of the electrostatic stabilization. Zeta potentials higher than  $\pm 30$  mV typically indicate good suspension stability (Wu et al. 2011).

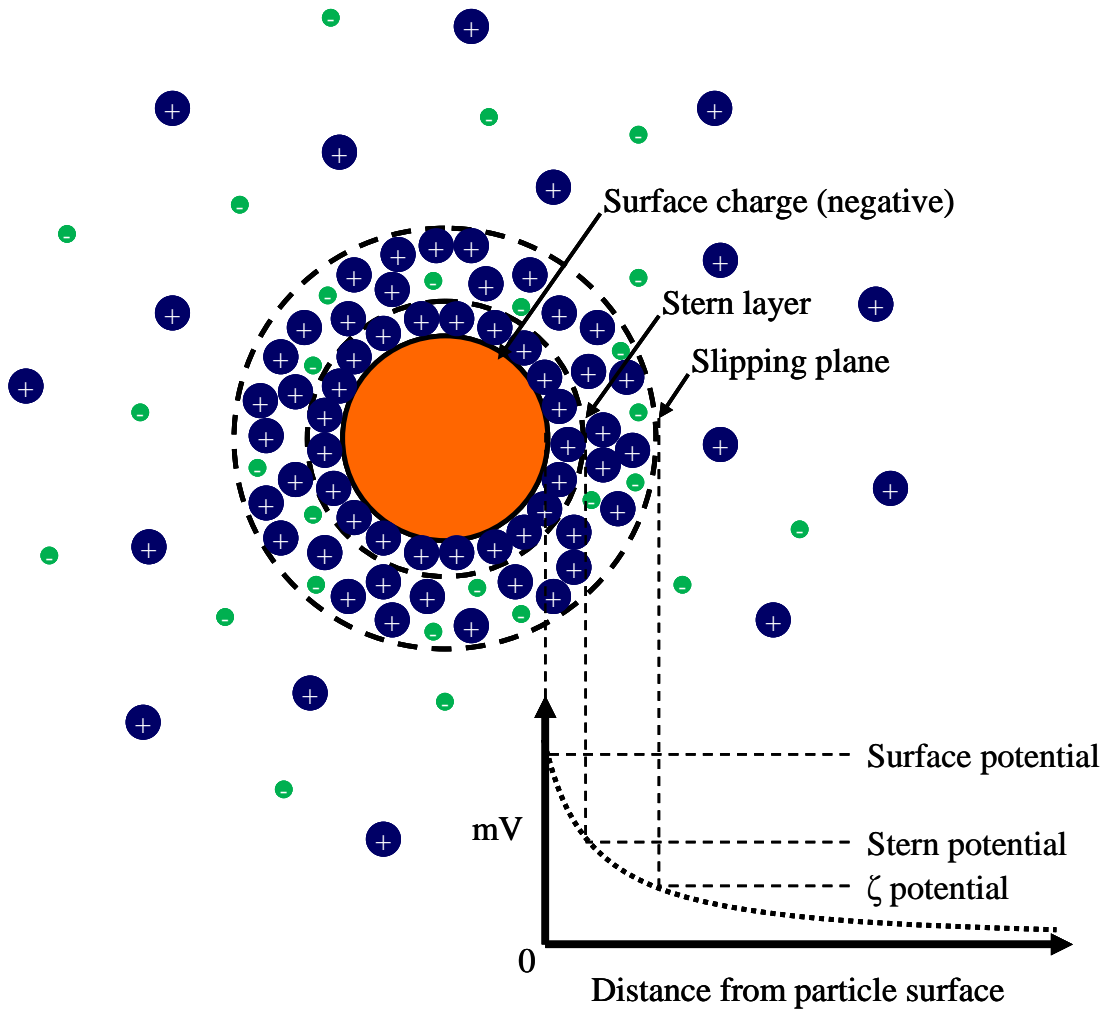


Figure A.2 Ionic concentration and electrokinetic potential as a function of distance from a negatively charged particle suspended in a dispersion medium

The balance of repulsive electrostatic and attractive van der Waals forces can be understood through Derjaguin-Landau-Verwey-Overbeek (DLVO) theory (Derjaguin and Landau 1941; Verwey and Overbeek 1948). In short, particle-particle interactions are characterized by a total potential energy ( $V_T$ ), which is the sum of the electrostatic repulsive potential ( $V_R$ ) and the van der Waals attractive potential ( $V_A$ ). Figure A.3 illustrates these potential energies as a function of interparticle distance. Attractive forces dominate at very small and large interparticle distances, leading to two potential energy

minimums, while repulsive forces dominate at intermediate distances preventing agglomeration through net repulsion (Wu et al. 2011).

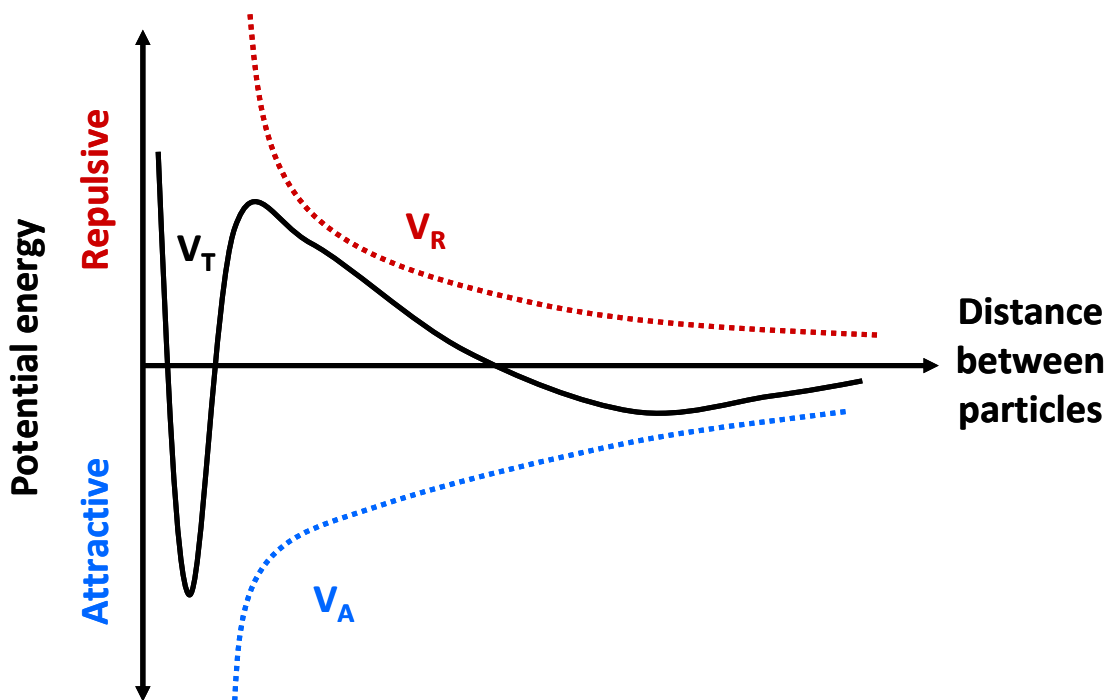


Figure A.3 Potential energy as a function of interparticle distance according to classical DLVO theory ( $V_T$  = total potential energy,  $V_R$  = repulsive potential, and  $V_A$  = attractive potential)

## A.2 Steric Stabilization

Steric stabilization is accomplished through the surface adsorption of non-ionic polymers or amphiphilic block copolymers through nonspecific interactions between the hydrophobic groups of the polymer and the drug particle surface, as shown in Figure A.4 (Thorat and Dalvi 2012). Depending on the functionalities of the polymer, the chains will not lie flat on the particle surface but will adapt various conformations in which some groups interact with the particle surface while others extend into solution. Just as electrostatic stabilization must occur below the CMC, steric stabilization must occur

below the critical flocculation concentration (CFC). At polymer concentrations above the CFC, an increase in osmotic pressure causes an increase in particle attraction. Also above the CFC, the polymer molecules will initiate either bridging flocculation or depletion flocculation depending on the strength of polymer–particle versus particle–particle interactions.

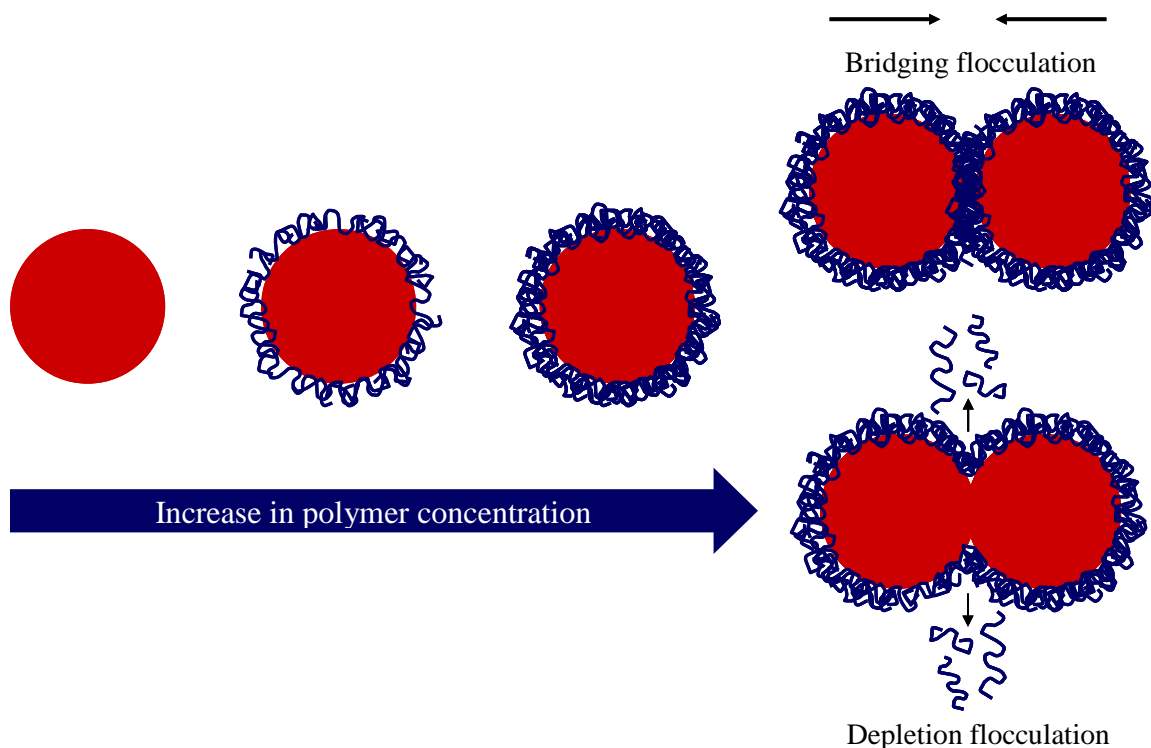


Figure A.4 Schematic of steric stabilization for a poorly water-soluble drug particle in aqueous media

The increase in osmotic stress caused by the interpenetration of adsorbed polymer layers from adjacent particles makes particle agglomeration thermodynamically unfavorable (Kesisoglou et al. 2007; Wu et al. 2011). In addition to preventing particle agglomeration, polymer adsorption at the drug particle surface reduces the interfacial

tension of the solid-liquid interface, thus increasing nucleation rates and decreasing particle size. Polymer chain length and molecular weight are important parameters in steric stabilization. While it is typically understood that bulkier polymers provide a greater steric barrier to agglomeration, the increased mobility of smaller polymer chains facilitates rapid diffusion to the particle surface, offering advantages for limiting particle growth (Kumar et al. 2009).

### **A.3 Stabilization of Itraconazole**

The mechanisms of stabilization discussed in sections A.1 and A.2 primarily apply when poorly water-soluble drug particles are crystallized using an aqueous antisolvent or suspended in an aqueous dispersion medium. To date there have been limited studies exploring the role that stabilizers play when used during crystallization by a compressed fluid antisolvent. Nonetheless, similarities can be drawn and the results observed in Chapter 4 related to the stabilization fundamentals discussed in the preceding two sections.

Itraconazole is a neutral, weakly basic molecule possessing no ionic surface charge, but three ionizable nitrogens (Chaubal and Popescu 2008; Miller et al. 2008). As such, itraconazole displays a higher dissolution rate in proton-rich acidic media where the drug can exist in its protonated form. Polymers capable of hydrogen bond donation will thus be better stabilizers for itraconazole. Hydrogen bond acceptor stabilizers would actually compete with itraconazole for free protons, inhibiting dissolution. Observation of this phenomenon was made through the more effective stabilization of itraconazole with Methocel<sup>TM</sup>, whose cellulose ethers contain hydroxyl groups capable of hydrogen bond



donation, as compared to Kollidon<sup>®</sup> (polyvinylpyrrolidone), which contains an electronegative carbonyl group (Miller et al. 2008). The hydrogen bond capabilities of Pluronic F-127, the polymeric stabilizer used in Chapter 4, would be expected to be intermediate to those of Methocel and Kollidon, suggesting that hydrogen bonding is not the dominating reason for the increase in itraconazole dissolution observed during Pluronic F-127 stabilization (Figure 4.13).

In another study, Pluronic F-127 was specifically found to improve itraconazole dissolution, through uptake into the core of polymer micelles, compared to other poorly water-soluble drugs due to the similar solubility parameters of itraconazole and the hydrophobic polypropylene oxide (PPO) group of Pluronic F-127 ( $\delta_{ITZ} = 21.6 \text{ MPa}^{1/2}$ ,  $\delta_{PPO} = 19.0 \text{ MPa}^{1/2}$ ). Furthermore, the PPO block ( $T_g = -75 \text{ }^\circ\text{C}$ ) of Pluronic F-127, which exists in the fluid state at room temperature, facilitates itraconazole dissolution by diffusing the drug into the bulk aqueous phase through dynamic polymer adsorption and desorption from the drug polymer surface, compared to other PEO copolymers with high glass transition temperature hydrophobic blocks such as polystyrene ( $T_g = 100 \text{ }^\circ\text{C}$ ) (Kumar et al. 2009). These observations suggest that the compatibility and fluidity of Pluronic F-127 are the dominating factors that contribute to the copolymer's ability to enhance itraconazole dissolution.

As shown in Figure A.4, high concentrations of polymer can cause either bridging flocculation or depletion flocculation, depending on the strength of the polymer–particle adsorption compared to particle–particle cohesion. It is postulated that the formation of loosely aggregated sheets of itraconazole microflakes during SAS crystallization with Pluronic F-127 (Figure 4.12) could be the result of bridging flocculation between the

PEO chains of the adsorbed Pluronic F-127. Should the bridging be due to depletion flocculation, the dissolution enhancements observed in Figure 4.13, attributed to microflake dispersion, would not be realizable. The improvements in itraconazole dissolution when stabilized with Pluronic F-127 thus suggest that the interaction between the PPO block of Pluronic F-127 and itraconazole is stronger than the van der Waals attraction between two adjacent itraconazole particles.

In general, sodium dodecyl sulfate (SDS) has been found ineffective for itraconazole stabilization when used alone (Cerdeira et al. 2010). The self-repulsion of the anionic SDS molecules inhibits their surface coverage, preventing effective stabilization. However, when used in combination with polymeric stabilizers, SDS can interact with the polymer which can reduce self-repulsion and facilitate polymer adsorption to the drug particle surface. In work conducted subsequent to that presented in Chapter 4, the synergistic effects of itraconazole nanosuspension stabilization with Pluronic F-127 and SDS were studied using central composite design to optimize the amount of each stabilizer. While the combination of steric (Pluronic F-127) and electrostatic (SDS) stabilization proved very effective at decreasing itraconazole particle size, the concentrations of stabilizer used (35 wt. % drug) well exceed those approved by the FDA (Sun et al. 2011). Based on the discussion contained in this Appendix, future work may examine the synergistic effects of itraconazole stabilization using FDA approved amounts of electrostatic and steric stabilizers during SAS crystallization.

#### A.4 References

- Cerdeira, A. M., M. Mazzotti, and B. Gander. 2010. Miconazole nanosuspensions: Influence of formulation variables on particle size reduction and physical stability. *International Journal of Pharmaceutics* 396(1): 210-218.
- Chaubal, M. V. and C. Popescu. 2008. Conversion of nanosuspensions into dry powders by spray drying: A case study. *Pharmaceutical Research* 25(10): 2302-2308.
- Derjaguin, B. V. and L. Landau. 1941. The theory of stability of highly charged lyophobic sols and coalescence of highly charged particles in electrolyte solutions. *Acta Physicochim URSS* 14(11): 633-652.
- Kesisoglou, F., S. Panmai, and Y. Wu. 2007. Nanosizing – Oral formulation development and biopharmaceutical evaluation. *Advanced Drug Delivery Reviews* 59(7): 631-644.
- Kumar, V., L. Wang, M. Riebe, H.-H. Tung, and R. K. Prud'homme. 2009. Formulation and stability of itraconazole and odanacatib nanoparticles: Governing physical parameters. *Molecular Pharmaceutics* 6(4): 1118-1124.
- Miller, D. A., J. C. DiNunzio, W. Yang, J. W. McGinity, and R. O. Williams III. 2008. Enhanced in vivo absorption of itraconazole via stabilization of supersaturation following acidic-to-neutral pH transition. *Drug Development and Industrial Pharmacy* 34(8): 890-902.
- Sun, W., S. Mao, Y. Shi, L. C. Li, and L. Fang. 2011. Nanonization of itraconazole by high pressure homogenization: Stabilizer optimization and effect of particle size on oral absorption. *Journal of Pharmaceutical Sciences* 100(8): 3365-3373.
- Thorat, A. A. and S. V. Dalvi. 2012. Liquid antisolvent precipitation and stabilization of nanoparticles of poorly water soluble drugs in aqueous suspensions: Recent developments and future perspective. *Chemical Engineering Journal* 181-182: 1-34.
- Verwey, E. J. W. and J. T. G. Overbeek. 1948. Theory of the Stability of Lyophobic Colloids. Amsterdam: Elsevier.
- Wu, L., J. Zhang, and W. Watanabe. 2011. Physical and chemical stability of drug nanoparticles. *Advanced Drug Delivery Reviews* 63(6): 456-469.

## Appendix B

### Thermodynamic Modeling of GAS Cocrystallization

To supplement the experimental work presented in Chapters 5 and 6, an approach for thermodynamically modeling the GAS cocrystallization technique is included in this Appendix. The following thermodynamic model will provide a rational for determining the appropriate amounts of drug and former needed for cocrystal formation based on the pressure dependent solubilities of components in solution when using compressed CO<sub>2</sub> as an antisolvent for cocrystallization. While the following thermodynamic model is not meant to be used as a cocrystal screen, it is intended to provide a quantitative prediction of cocrystal formation by GAS cocrystallization for drug and former pairs already known to form cocrystals (preferably in solution).

Based on the availability of physical property and solubility literature data, an acetaminophen–oxalic acid cocrystal was selected for illustration of the thermodynamic model. The structures of acetaminophen and oxalic acid are shown in Figure B.1. Cocrystallization of acetaminophen (paracetamol) has been examined for improving the mechanical properties of the drug critical for effective tableting. Acetaminophen cocrystallizes with oxalic acid through hydrogen bond donation from the amide –NH and phenol –OH and hydrogen bond acceptance through the amide –CO and phenol –OH, resulting in the formation of four hydrogen bonds for each acetaminophen molecule as

shown in Figure B.2 (Karki et al. 2009). Thus, the enhancement in mechanical properties is attributed to the layered structure which results from the hydrogen bonding motif.

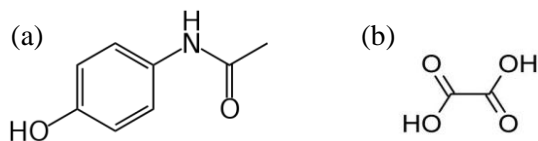


Figure B.1 Chemical structures of (a) acetaminophen and (b) oxalic acid

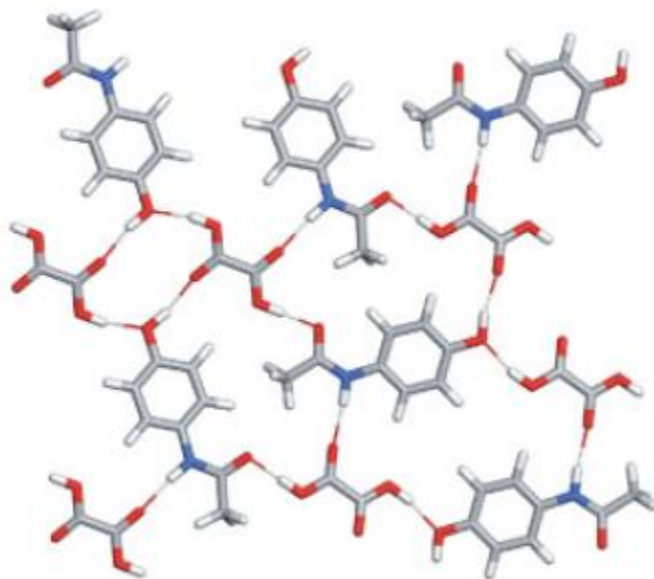


Figure B.2 Hydrogen bonding motif in a 1:1 acetaminophen-oxalic acid cocrystal

Ethanol has been used as a solvent in producing a number of acetaminophen cocrystals, as well as a solvent for the GAS crystallization of acetaminophen using CO<sub>2</sub> as an antisolvent (Oswald et al. 2002; Weber et al. 2005). Thus, the solvent/antisolvent system of ethanol/CO<sub>2</sub> will be used for illustration of the thermodynamic modeling of acetaminophen-oxalic acid cocrystal formation by GAS cocrystallization. The following

two sections describe the phase equilibria, fugacity relations, and binary interaction parameters which comprise the thermodynamic description of GAS cocrystallization.

### B.1 Phase Equilibria

Gas antisolvent crystallization has traditionally been modeled by a ternary system consisting of antisolvent, solvent, and solute in which all three phases (solid, liquid, and vapor) are in equilibrium (Shariati and Peters 2002; De la Fuente et al. 2004; Kikic et al. 2010). The equilibrium criteria for this system are the equality of temperature, pressure, and the fugacity of component “*i*” in all three phases,

$$T^S = T^L = T^V \quad (1)$$

$$P^S = P^L = P^V \quad (2)$$

$$f_i^S = f_i^L = f_i^V \quad (3)$$

The only difference for GAS cocrystallization is the incorporation of two additional components. Gas antisolvent cocrystallization can be effectively represented by a three phase quinary system where  $i = 1$  for the antisolvent (CO<sub>2</sub>),  $i = 2$  for the solvent (ethanol),  $i = 3$  for the API (acetaminophen),  $i = 4$  for the former (oxalic acid), and  $i = 5$  for the cocrystal (acetaminophen–oxalic acid cocrystal). The dilute nature of the solutes in solution prevents significant interaction between the three, such that the quinary system can be represented by three ternary systems (CO<sub>2</sub>-ethanol-acetaminophen, CO<sub>2</sub>-ethanol-oxalic acid, and CO<sub>2</sub>-ethanol-cocrystal). The solubility of CO<sub>2</sub> and ethanol in the solid phase can be neglected such that the solute in each system is considered pure.

The equilibrium equations for the three ternary systems are given in Table B.1, where  $\phi^V$ ,  $\phi^L$ , and  $\phi^S$  are the vapor, liquid, and solid phase fugacity coefficients,  $y$  is

the vapor phase mole fraction, and  $x$  is the liquid phase mole fraction. Each system is described by a vapor-liquid equilibrium for each component, a solid-liquid equilibrium for the crystallizing solute, and two constraints for the composition of the liquid and vapor phases. The CO<sub>2</sub>-ethanol-acetaminophen system is described by equations (4)-(9) for which there are 6 unknowns ( $y_1, y_2, y_3, x_1, x_2, x_3$ ). Likewise the CO<sub>2</sub>-ethanol-oxalic acid system is described by equations (10)-(15) for which there are 6 unknowns ( $y_1, y_2, y_4, x_1, x_2, x_4$ ), and the CO<sub>2</sub>-ethanol-cocrystal system is described by equations (16)-(21) for which there are also 6 unknowns ( $y_1, y_2, y_5, x_1, x_2, x_5$ ).

Table B.1 Phase equilibria equations for ternary three phase systems

<b>System 1</b>	<b>System 2</b>	<b>System 3</b>
CO <sub>2</sub> -ethanol-acetaminophen	CO <sub>2</sub> -ethanol-oxalic acid	CO <sub>2</sub> -ethanol-cocrystal
$\frac{\hat{\phi}_1^L}{\hat{\phi}_1^V} x_1 - y_1 = 0$ (4)	$\frac{\hat{\phi}_1^L}{\hat{\phi}_1^V} x_1 - y_1 = 0$ (10)	$\frac{\hat{\phi}_1^L}{\hat{\phi}_1^V} x_1 - y_1 = 0$ (16)
$\frac{\hat{\phi}_2^L}{\hat{\phi}_2^V} x_2 - y_2 = 0$ (5)	$\frac{\hat{\phi}_2^L}{\hat{\phi}_2^V} x_2 - y_2 = 0$ (11)	$\frac{\hat{\phi}_2^L}{\hat{\phi}_2^V} x_2 - y_2 = 0$ (17)
$\frac{\hat{\phi}_3^L}{\hat{\phi}_3^V} x_3 - y_3 = 0$ (6)	$\frac{\hat{\phi}_4^L}{\hat{\phi}_4^V} x_4 - y_4 = 0$ (12)	$\frac{\hat{\phi}_5^L}{\hat{\phi}_5^V} x_5 - y_5 = 0$ (18)
$\frac{\phi_3^S}{\hat{\phi}_3^L} - x_3 = 0$ (7)	$\frac{\phi_4^S}{\hat{\phi}_4^L} - x_4 = 0$ (13)	$\frac{\phi_5^S}{\hat{\phi}_5^L} - x_5 = 0$ (19)
$\sum_{i=1}^3 x_i - 1 = 0$ (8)	$\sum_{i=1}^3 x_i - 1 = 0$ (14)	$\sum_{i=1}^3 x_i - 1 = 0$ (20)
$\sum_{i=1}^3 y_i - 1 = 0$ (9)	$\sum_{i=1}^3 y_i - 1 = 0$ (15)	$\sum_{i=1}^3 y_i - 1 = 0$ (21)

The liquid and vapor phase fugacity coefficients ( $\hat{\phi}_i^L$  and  $\hat{\phi}_i^V$ ) can be obtained using the Peng-Robinson equation of state. As briefly described in subsection 1.6.2, the Peng-Robinson equation of state for a pure substance is given by,

$$P = \frac{RT}{v-b} - \frac{a(T)}{v(v+b) + b(v-b)} \quad (22)$$

where  $P$  is pressure,  $R$  is the gas constant,  $T$  is temperature,  $v$  is the molar volume, and  $a$  and  $b$  are the van der Waals energy and volume parameters, respectively (Peng and Robinson 1976). For application to multicomponent mixtures, the following mixing rules are applied,

$$a = \sum_i \sum_j x_i x_j a_{ij} \quad (23)$$

$$b = \sum_i x_i b_i \quad (24)$$

where

$$a_{ij} = (1 - \delta_{ij}) a_i^{1/2} a_j^{1/2} \quad (25)$$

The parameter  $\delta_{ij}$  is an empirically determined binary interaction parameter obtained from the regression of experimental data. The pure component equation of state parameters  $a_i$  and  $b_i$  are obtained from,

$$a_i(T) = 0.457235 \frac{\alpha_i(T_r, \omega_i) R^2 T_c^2}{P_c} \quad (26)$$

$$\alpha_i(T_r, \omega_i) = [1 + (0.37464 + 1.54226\omega_i - 0.26992\omega_i^2)(1 - \sqrt{T_r})]^2 \quad (27)$$

$$b_i = 0.077796 \frac{RT_c}{P_c} \quad (28)$$

where  $T_c$  is the critical temperature,  $T_r$  is the reduced temperature,  $P_c$  is the critical pressure, and  $\omega$  is the acentric factor. The critical properties and acentric factors for the components of interest are given in Table B.2.



Table B.2 Critical properties and acentric factors for CO<sub>2</sub>, ethanol, acetaminophen, and oxalic acid

Component	T <sub>c</sub> (K)	P <sub>c</sub> (bar)	ω	Reference
CO <sub>2</sub>	304.2	73.8	0.224	Kikic et al. 2010
Ethanol	516.2	63.7	0.635	Kikic et al. 2010
Acetaminophen	820.0	42.1	0.786	Kikic et al. 2010
Oxalic Acid	796.9	69.6	0.914	Abderafi and Bounahmidi 1999

Finally, the liquid and vapor phase fugacity coefficients of component  $k$  in a mixture can be calculated using,

$$\ln \hat{\phi}_k^L = \frac{b_k}{b} (Z - 1) - \ln(Z - B) - \frac{A}{2\sqrt{2}B} \times \left( \frac{2\sum_i x_i a_{ik}}{a} - \frac{b_k}{b} \right) \ln \left( \frac{Z + \sqrt{Z^2 + 2B}}{Z - \sqrt{Z^2 + 2B}} \right) \quad (29)$$

$$\ln \hat{\phi}_k^V = \frac{b_k}{b} (Z - 1) - \ln(Z - B) - \frac{A}{2\sqrt{2}B} \times \left( \frac{2\sum_i y_i a_{ik}}{a} - \frac{b_k}{b} \right) \ln \left( \frac{Z + \sqrt{Z^2 + 2B}}{Z - \sqrt{Z^2 + 2B}} \right) \quad (30)$$

where the parameters  $A$ ,  $B$ , and  $Z$  are defined as,

$$A = \frac{aP}{R^2T^2} \quad (31)$$

$$B = \frac{bP}{RT} \quad (32)$$

$$Z = \frac{Pv}{RT} \quad (33)$$

Since the crystallization of acetaminophen–oxalic cocrystals is interrelated to the crystallization of both acetaminophen and oxalic acid and the critical properties and acentric factor of the cocrystal are unknown, the phase equilibria equations for System 3 described in Table B.1 will not be solved at this point. Rather, it will be assumed that the

stoichiometric and simultaneous crystallization of acetaminophen and oxalic acid in CO<sub>2</sub>-expanded ethanol will result in the formation of cocrystals which can be effectively represented by crystallization of the two pure components. Validating or invalidating this assumption could be a focus of future work.

In addition to the liquid and vapor phase fugacity coefficients obtained from the Peng-Robinson equation of state, a relationship is needed to represent the behavior of the solid phase. The fugacity of a pure solute at the triple point as proposed by Prausnitz et al. (1998) can be found from,

$$\ln \frac{f_3^S(T, P_{tp})}{f_3^L(T, P_{tp})} = \frac{\Delta H_{fus}}{R} \left( \frac{1}{T_{tp}} - \frac{1}{T} \right) - \frac{\Delta C_p}{R} \left[ \ln \left( \frac{T_{tp}}{T} \right) - \frac{T_{tp}}{T} + 1 \right] \quad (34)$$

where  $P_{tp}$  is the triple point pressure,  $\Delta H_{fus}$  is the enthalpy of fusion,  $T_{tp}$  is the triple point temperature, and  $\Delta C_p$  is the isobaric heat capacity. To extend this definition to other pressures the Poynting correction is employed,

$$f_3^L(T, P) = f_3^L(T, P_{tp}) \cdot \exp \int_{P_{tp}}^P \frac{v_3^L}{R \cdot T} dP \quad (35)$$

$$f_3^S(T, P) = f_3^S(T, P_{tp}) \cdot \exp \int_{P_{tp}}^P \frac{v_3^S}{R \cdot T} dP \quad (36)$$

The solid phase fugacity coefficient ( $\phi^S$ ) can be calculated from the physical properties of the solute given in Table B.3 using:

$$\ln \phi_3^S = \ln \phi_3^L + \frac{\Delta H_{fus}}{R} \left( \frac{1}{T_{tp}} - \frac{1}{T} \right) - \frac{\Delta C_p}{R} \left[ \ln \left( \frac{T_{tp}}{T} \right) - \frac{T_{tp}}{T} + 1 \right] + \frac{v_3^S (P - P_{tp})}{RT} \quad (37)$$

Table B.3 Physical properties of acetaminophen and oxalic acid

	$\Delta H_{fus}$ (J/mol)	$T_{tp}$ (K)	$\Delta C_p$ (J/mol·K)	$v^S$ (cm <sup>3</sup> /mol)	$P_{tp}$ (bar)	Reference(s)
Acetaminophen	27700	441	99.8	117	0.0482	Daubert and Danner 1989
Oxalic Acid	58200	463	50.0	--	0.0215	Daubert and Danner 1989 Schröder et al. 2010

Through the iterative calculation of the fugacity coefficients and liquid and vapor phase compositions the sets of equations given in Table B.1 can be solved using only the critical and physical properties of the components of interest. However, thermodynamic modeling conducted via this approach neglects effects due to interactions between the components. These effects, best elucidated through experimental studies, can be accounted for by the regression of experimental data and the incorporation of binary interaction parameters, as described in the following section.

## B.2 Binary Interaction Parameters

Since experimental data for the ternary systems of CO<sub>2</sub>-ethanol-acetaminophen and CO<sub>2</sub>-ethanol-oxalic acid are extremely limited if available at all, experimental data for the constituent binary systems can be used to determine the binary interaction parameters for the ternary systems (Kikic et al. 2010). The first binary system to consider is CO<sub>2</sub>(1)-ethanol(2). Experimental vapor-liquid equilibrium (VLE) data for CO<sub>2</sub>-ethanol at 40 °C have been reported by a number of researchers (Suzuki et al. 1990, Chang et al. 1997, Galicia-Luna et al. 2000, Joung et al. 2001, Secuianu et al. 2008, Knez et al. 2008), as shown in Figure B.3. The fugacity relations for this system are,

$$x_1 \cdot \hat{\phi}_1^L \cdot P = y_1 \cdot \hat{\phi}_1^V \cdot P \quad (38)$$

$$x_2 \cdot \hat{\phi}_2^L \cdot P = y_2 \cdot \hat{\phi}_2^V \cdot P \quad (39)$$

Modeling the VLE behavior of CO<sub>2</sub>-ethanol in Aspen Properties® (Aspen Technology, Inc., Burlington, MA) using the Peng-Robinson equation of state with  $\delta_{ij} = 0$  gave a poor fit, as shown by the dashed line in Figure B.3. Quantitatively, the goodness of fit for the Peng-Robinson equation of state when modeling experimental data can be assessed by the absolute average relative deviation (AARD),

$$AARD = \frac{100}{N} \sum_1^N \left( \frac{|Calculated - Observed|}{Observed} \right) \quad (40)$$

where  $N$  is the number of data points. Compared to an AARD = 37.2% for  $\delta_{ij} = 0$ , regression of all available experimental data with the Peng-Robinson equation of state gave  $\delta_{ij} = 0.0938$  and an excellent fit with AARD = 4.7%, as shown by the solid line in Figure B.3.

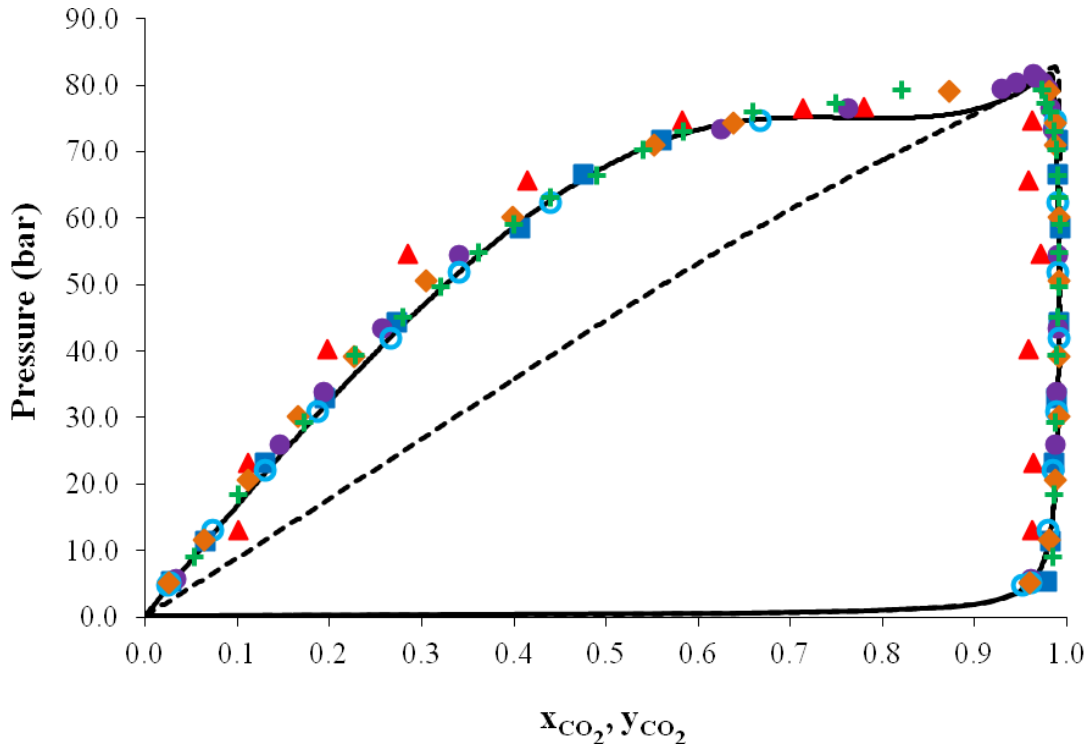


Figure B.3 Vapor-liquid equilibrium of CO<sub>2</sub>-ethanol at 40 °C (Experimental data: Secuianu et al. 2008 (■), Knez et al. 2008 (▲), Joung et al. 2001 (●), Galicia-Luna et al. 2000 (○), Suzuki et al. 1990 (◇), Chang et al. 1997 (+); ..... Peng-Robinson correlation with  $\delta_{ij} = 0$ , — Peng-Robinson correlation with  $\delta_{ij} = 0.0938$ )

The next binary system to consider is ethanol(2)-acetaminophen(3), which can be represented by a solid liquid equilibrium,

$$f_3^S = x_3 \hat{\phi}_3^L P \quad (41)$$

where the mole fraction of acetaminophen in the liquid phase ( $x_3$ ) is equal to the ratio of the solid phase fugacity coefficient to the liquid phase fugacity coefficient since the solid phase is pure acetaminophen. The Peng-Robinson equation of state was used to calculate the liquid phase fugacity coefficient while equation (37) was used to calculate the solid phase fugacity coefficient for a number of temperatures corresponding to experimental data obtained from the literature. The results are shown in Figure B.4. The Peng-

Robinson correlation with  $\delta_{ij} = 0$  was close to the experimental data (AARD = 23.8%), but a  $\delta_{ij}$  of 0.0051 improved the model's fit (AARD = 4.6%), especially around the temperature of interest (40 °C).

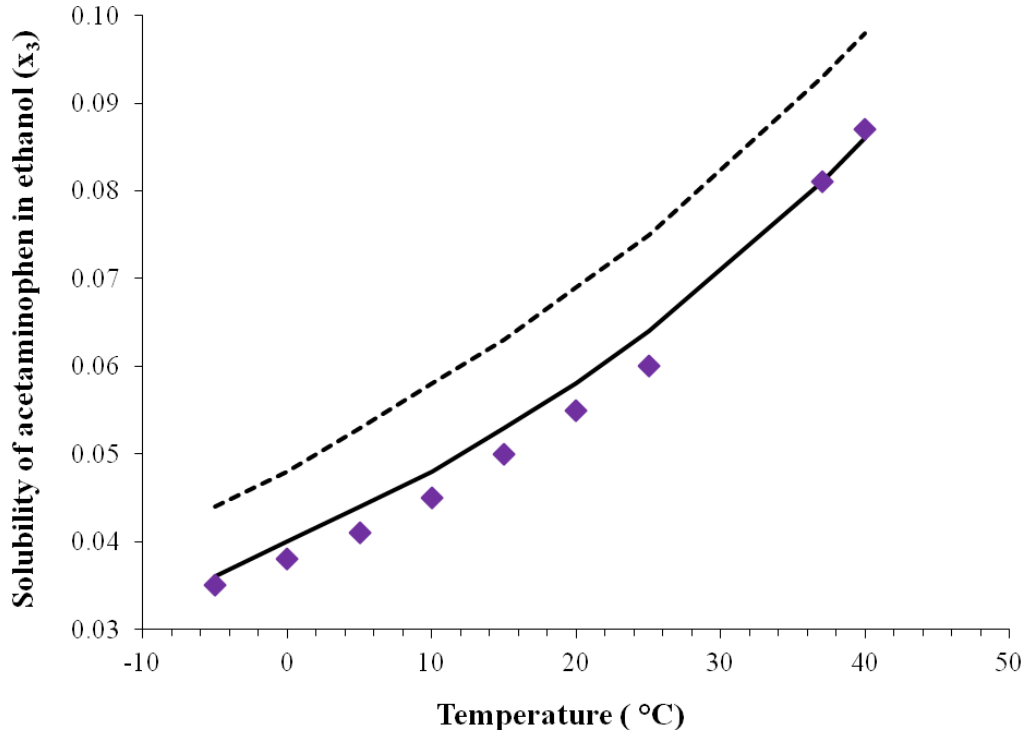


Figure B.4 Solubility of acetaminophen in ethanol as a function of temperature (Experimental data: Granberg and Rasmuson 1999 and Mota et al. 2009 (◆); ..... Peng-Robinson correlation with  $\delta_{ij} = 0$ , — Peng-Robinson correlation with  $\delta_{ij} = 0.0051$ )

The solubility of acetaminophen (3) in supercritical CO<sub>2</sub> can be represented by a solid vapor equilibrium,

$$f_3^S = y_3 \hat{\phi}_3^V P \quad (42)$$

where the fugacity of the solid phase can be written as,

$$f_3^S = P_3^S \hat{\phi}_3^S \exp \left( \int_{P_3^S}^P \frac{V_3^S}{RT} dP \right) \quad (43)$$

The low vapor pressure of acetaminophen allows  $\hat{\phi}_3^S$  to be taken as unity. The incompressibility of solids allows  $v_3^S$  to be considered independent of pressure. Using these simplifications, the solubility of a solid solute in compressed CO<sub>2</sub> is,

$$y_3 = \frac{P_3^S}{P} \left[ \frac{1}{\hat{\phi}_3^V} \exp\left(\frac{v_3^S (P - P_3^S)}{RT}\right) \right] \quad (44)$$

where the fluid phase fugacity coefficient can be calculated from the Peng-Robinson equation of state (Gupta and Shim 2007). The results are shown in Figure B.5. The Peng-Robinson correlation with  $\delta_{ij} = 0$  varied from the experimental data (AARD = 41.8%), but a  $\delta_{ij}$  of 0.0150 improved the model's fit (AARD = 24.7%).

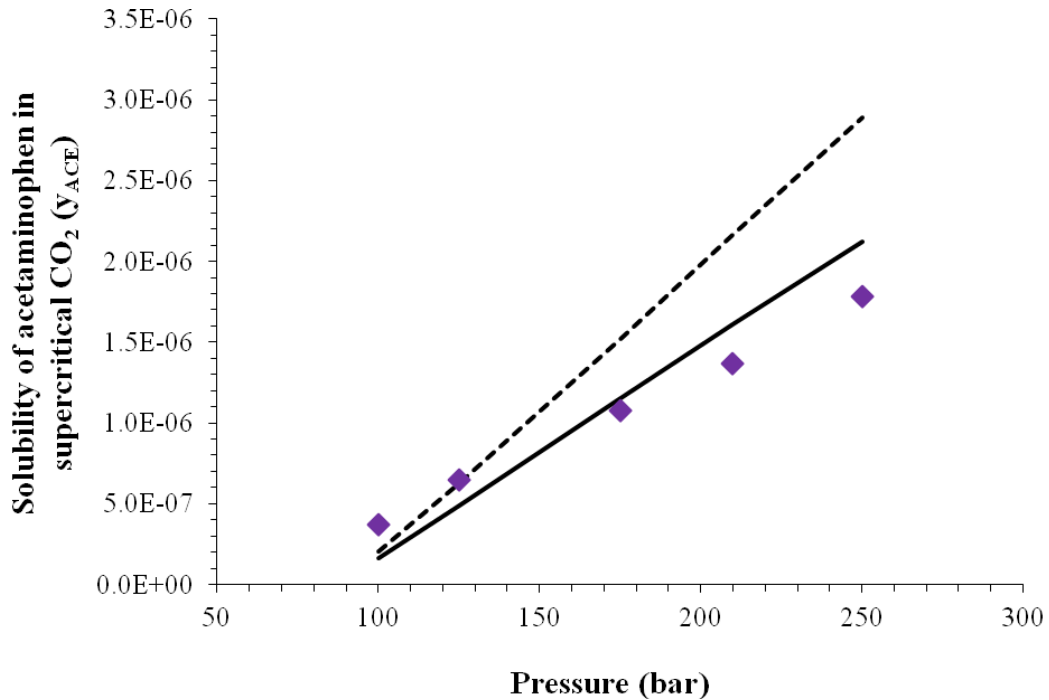


Figure B.5 Solubility of acetaminophen in supercritical CO<sub>2</sub> (Experimental data: Bristow et al. 2001 (◆); ..... Peng-Robinson correlation with  $\delta_{ij} = 0$ , — Peng-Robinson correlation with  $\delta_{ij} = 0.0150$ )

By regressing three types of binary experimental data (CO<sub>2</sub>(1)-ethanol(2), ethanol(2)-acetaminophen(3), and CO<sub>2</sub>(1)-acetaminophen(3)), three binary interaction parameters ( $\delta_{12} = 0.0938$ ,  $\delta_{23} = 0.0051$ , and  $\delta_{13} = 0.0150$ ) for the Peng-Robinson equation of state were determined. These binary interaction parameters can be subsequently used to predict the phase behavior of the ternary system of CO<sub>2</sub>, ethanol, and acetaminophen. An identical procedure would then be carried out for the ternary system of CO<sub>2</sub>-ethanol-oxalic acid to determine its binary interaction parameters.

Application of the binary interaction parameters to the sets of equations given in Table B.1 allows determination of the pressure dependent solubilities, and thus the rates of crystallization, for acetaminophen and oxalic acid in CO<sub>2</sub>-expanded ethanol at 40 °C. Since acetaminophen and oxalic acid form a 1:1 cocrystal, their desired rates of crystallization should be stoichiometrically identical. With knowledge of their pressure dependent solubilities, the starting quantities of acetaminophen and oxalic acid needed to achieve stoichiometric crystallization can be calculated. While it is proposed that stoichiometric matching of drug and former crystallization will facilitate cocrystal formation, experimental confirmation will need to follow thermodynamic model development.

### **B.3 References**

- Abderafi, S. and T. Bounahmidi. 1999. Measurement and estimation of vapor-liquid equilibrium for industrial sugar juice using the Peng-Robinson equation of state. *Fluid Phase Equilibria* 162(1-2): 225-240.
- Bristow, S., T. Shekunov, B. Y. Shekunov, and P. York. 2001. Analysis of the supersaturation and precipitation process with supercritical CO<sub>2</sub>. *Journal of Supercritical Fluids* 21(3): 257-271.



Chang, C. J., C.-Y. Day, C.-M. Ko, and K.-L. Chiu. 1997. Densities and *P-x-y* diagrams for carbon dioxide dissolution in methanol, ethanol, and acetone mixtures. *Fluid Phase Equilibria* 131(1-2): 243-258.

Daubert, T. E. and R. P. Danner. 1989. Physical and Thermodynamic Properties of Pure Compounds: Data Compilation. New York: Hemisphere.

De la Fuente, J. C., A. Shariati, and C. J. Peters. 2004. On the selection of optimum thermodynamic conditions for the GAS process. *Journal of Supercritical Fluids* 32(1-3): 55-61.

Galicia-Luna, L. A. and A. Ortega-Rodriguez. 2000. New apparatus for the fast determination of high-pressure vapor-liquid equilibria of mixtures and of accurate critical pressures. *Journal of Chemical & Engineering Data* 45(2): 265-271.

Granberg, R. A. and Å. C. Rasmuson. 1999. Solubility of paracetamol in pure solvents. *Journal of Chemical & Engineering Data* 44(6): 1391-1395.

Gupta, R. B. and J.-J. Shim. 2007. Solubility in Supercritical Carbon Dioxide. Boca Raton: Taylor & Francis Group.

Joung, S. N., C. W. Yoo, H. Y. Shin, S. Y. Kim, K.-P. Yoo, C. S. Lee, and W. S. Huh. 2001. Measurements and correlation of high-pressure VLE of binary CO<sub>2</sub>-alcohol systems (methanol, ethanol, 2-methoxyethanol and 2-ethoxyethanol). *Fluid Phase Equilibria* 185(1-2): 219-230.

Karki, S., T. Friščić, L. Fábián, P. R. Laity, G. M. Day, and W. Jones. 2009. Improving mechanical properties of crystalline solids by cocrystal formation: New compressible forms of paracetamol. *Advanced Materials* 21(38-39): 3905-3909.

Kikic, I., N. De Zordi, M. Moneghini, and D. Solinas. 2010. Solubility estimation of drugs in ternary systems of interest for the antisolvent precipitation processes. *Journal of Supercritical Fluids* 55(2): 616-622.

Knez, Ž., M. Škerget, L. Ilič, and C. Lütge. 2008. Vapor-liquid equilibrium of binary CO<sub>2</sub>-organic solvent systems (ethanol, tetrahydrofuran, *ortho*-xylene, *meta*-xylene, *para*-xylene). *Journal of Supercritical Fluids* 43(3): 383-389.

Mota, F. L., A. P. Carneiro, A. J. Queimada, S. P. Pinho, and E. A. Macedo. 2009. Temperature and solvent effects in the solubility of some pharmaceutical compounds: Measurements and modeling. *European Journal of Pharmaceutical Sciences* 37(3-4): 499-507.

Oswald, I. D. H., D. R. Allan, P. A. McGregor, W. D. S. Motherwell, S. Parsons, and C. R. Pulham. 2002. The formation of paracetamol (acetaminophen) adducts with hydrogen-bond acceptors. *Acta Crystallographica Section B* 58(6): 1057-1066.

- Peng, D.-Y. and D. B. Robinson. 1976. A new two-constant equation of state. *Industrial & Engineering Chemistry Fundamentals* 15(1): 59-64.
- Prausnitz, J. M., R. N. Lichtenthaler, and E. G. de Azevedo. 1998. Molecular Thermodynamics of Fluid-Phase Equilibria, 3rd Ed. Upper Saddle River: Prentice Hall.
- Schröder, B., L. M. N. B. F. Santos, I. M. Marrucho, and J. A. P. Coutinho. 2010. Prediction of aqueous solubilities of solid carboxylic acids with COSMO-RS. *Fluid Phase Equilibria* 289(2): 140-147.
- Secuianu, C., V. Ferioiu, and D. Geană. 2008. Phase behavior for carbon dioxide + ethanol system: Experimental measurements and modeling with a cubic equation of state. *Journal of Supercritical Fluids* 47(2): 109-116.
- Shariati, A. and C. J. Peters. 2002. Measurements and modeling of the phase behavior of ternary systems of interest for the GAS process: I. The system carbon dioxide + 1-propanol + salicylic acid. *Journal of Supercritical Fluids* 23(3): 195-208.
- Suzuki, K., H. Sue, M. Itou, R. L. Smith, H. Inomata, K. Arai, and S. Saito. 1990. Isothermal vapor-liquid equilibrium data for binary systems at high pressures: carbon dioxide-methanol, carbon dioxide-ethanol, carbon dioxide-1-propanol, methane-ethanol, methane-1-propanol, ethane-ethanol, and ethane-1-propanol systems. *Journal of Chemical & Engineering Data* 35(1): 63-66.
- Weber, A., L. V. Yelash, and T. Kraska. 2005. Effect of the phase behaviour of the solvent-antisolvent systems on the gas-antisolvent-crystallisation of paracetamol. *Journal of Supercritical Fluids* 33(2): 107-113.

## Appendix C

### Peer-Reviewed Publications

1. Ober, C. A. and R. B. Gupta. 2012. Formation of itraconazole-succinic acid cocrystals by gas antisolvent cocrystallization. *AAPS PharmSciTech* 13(4): 1396-1406.
2. Ober, C. A., S. E. Montgomery, and R. B. Gupta. 2012. Formation of itraconazole/L-malic acid cocrystals by gas antisolvent cocrystallization. *Powder Technology* 236: 122-131.
3. Ober, C. A., L. Kalombo, H. Swai, and R. B. Gupta. 2012. Preparation of rifampicin/lactose microparticle composites by a supercritical antisolvent-drug excipient mixing technique for inhalation delivery. *Powder Technology* 236: 132-138.
4. Ober, C. A. and R. B. Gupta. 2012. pH control of ionic liquids with carbon dioxide and water: 1-ethyl-3-methylimidazolium acetate. *Industrial & Engineering Chemistry Research* 51(6): 2524-2530.
5. Ober, C. A. and R. B. Gupta. 2011. Nanoparticle technology for drug delivery. *Ide@s CONCYTEG* 6: 719-731.
6. Sathigari, S. K., C. A. Ober, G. P. Sanganwar, R. B. Gupta, and R. J. Babu. 2011. Single-step preparation and deagglomeration of itraconazole microflakes by supercritical antisolvent method for dissolution enhancement. *Journal of Pharmaceutical Sciences* 100(7): 2952-2965.
7. Costanzo, J. A., C. A. Ober, R. Black, G. Carta, and E. J. Fernandez. 2010. Evaluation of polymer matrices for an adsorptive approach to plasma detoxification. *Biomaterials* 31(10): 2857-2865.

## Appendix D

### Conference Presentations and Posters

1. M. J. DeCuir, C. A. Ober, and R. B. Gupta. A comparison of the effectiveness of solid and solubilized dioctyl sodium sulfosuccinate on oil dispersion using a baffled flask test. *AIChE Southern Regional Conference*, Lexington, KY. April 2013.
2. Ober, C. A., M. J. DeCuir, and R. B. Gupta. A smart oil spill dispersant formulation for reduced environmental impact and consumption. *Gulf of Mexico: Oil Spill & Ecosystem Science Conference*, New Orleans, LA. January 2013.
3. Ober, C. A., M. J. DeCuir, and R. B. Gupta. A smart oil spill dispersant formulation for reduced environmental impact and consumption. *AIChE Annual Meeting*, Pittsburgh, PA. October 2012.
4. Ober, C. A. and R. B. Gupta. Formation of itraconazole-succinic acid cocrystals by CO<sub>2</sub> antisolvent cocrystallization. *AIChE Annual Meeting*, Pittsburgh, PA. October 2012.
5. Ober, C. A. and R. B. Gupta. Dissolution enhancement of itraconazole by gas antisolvent cocrystallization. *AAPS Annual Meeting*, Chicago, IL. October 2012.
6. Ober, C. A. and R. B. Gupta. Design and development of an itraconazole cocrystal with enhanced dissolution. *Auburn University Graduate Engineering Research Showcase*, Auburn, AL. September 2012.
7. R. B. Gupta and C. A. Ober. Nanoscale materials in medicine. *U.S. Department of Energy Sustainable Nanomaterials Workshop*, Washington, DC. June 2012.
8. C. A. Ober and R. B. Gupta. Formation of itraconazole-succinic acid cocrystals in a CO<sub>2</sub>-expanded liquid. *Graduate Student Council Research Symposium at Auburn University Research Week*, Auburn, AL. April 2012.
9. C. A. Ober and R. B. Gupta. A smart dispersant formulation for reduced environmental impact and consumption. *1<sup>st</sup> Annual Meeting of the Consortium for the Molecular Engineering of Dispersant Systems*, San Diego, CA. March 2012.
10. C. A. Ober and R. B. Gupta. Formation of itraconazole-malic acid cocrystals in a CO<sub>2</sub>-expanded liquid. *AIChE Annual Meeting*, Minneapolis, MN. October 2011.

11. S. E. Montgomery and C. A. Ober. Itraconazole cocrystallization by CXL-CF process: effect of operating conditions on particle size." *NSF REU Fellows Program*, Auburn, AL. July 2011.
12. C. A. Ober, S. K. Sathigari, G. P. Sanganwar, R. J. Babu, and R. B. Gupta. Simultaneous production and co-mixing of itraconazole microflakes: a supercritical antisolvent method for dissolution enhancement. *Auburn University Graduate Student Council Research Symposium*, Auburn, AL. April 2011.
13. C. A. Ober, S. K. Sathigari, G. P. Sanganwar, R. J. Babu, and R. B. Gupta. Simultaneous production and co-mixing of itraconazole microflakes with stabilizers and excipients by a supercritical antisolvent method for dissolution enhancement. *AICHE Annual Meeting*, Salt Lake City, UT. November 2010.
14. S. K. Sathigari, C. A. Ober, G. P. Sanganwar, R. J. Babu, and R. B. Gupta. Simultaneous production and co-mixing of itraconazole micro/nanoflakes with stabilizers and pharmaceutical carriers by a supercritical antisolvent method for dissolution enhancement. *AAPS Annual Meeting*, New Orleans, LA. November 2010.